N° d'ordre : 4312

THESE

PRESENTEE A

L'UNIVERSITE DE BORDEAUX I

ECOLE DOCTORALE DES SCIENCES PHYSIQUE DE L'INGENIEUR

Par **YOUNUS AYESHA**

POUR OBTENIR LE GRADE DE

DOCTEUR

Spécialité : Lasers Matière et Nanosciences

****

Imagerie Térahertz 2D et 3D: Application pour l'étude des matériaux du patrimoine culturel

****

Devant la Commission d'examen formée de :

Dominique Coquillat	Directeur de Recherche, Montpellier 2	Rapporteur
Jean-Louis Coutaz	Professeur, Université de Savoie	Rapporteur
Michel Menu	Ingénieur de Recherche, Paris	Examinateur
Jean-Pierre Delville	Directeur de laboratoire, Bordeaux 1	Président
Patrick Mounaix	Directeur de Recherche, Bordeaux1	Co-directeur de thèse
Emmanuel Abraham	Maître de conférences, Bordeaux 1	. Directeur de thèse
Pascal Desbarats	Maître de conférences, Bordeaux 1	Invité

Acknowledgments

First and foremost, I express my deep sense of profound gratitude and indebtedness to my supervisors Dr. Emmanuel Abraham and Dr. Patrick Mounaix for their dynamic supervision, propitious guidance, keen interest, philanthropic attitude, generous assistance and technical guidance all along the course of this research period and encouragement/suggestions during the write up of the manuscript. It was certainly a matter of pride to work under their guidance.

I would like to thanks my jury members for sparing some of their precious time in order to review and evaluate my research work: Dr. Dominique Coquillat, Dr. Jean-Louis Coutaz, Dr. Michel Menu, Dr. Jean-Pierre Delville and Dr. Pascal Desbarats.

I like to thanks my collaborators without whom some of my work would not have been possible, the group of Dr. Pascal Desbarats (LaBRI University of Bordeaux 1), especially Benoit Recur and Cédric for providing their skills and invaluable insights for the analysis of THz tomography data. I would like to thanks Jean-Pascal Caumes and his colleagues (ALPhANOV University of Bordeaux 1) for their collaboration and helpful assistance in the development of optical system. I would like to pay my thanks to William Benharbone for programming the Labview and all his help in this context. I wish to extend my thanks to administrative and computer science staff, especially Laurette, Isabelle, Annie, Richard Perrier and Hassan Akrache.

Special thanks to all my colleagues and friends in TERASLAM: Prof. Lionel Canioni, Dr. Jean-Christophe Delagne, Dr. Bruno Bousquet, Dr. Inka Manek-Hönninger, Dr. Arnaud Royon, Dr Mathieu Bellec, Dr. Grégoire Travaillé, Dr. Edwin Nguema, Dr. Riad Yahiaoui, Dr. Yanick Petit, Dr. Nicolas Marquestaut, Dr. Jean-Paul, Amina Ismaël, Josette El Haddad and Gautier Papon for all their company and cooperation.

I fully acknowledge the financial support i have received from the Higher Education Commission (HEC) Pakistan for completing my PhD in France. I would like to thanks all my Pakistani colleagues and friends in Bordeaux for their help, moral support and cheerful company throughout this time period.

Last but not least, this work would not have been possible without the constant support and encouragement of my lovely parents and family over the years, thank you all for believing in me.

Dedicated

To My Dear Parents

Who have always preoccupied themselves
for my education and my success

TABLE OF CONTENTS

Summary

List of Figures

List of Tables

List of Abbreviations

Acronym	Meaning
THz	Terahertz
CW	Continuous Wave
SNR	Signal-to-Noise Ratio
CCD	Charged Coupled Device
QCL	Quantum Cascade Laser
BWO	Backward Wave Oscillator
TDS	Time-Domain Spectrometer
LIA	Lock-in Amplifier
AOM	Acoustic Optic Modulator
HDPE	High Density Polyethylene
CT	Computed Tomography
SART	Simultaneous Algebraic Reconstruction Technique
OSEM	Ordered Subsets Expectation Maximization
BFP	Back-Filtered Projection
2D	Two-Dimensional
3D	Three-Dimensional

General Introduction

O, how much simpler things would be
If eyes could paint or brush could see.
(Robert Brault)

Art is a question mark in the minds of those who want to know what's happening. There are several rapidly developing non-destructive physical methods that are increasingly used for the analysis and assessment of art objects. These technologies are posed to bring about drastic changes in the attribution and inventory characterization procedures carried out by museums, private collections, art dealers and art community as a whole. Certainly today non-destructive evaluation of art objects is becoming more and more sophisticated. The care for cultural patrimony has a long history including methods for deterioration detection, authentication, revealing forgeries and fakes, preservation and restoration. With their latest techniques, the researchers are breaking new grounds, for the first time allowing curators and others to detect the specific composition of each and every stroke, truly getting into the depth of the artwork, finding secrets and hidden master pieces. Maurizio Seracini, an art diagnostic, used his investigational skills to show that Leonardo's "Adoration of the Magi" has been painted over by other artists and can no longer be considered as a true Da Vinci. Another news was revealed in NewYork times in 2002 by the Seracini statement that lost fresco "Battle of Anghiari" masterpiece of great Leonardo, may be lying behind murals of Giorgio Vasari in Florence's Palazzo Vecchio [Times]. Scientific analysis led to the discovery of a narrow cavity behind the Vasari fresco "Battle of Marciano," intentionally created by the artist to preserve the master's work by Leonardo [Pieraccini 2005].

The examination of artworks is of high importance for curators, art historians and restorers. These investigations reveal information, which is of general art historical interest. The knowledge on the artists' materials that were available in particular regions and periods can help in dating artefacts. Knowing the ingredients can help identify, authenticate and perhaps most importantly, repair some of the world's most valuable and historically significant art pieces. Several techniques are used for the inspection of artwork ranging from infrared to ultraviolet and X-rays to acoustical methods. The suitability of each method can depend upon the composition, dimension, condition and nature of the sample under test. Each of the existing technique has some limitations depending upon the nature of utilized radiation source. For instance X-rays sometimes cannot be applied to delicate samples owing to the fragility/uniqueness of the sample and the possible problem of sample radiometric dating after X-ray irradiation especially for ceramics samples [Aitken 1985]. Ideally the method of evaluation should be non-destructive, contactless, non-invasive, spatially precise and applicable in *situ*. Fortunately one part in electromagnetic spectrum known as "Terahertz region" fulfills above mentioned criteria. In this thesis, we restrict ourselves to this Terahertz (THz) area and propose to explore wide applications of THz radiation especially in the field of art science to provide complementary data for the art scientists.

Previously known as the *Far Infrared Range*, the THz frequency domain (roughly 100 GHz - 10 THz) represents an exceptionally under-used domain of the electromagnetic spectrum. Nevertheless, from the past decade, due to its unique features, the THz waves has emerged as a unique radiation for applications in various disciplines such as physics, chemistry, astronomy, medicine, telecommunication, industrial inspection, biology, pharmaceutics, security and screening etc [Chan 2007, Jepsen 2011]. Being non-destructive and contactless in nature the radiation can penetrate opaque materials and can be used to obtain fingerprint spectra whose characteristics depends on the intermolecular behaviour. THz waves are able to perform three-dimensional (3D) material mapping and can reveal the internal structure of non-metallic objects. This can be particularly interesting in art science to explore unopened doors, observing hidden underdrawings and paint layers embedded behind various surfaces.

The scope of our research work is to demonstrate the potential of THz imaging for the non-destructive and contactless analysis of artworks. We expect that THz spectroscopy and imaging techniques can become a new analytical method for heritage science applications. As a preliminary research work during my Master internship, we started working on a previous local project "TeraBook" in collaboration with a local private company i2S[1]. During this project, we investigated the THz spectroscopic properties of various inks and papers in order to evaluate the potential of THz radiation to recognize the characters deposited on a document and scan different pages without touching them. Naturally we analyze materials such as graphite, papers and inks strongly connected to the world of artwork. From this preliminary research, we move ahead for exploring in details various art objects. By art objects, one can think of paints on canvas, frescos, painted wood or sculptures, pottery, jars and real historical master-pieces. In this context we advanced our work for the spectroscopic analysis of pigments and two-dimensional (2D) imaging of painting by standard pulsed THz time-domain spectrometer (THz-TDS).

Meanwhile during the TeraBook project, we started interacting with researchers from the LaBRI[2] (Laboratoire Bordelais de Recherche en informatique) experts in image vision and data processing. Especially, the group of Pascal Desbarats is specialized in developing reconstruction algorithms for X-ray computed tomography (CT). We planned to perform THz CT and collaborated with LaBRI fellows for THz CT data analysis and image reconstruction. Naturally, THz CT is also the scope of research work presented in this thesis since a complete 3D volumetric scan is essential to explore every feature of investigated art samples. Simultaneously, we feel the need to build some optical bench which should be compact, simple and portable so that it can facilitate *on site* 2D and 3D investigation of art samples. For this purpose we collaborated with Jean-Pascal Caumes in

[1] http://www.i2s.fr/
[2] http://www.labri.fr/

ALPhANOV[3] (Centre Technologique Optique et Lasers) for the development of a portable THz imaging setup. We build a continuous wave (CW) millimeter system which was further carried for *on-site* imaging at the museum of Aquitaine (France).

The presented research work seeks to advance the applications of THz radiation as a non-destructive evaluation tool by investigating various opaque objects particularly artworks and extracting information about the sample content that will aid in the assessment of object structure and will provide contextual knowledge about the sample. The manuscript is divided into four main chapters, which are listed below with a brief description:

- Chapter 1 provides short background information about THz radiation sources, sensors and their wide applications in various fields. General imaging techniques for non-destructive evaluation of materials within and out of THz range will be mentioned.

- Chapter 2 is devoted to illustrate the experimental configurations that we developed in order to carry out this imaging work. Techniques for generating and detecting THz radiation along with optical benches and other necessary information will be described. We will provide the system resolution, beam propagation and theoretical study to extract spectroscopic information about the sample. To illustrate the potential of these optical setups for THz imaging, a general image gallery will be presented.

- Chapter 3 demonstrates the use of pulsed and continuous THz imaging methods for the evaluation and inspection of various artworks. Pigments and other artist's media were measured to find their characteristics spectra in THz range. The temporal delays and intensity features of transmitted/reflected THz pulses were measured in order to try to identify hidden underdrawing. From graphite written inscriptions to art paintings, wax seals to real historical art samples from Museum of Aquitaine, this chapter will explore several applications of THz radiation proving their potential to definitely help art scientists and curators.

- Chapter 4 presents some results of THz CT obtained by our optical systems. A detailed analysis about THz beam refraction losses and possible difficulties in signal analysis for final image reconstruction will be shown. Two iterative methods are utilized for the first time to reconstruct THz CT images and compared with standard back-filtered algorithm. A study of image quality with respect to the choice of reconstruction method with optimized projection angles will be elaborated. Finally we will show CT results for a complete volumetric visualization of 3D opaque samples and art objects.

[3] http://www.alphanov.com

- Finally, we will give a summary of this research work and will propose some future perspectives for the advancement, progress and improvement of this THz imaging work. A list of references for all chapters, along with two annexes is included at the end of thesis.

CHAPTER 1

BackGround

This chapter is divided into two main sections. The first section will give a brief introduction about THz radiation. THz radiation sources and detectors will be discussed. The unique distinct properties of THz radiation along with their application in the field of THz imaging and spectroscopy will be presented. In the second section, common imaging techniques and methods associated with non-destructive material evaluation will be mentioned.

Section 1: Introduction

1.1. Electromagnetic Spectrum and THz Region

THz radiation occupying a large section of the electromagnetic spectrum was first isolated in 1897 by Heinrich Rubens [Rubens 1897]. The first occurrence of the term "THz" in this transaction is attributed to Fleming in 1974, where the term was used to describe the spectral line frequency coverage of a Michelson interferometer [Fleming 1974]. However, new initiatives and advanced developments remain unexplored and inaccessible in this region for a long time. "THz Region" in its broadest description encompasses frequencies invisible to naked eye in the range from 100 GHz to roughly 10 THz, corresponding to the sub-millimeter wavelength range between 3 mm and 30 µm (Figure 1.1).

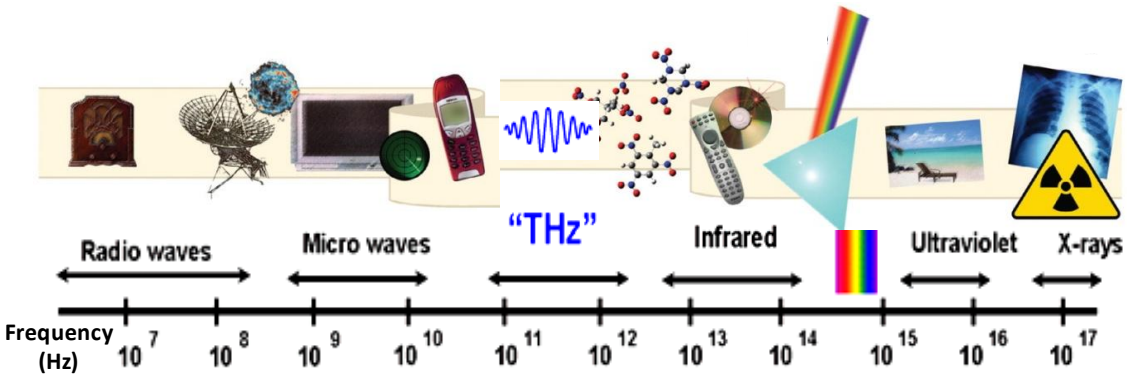

Figure 1.1: The electromagnetic spectrum with different sections scaled by corresponding frequency and abundantly used symbol items.

Bridging the boundary of infrared and microwave regions this so-called shadowy gap remains nearly untapped for a long time period due to failure of the optical techniques to operate below a few hundred THz and likewise the failure of electronic methods to operate above a few hundred gigahertz. Below the THz range, one typically detects the electric field of a propagating wave using an antenna, whereas at higher frequencies one generally speaks of the intensity or irradiance, proportional to the flux. In the optical and infrared ranges, photon energies and the relevant energy level spacing is generally much larger or comparable to k_BT, the thermal energy at room temperature. In contrast, in the microwave regime, energy level spacings are smaller than k_BT. The THz region is therefore a natural bridge between the quantum mechanical and classical descriptions of electromagnetic waves

and their interaction with materials. Therefore, THz radiation uniquely straddles these two different worlds of opinions and originates by melding of both concepts.

1.2. Brief History of THz Sources and Detectors

Lack of high power, low cost and portable room temperature THz sources/detectors is the most significant limitation for the development of efficient THz systems. However there appears a vast array of potential sources/detectors with relative development and advances in high speed opto-electronics and materials research, which continue to provide new candidates. We cannot go into the deep details and working theories of these sources/detectors in this thesis but a brief description is given below.

1.2.1. THz Sources

THz radiation is emitted as part of the blackbody radiation from any materials with temperatures greater than about 12 K, but this thermal emission is very weak. Scientifically, producing coherent THz radiation was technically challenging until late 1980's but the fundamentals of free space THz optoelectronics have seen significant advances with the development of stable, turn-key, ultrafast lasers and progresses in microelectronics fabrication. Today THz sources may be broadly classified as incoherent thermal sources, broadband pulsed sources or narrowband CW sources. Each of these sources has different output power, efficiency, bandwidth, dynamic range and technological implementation [Coutaz 2008].

Broadband THz sources are usually laser driven, utilizing short laser pulses to excite or probe different materials. Photoconduction and optical rectification are commonly used techniques for producing broadband THz sources. In mid-seventies, Auston first employed a photoconductive switch to generate THz signals by utilizing phenomenons of both optics and electronics [Auston 1975]. Photoconductive emitters are capable of producing relatively large average THz powers in excess of 40 μW with normal bandwidth range of 4 THz [Zhao 2002]. Typical photoconductors used materials like semi-insulating Gallium Arsenide (GaAs), low-temperature grown GaAs [Tani 1997] and Indium GaAs (InGaAs) semiconductor [Suzuki 2005]. The bandwidth of the radiated THz spectrum depends on the laser bandwidth along with the emitter and detector properties. Emission up to 15 THz has been reported [Tani 2002, Shen 2004]. Another alternative method, named optical rectification is a second-order optical non-linear effect based on difference-frequency mixing. The first demonstration of this technique was given by Yang *et al.* by utilizing a lithium niobate ($LiNbO_3$) crystal for generating far infrared radiation [Yang 1971]. To improve optical rectification, much research was focused on investigating different material properties for this purpose such as GaAs and zinc telluride (ZnTe), organic crystals such as the ionic salt 4-dimethyamino-N-methylstilbazolium tosylate (DAST) and many other materials [Zhang 1992, Rice 1994]. Currently, ZnTe is the material of choice due to high

laser damage threshold and best phase-match conditions with Ti:Sapphire laser. The optical rectification method has the advantage of providing very high bandwidths usually up to 50 THz [Huber 2000]. Semiconductor surfaces have been widely adopted for generating THz radiations, by illuminating with ultra-short laser pulses [Lewis 2006, Ko 2008]. This phenomenon known as surface emission will be explained later in detail in chapter 2. THz radiation can also be generated using air [Xie 2006, Thomson 2010]. In brief, an infrared laser pulse is focused onto ambient air to generate air plasma. Before the focal point, a beta barium borate (BBO) crystal is inserted to create second harmonic generation, which acts as AC bias at the focal point to polarize the plasma by drifting the electrons field away from nuclei. This process creates a transient photocurrent and as a result a strong THz field is generated. Using an air-plasma, coherent generation of THz radiation with a continuous spectrum covering the range up to 100 THz has been demonstrated [Blank 2010]. Some general specifications of commonly used broadband THz sources are given in table 1.1. Another high power source was first demonstrated by Carr *et al.* [Carr 2002]. They used a method based on energy recovered linacs to accelerate electrons to relativistic energies. This method produces THz radiation with an average power of nearly 20 W which is much higher than any other source.

	Photoconductive Antenna	**Surface Emission**	**Optical Rectification**	**Plasma**
Bandwidth	Limited through carrier collison time, typically 4 THz, up to 50 THz demonstrated	Limited through carrier collision time	Very broad possible (up to 100 THz) dependant on phase matching and absorption of material	Maximum bandwidth (limited by pump pulse lenght)
Spectral Quality	Good	Good	Varying (dependant on bandwidth)	Excellent
Efficiency	High (10^{-3}) but limited to low intensities	Medium (10^{-5}), limited intensity (damage to material, saturation)	Dependant on pump intensity, 10^{-3} from 30 µJ pulses demonstrated	Pump intensity dependent, 10^{-4} from 0.5 mJ pulses demonstrated

Table 1.1: Normal bandwidth range, spectral quality and efficiency of commonly used broadband THz generation methods.

Narrowband THz sources could be based upon up-conversion of electronic radio frequency sources, down-conversion of optical sources, with different kinds of lasers including gas lasers, free electron lasers and particularly quantum cascade lasers. One of the earliest THz sources developed in 1964 was a hydrogen cyanide CW gas laser operating at 1.12 THz [Gebbie 1964]. Original efforts for generating narrowband sources began in 1970 using non-linear photo-mixing of two laser sources. Tunable continuous wave radiation has been demonstrated by mixing two frequency offset lasers in

low temperature grown GaAs [Morris 1977]. Semiconductor THz lasers are further technique with extreme promises. In the past, these lasers have revolutionist applications because of their small size, low costs and high efficiency. Such a laser was first demonstrated over 20 years ago in lightly doped P-type germanium as a result of hole population inversion induced by crossed electric and magnetic fields [Komiyama 1982]. These lasers are tunable through the applied magnetic field or external stress. However, they exhibit many inherent limitations such as low efficiency, low output power and need for cryogenic cooling.

Quantum Cascade Laser (QCL) was first demonstrated by J. Faist *et al* in 1994, based on a structure of a series of coupled quantum wells constructed by molecular beam epitaxy [Faist 1994]. In QCL, inter sub-band or inter mini-band transitions in layered semiconductor hetero-structures are used to generate photons in the mid-infrared region of the spectrum. By appropriately engineering the thickness of the different semiconductor layers, the electron motion is confined along the growth direction, thereby splitting the conduction band into a number of discrete states. The corresponding electron transition energies can, in principle, be tailored to cover a wide range of wavelengths, from the far to the mid-infrared, using InP or GaAs based III–V compounds. These unipolar injection lasers were named "Quantum Cascade" from the possibility of stacking together successive active regions to generate a multiplicity of photons for each injected electron. At present depending upon the generated wavelength, QCL can be operated well above liquid helium temperature and comes close to the liquid nitrogen temperature, which facilitates the use and development of such THz lasers [Belkin 2008, Wade 2008].

Solid state electronic devices also entered the low frequency part of the THz region. In this context, photo-mixing technique which relies on the non-linear mixing of two closely spaced laser wavelengths, generating a beat oscillation at the difference frequency, is very effective. One of the benefits of using this method is the wide tunability of the output frequency. The uni-travelling carrier photodiode which produces high quality sub-THz waves by means of photo-mixing is one of the most promising devices. In this method, THz waves are generated by the optical beat of the light from two different wavelength laser diodes, the emission frequency is typically tunable up to 1.5 THz. Being first reported in 1997 [Ishibashi 1997], uni-travelling carrier photodiodes have become very promising by demonstrating output powers of 20 mW at 100 GHz [Nagatsuma 2003] and 25 μW at 0.9 THz [Renaud 2006].

Free electron based sources like Klystrons, traveling wave tubes, backward wave oscillators (BWO) and Gyrotrons [Gold 1997] are also been extensively studied. With the exception of Gyrotrons designed for reaching high powers, these sources suffer from simple scaling problems, metallic wall losses and need of high magnetic and electric fields. BWO is a slow wave table top device operating at moderate powers between 1-100 mW. They operate with an accelerating potential in the range of 1 to 10 KV and axial magnetic field of 1 T. A number of different BWOs can be implemented in integrated system to cover altogether a range of 30 GHz to 1.7 THz [Dobroiu 2004].

In addition, THz wave parametric oscillators [Kawase 2005], plasma wave photo-mixers [Ryzhii 2006], Bloch oscillators [Alekseev 2004] and generation from resonant tunneling diodes and photonic crystals [Shao-wei 2003] became new sources of THz radiation. High frequency Gunn, IMPATT and TUNNET diodes are being developed by several research groups [Eisele 2005]. We have also used a Gunn Diode in our developed optical setup which will be described later in the next chapter. A general overview of output powers and usable range obtained by different THz systems is given in figure 2.

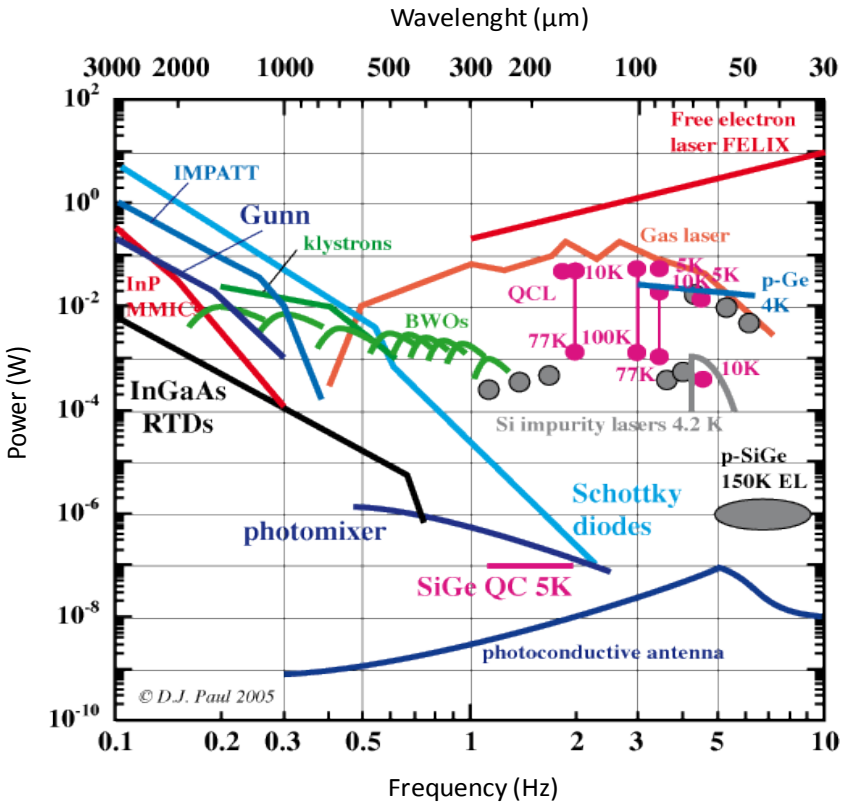

Figure 1.2: Average power, usable frequency range and output type in different THz sources.

1.2.2. THz Detectors

The detection of THz signal is another active research area. The low output power of THz sources coupled with relative high levels of thermal background radiation in this spectral range has necessitated highly sensitive detection methods. THz systems detection can be subdivided into two groups:

- Non-coherent detection systems (with direct detection sensors), which allow only signal amplitude detection and which, as a rule, are broadband detection systems. Their main advantage lies in the relative operation simplicity without the need of adjustment in wide frequency band.

- Coherent detection systems, which allow detecting not only the amplitude of the signal but also its phase. This feature is important from the point of view of increasing information received from the object. It also allows us to realize higher detector sensitivity and spectral resolution characteristics.

Direct broadband detectors based on thermal absorption are commonly used for detecting THz radiation, like bolometer, Golay cell and pyroelectric detector. Bolometer and pyroelectric sensors are the oldest and most conventional methods of detection [Kreisler 2000]. Liquid-helium cooled bolometers are broadband and sensitive THz wave detectors, but they are difficult to implement in real fields because they use liquid-helium. Compact Golay cells can detect a frequency range of 0.02–20 THz with a high dynamic range of 50 dB [Hargeaves 2007]. However they suffer from a long response time (a few tens of ms) and the maximum input power is limited to a few tens of µW [Tydex]. Pyroelectric detectors cover a spectral range from 0.1 to beyond 20 THz with millisecond response time and compact units are available [Spectrum detector]. Performance of these direct detectors is limited to level of background noise in the system. The advantage of direct detection is relative simplicity and possibility of designing large format arrays [Staguhn 2003].

In applications requiring high spectral resolution, heterodyne sensors are preferred [Siegel 2002, Hubers 2008]. These methods can achieve very low detection limits, which are several orders lower than that of the direct detection methods. In heterodyne detectors signals from THz and sub-THz frequencies are down converted to intermediate frequency signals, preserving the amplitude and phase information of the incoming radiation. Any non-linear electronic device can be used as a mixer. Frequently used mixers are forward biased Schottky diodes, superconductor-insulator-superconductor tunnel junctions or super-lattices [Karpov 2004, Shiktorov 2006]. A planer Schottky diode mixer has also been operated successfully at 2.5 THz [Gaidis 2000]. Schottky diodes are fairly compact but their cost is very high beyond 1 THz. Alternative narrowband detectors, such as electronic resonant detectors based on fundamental frequency of plasma waves in field effect transistors has been also demonstrated [Teppe 2006, Knap 2009]. The physical mechanism of the detection is related to the plasma waves excited in the transistor channel and significant improvement in the active devices demonstrated the possibility of using High Electron Mobility Transistors as an efficient detector in future works [Knap 2002]. Our group has also reported the possibility of using High Electron Mobility Transistors as an efficient device for detection of pulsed THz electric field [El Fatimy 2009]. Recently, THz detection and imaging is reported by highly sensitive silicon CMOS detector. These detectors are efficient for imaging in a very wide frequency range from ~0.27 THz up to 1.05 THz [Schuster 2011].

For pulsed THz detection, two commonly utilized coherent methods are based upon photoconductive sampling and electro-optic sampling, each of which relies on ultrafast laser sources. Historically a photoconductive antenna was first used to detect THz radiation [Auston 1983].

Ultrahigh bandwidth detection has been demonstrated by using photoconductive antenna detectors with detectable frequencies in excess of 60 THz [Kono 2001]. Electro-optic detection is an alternative widely used method with ultra wide bandwidth and parallel imaging capability [Wu 1995]. Extremely high detection bandwidths in excess of 100 THz have been demonstrated [Brodschelm 2000].

1.3. Characteristic Features of Terahertz Radiation

Several remarkable features of THz radiation triggered research to develop this frequency band for imaging applications. THz waves are non-destructive and intrinsically safe in nature, having low photon energy (nearly 4 meV at 1 THz) [Siegel 2002]. In comparison, a typical X-ray photon has energy in KeV range, which is 1 million times higher than a usual THz photon. Research into safe level of THz exposure has also been carried out in medicine through studies on keratinocytes [Bourne 2008] and blood leukocytes [Berry 2003], neither of which has revealed any detectable alternations. This proves the non-ionizing nature of THz radiation in the best of our knowledge.

THz radiation interacts strongly with polar molecules, a prime example being water. Water molecules absorb THz waves, on the one hand limiting penetration of the radiation in moist substances, and on the other hand making it readily detectable even in very low concentrations [Banergee 2008]. For this reason, THz waves can provide a better contrast for soft tissues then X-rays. THz radiation can penetrate most dielectric materials and non-polar substances such as wood, paper, cloth, plastic, ceramic, etc. with reasonable attenuation. The radiation is totally reflected from metallic surfaces and partially reflected from interfaces between non-metallic materials with different refractive indices, enabling objects to be detected beneath various surfaces.

Certain molecules have dense and distinctive absorption spectra and characteristic fingerprints in the far-infrared range. The unique rotational, vibrational and translational responses of materials within the THz range provide information that is generally absent in optical, X-ray and nuclear magnetic resonance images. This mechanism leading to THz absorption in molecular and bimolecular systems is dominated by the excitation of intramolecular as well as intermolecular vibrations between weakly bound molecular entities [Watler 2010]. Owing to the highly collective character of these low-frequency vibrational modes, involving the movement of large portions of the molecules, spectroscopy with THz radiation enables the investigation of materials with respect to their molecular structure and composition [Yamaguchi 2005].

1.4. Potential Applications of THz Imaging

The principle applications of THz technology are applicable to various domains which provide unprecedented sensing capabilities for many research fields (Figure 1.3) including biology, pharmaceutics, medical science, industrial non-destructive evaluation, material science, environmental monitoring, security, astronomy and basic science [Chan 2007]. Information and communication

technologies have also a strong potential to benefit from THz technology where it is used for a wide range of applications, such as wireless communication, high speed data processing and satellite communications. Beside this, semiconductor device diagnostics, trace gas analysis, moisture analysis for agriculture, quality control of packaged goods, conservation of artwork, palaeontology, atmospheric sensing, chemical analysis and many other disciplines of physics and chemistry are among a growing number of potential THz applications [Jansen 2010, Jepsen 2011].

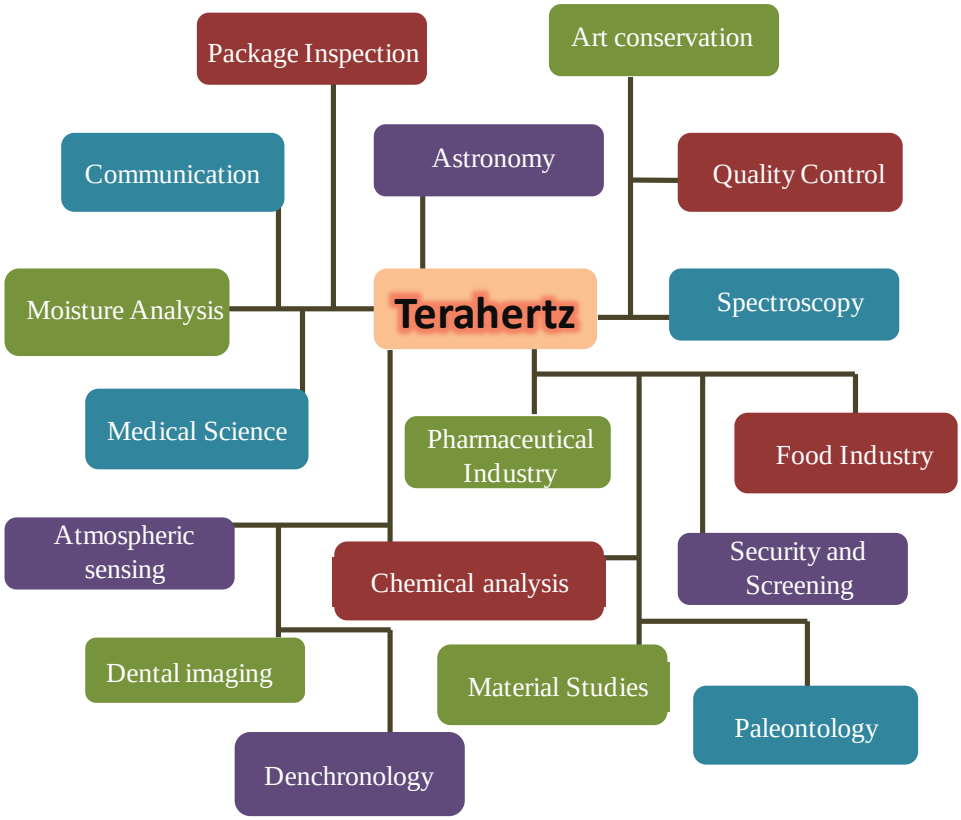

Figure 1.3: General scheme of explored and future THz spectroscopy and imaging applications.

THz imaging and spectroscopy have been applied to huge variety of materials in numerous fields in order to determine the potential of this emerging technology and subsequent development of systems. Imaging electronic components and microchips [Kawase 2004], tissue burn reflectometry [Ciesla 2000, Dougherty 2007] and tooth cavities [Zinoyev 2002] are some of the explored examples. As an example, THz image of a sliced tooth sample is shown in figure 1.4. This example demonstrates that THz radiation can be used as a potential indicator for crystallinity of dental tissues. THz radiation is capable of distinguishing between enamel and dentin portions of the tooth sample [Schimer 2010].

Medical science is a fertile field for THz imaging because unlike X-rays they are not harmful to the tissues [Pickwell 2006]. Although THz waves do not penetrate far into the body, it would be possible to project THz endoscopically, as in optical coherence tomography. Examples of diagnosis of

cancerous tissues with THz radiation are reported as they exhibit different hydration levels from normal tissues [Nikagima 2007, Brun 2010]. The poor transmittance of the THz radiation is one of the main hurdles in medical diagnosis as they have limited penetration of few millimeters. However researchers have found that THz waves can go deeper (up to depths of 2 centimeters) in breast because fatty tissue is more transmissive [Fitzgerald 2006, Grachey 2010].

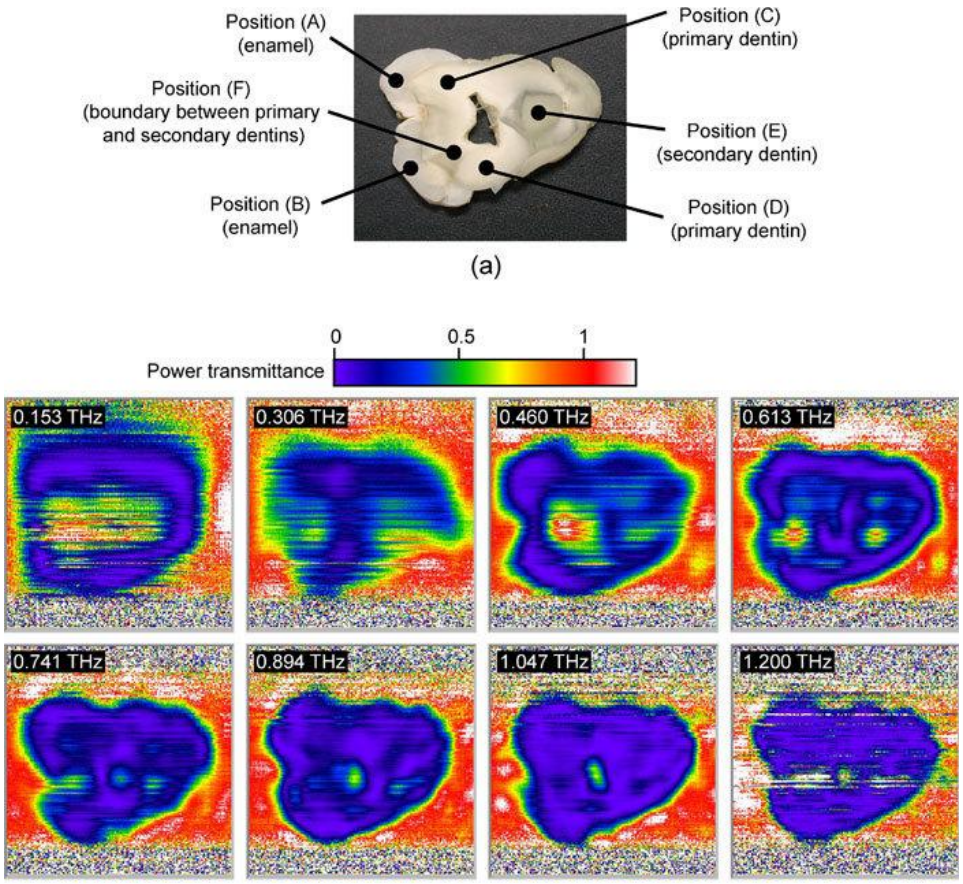

Figure 1.4: Top, Photograph of a sliced tooth sample. Bottom, THz spectral images of transmittance in the tooth sample at various frequency values. [Schimer 2010].

Gas sensing is an application of THz spectroscopy that was of early interest for industrial and homeland security monitoring. The identification of gases signature can be done in milliseconds through lookup tables once an exact determination of the spectral line frequency has been made [Mittleman 1998]. Analysis of cigarette smoke was carried out showing spectral signatures of various gases [Bigourd 2006]. Guo *et al*. demonstrated that high resolution spectra of polar gases (CO, NO etc) can be measured in a wide frequency region 0.6–2.4 THz. They performed real-time detection of the absorption line due to rotational transitions of the water molecule (Figure 1.5) and determined their pressure-broadening coefficient [Guo 2007]. This can be particularly useful in astronomy.

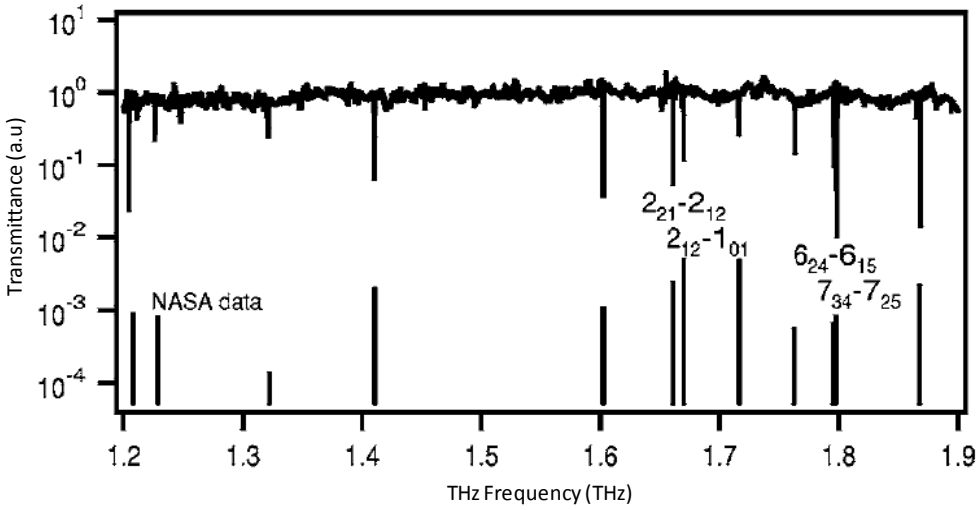

Figure 1.5: Accurate, rapid measurements of the absorption spectrum of the 12 purely rotational transitions of water vapor. The stick line shows the spectral data from the NASA database for comparison [Guo 2007].

Utilizing the fact that every explosive and narcotic has a distinct signature in THz spectra a number of different concealed-threat detection applications have been explored including screening of humans, postal screening of suspected letters and baggage screening (Figure 1.6). Mail screening applications under development include the detection of drugs-of-abuse through their characteristic THz spectra as well as explosives [Shen 2005, Kawase 2007]. In addition, the anthrax letter attacks in the USA in 2001 have prompted investigations into the detection of "white powders" using both spectroscopy and imaging [Yamamoto 2004]. People screening applications focus on the research and recognition of weapons and explosives in security as well as on standoff suicide bomber detection and the detection of weapons carried by potential intruders or assailants. An example which has been extensively presented in the news is the use of full body scanners at international airports (working frequency 28-90 GHz). In such scanners nothing can be kept secret and the operator can see any suspected object carried by the passenger as shown in figure 1.7.

Material evaluation and characterization by THz imaging is also a well-known application [Nagai 2004]. THz radiation is capable of evaluating various semiconductor properties, such as carrier mobility, conductivity and carrier density. It can be used for inspection of silicon solar cells, nanocomposities, polymer films, dielectric films and meta-materials [Yahiaoui, 2009]. Quality control of packages in food industry, monitoring of coating process in pharmaceutical industries [Zeitler 2007], checking voids and defaults in space shuttles and aircraft composites [Stoik 2008] and many more disciplines and applications are already reported long time ago and progressing day by day.

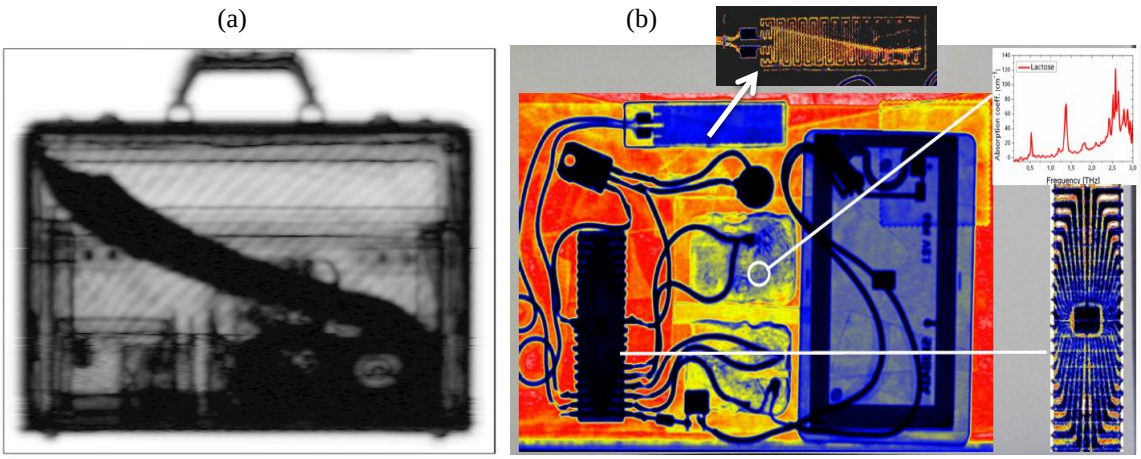

Figure 1.6: Examples of concealed threat inspection by THz. (a) THz transmission CW image of leather briefcase holding a large knife and various harmless contents such as a compact disc, a video cassette, and audio cassette and pens, (b) THz image of mock-up letter bomb, revealing electronic components, explosive powder, etc. [Karpowtrc 2005].

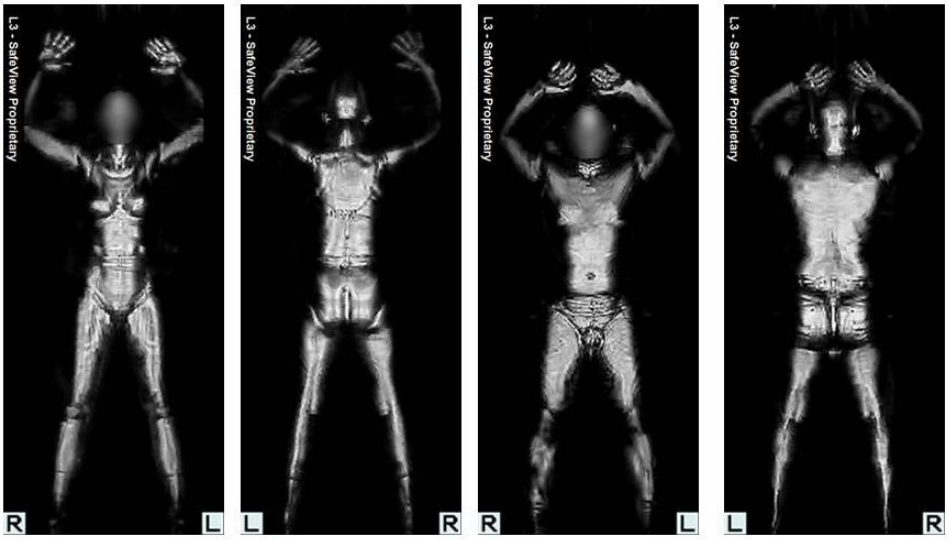

Figure 1.7: Images from a whole body scanner (United States Transportation Security Administration). Full body scanners operate at sensitive places such as airports having possible security threads [hw.Perry].

Activities and efforts geared towards the implementations of THz applications are unbounded. However, in order to realize progress in such applications, it is obvious that higher power THz sources, more sensitive detectors and more functional real time devices and materials are required.

Section 2: Non-Destructive Imaging Techniques

The field of non-destructive evaluation is a very broad interdisciplinary field that plays a critical role in assuring that structural components and systems perform their function in a reliable and cost effective fashion to aid in its preservation, conservation or replacement. Non-destructive testing techniques typically use a probing energy to determine material properties or to indicate the presence of material discontinuities (surface, internal or concealed). Generally speaking, non-destructive

evaluation is used to describe measurements that are more quantitative in nature, i.e. locating a defect with its size, shape and orientation. It may be used to determine material properties such as fracture toughness, formability and other physical characteristics.

Non-destructive techniques are often chosen by the quantity and quality of the data that can be extracted from a measurement, in addition to the financial cost and time required to make the measurement. Localized or single point measurements, can provide specific and highly quantified details about a material or system. On the other hand, large area measurements may provide fast, highly qualitative but essential information.

2.2. Common Non-Destructive Techniques

For non-destructive inspection, ultrasonic, X-ray, infrared or visible radiations are employed from decades [Thomas 2005], in order to probe interior microstructures and characterize the sub-surface features of materials.

In ultrasonic testing, high frequency sound waves are sent through the samples under test and after interacting and passing through the material, the waves are received by the transducer [Maev 2006]. The amount of transmitted or received energy and the receiving time are analyzed to determine the presence of flaws and sub-surface defects. This method can provide good penetration depth for flaw detection and provides distance information to characterize the properties of material with a sub-millimeter depth resolution. The main drawback is the accessible interaction with the surface to be probed (non contactless method). Also surface finish and roughness can affect the inspection process.

Radiographic testing is the general term given to the material examination method based on the differential absorption of penetrating radiation such as electromagnetic radiation of very short wavelength like X-rays, gamma rays, etc [Radiography]. Because of variations in density and thickness of sample, different portions of an object absorb different amounts of penetrating radiation. These variations in the absorption of the penetrating radiation can be monitored by detecting the unabsorbed radiation that passes through the object. This technique has the ability to inspect complex shapes and multilayered structures without disassembly, confirming the location of hidden parts and measuring the thickness of layered object. However possible radiation hazards with human operators can be a critical issue.

Infrared thermal imaging remotely senses surface temperatures and temperature gradients [Ravel 2006]. Materials that experience fatigue spots, imperfections or damage may exhibit temperature gradients around the affected region, which can be measured. While this technique is contactless and permits real-time acquisition, its sensitivity to ambient room temperatures and surface emissivity variations can be problematic.

In medical field, various techniques and methods for effective diagnosis are abundantly adopted. In magnetic resonance imaging, powerful magnets are used to polarize and excite hydrogen nuclei (single proton) in human tissue, producing a detectable signal which is spatially encoded, resulting in images of the body. Positron emission tomography is a nuclear medicine imaging technique that produces a 3D image or picture of functional processes in the body [Peterson 2008]. The system detects pairs of gamma rays emitted indirectly by a positron emitting radionuclide (tracer), which is introduced into the body on a biologically active molecule. Nuclear magnetic resonance is a research technique that exploits the magnetic properties of certain atomic nuclei to determine physical and chemical properties of atoms or the molecules in which they are contained. It relies on the phenomenon of nuclear magnetic resonance and can provide detailed information about the structure, dynamics, reaction state, and chemical environment of molecules.

All of the above mentioned techniques have received much more attention from decades and currently offer enhanced resolution, greater penetration, higher acquisition speeds and specifically targeted contrast mechanism. However, all these methods suffer from some drawbacks depending upon the properties of utilized radiation. Thus non-ionizing and contactless THz imaging technique can find a niche in this barrage of already favorable modalities owing to their distinct characteristics features, mentioned earlier in sub-section 1.3.

2.1. Non-destructive Evaluation Techniques in THz Domain

The non-destructive imaging techniques and methods coming under the THz discipline can be broadly categorized into two main groups - passive imaging and active imaging techniques - depending on the origin of the THz radiation measured by the detector.

2.1.1 Passive Imaging

In passive imaging, the contrast is provided from the thermal radiation emitted from the object or reflected from another thermal source illuminating the object from its surroundings. For example in astronomy passive imaging is used to analyze celestial objects [Nrao, Mueller 2000]. Although this approach gives little information about the identity of object other than its exterior profile, passive imaging seems simple as there is no need of THz sources and the only primary challenge is the development of sensitive detectors or detector arrays.

Heterodyne techniques are frequently used when a strong local oscillator is available. For example, Rodriguez-Morales *et al*. developed a superconducting bolometer integrated with gain circuitry [Rodriguez 2006]. The device operates at a design frequency of 1.6 THz, with a far-infrared gas laser used as a local oscillator. Also some groups such as Mann *et al.* at the European Space Agency investigated heavily in the development of a passive charge-coupled device (CCD) camera operating at THz frequencies [Mann 2006]. Dietlein *et al*. presented some THz images (Figure 1.8)

which are obtained by raster scanning a single pixel superconducting antenna coupled with a micro-bolometer over a scene [Dieltein 2006].

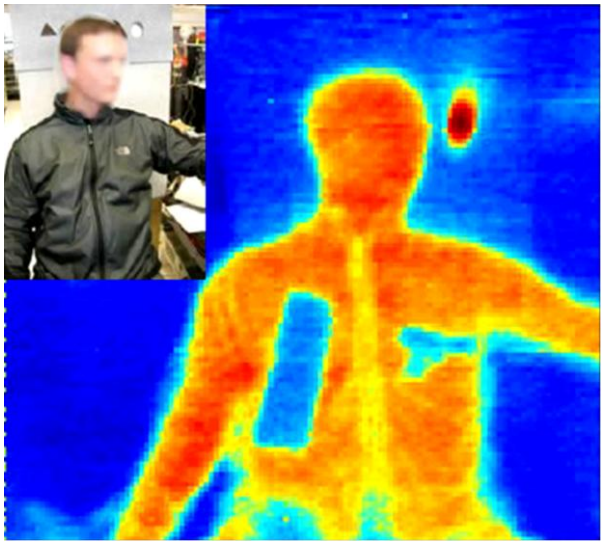

Figure 1.8: A passive THz image measured with noise equivalent temperature difference (NETD) = 0.2 K in the background, revealing a ceramic knife and small metallic hand Gun hidden under two layers of clothing [Dietlein 2006].

Luukanen *et al.* reported passive imaging results of concealed objects at stand-off distances in excess of a few meters [Luukanen 2008]. They used a 16-pixel array of superconducting antenna-coupled NbN vacuum-bridge micro-bolometer, operated within a cryogen-free, turn-key refrigerator. This system was capable of sub-Kelvin (NETD) at video frame rates. Recently, Grossman and colleagues developed a passive, real-time THz camera based on a modular, 64-element linear array of cryogenic hotspot micro-bolometers. A reflective conical scanner sweeps out a 2 m×4 m (vertical × horizontal) field of view at a standoff range of 8 m [Grossman 2010].

Imaging technology is somewhat more mature up to 100 GHz and systems are commercially available from multiple vendors [Thruvision]. Above 100 GHz, few passive imagers are available commercially, operating at 250 GHz by heterodyne down-conversion.

Finally, passive approaches have the advantage of natural illumination, a configuration for which human vision or image processing is best adapted. However drawbacks of the passive detection approach include an unfavorable tradeoff between thread contrast and image resolution at frequencies exceeding 100 GHz, as well as weak signals from objects concealed by multiple layers of various substances.

2.1.2 Active Imaging

Active imaging refers to the technique of illuminating the target with a source of radiation and then measuring transmitted, reflected or scattered radiation. In an active imager, strong scene illumination can overcome the low contrast of passive detection, especially at high frequencies where

spatial resolution is greatest. Penetration through thick objects/samples can also be accomplished by increasing the transmitting power. Active transceivers confront no fundamental detection sensitivity limit determined by a scene's thermal background temperature, a very high signal-to-noise ratio (SNR) can be achieved. Active imaging systems can be pulsed or continuous depending on the utilized source. Here we briefly discuss both systems with some examples.

2.1.2.1. Continuous Wave THz Imaging

A typical CW THz system employs a single fixed frequency source or several discrete frequency outputs, some of which can be tuneable. Since the first examples of CW THz systems, tremendous strides have been made in this context. Usually phase information is absent in CW THz imaging system as the source is not synchronized (phase locked) to an optical source that is used for sampling, thus source and detector are independent devices rather than two components of coupled devices. However the pioneered work of Nahata and co-workers used an up-conversion of THz radiation followed by homodyne detection [Nahata 1999]. Roskos also used an electro-optical sensing with femtosecond laser to measure the amplitude and phase of a CW signal from a Gunn oscillator at 0.6 THz [Löffler 2007]. Real-time CW imaging by a pyroelectric camera is demonstrated by Jun yang *et al.* for non-destructive inspection of objects inside opaque wrapping materials [Yang 2008]. Typically, CW THz imaging systems employ an incoherent device for direct detection of the THz wave, such as a bolometer, Golay cell or pyroelectric detector. Array detectors are also available for direct (not heterodyne) detection, including micro-bolometer arrays [Lee 2006], germanium detector arrays [Fujiwara 2003] and pyroelectric cameras.

CW THz imaging is advantageous for specific applications due to its higher single-frequency dynamic range and the nature of possessing a narrow spectral bandwidth. One important advantage of imaging with a single-frequency source is the ability to select the source wavelength to optimize the imaging capability. This is relevant, for example, in the case of imaging at a stand-off distance. Stand-off imaging (i.e. at greater than a few meters distance) is challenging because of the presence of atmospheric water vapour, which significantly attenuates the THz beam. However, at certain frequencies within the THz range, the atmospheric attenuation is minimized because there are no nearby strong water vapours absorption lines. The ability to tune the THz source to a water window is a considerable advantage. For example, for a 25 m stand-off, the power throughput from transmitter to receiver increases by more than a factor of 10 if the atmospheric loss decreases by 0.5 $dB.m^{-1}$ [Chan 2007]. For comparison, variations of several $dB.m^{-1}$ can be achieved by frequency tuning within narrow windows in the 4–5 THz range. Real-time imaging at a 25 m stand-off has been demonstrated using a THz QCL and a room-temperature micro-bolometer array [Kawase 2003]. In addition, because time-delay scan is not a compulsion requirement in a CW system, the acquisition speed of a CW THz

imaging system can be increased relative to that of a pulsed system, in which time-delay scanning is generally necessary.

Spectral information can be retrieved with a CW THz imaging system by continuously tuning it over a large bandwidth, such as photo-mixing and THz wave parametric oscillators. Kawase *et al*. used a tuneable THz parametric oscillator and a pyroelectric detector to image a collection of powders inside an envelope, by raster scanning the sample through the THz beam. In such way, a spectrum is collected by tuning the source between 1 and 2 THz for each pixel. These crystalline materials have significant THz absorption in this range, even in powdered form at room temperature. This can be used for material identification with a multispectral analysis [Kawase 2003]. An example of CW imaging system is shown in figure 1.9. It shows an image of hidden sample of plastic explosive Semtex surrounded by two confusion materials of similar density and consistency at various frequencies. By taking different images using frequency components of 200 GHz to 900 GHz, Semtex can be isolated and identified.

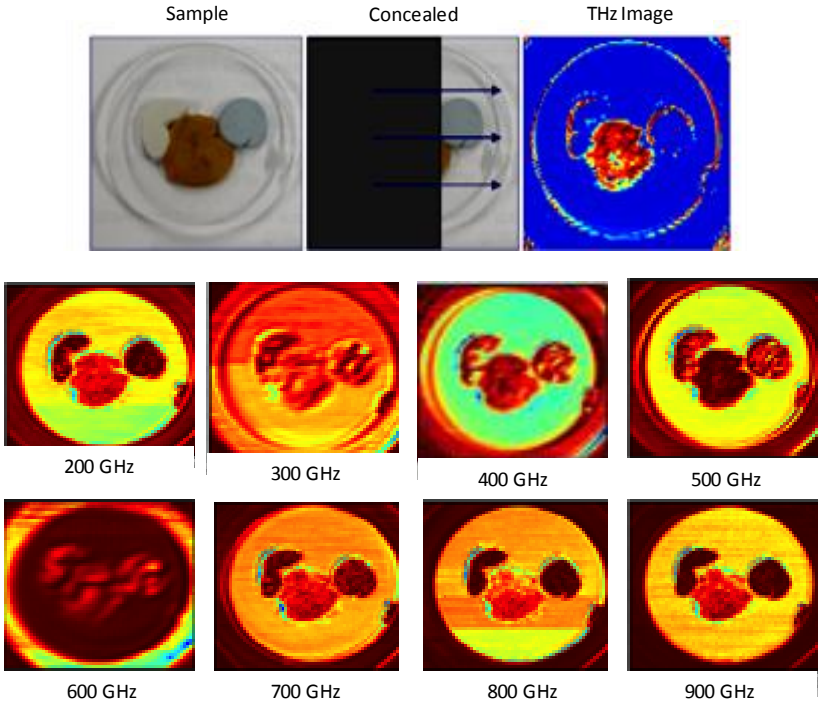

Figure 1.9: A concealed sample composed of Semtex (plastic explosive containing RDX and PETN) and two other confusing materials is imaged by reflective CW imaging. From the THz images Semtex can be isolated from the other two materials [Image courtesy TeraView].

Imaging with a CW system requires a specific method for associating the radiation received with its location in space. There are two methods that are commonly used: a raster scan of a focused incident beam, or the formation of an image on a detector array. In the former, a single detector, such as a Schottky diode, Golay cell or pyroelectric detector, is used to detect the full power of the beam. This has the advantage of a high dynamic range, but the disadvantage that the image must be formed point by point using a scanning system, which is time-consuming and not applicable to moving

targets. The development of a sensitive THz detector array [Ortolani 2011] is still an active research area. Pyroelectric arrays are commercially available, but their sensitivity in the THz range is poor and they are too small to provide high-resolution images of large targets. Detector arrays also have the disadvantage of being severely affected by distortions and aberrations in the focusing system, whereas for a raster scanning system, the beam can be focused to a diffraction-limited spot.

2.1.2.2. Pulsed THz Imaging

A THz pulsed imaging system is generally based on electromagnetic wave pulses in the range of picosecond duration. These optical pulses are used to generate broadband THz radiation. The THz pulses are focused on the sample and the resulting temporal waveform is coherently recorded in time-domain. The basic technology and method of pulsed THz imaging was developed by Lucent Bell Laboratories and other researchers in the 1980s [Auston 1984, Fattinger 1988]. However, early THz-TDS instrumentation was large and confined to an optical table. Today, the most advanced commercial THz-TDS instruments are portable, with interchangeable fiber-optic coupled remote scanning sensors. These instrumentation platforms provide a powerful, compact, rugged and highly flexible system for implementing a broad range of pulsed THz measurements [Picometrix, Teraview].

This active imaging method provides most information about sample and highest SNR. The main advantages include broadband nature and coherent detection so that the amplitude and phase of the THz electric field can be obtained at once. The temporal waveforms can be further Fourier Transformed to give the spectra. This allows precise measurement of the refractive index and absorption coefficient of samples without restoring to the Kramers-Kronig relation. The earliest pulsed THz imaging experiment was done by raster scanning the sample with a focused THz beam [Hu 1995]. In this method, the change in refractive index is shown in the time-delay and phase of the pulse, whereas the density variation modulates the pulse peak amplitude. After this pioneering work, various imaging configurations have been demonstrated, and even commercialized, with excellent examples of THz imaging. This technique has wide application in sensing and spectroscopic imaging since many common packaging materials are almost transparent for THz radiation and many chemical compounds show characteristic absorption fingerprints in the THz region.

Pulsed THz reflection imaging provides additional capability to investigate the structure of a layered sample by measuring the time-of-flight of the THz pulses. The resulting 3D imaging was first demonstrated in 1997 by Mittleman [Mittleman 1997]. In reflection mode, portions of the THz pulse will return from any structural interface that has a change in its refractive index [Wang 2004]. Because the speed of light within the sample is finite, a series of interfaces will result in a series of pulses within THz waveform that have spacing proportional to the distance between the interfaces. In many ways, THz reflection imaging is a non-contact electromagnetic analogue to pulsed ultrasound imaging. However, in addition to structural information, THz reflection images can also provide information on

the spectral or material composition of a sample, owing to changes in the spectral content of the reflected THz wave. An example, illustrating the 3D volumetric image of test sample consisting of stacked Si and vinyl chloride plates, is shown in figure 1.10.

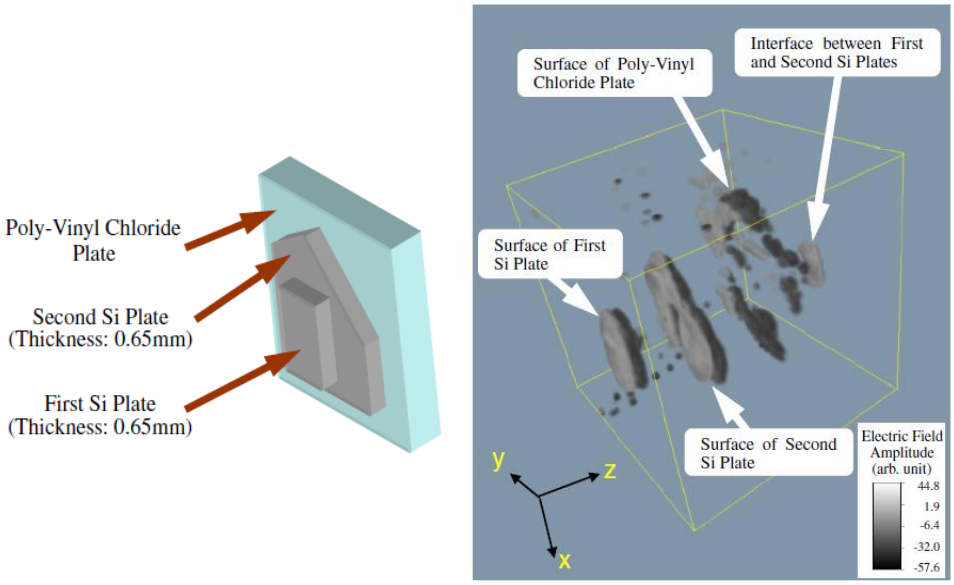

Figure 1.10: Investigated Sample of stacked high-resistivity Si and poly-vinyl chloride plates. THz image of the sample, coordinate z is the propagation direction of the THz wave [Kitahara 2010].

In a time-of-flight imaging system, one of the important considerations is depth resolution. For two closely spaced reflecting interfaces, how close can they be before it is no longer possible to resolve them? There are several different techniques which can be used to improve this depth resolution. One technique relies on interferometry in a mode which is the time-domain analog of optical coherence tomography [Johnson 2001]. In optical coherence tomography, an interferometer is used to temporally resolve a broadband light pulse by interfering it with a reference pulse, and thereby determine the time-of-flight in reflection geometry. A very high depth resolution in order of 1µm has been demonstrated [Kitahara 2010].

THz-TDS also allows us to develop various 3D THz tomographic imaging modalities. The 3D THz tomographic imaging techniques include THz diffraction tomography, THz CT, THz binary lens tomography and THz digital holography. THz diffraction tomography uses the THz wave as a probe beam to interact with a target and then reconstructs the 3D image of the target using the THz waves scattered by the target. THz CT, which will be largely presented in this thesis, is based on geometrical optics and inspired by X-ray CT. THz binary lens tomography, uses the frequency dependent focal length property of binary lenses to obtain tomographic images of an object. THz 3D holography combines radar and conventional holography technology. More details about each tomographic technique will be presented later in chapter 4.

Single-shot pulsed THz imaging [Rungsawang 2004] and video rate imaging is also demonstrated to avoid raster scanning of objects and making fast acquisition. Video rate THz imaging has been demonstrated by work of X-C. Zhang and co-workers who have used large area electro-optic sensors to demonstrate real-time THz imaging over few cm^2 focal plane area [Jiang 1999]. This group has also developed a chirped-pulse technique for measuring an entire THz waveform along a line (1D imaging) using a single-shot measurement [Jiang 1998]. Utilizing the fact that CCD detector array can refresh at video rates, this technique can be used to generate THz movies [Hermann 2000]. More, recently, a real-time THz color scanner, based on electro-optical time-to-space conversion, has been successfully demonstrated to image moving objects [Yasui 2008].

One of the clear limitations of all of the THz imaging techniques described so far is the spatial resolution. With a diffraction-limited optical system, the spot size of a focused beam is roughly equal to the wavelength multiplied by the *f*-number of the focusing optics. As a result the smallest resolvable features in an image are generally in the order of the illuminating wavelength. For radiation at 1 THz, one finds a spatial resolution (~0.5 mm) which is comparable to the resolution of the human eye. This resolution clearly limits the applicability of THz imaging. For improving the system imaging resolution, variety of techniques has been developed. After the first demonstration of THz sub-wavelength imaging in 1998 [Hunche 1998], the study of near-field techniques has become one of the most active research areas in the THz community. Among these techniques, dynamic aperture [Chen 2001] and aperture less near-field THz imaging have been reported and widely used [Valk 2002, Chen 2003]. In near field imaging with sub-wavelength aperture spatial resolution as small as 7 µm at 0.2 THz (better than $\lambda/200$) could be achieved [Mitrofanov 2001]. With a CW THz source at λ = 207 µm, imaging with 12 µm resolution ($\lambda/17$) was demonstrated [Ishihara 2006]. The limit of any of these techniques is determined by the amount of light that is transmitted through the aperture. More details can be found in article by Mittleman *et al.* [Chan 2007].

Conclusion

In this chapter, we have given a brief introduction of THz radiation and their dynamic applications in various fields along with the description of commonly used experimental methods in THz imaging domain. In this thesis, we will mainly focus on THz imaging applied to art science and THz CT for the visualization of 3D volumetric objects. In the next chapter, we will present the experimental methods that we have specifically developed in order to perform 2D and 3D THz imaging.

CHAPTER 2

Experimental Techniques

This chapter will present the experimental configurations that we have developed in order to perform THz imaging. Two principle THz imaging architectures have been selected. The first one is based on a time-domain spectrometer modified for imaging, referred as THz-TDS imaging system. The second one employs a CW THz source and is referred as CW imaging system. We will give a detailed description of these two imaging setups in the first two sections. We will present the general phenomena of THz generation and detection that we have used, together with the selected optical setups and imaging configurations. Especially, the data analysis procedure for spectroscopic and imaging experiments adopted in two setups along with essential characteristic features of these optical systems will be explained. In the third section, some general results will be presented.

Section 1: THz Time-Domain Spectroscopic Imaging

Conceptually, the pulsed THz imaging system we have developed is a simple extension of standard THz-TDS spectrometer along with some additional modified changes in order to perform imaging. In our case, a femtosecond Ti-Sapphire laser (Spectra physics) at the wavelength of 800 nm, emitting at 76 MHz repetition rate is utilized. The laser output (640 mW) is divided into a pump and a probe beam by the insertion of a beam-splitter. The pump beam (160 mW) is used for generating THz radiation whereas the probe beam (30 mW) is employed for THz detection. A scanning THz system is constructed and the usual experimental scheme is given in figure 2.1.

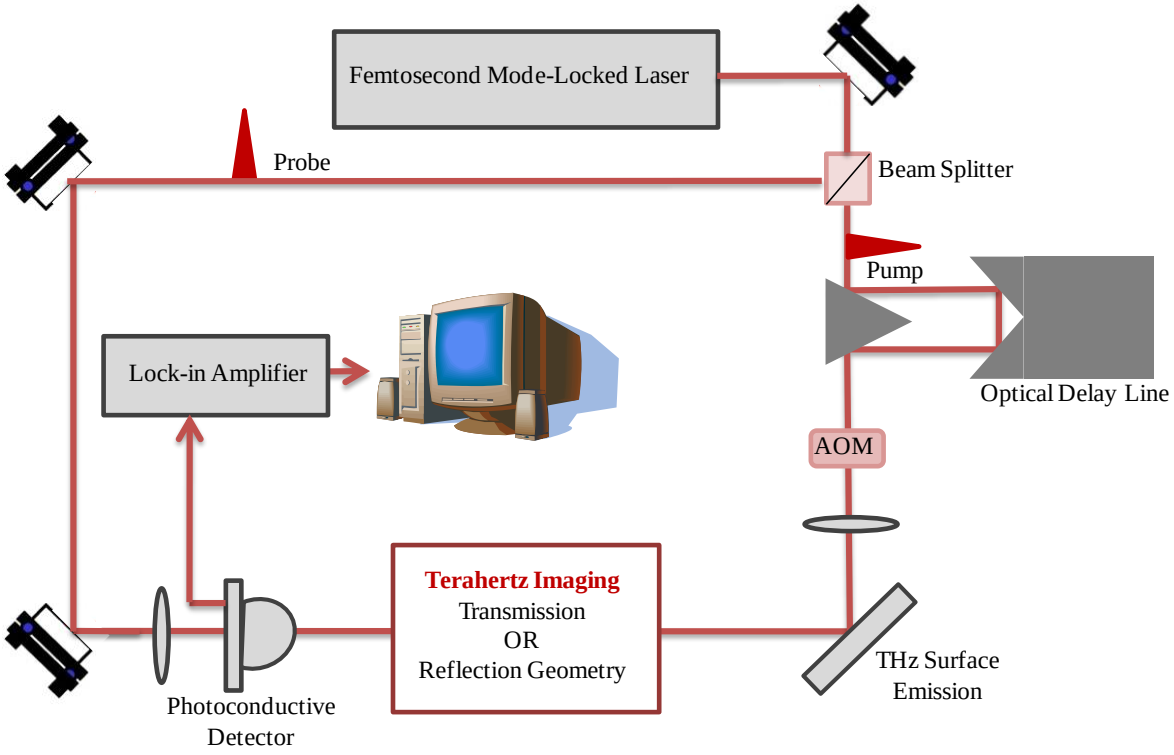

Figure 2.1: Illustration of typical THz-TDS imaging system, showing main components and their position in the path of pump and probe beams. AOM: Acousto-optic modulator.

For a better understanding of the THz-TDS imaging system, we will first discuss the emission and detection process of THz radiation. Then optical components used in this system will be presented along with a description of experimental geometries used for performing imaging. In the end, various other necessary equipments and system acquisition speed will be exposed.

1.1. Generation of THz Radiation

The THz emission method that we selected is based on surface emission process. We chose this method for specific reasons. First the emitted THz pulses have similar amplitude and spectral characteristics, as those obtained with a usual photoconductive antenna. Then, the pump infrared laser pulse, after being reflected from the THz surface emitter can be utilized for the alignment of the optical system and facilitates the positioning of sample.

We used a piece of bare InAs semiconductor for THz generation [Lewis 2006, Gu 2002]. P-doped InAs has been selected because it emits THz transients with more magnitude power than commonly used wide band-gap semiconductors such as InP and GaAs, under similar conditions [Kono 2000, Johnson 2002].

THz emission from semiconducting surfaces such as InAs requires the formation of electric dipoles, which can be created by different mechanisms. The exact mechanism of their generation is still controversial. THz emission may originate from several factors including (1) photocurrent induced by surface-field, (2) photocurrent induced by photo-Dember effect and (3) non-linear optical process.

(1) When an ultrashort optical pulse illuminates a semiconductor with a wavelength (energy) above the energy band-gap of the material, it photo-generates mobile carriers. Given that absorption of the pulse is an exponential process, most of the carriers are generated near the surface (typically within 1 μm). The built-in static field drives the two kinds of carriers in opposite directions, the electrons to the surface and the holes to the wafer. The free carriers are swept across the depletion width. The photocurrent flows in and a dipole layer builds up. The rise time of the photocurrent is in the order of the laser pulse duration and generally the decay time is the transit time of free carriers crossing the depletion layer (assuming the carrier lifetime is longer than the carrier transit time). It generates a band bending due to Fermi-level pinning by surface states, which has the effect of accelerating carriers of different signs in opposite directions (normal to the surface) creating a built-in electric field. This effect is known as surface field emission [Zhang 1990]. The angle-dependent photocurrent J_s across the depletion layer can be written as:

$$J_s = \frac{\mu e}{h\omega} W_{op}\left[1 - R\left(\theta_{op}\right)cos\theta_{op}\right] \int E_d\,(x) e^{-\alpha x}\mathrm{dx} \qquad (2.1)$$

where μ is the carrier mobility, e is the electron charge, $h\omega$ is incident photon energy in eV, θ_{op} is the optical incident angle, W_{op} is the optical intensity, $R\ (\theta_{op})$ is the optical reflectivity at the surface, $E_d(x)$ is the built-in field and α is the optical absorption length.

(2) Secondly, a photo-Dember effect can also occur at the surface of a semiconductor after photo-excitation [Klatt 2010]. Two factors lead to this process: a difference in diffusion coefficients for electrons and holes, and a structural asymmetry. In a typical semiconductor, electrons have a larger diffusion coefficient than holes. Therefore, after photo-excitation, the electron population diffuses more rapidly than the hole population as shown in figure 2.2, where one can notice a change in electrons (-) and holes (+) concentration due to their different diffusion speed. This inhomogeneous distribution causes electrons and holes to move into the semiconductor, where the diffusion speed is:

$$\frac{\partial N}{\partial t} = D\frac{\partial^2 N}{\partial z^2} \tag{2.2}$$

where z is the coordinate unit toward the inside of the semiconductor and D is the diffusion co-efficient, which can be obtained from the Einstein relationship:

$$D = \frac{\mu k_B T}{e} \tag{2.3}$$

where k_B is the Boltzman constant, T is the temperature, e electron charge and μ the carrier mobility.

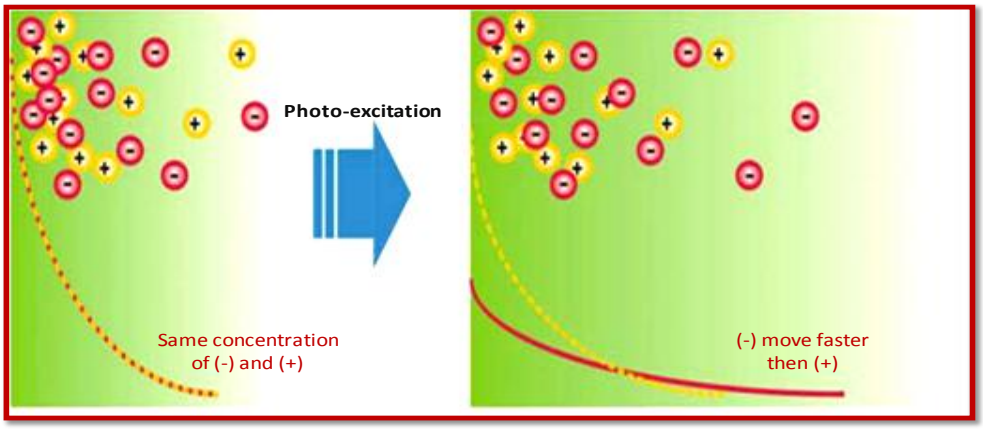

Figure 2.2: Photo-Dember effect on InAs surface, illustrating diffusion of holes (+) and electrons (-).

In the absence of a surface boundary, there would be no net dipole field, since the center of charge does not change. However, in the vicinity of the surface, reflection or capture of charges results in the center of charge for electron and holes moving away from the surface. A dipole is thus formed perpendicular to the surface, leading to THz emission. This effect is particularly strong in high-mobility semiconductors.

(3) Lastly, non-linear optical processes resulting in THz radiation emission are bulk or surface-field induced optical rectification of incident femtosecond laser pulses [Ko 2008]. The amplitude of a THz radiation pulse generated by optical rectification in a non-linear optical crystal depends on the following parameters: (1) the non-linear electric susceptibility of the crystal, (2) amount of optical laser radiation transmitted into the crystal, (3) crystallographic orientation of the crystal and (4) microcrystal grain size. The amount of laser radiation transmitted into the crystal depends on the index of refraction. The magnitude of THz generation due to surface-field induced optical rectification is determined by the third order non-linear electric susceptibility of the material and THz generation due to bulk optical rectification depends on the second-order non-linear electric susceptibility [Reid 2005].

Characteristics	**InAs**		
Index of Refraction at 800 nm	3.729		
Index of Refraction at 1 THz	3.778		
Second order Susceptibility at 800 nm	$1.3 * 10^{-6}$		
Number of Equivalent Valleys	Γ(1)	L (4)	X(3)
Energy Gap	0.355	1.455	1.955
Effective Mass	0.022	0.29	0.64

Table 2.1: Main optical and structural features of InAs semiconductor.

InAs, a narrow band-gap semiconductor (*Eg*=0.355 eV) has demonstrated the strongest THz radiation emission of all III-V semiconductor systems. The main features of InAs are mentioned in table 2.1, values adapted from [Ko 2008]. The origin of THz radiation emission from InAs is primarily attributed to the photo-Dember effect [Reklaitis 2010, Takahashi 2003, Liu 2006] and surface-field induced optical rectification [Reid 2005, Adomavicius 2005, Bičiūnas 2009]. A Standard way to separate these mechanisms consists of measuring azimuthal angle dependences of the radiated THz pulse amplitudes. Mostly, in InAs the origin of THz emission is the photo-Dember effect. The magnitude of THz radiation emitted due to the photo-Dember effect depends on the electron and hole concentrations, the ratio of electron and hole mobilities and the electron temperature. In our case, this simple and easily aligned surface emission technique delivers a THz output power in the order of microwatts with a spectral bandwidth of nearly 3 THz, limited by the duration of the incident laser pulses.

1.2. Detection of THz Radiation

For the detection of pulsed THz signal, we used a photoconductive antenna [Jepsen 1996, Zhao 2002]. Typically the two antenna electrodes are patterned on a low temperature grown GaAs semiconductor. The electrodes having a length of 1.5 cm are separated by a distance of 80 μm from each other (Figure 2.3). They are formed into the shape of a simple dipole antenna with a gap of 5 μm. A silicon lens of hyper-hemispheric form (5 mm) is coupled to the antenna in order to eliminate the reflections at the interface and to collect more radiation [Jepsen 1995, Filipovic 1993]. The antenna is gated with the femtosecond probe pulse. The bias electrical field across the antenna leads is generated by the electric field of the THz pulse itself, focused onto the antenna, rather than being applied externally. The femtosecond probe laser pulse excites the electrons across the bandgap of the semiconductor substrate. At equilibrium the conductivity σ of the semiconductor is defined by its dark conductivity σ_o:

$$\sigma_0 = e(\mu_n n_0 + \mu_p \rho_0) \tag{2.4}$$

where e is the electron charge, n_o and ρ_o are the respective intrinsic electron and hole densities, and μ_n and μ_p are their respective carrier mobility's. In the semiconductor the electron and hole pairs are generated at the rate G(t) given by:

$$G(t) \infty N_0 e^{-(t/\delta t)^2} \tag{2.5}$$

where δt is the optical pulse width and N_0 is the maximum of generated photo-carriers density. Effectively, the semiconductor changes abruptly from being an insulator into being a conductor. This carrier mobility and the presence of the THz electric field generate a photocurrent J_d across the antenna:

$$J_d(t) \propto \int_{-\infty}^{+\infty} E_{THz}(t) n(t-\tau) dt \tag{2.6}$$

where $n(t-\tau)$ is the carrier response function of the semiconductor proportional to the laser pulse envelope. This current may persist for only a few hundred femtoseconds, up to several nanoseconds, depending on the material of which the substrate and the active layer are composed. Because it is a resonant excitation method, the detection is limited not only by the excitation laser pulse width, but also the response time of the material [Dekorsy 1993, Piao 2000].

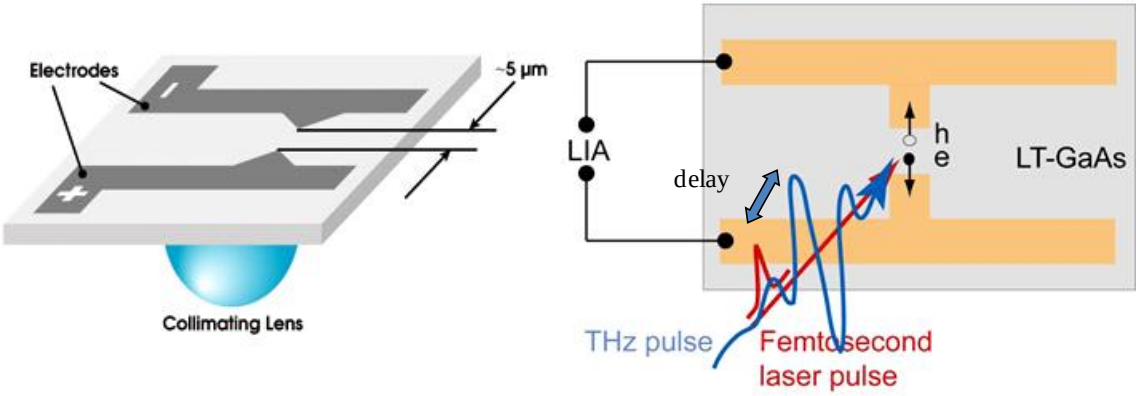

Figure 2.3: Diagram of typical photoconductive switch along with the scheme illustrating the detection of THz radiation. h: Hole, e: Electron, LIA: Lock in amplifier

The generated current is usually amplified using a low-bandwidth amplifier. This amplified current is the measured parameter which corresponds to the THz field strength. To measure the temporal evolution of the THz electric field (THz temporal waveform), a standard optical sampling is performed as follows (Figure 2.4). Owing to the periodicity of the infrared laser pulses, it is possible to use a pump probe method to measure the entire THz waveform. By changing the distance between the pump and probe laser beams with an optical delay line, one can change the time-delay between these two pulses and map the electric field of the THz pulse as a function of time. For a given time-delay, the detected THz signal gives the corresponding amplitude of the THz electric field.

The correct measurement of the THz electric field is performed with the help of a lock-in amplifier (LIA) (Stanford, SR830 DSP). This device selectively amplifies the incoming signal in order to boost it above the noise level. In our case, the amplitude modulation of the signal is performed with an acousto-optic modulator (AOM) placed along the path of pump laser beam. The LIA mainly requires a reference frequency and an integration time-constant for signal demodulation. The modulation frequency should be as high as possible in order to perform fast THz raster scanning imaging. In our case, the modulation frequency was set to 300 kHz, which allows an integration time of 300 µs for the LIA. To measure the entire THz waveform, a fast optical delay line is inserted along the pump laser beam pathway. Again, for imaging applications, a fast waveform acquisition is required. Generally, up to 5 waveforms were acquired within one second (oscillation frequency of 5 Hz for the optical delay line), with a typical 33 ps temporal window (1000 data points with a spacing of 33 fs). A more complete description and analysis of the THz waveform will be presented in sub-section 1.5.

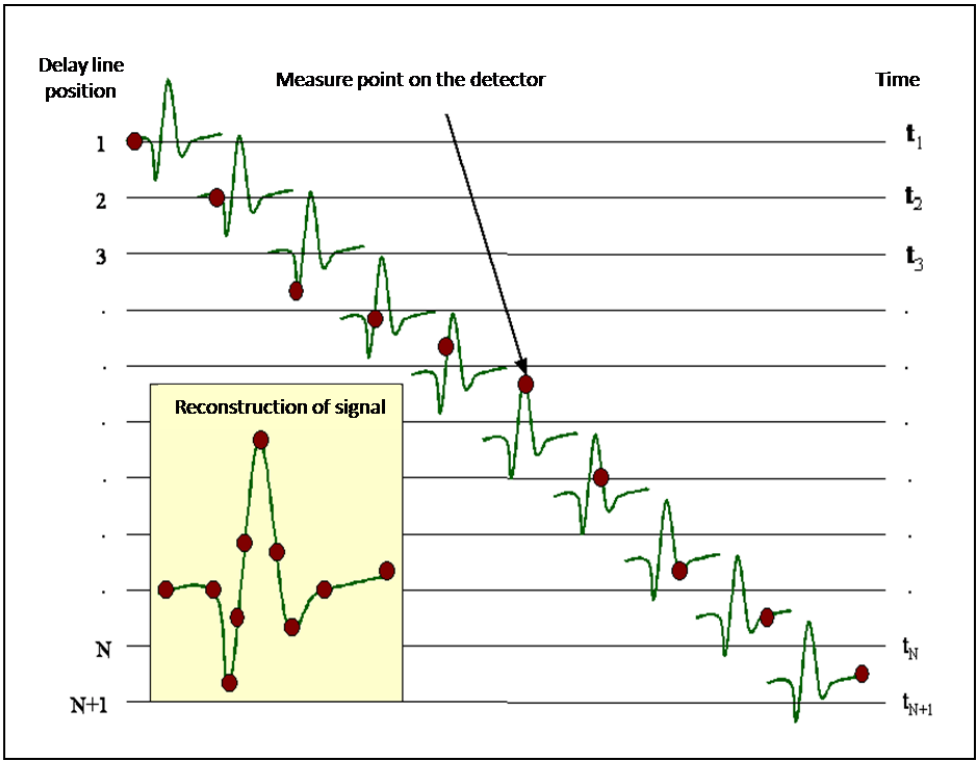

Figure 2.4: Time-gated sampling technique for the measurement of the entire THz waveform.

1.3. Description of Optical Configurations

Mainly two optical configurations - transmission and reflection modes - were used for pulsed THz imaging. These optical benches are different according to the basic optical components and their position in the THz beam path. In this sub-section we will describe the different optical setups that we have developed.

To conduct THz imaging in transmission mode, the first build optical setup is shown in figure 2.5(a). Normally, in any THz imaging system, to maximize the transmission of the THz radiation, optical lens material should have a low absorption in THz wavelengths [Rudd 2002]. In the THz domain, several materials have low absorption (<few cm^{-1}) and respond well to our objectives: these are Teflon, High-density Polyethylene (HDPE) and Picarin. From these materials we selected Picarin due to its specific features. Picarin is highly transparent in both THz and visible spectral ranges [Picarin]. The refractive index of Picarin is almost the same for THz and visible light (n=1.52), which facilitates beam alignment and sample positioning. The only drawback is its cost and the restricted catalogue of available lenses. This optical setup uses four identical Picarin lenses of 50 mm focal length inserted between the transmitter and receiver. Their role is to modify the propagation of the THz beam in order to obtain a focal point at the sample position. The first lens is used to collimate the generated wave, the second lens creates a THz focal point, the third lens recovers the THz field which diverges after the focal point and sends it towards the fourth lens. This one concentrates by focusing

the THz radiation to the detector. The sample is placed on a XY translational motor stage along with a rotational (θ) motor stage. This optical system was used for THz imaging, especially for performing 3D computed tomography which will be presented in chapter 4. This setup is analog to traditionally used THz-TDS system with four parabolic mirrors.

The second optical setup (Figure 2.5(b)) that we used is a modified version of the above scheme. In order to improve the spatial resolution, we inserted two homemade HDPE lenses in between the second and third focusing Picarin lens. This configuration is useful for imaging thin and fine samples of small dimensions like written documents and various painting artworks.

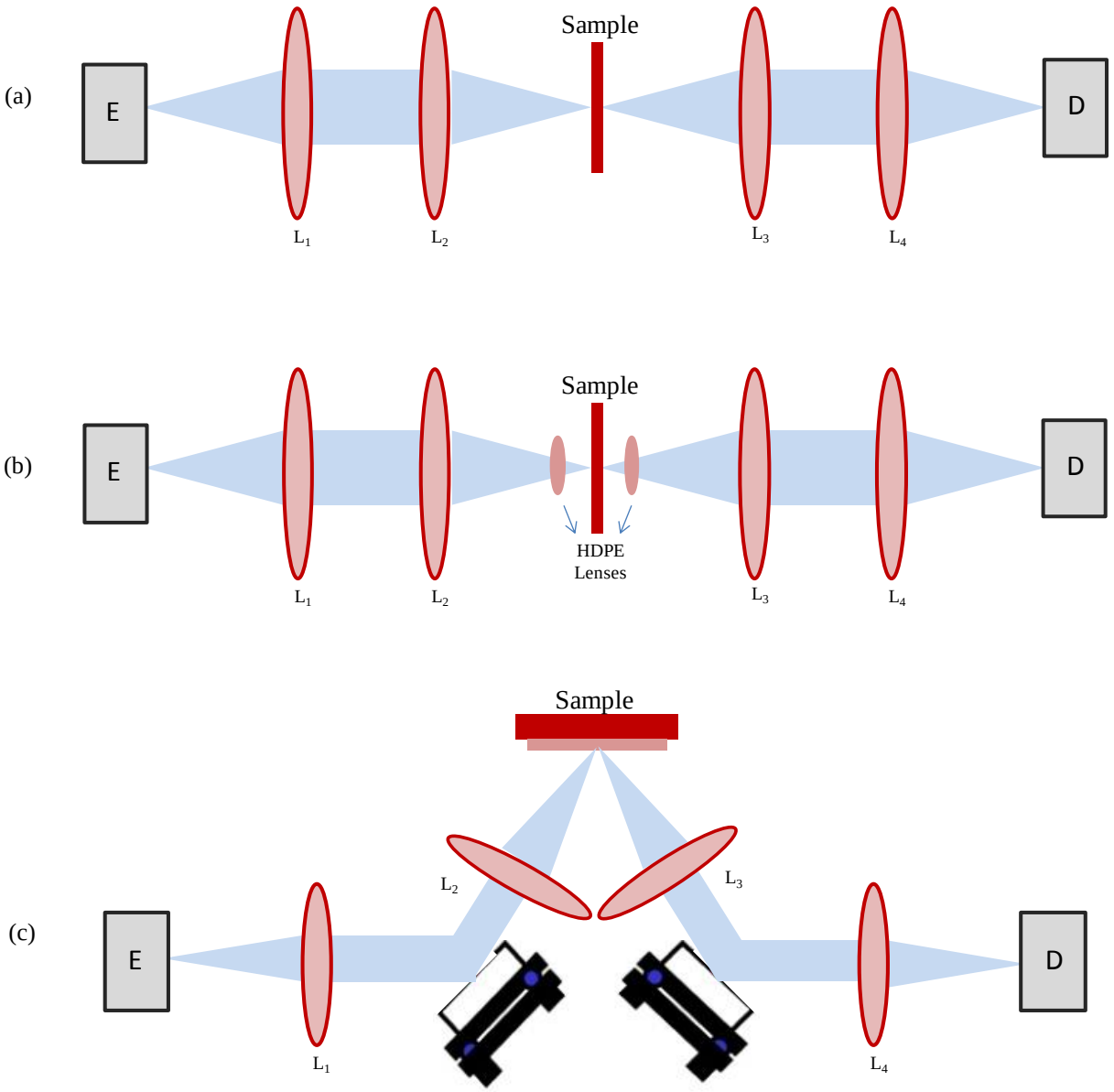

Figure 2.5: THz-TDS optical setups. (a) Transmission configuration with four Picarin lenses (L_1 to L_4), (b) Transmission configuration with four Picarin lenses (L_1 to L_4) and two additional HDPE lenses inserted between them, (c) Reflection configuration with off-axis or pitch catch reflection geometry with two plan flat mirrors and four Picarin lenses (L_1 to L_4).

To perform THz imaging in reflection mode, two optical configurations, on-axis and off-axis, are widely adopted. In on-axis or collinear geometry, normally a beam-splitter is inserted in the path of collimated THz beam and the transmitted beam is focused onto the sample at normal incidence. After reflection from the sample, the reflected THz beam again passes through the beam-splitter from where it is directed towards the detector. The advantage of this method is sending and receiving the THz pulses at normal incidence to the sample. However, in such a configuration, the amplitude of the detected THz beam is reduced according to the transmittance and reflectance properties of the beam-splitter. At best, with 50% transmission and reflection, the amplitude of the signal is divided by a factor 4. In our case, most samples have a limited reflectance due to surface roughness. For example, the reflectance of a standard painting layer is in the order of 10% with respect to mirror. Consequently, to keep a reasonable SNR in reflection imaging, we adopted an off-axis configuration, where the THz beam reflected from the sample is entirely sent onto the detector. Moreover, the use of a beam-splitter provides an additional THz peak in the measured waveform due to the backside reflection of the beam-splitter. With a Si beam-splitter [Home 2007] with a 350 µm thickness, two opposite peaks delayed by 7 ps apart from each other have been measured. This additional signal is highly problematic to analyze, while performing imaging of a layered sample having multiple reflections from each interface.

The optical setup developed for off-axis reflection mode imaging is presented in figure 2.5(c). The THz beam is guided towards the sample at an incidence angle of 30°, with the help of flat mirror placed in its path. After reflecting from the sample, the THz beam is collected and send towards the detector with the help of another identical piece of lens and mirror. In such alignment, as already noticed, the entire reflected signal by the sample is collected by the detector without any loss (except lens losses). Nevertheless, this configuration is not well adapted for the analysis of thick layered samples, owing to the inevitable walk-off of the THz beam reflected by the different interfaces.

1.4. Spectroscopic Analysis in THz-TDS System

The temporal evolution of the electric field of THz pulse is shown in figure 2.6(a) as a function of the time delay of the probe pulse. After Fourier transform, the corresponding amplitude spectrum can be obtained, which extends from 100 GHz to nearly 3 THz (Figure 2.6(b)). The numerous sharp dips visible in the spectrum are coming from rotational transitions of water vapors. The noise level in the setup is very small, nearly 10 µV, with a maximum amplitude value of 45000 µV in the THz signal. It gives a high accordable SNR of 4500, which is suitable for performing THz imaging.

The frequency resolution that is theoretically achievable is determined by the total scanning length l of the optical delay line. The Δf between two neighbouring points in the frequency spectrum is given by:

$$\Delta f = \frac{c}{2l} \tag{2.7}$$

where c is the speed of light. In our case, the choice of the parameter l depends on the sample characteristics. For THz imaging of non-specific materials without any fingerprint signature, a scanning length l = 5 mm can be sufficient, providing a final frequency resolution Δf = 30 GHz. This resolution can be changed by increasing the parameter l, in the expense of the global acquisition time.

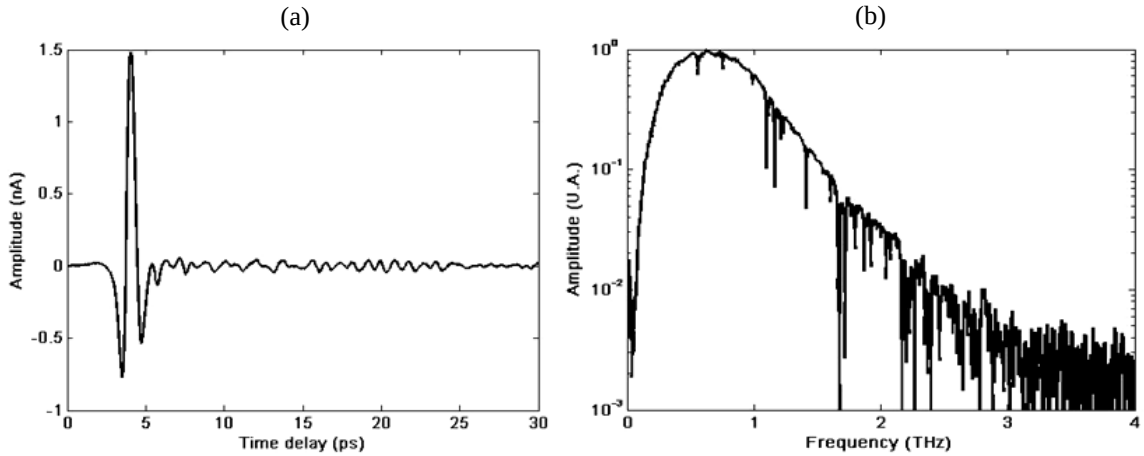

Figure 2.6: (a) Typical THz waveform signal, (b) Corresponding amplitude spectrum.

Keen interpretation and analysis of the data is necessary in any imaging system in order to extract all the desired information about the sample. In THz-TDS system, the THz beam interacts with the sample and undergoes changes depending on the optical, biological, chemical and structural properties of the material under test. Typically the transmitted/reflected THz pulse will experience delay, attenuation and broadening.

In general there are three main physical effects to be taken into account in the imaging process namely absorption, transmission/reflection and eventually scattering. Absorption is the energy transfer (coupling) from the THz wave to certain modes of the sample. In general, the intensity $I(x)$ of a light beam propagating through a material obeys the Beer-Lambert law:

$$I(x) \propto I_o \exp(-\alpha.x) \tag{2.8}$$

where I_o is the intensity of the beam prior to propagation through the thickness x of the material and α is the absorption coefficient.

Normally, in THz spectroscopy, for material characterization, one requires the measurement of two quantities: the sample electric field $E_{sam}(t)$ when the THz beam passes through the sample, and the reference electric field $E_{ref}(t)$ measured without any sample, permitting the THz beam propagation in air as described in figure 2.7(a).

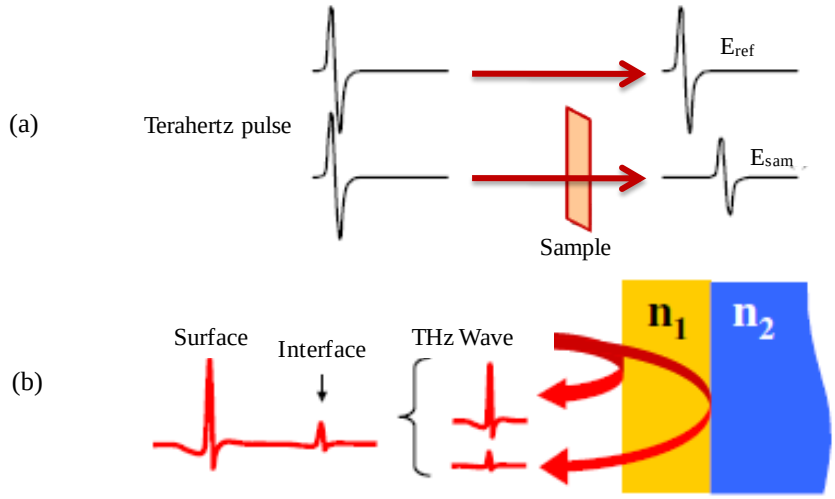

Figure 2.7: (a) Method of acquiring THz waveforms for the spectroscopic analysis in transmission imaging, (b) Typical reflected THz waveform in reflection geometry showing the main reflected peak and the sub-peak coming from one interface having different refractive index.

After these measurements the Fourier transform of the temporal waveforms allows us to obtain the complex spectrum (amplitude and phase) of each electromagnetic pulse.

$$E_{ref}(\omega) = \frac{1}{2\pi} \int_{-\infty}^{+\infty} e^{-i\omega t} E_{ref}(t) dt \tag{2.9}$$

$$E_{sam}(\omega) = \frac{1}{2\pi} \int_{-\infty}^{+\infty} e^{-i\omega t} E_{sam}(t) dt \tag{2.10}$$

To analyze the data properly several assumptions about the geometry of the spectroscopic setup has to be made. In our analysis, the Fabry-Perot effect coming from the sample interfaces has been neglected. A more complete study can be found in [Duvillaret 1996]. When the THz pulse crosses the sample, it undergoes reflections at the sample interfaces and it gains a phase P_{sam}. In the simplest case we consider only reflection and transmission at the first and second interface. If we assume normal incidence and planar surfaces without scattering, we can use the well known expressions for the Fresnel equations. Further, we assume that the medium surrounding the sample is dry air so we can set the complex refractive index to 1. The complex spectrum of the sample electric field is given by:

$$E_{sam}(\omega) = E_0(\omega).t_{air-sam}(\omega).P_{sam}(\omega,d).t_{sam-air}(\omega) \quad (2.11)$$

where:

$$t_{air-sam} = \frac{2}{1+\tilde{n}(\omega)} \quad (2.12)$$

$$t_{sam-air} = \frac{2.\tilde{n}(\omega)}{1+\tilde{n}(\omega)} \quad (2.13)$$

where $\tilde{n}(\omega) = n + iK$ is the complex refractive index of the sample and d is the sample thickness. The phase accumulated by the pulse while crossing the sample is described by:

$$P_{sam} = \exp\left(i\frac{\tilde{n}.d.\omega}{c}\right) \quad (2.14)$$

For the reference pulse we have no reflections at interfaces, only the phase accumulated by crossing the distance d through air:

$$E_{ref} = E_0(\omega)\exp\left(i\frac{\omega.d}{c}\right) \quad (2.15)$$

Now, one can evaluate the transmittance spectrum $T(\omega)$ of the sample:

$$T(\omega) = \frac{E_{sam}(\omega)}{E_{ref}(\omega)} \quad (2.16)$$

by inserting corresponding values in equation (2.16) and solving it further, we obtain:

$$T(\omega) = \frac{4.\tilde{n}(\omega)}{[\tilde{n}(\omega)+1]^2} exp\left[i\frac{\omega.d}{c}(\tilde{n}(\omega)-1)\right] \quad (2.17)$$

The first term represents the Fresnel reflection. The exponential describes the propagation in the sample, the real part of the argument is responsible for the delay of the waveform while its imaginary part accounts for the absorption in the sample. Interesting parameters are the absorption coefficient $\alpha=2K\omega/c$ and the real part n of the refractive index. The ratio of the Fourier transform is a complex number that can be written as:

$$\frac{E_{sam}}{E_{ref}} = R(\omega)e^{i\phi(\omega)} \quad (2.18)$$

After further solving equations (2.17, 2.18), we can obtain the index of refraction (n) and the absorption coefficient as follows:

$$n(\omega) = 1 + \frac{c}{\omega d}\phi(\omega) \tag{2.19}$$

$$\alpha(\omega) = -\frac{2}{d} ln\left[\frac{(n(\omega)+1)^2}{4n(\omega)} R(\omega)\right] \tag{2.20}$$

Finally, from equations (2.19) and (2.20), the complex permittivity ε can also be deduced as:

$$\varepsilon = \acute{\varepsilon} - i\acute{\varepsilon}\acute{\varepsilon}', \quad \acute{\varepsilon} = n^2 - k^2\,, \quad \acute{\varepsilon}\acute{\varepsilon}' = 2nk \tag{2.21}$$

Spectroscopic information about the sample under test can also be calculated from the data corresponding to reflection mode acquisition. In reflection mode, the reference signal can be obtained either by replacing the sample with some mirror or metallic surface, or by placing a window in contact with the sample and using the front surface reflection as reference signal and reflection from back surface as sample signal. With a mirror surface (100% reflection) as a reference at normal incidence of THz radiation, the ratio of the sample reflection to the reference is:

$$|r|e^{i\varphi} = \frac{\tilde{n} - 1}{\tilde{n} + 1} = \frac{n + ik - 1}{n + ik + 1} \tag{2.22}$$

where ñ is again the complex refractive index of the sample. This expression can be inverted to yield the real part n of the refractive index and absorption coefficient as follows:

$$n(\omega) = \frac{1 - |r|^2}{1 + |r|^2 - 2|r|cos\varphi} \tag{2.23}$$

$$\alpha(\omega) = \frac{4\pi v}{c} \frac{2|r|sin\varphi}{1 + |r|^2 - 2|r|cos\varphi} \tag{2.24}$$

However, in such measurements, there comes a complication since the reflection surface must be accurately positioned in comparison with the sample surface. A small difference Δd between the position of sample and reference surface plane leads to an additional slope in the phase difference given by $\Delta\varphi = 2\omega\Delta d/c$. In practice, this makes difficult to analyze the sample spectroscopic properties in reflection mode. Also, polarization of the laser beam should be taken into account while doing measurements. Nevertheless, in case of layered samples, the presence of multiple reflections in THz signal (Figure 2.7(b)) offers a method of extraction of sample thickness or refractive index. By a careful analysis of reflection sequence following the main reflected peak, one can extract these

parameters. As an example of time-of-flight thickness measurement, the reader is referred to the figure 2.21 presented at the end of this chapter.

1.5. Image Formation in THz-TDS System

In order to record THz images with the TDS system, we developed a specific procedure, taking into account that the acquisition time should be as short as possible. However, the temporal scanning range should also be sufficient, in order to get a reasonable frequency resolution after Fourier transform of the temporal waveforms. This procedure has been established in close collaboration with the electronic engineers of the laboratory that especially developed the labview program for the automatization of the data acquisition. The imaging sequence is organized as follows.

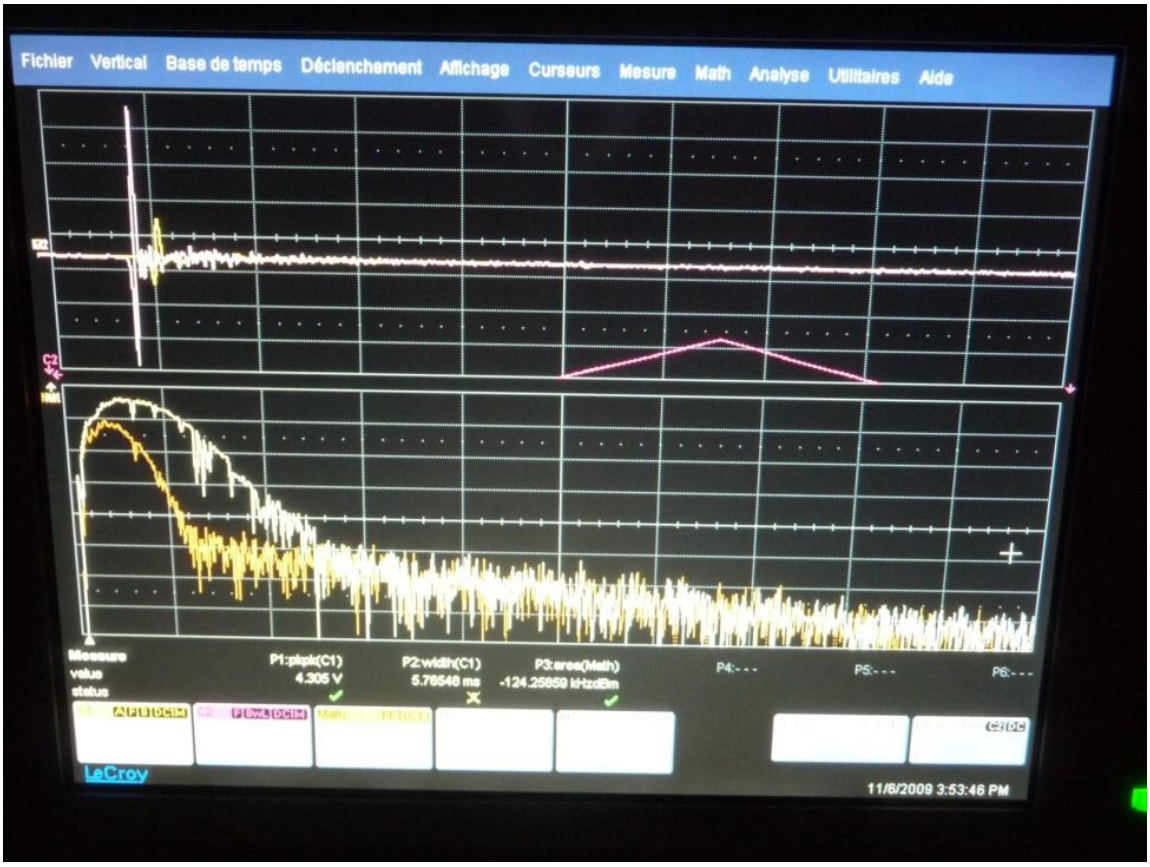

Figure 2.8: Capture screen of the oscilloscope, showing the reference waveform (white colour) and sample waveform (yellow colour) with their corresponding frequency spectrum in real-time.

First, the fast optical delay line makes it possible to record the temporal waveforms of the THz electric field with an acquisition rate of 5 Hz. The data is sent to the LIA and then digitally displayed in real-time on a digital oscilloscope (Lecroy 424 Wave-surfer, 200 MHz) together with the exact position of the optical delay line in order to calibrate the temporal axis. The data is also synchronized with the translational motor stages XYθ in order to record THz signal with exact knowledge of each pixel. A capture screen of the oscilloscope is presented in figure 2.8. This picture shows the stored

reference waveform (upper part, white curve), the real-time delayed sample waveform (upper part, yellow curve) and the corresponding spectra (lower part of the picture) illustrating in real-time the THz transmission properties of the sample.

As already mentioned, the data is acquired with a frame rate of 5 Hz, which is essential for THz imaging. This data is then stored into the computer, with a possible averaging operation depending on the selected options in the Labview program.

Figure 2.9: Visual view of front panel of labview program, where the user can select the options for the displacement of XY motor and delay line motor. More details about labview program can be found in Annex2.

Here, from the Labview program interface, the user can select the number of data points stored in the THz waveform together with the duration of the temporal window (Figure 2.9). Then, the sample has to be translated in order to record the next pixel of the final 2D THz image. This step is also automatically performed line by line by the Labview program, starting by a horizontal X scanning and then moving to the next vertical position for the upcoming horizontal line. The user simply has to

select the number of pixels in the X and Y directions and the step size (in millimetres) for the displacement of the translation X and Y stages. Another option makes it possible to control an additional rotational stage (angle step size, number of steps) in order to perform THz CT, which will be described in more detail in chapter 4.

At present, it is important to provide some quantitative information concerning the acquisition time of a 2D THz image. Even if the acquisition rate of the THz waveforms is set to 5 Hz, the acquisition speed of each pixel is reduced to approximately 2 Hz owing to the computing procedures such as data storage, eventual averaging process, etc. This means that the total acquisition time for a 100x100 pixels image it about 80 minutes, which is reasonable for imaging of still samples. However, we can notice that this time is longer than commercially available THz imaging system for example by Picometrix company (from 100 to even 1000 THz waveforms per second) [Picometrix].

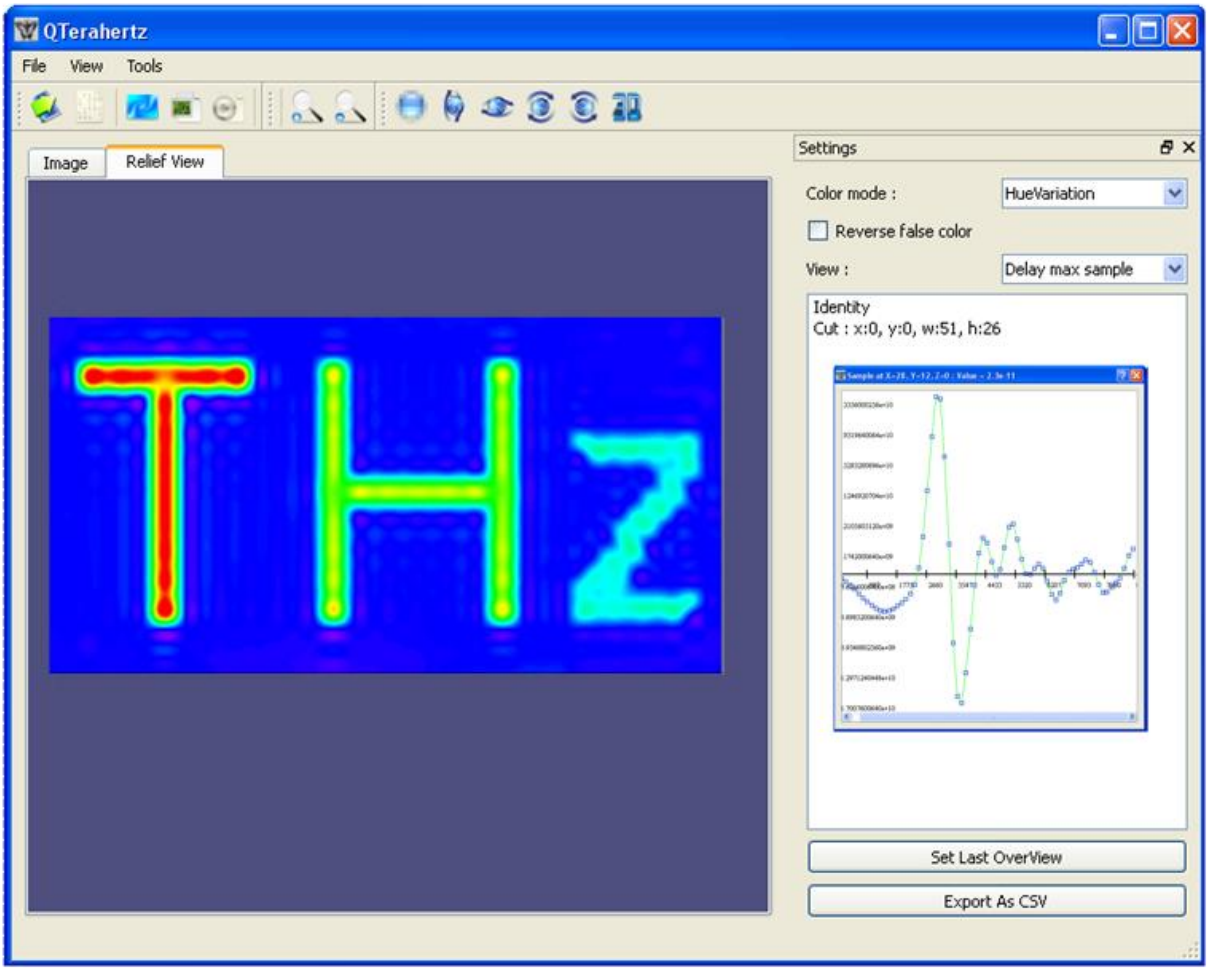

Figure 2.10: Capture screen of Q-Terahertz program for the analysis of THz data. THz images can be obtained utilizing any parameter. THz waveform corresponding to each pixel can be viewed by simply clicking on that pixel.

After this presentation of data acquisition, the final step is the description of the THz image formation. As already explained, a full data set, after raster scanning the sample, consists of a set of

THz time domain waveforms corresponding to each pixel of the image. These waveforms obviously contain a great deal of information: the amplitude and phase of the transmitted THz electric field in the time domain and also in the frequency domain after Fourier transformation, the amplitude of the THz spectrum at given frequency.

In order to visualize the THz images, a specific imaging program (Q-Terahertz) has been developed by the group of Pascal Desbarats (LaBRI, Bordeaux University). The program makes it possible to select a specific parameter employed to build the image, as presented by the capture screen in figure 2.10. In the time domain, we can select the amplitude for a specific time-delay, the maximum or minimum amplitudes, the contrast (difference between maximum and minimum values) or the time delay corresponding to the maximum amplitude (so called "phase-delay" image). In the frequency domain, we can simply select the amplitude for a specific frequency in order to perform spectroscopic THz imaging from 0.1 to 3 THz.

As an example, the figure 2.11 illustrates the different THz images that we can obtain from a single set of THz waveforms, depending on the selected parameters. The sample consists of two metallic pins, with plastic heads, inserted into white opaque foam. From the THz images, we can easily distinct the plastic heads, metal pin and the foam due to the difference in THz transmission. The thickness of the foam can also be calculated (about 3 mm) from the phase-delay image, assuming a foam refractive index of 1.1.

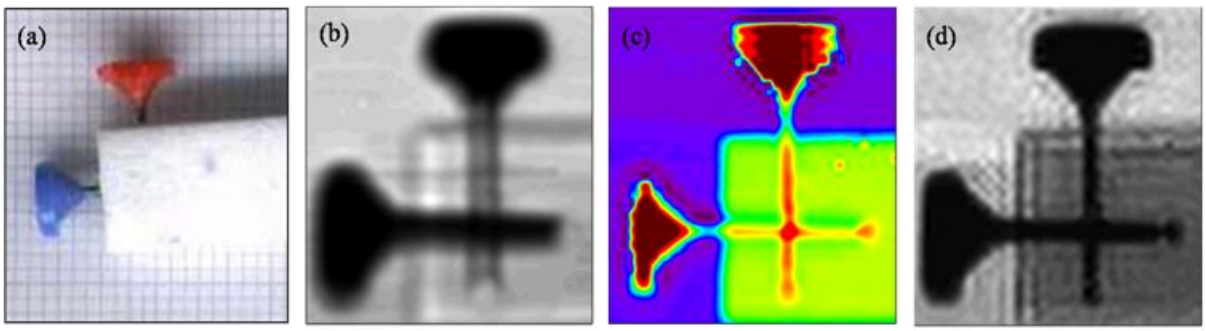

Figure 2.11: (a) Sample photograph: Two metallic needles inserted into a piece of foam, (b) THz image corresponding to the maximum amplitude of the THz waveform, (c) THz image corresponding to evolution of time-delay for each pixel (phase-delay image), (d) THz image obtained at 2 THz.

After explaining in detail the system acquisition and image formation procedure, in the next sub-section we will present the system resolution and beam propagation.

1.6. Beam Metrology and Resolution in THz-TDS Imaging System

By THz beam metrology, one means the study of the evolution of the beam transverse profile during the propagation between the transmitter and the detector. This study is really crucial in our work. Especially to perform raster scanning, the sample should be positioned at the focus of the THz beam. It is essential to precisely determine the position of the THz beam waist, its diameter and the

corresponding Rayleigh range, which is an additional important factor for thick samples and 3D CT, as explained later in chapter 4.

The standard "knife edge" technique is utilized for the measurement of the beam spatial profile in the experimental configuration called (a) (transmission imaging with four Picarin lenses, already presented in figure 2.5). We placed a knife blade on the motorized XY stage in a direction perpendicular to the THz beam propagation. By changing the longitudinal position z of the knife blade, we can estimate the transverse profile of the THz beam along its propagation according to the expression:

$$I_{THz}(z) = \frac{I_0}{2}\left[1 + erf\left\{2\sqrt{ln2}\,\frac{x-x_0}{w_0}\right\}\right] \tag{2.25}$$

where I_o is the total intensity of THz beam, x is the position of the knife blade, x_o is the center position of the THz beam, w_o is the beam waist and *erf* the error function. From the measured waveforms, it is possible to visualize different THz beam profiles depending on the selected parameters (amplitude in time domain or in frequency domain). As the frequency domain is important to evaluate the imaging spatial resolution of the system, the evolution of the transverse beam profile is estimated at 1 THz and 2 THz, in the region between the two central Picarin lenses L_2 and L_3 (Figure 2.5(a)). As explained previously, the sample will be placed at the position z=0 for THz imaging. The propagation of the THz beam exhibits an expected Gaussian profile like the one presented in figure 2.12. The beam diameter at the waist position is estimated to 2 mm at 1 THz with a corresponding Rayleigh range of 5 mm. At 2 THz, the beam diameter is about 1.2 mm with a Rayleigh range of 4.4 mm. These results show that the diameter of the THz beam is not diffraction limited at the focus plane. These above mentioned values indicate the spatial resolution of the imaging system. To improve this resolution, as already presented in figure 2.5, we also developed a configuration (b) by inserting two additional HDPE lenses (10 mm focal length) around the sample.

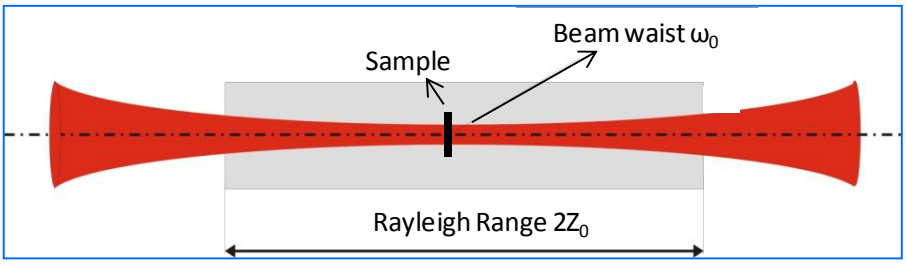

Figure 2.12: Representation of THz beam propagation around the sample and between the 2 Picarin lenses in optical setup (a) of figure 2.5.

With the configuration (b) setup, since the space between the two HDPE lenses is reduced, it is difficult to properly perform the knife edge technique. Consequently, to determine the spatial

resolution of this additional imaging configuration we simply used a calibrated test target. We chose a 1951 USAF resolution test chart printed on regular white sheet paper. This target is widely used to test the resolving power of an optical imaging system. In our case, the investigated pattern consists of lines having dimensions of 280 µm and 220 µm (indicated by the red box in figure 2.13(a). With the THz-TDS imaging system (configuration (b)), we measured the THz images of the bars for all frequencies up to 2 THz. For higher frequencies, the paper absorption starts to limit the SNR of the detection. At 2 THz, the figure 2.13(b) and 2.13(c) shows the corresponding THz images obtained with a 50 µm scan step for both patterns. The three bars (white color) are easily visible indicating that the transverse resolution of the THz imaging system is about 200 µm at 2 THz.

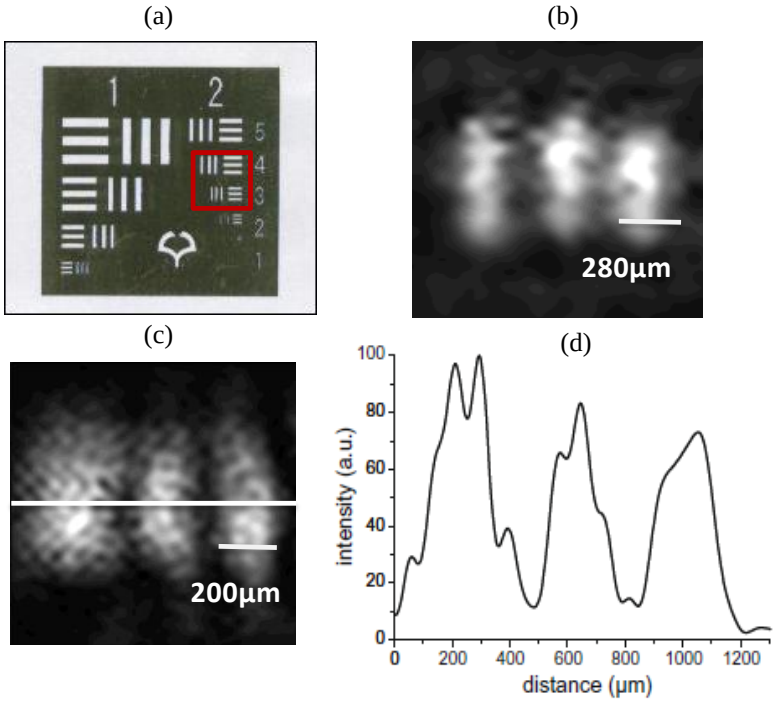

Figure 2.13: (a) Pattern of used calibrated USAF test target with box indicating the position of imaged lines, (b) THz image corresponding to line spacing of 280 µm, (c) THz imaging corresponding to region of 200 µm thickness obtained at 2 THz, (d) Intensity profile corresponding to the horizontal line indicated in (c) on 200 µm pattern.

Figure 2.13(d) indicating the intensity profile corresponding to the horizontal white bar in figure 2.13(c). If the imaging system is diffraction limited, the diameter d_{min} of the THz beam at the focus position can be expressed by:

$$d_{min} = 0.61\frac{\lambda}{NA} \tag{2.26}$$

where, λ is the wavelength and *NA* the numerical aperture of the first HDPE lens. In our case with NA=0.44, we obtain a value of 210 µm. This indicates that the imaging configuration (b) is diffraction

limited, with an ultimate spatial resolution in the order of the wavelength. In our work, this configuration (b) will be essentially used in the case of relatively thin samples (only 20 mm between the two HDPE lenses).

After describing the THz-TDS imaging system and explaining the image formation procedure with all the characteristic features of the system, in the next section we will present the second THz imaging apparatus that we have developed.

Section 2: Continuous Wave Imaging System

We have developed a second alternative imaging system, employing a continuous millimeter wave source for imaging purpose. The main advantage compared to pulsed THz-TDS system is its compactness, stability and ability to reduce the measurement time to get single frequency absorption based transmission images. Indeed, this imaging system only requires scanning the sample over the focused THz beam, without any additional time-delay scanning as in THz-TDS imaging system. Therefore, THz phase information is not available in the CW imaging setup. This optical system is easy to align and portable. It can be displaced to perform non-destructive imaging directly on the interested sites.

2.1. Generation of THz Radiation

For generating THz radiation in this imaging system, we employed a diode Gunn. A Gunn diode is a two terminal device used in high frequency electronics, typically made of materials such as GaAs [Bosh 1975]. It is somewhat unusual in sense that it consists only of N-doped semiconductor material. In the Gunn diode, two regions are heavily N-doped on each terminal, with an additional centered thin layer of lightly doped material. When a voltage is applied to the device, the electrical gradient will be largest across the thin middle layer. This layer starts to conduct, reducing the gradient across it, preventing further conduction [Voelcker 1989, Gribnikov 2001]. In practice, this means a Gunn diode has a region of negative differential resistance, which allows, in combination with the timing properties of the intermediate layer, the construction of an RF relaxation oscillator simply by applying a suitable direct current through the device [Carrol 1970, Greenwald 1988]. The oscillation frequency is determined by the properties of the thin middle layer and the applied external voltage. More details about the functioning of diode Gunn and their fabrication can be found in the article by R. Van Zyl and colleagues [Gunn Diode].

Gunn diodes are commercially available, with oscillation frequencies typically above 100 GHz. In that case, the output power of the CW emitting radiation is up to tens of milliwatts. Generally, the output beam is coupled by using an additional specially designed horn antenna. To increase the output frequency of the emitter, frequency doubler or tripler can be used at the cost of a dramatic decrease in the output power.

In our work, two types of Gunn diodes from Radiometer Physics GmbH (RPG) have been used: a 80 GHz diode coupled to a frequency tripler delivering 0.3 mW at 240 GHz and a 110 GHz diode emitting 20 mW (Figure 2.14(a)). Both diodes are employed with an additional horn antenna. The advantage of the 240 GHz source is essentially the better spatial resolution owing to the longer wavelength (λ= 1.25 mm), whereas the second source has a much larger output power. The precise description of spatial resolution of CW imaging will be presented in the sub-section 2.5.

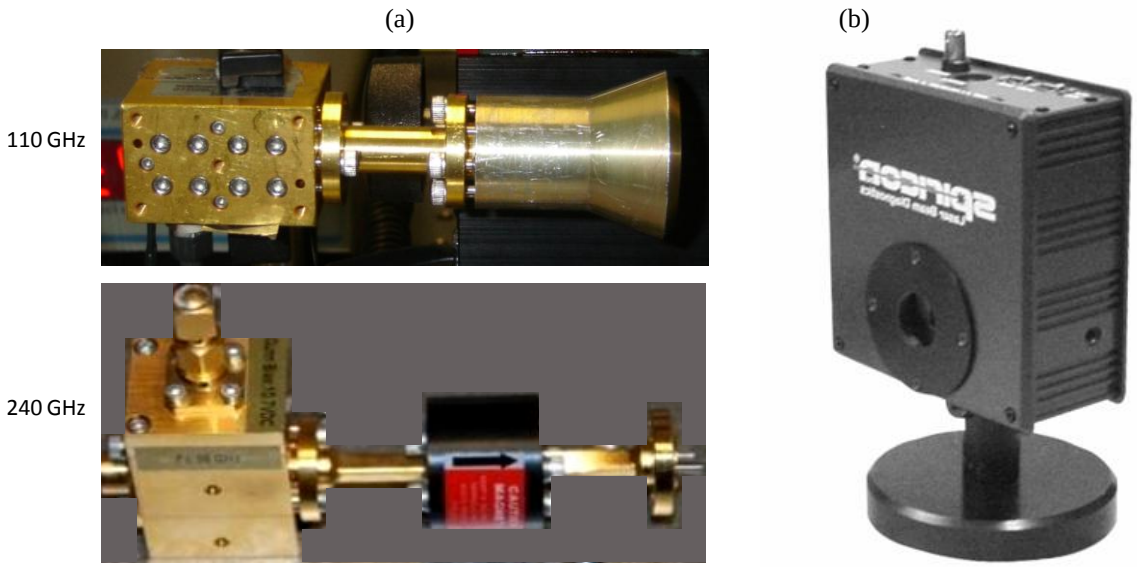

Figure 2.14: (a) Visual photos of two utilized Gunn diodes, (b) Picture of pyroelectric thermal detector (Spectrum detector).

2.2. Detection of THz Radiation

For the detection of the CW radiation, we used a pyroelectric thermal detector from Spectrum Detectors Inc (Figure 2.14(b)). The device is based on the change of internal polarizability when heated by infrared radiation. Below a temperature T_c, known as the Curie point, many pyroelectric and ferroelectric materials exhibit a large spontaneous electrical polarization. If temperature of such material is altered by an incident radiation, the material polarizability is modified. This change may be observed as an electrical signal if electrodes are placed on opposite faces of a thin slice of the material to form a capacitor. However, the sensor will only produce an electrical output signal if the temperature changes. It means that the THz beam has to be periodically modulated by using an optical chopper in order to properly measure the amplitude of the corresponding THz radiation sent onto the detector. This electrical output signal is independent of the wavelength of the incident radiation. Consequently, pyroelectric sensors have a flat response over a very wide spectral range.

In our work, the CW radiation is modulated at 20 to 100 Hz by the use of an optical chopper. This value is limited by the response time of the detector. The amplitude of the THz signal is

measured with a LIA with an integration time constant of 30 to 100 ms. The amplitude of this signal varies from few hundreds of microvolts (noise level) up to about 1 V (saturation of the detector).

2.3. Description of Optical Configurations

For performing CW imaging, three imaging configurations have been developed: (1) transmission mode (2) on-axis reflection mode (3) off-axis reflection mode.

The transmission setup of the CW imaging system is presented in figure 2.15. The output signal from the source is collimated via a parabolic mirror having a focal length of 150 mm. Afterwards, the THz beam is focused with a HDPE lens (60 mm focal length) on the sample which is positioned on a three-axes XYθ motorized stage. After transmission through the sample, the focal volume is imaged using a similar arrangement (lens f=60 mm and parabolic mirror f=150 mm) on the pyroelectric sensor.

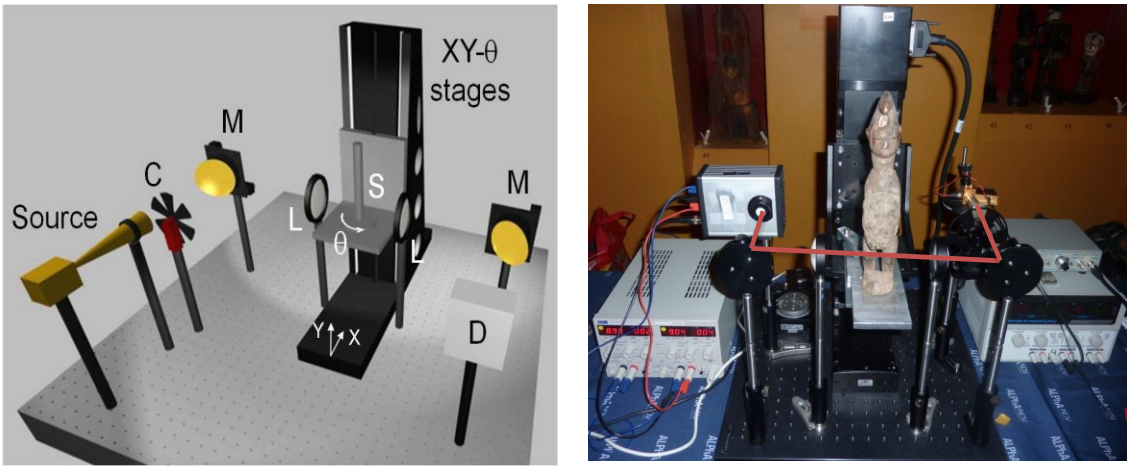

Figure 2.15: Left: Experimental setup for CW imaging system in transmission mode (C: chopper, L: HDPE lens, M: parabolic mirror, S: sample and D: detector), Right: Real picture of the optical setup installed at the Museum of Aquitaine.

The two reflection imaging setups are presented in figure 2.16. For normal incidence (Figure 2.16(b)) a simple HDPE beam-splitter has been used in spite of the important signal losses due to low reflectance. Other optical components are similar to those previously described in transmission mode. For oblique incidence, we chose an incident angle of nearly 30° for sending the THz beam onto the sample. This configuration is selected in case of thin objects with low reflectance properties.

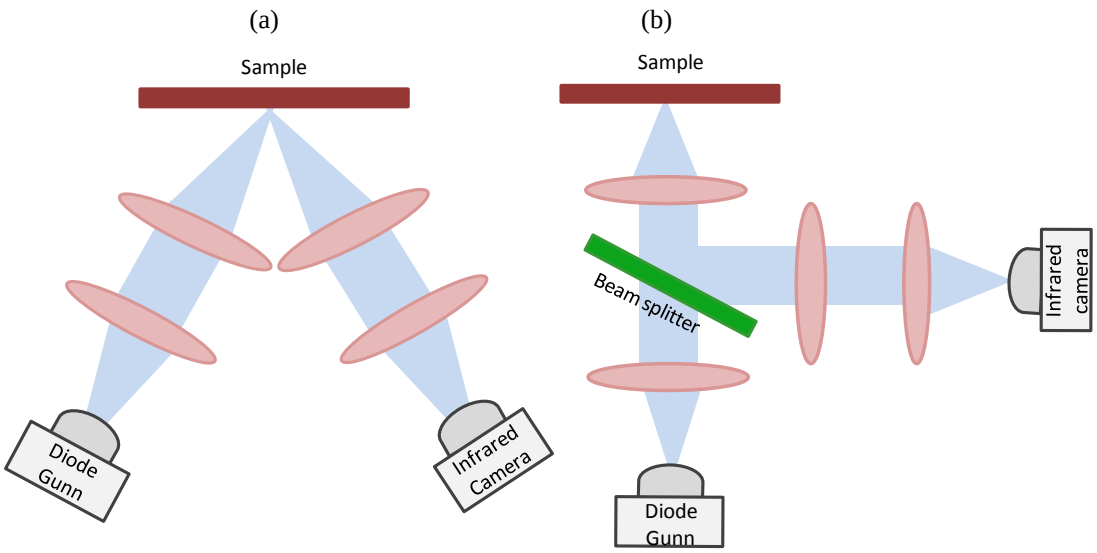

Figure 2.16: Experimental configurations for reflection mode imaging (a) Oblique incidence or pitch catch geometry, (b) Normal incidence or collinear geometry.

2.4. Image Formation in CW Imaging System

In order to form THz images with the CW system, raster scanning of the sample is required. However, as the acquired data is a single value corresponding to each pixel (no delay-line), the acquisition time for performing imaging is shorter than with the THz-TDS system, as already mentioned. The system only requires storing a single value corresponding to each pixel, given by the detector. The detector output is connected to the LIA which further amplifies the given signal. The LIA and displacement motors XY (carrying sample) are synchronized and can be controlled by labview program. Within labview program the user can select all the parameters like image size, scan rate and step size before starting the experiment. Labview program can also give us a real-time visualizing of the sample image during the raster scanning process. A front panel screen shot of Labview program is shown in figure 2.17. With a 10 Hz scanning repetition rate, we can obtain up to 10 pixels per second. For a typical sample having size of 100*100 pixels and pause in displacement of XY motor equal to 1 ms, it takes nearly 10-15 min to form an image.

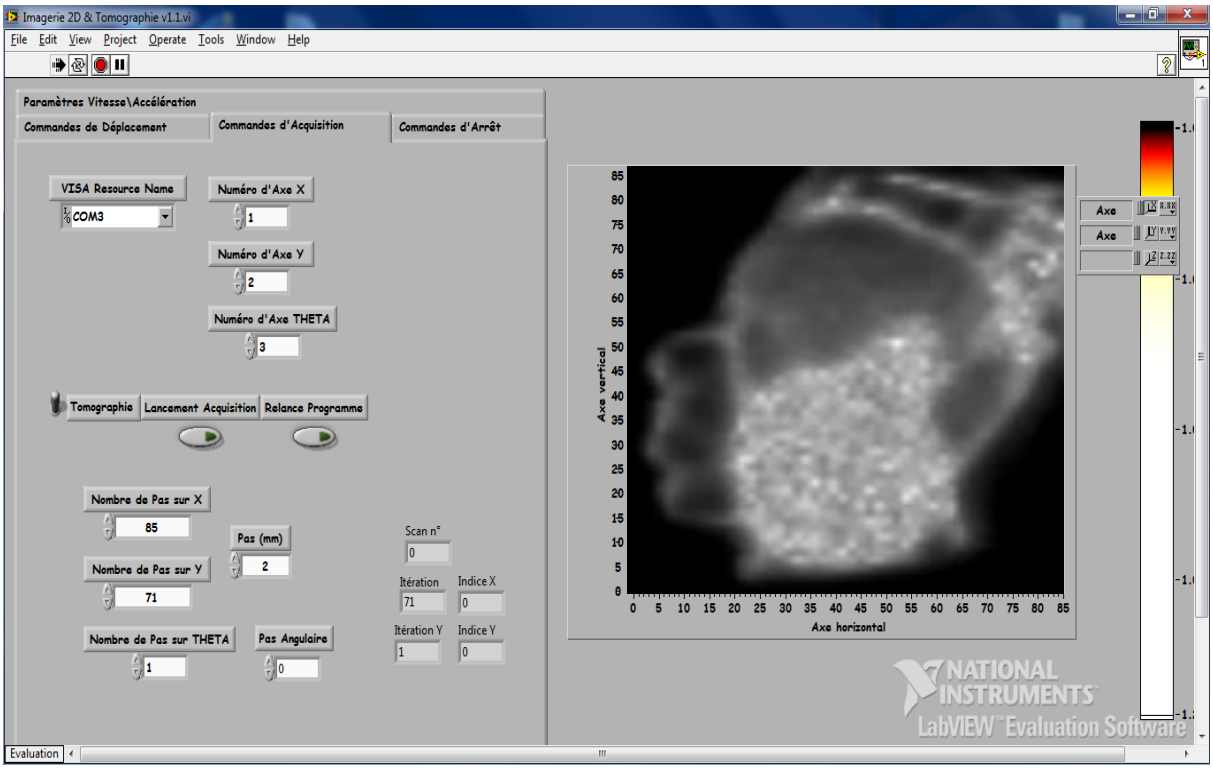

Figure 2.17: Front panel screen shot of Labview program utilized for CW imaging system.

2.5. Beam Metrology and Resolution of CW Imaging System

To evaluate the spatial resolution of the CW imaging system, we first investigated the spatial characteristics of the THz beam at the focal point of the focusing lens. At this position, the beam waist is limited by the incident beam diameter (about 15 mm) and the 60 mm focal length of lens. As the USAF test target patterns were too small to be visualized using the 110 GHz source, we used a thermal camera (Spiricon III) to image the beam waist. Figure 2.18(a) shows the 2D transversal profile of the THz beam at the beam waist visualized by the camera. At this position, the THz beam is homogenous with a quasi circular shape even if some spatial distortions can be noticed.

In order to precisely evaluate the beam size at this position, we also measured the beam diameter using the knife-edge procedure (Figure 2.18(b)). The result indicates a beam diameter of 4 mm (measured at 1/e the value of the maximum amplitude) and corresponding Rayleigh range of nearly 18 mm. This is in agreement with the theoretical values obtained from the propagation of Gaussian beams expressed by:

$$\omega_0' = \frac{\lambda f'}{\pi \omega_0} \tag{2.27}$$

where λ=2.7 mm is the wavelength of the THz radiation, f'=60 mm is the focal length of the focusing lens, ω_o=16 mm the radius of the THz beam before the lens and ω_0' the radius of the THz beam at the

beam waist (at the focal point of the lens). For determining the resolution of the Gunn source emitting at 240 GHz, we utilized the USAF test target with -2 and -1 groups. The square area in the figure 2.19(b) shows clearly the fully resolved horizontal and vertical bars having dimensions of 1.8-2 mm.

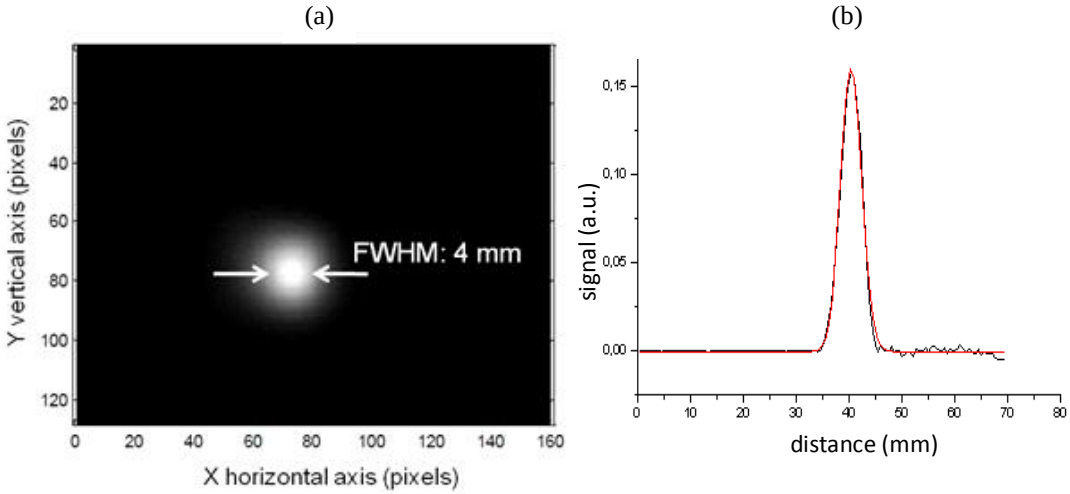

Figure 2.18: (a) THz beam waist for the 110 GHz source, visualized with a thermal camera (Spiricon III), (b) 1D horizontal profile of the THz beam waist at the sample position obtained with a knife-edge procedure.

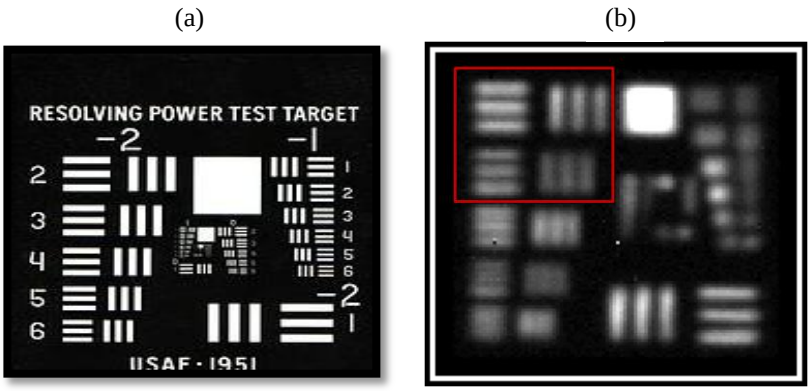

Figure 2.19: (a) Pattern of calibrated USAF test target, (b) THz image obtained with the 240 GHz source, having bars of dimensions 1.8-2.0 mm highlighted in rectangular area.

These obtained results clearly indicate that the spatial resolution of the CW imaging system is limited to a few millimeters owing to the long wavelength of the emitting source. Consequently, the CW system is more adapted for the visualization of sub-centimeter structures within large size object, typically more than (100x100) mm^2.

The long coherence length of the millimeter CW sources (several tens of cm) can cause an interference pattern on the final image which is characteristic of the sample surface. This process has been employed to measure the frequency of each emitting sources. For this purpose, we utilized a tilted plastic plate sample. The sample was imaged by placing at the focus point of the THz beam

between the two central lenses. The sample was further tilted in a gradual manner with fixed angle θ. 2D THz image is shown in figure 2.20 (a), in which one can observe darker (low transmitted signal) and brighter (higher transmitted signal) regions. Figure 2.20(b) shows the line profile presenting the systematic variations in signal corresponding to one horizontal line in 2D image. The curve in figure 2.20 (c) presents the fringe spacing (mm) as a function of the tilted angle (θ). We can calculate the frequency of the emitting source by the relation:

$$i = \frac{\lambda}{2tan\theta} \tag{2.28}$$

By getting λ=1.3 mm, the frequency of the emitting source can be determined as 230 GHz. Same procedure is also repeated for second source (data not shown).

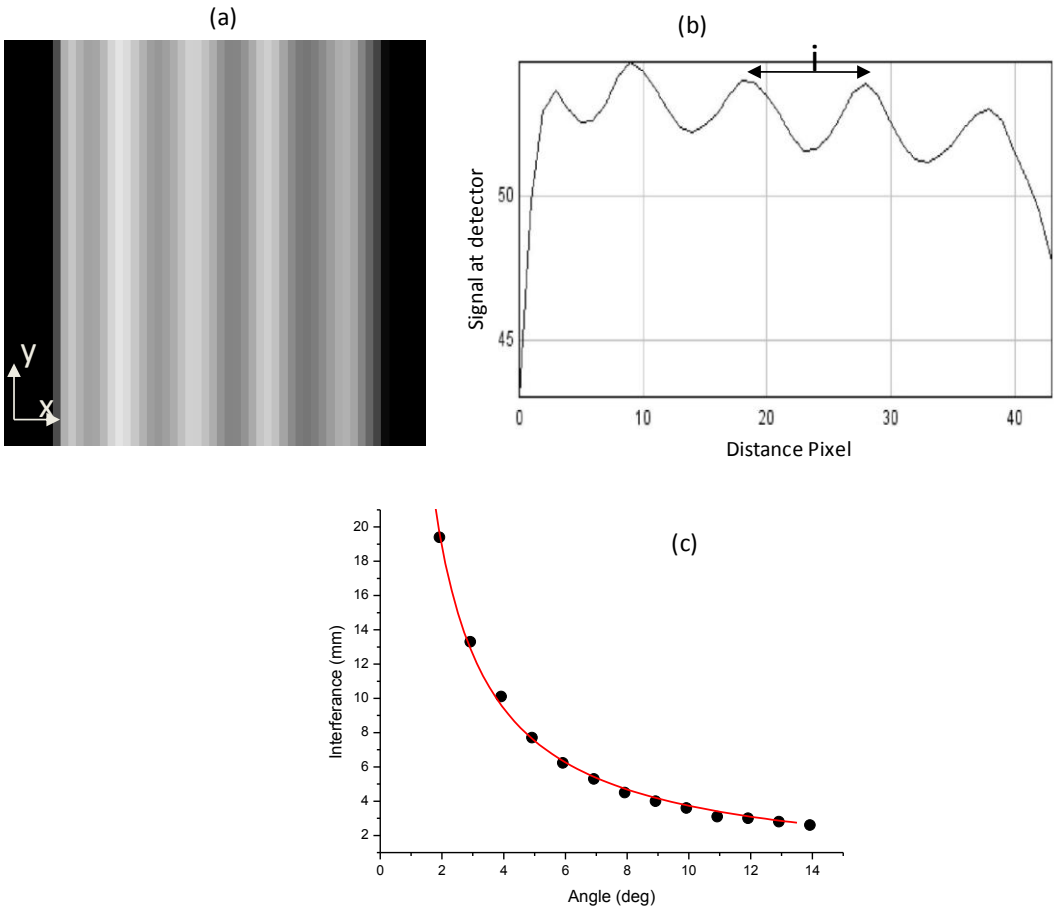

Figure 2.20: (a) 2D THz image of plane plastic plate illustrating interference pattern, (b) variation in transmitted THz signal corresponding to one horizontal line in 2D image, (c) fringe spacing (mm) as a function of incidence angle (θ) of radiation arriving on the sample.

Finally, after a complete description of THz-TDS and CW imaging configurations, the main characteristics of both setups are summarized for convenience in table 2.2 in order to facilitate a simple comparison between these two imaging techniques.

Characteristics	THz-TDS System	CW System
Frequency Range	0-3 THz	0.11 or 0.24 THz (Monochromatic)
Functioning Mode	Pulsed	Continuous
Mean Output Power	~nW	0.3 mW (0.24 THz) 20 mW (0.11 THz)
Detection Type	Coherent	Incoherent
Signal-to-noise Ratio	4500:1	2000:1
Lateral Resolution	200-280 µm (2 THz) (optical Setup 2.5(b))	1.8-2 mm (0.24 THz) 3.5-4 mm (0.11 THz)
Depth Resolution	30 µm (n=1.5)	----
Rayleigh Range	5 mm	8 mm (0.11 THz)
Acquisition Time (Pixels/sec)	2-3	10
Time 2D Image (100*100) pixels	60 min	15 min

Table 2.2: Characteristic features of THz-TDS and CW imaging systems.

Now, in the next section we will show some preliminary imaging results obtained with these optical setups.

Section 3: THz Image Gallery

In this last section, we will present some general results obtained with the THz-TDS imaging and the CW imaging systems, before moving to next chapters. Both these systems have the potential and capability for the non-destructive evaluation of materials and imaging process in various disciplines.

3.1. THz-TDS Imaging

Here, some THz-TDS imaging results will be presented showing the capability and potential of our developed system. We have done many experiments for the non-destructive evaluation of

various materials, like wood, medicines, plastic, metallic objects etc. Few examples are shown here in figure 2.21. To demonstrate that THz imaging has the ability to see through the materials and give an idea about their internal structure, we scanned an object made from a piece of wood (thickness 5 mm), with a screw and a hole (3 mm diameter) inside. Scanning was taken for an area of 10*20 mm by a step of 0.5 mm pixel size. The THz image corresponding to phase-delay can reveal the variation of optical pathway (Figure 2.21(a)). We can clearly identify the vertical screw penetrating the wood and also the perpendicular hole. The height of the hole is about 3 mm. More precisely, we can also measure the depth of the hole. The time-delay between the THz waveforms obtained in wood and in the region of the hole indicates that the hole has a 3.2 mm cylindrical shape, in perfect agreement with the experiment. Also, with the time-delay between the THz waveforms obtained in air and in wood, we can evaluate the mean refractive index of the wood as n=1.31. THz imaging can also be used for spectroscopy purpose, e.g. to image medicine capsules as shown in figure 2.21(b), for extracting their spectral fingerprints.

THz imaging can also be used to see through opaque materials to find hidden cavities. An example is shown in figure 2.21(c). The word THz in engraved on a Teflon slab such that each word, T, H and Z has a different depth of 3, 2 and 1 mm respectively. After this, the sample is covered by 2 mm thick piece of another Teflon slab and was raster scanned. THz image clearly reveals the three hidden letters, having different contrast owing to the difference in their corresponding depth. A distance versus thickness curve can also be plotted, illustrating clearly the depth thickness of the three letters. We have also performed THz-TDS measurements to characterize a photopolymer resin (Full care materials) in the THz range and the obtained results underline the promising applications of such materials for the fabrication of 3D THz phantoms, (more details can be found in Annex A).

THz-TDS imaging can also be performed in reflection mode to get an idea about the layer structure of the sample. It can be used in various disciplines, e.g. this technique is widely used in pharmaceutical industry to evaluate the thickness of tablet coatings, to avoid uneven layers and flaws in their internal structure. An example image is shown in figure 2.21 (d). We have performed single horizontal line scan to evaluate surface of various tablets such as Ketek and Spasfon. From the reflected THz signal having multiple peaks in the THz waveform coming from various coating layers of tablets corresponding thickness of each layer can be extracted. THz-TDS reflection imaging can also be used in the measurement of inaccessible tree ring sections for the purpose of tree-ring cross-dating. Figure 2.21(e) shows the reflected THz waveform coming from a pine wood piece, having various sub-reflections coming from various rings interface. Axial and lateral 2D THz images of obscured ring patterns can be formed. This application can be useful in dendrochronology field.

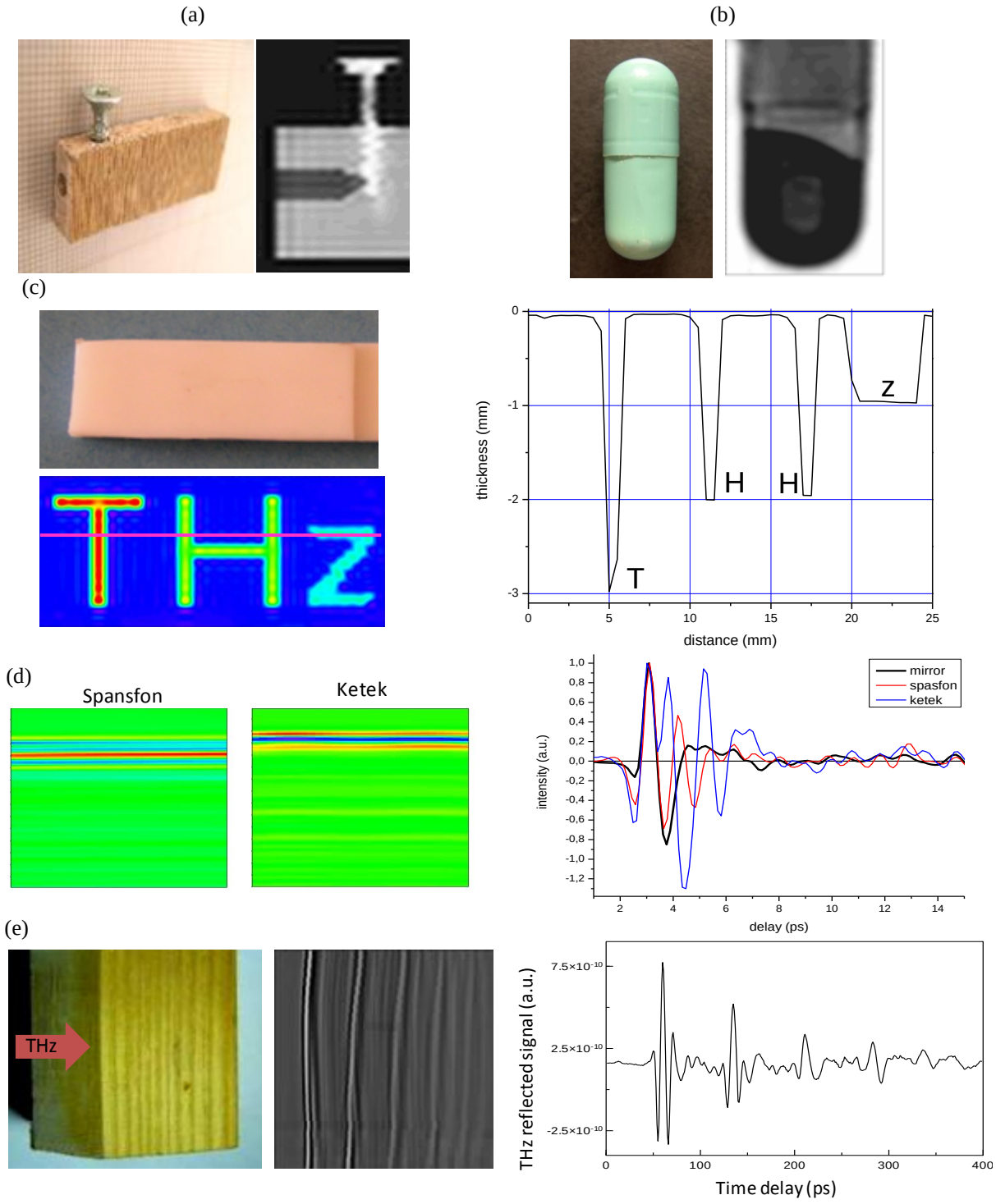

Figure 2.21: (a) Photograph of the sample along with the THz image obtained by working on phase-delay values, (b) Sample picture of a medicine capsule along with the THz image corresponding to maximum amplitude value, (c) Picture of Teflon sample, THz image formed by delay values, along with a curve showing the difference of sample thickness corresponding to the horizontal line in THz image, (d) THz reflection image corresponding to one horizontal scan along tablets surface showing multiple reflections, (e) THz reflection waveform coming from a piece of wood along with THz image showing various interface in the wood.

3.2. Continuous Wave Imaging

At the end of this chapter, we would like to present some general imaging results obtained with the CW imaging system. This imaging system has the potential for non-destructive evaluation of the materials. Although phase information is not available, absorption/reflection based images are found sufficient to provide information about the sample structure. Some specific examples are presented in figure 2.22. Figure 2.22(a) shows the optical and THz image of a opaque plastic toy obtained with the 110 GHz source. The plastic toy contains a hidden plastic animal inside, which can be easily seen in the THz image.

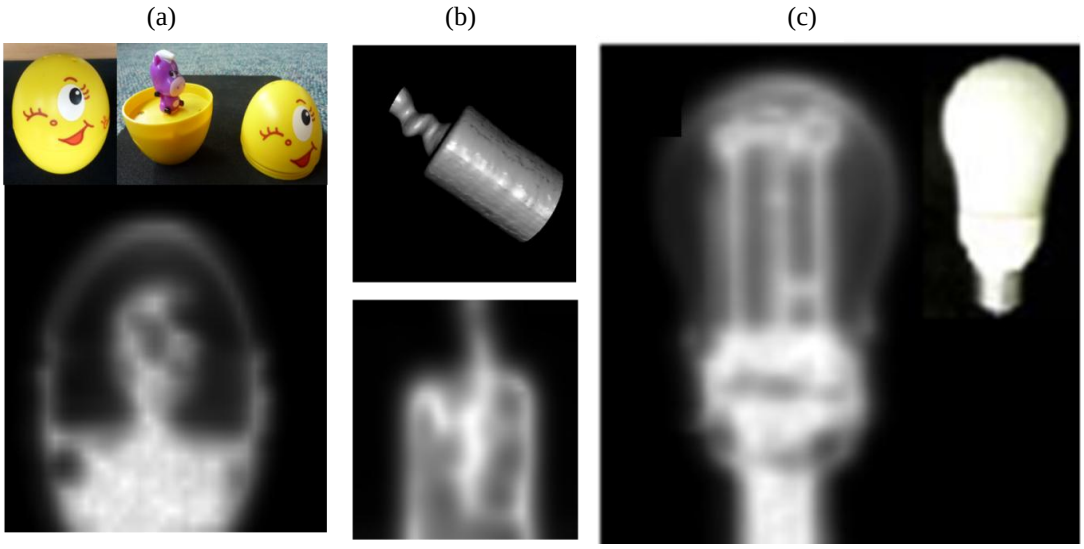

Figure 2.22: (a) Optical and THz image of a plastic toy obtained at 110 GHz, (b) Image of the corkscrew inside a cork, (c) Photograph and THz image of the fluorescent light bulb obtained with the 110 GHz source.

Figure 2.22(b) presents the image of a corkscrew in a cork. It can be noticed that the transmission of the THz beam is strongly attenuated through the cork, so we cannot notice a clear contrast between the metal screw and cork. As a result it is really hard to distinguish between the helical shape of the screw inside the cork. The THz image of a fluorescent light bulb along with its optical picture is shown in figure 2.20(c). Here we can clearly reveal the two fluorescent bars inside the opaque material. These examples show that this imaging system is capable of exploring hidden structures inside opaque materials. However owing to the longer wavelength and resolution of the imaging system, it is more preferable for imaging sub-centimeters structures having large dimensions.

Conclusion

In summary, we have developed and optimized two imaging configurations, namely THz-TDS imaging system and CW imaging system. We presented both experimental methods with their main features. We explained the general procedure of data analysis and image formation that we have developed. Both of these systems have many applications in non-destructive evaluation, mainly

leading to viable techniques for scanning opaque objects. The ultimate goal of this thesis is to perform a complete analysis for inspection of artworks, to detect hidden underdrawing and for 3D non-invasive inspection of opaque objects. In fact the key to successful applications is a combination of imaging and spectroscopy, which can provide access to sample information, but also about its chemical composition. At present, we will discuss our major results in the upcoming chapters, obtained from both imaging systems concerning 2D and 3D THz imaging, applied to art science.

CHAPTER 3

THz Imaging for Art Science

In this chapter we want to present the feasibility of using THz spectroscopic and imaging techniques for non-contact and non-destructive inspection of artworks. We demonstrate that THz imaging can provide complementary data for art historians, restorers and curators.

This chapter is divided into three main sections. The first one consists of a brief background with a selection of past reported works, along with the comparison of other frequently used techniques in the field of art conservation. In the second section, we will present and discuss our spectroscopic and imaging results obtained with the pulsed THz-TDS system, described in the previous chapter. Especially, THz-TDS imaging can provide specific information on material composition and thickness measurements owing to the time-of-flight analysis of the THz pulses. Therefore, in this section, we will mainly present some results concerning the investigation of painting artworks. In the last section, we will show the potential of the CW imaging system, also described in the previous chapter, for certain applications regarding to art science. After showing few results concerning painting artworks, we will also present additional *on-site* results obtained at the museum of Aquitaine (Bordeaux) concerning THz imaging of historical unique objects.

Section 1: Background

The cultural heritage field is related to archaeology, anthropology, art history, paleoecology, geography, dendrochronology, paleontology, paleobotany and other architecture work. In anthropology, body fossils (mummies and bones) are the principal type of evidence about ancient life [Brasier 2006]. Antique museum objects [Targowski 2004] involve historical pottery, jars, funeral urns, metallic coins, figurines, weapons, silver and gold utensils, ancient stones and shells, painting artworks [Gora 2006], written manuscripts [Carter 1996], etc. These historical objects cannot be altered or destroyed owing to their uniqueness and they should be preserved with special care. The traditional role of the curator/restorer involves the examination, conservation and preservation of cultural heritage using "any method that proves effective in keeping that property, in as close to its original condition as possible, for as long time as possible" [Pye 2001, Stoner 2005].

In the field of painting artworks, scientists and researchers are forever interested in the material composition and substructure of paintings [Casini 1999, Pinna 2009], murals [Pieraccini 2005] or frescoes [Barilaro 2005] for protecting our cultural heritage. This scientific analysis is essential for curators as it can be employed to reveal the history of the artwork, investigate the original material composition and discover how the artwork has been restored in the past centuries. Beyond this, for the restorers, the scientific analysis of art materials provides information about the artist’s technique and allows an accurate material selection for the future restoration.

1.1. Techniques for Investigating Artworks

Various physical methods of diagnosis are frequently used for the purpose of material identification and investigating artist strategy. Fourier-transform infrared spectroscopy (FTIR) [Ferrer 2005], Raman microscopy [Clark 2007], optical coherence tomography [Arecchi 2005, Targowski 2006] and X-ray radiography [Hahn 2005, Calza 2007] are some of the commonly used methods for the analysis of artwork.

To obtain detailed information about the sample, multiple spectroscopic imaging techniques are generally utilized. Various multispectral acquisition systems utilizing different methods collectively, based on X-rays, ultraviolet (UV) [Pelagotti 2006] or infrared (IR) [Derrick 1999, Delaney 2010], were reported in the last few years [Burrafato 2004, Giakoumaki 2006]. This multispectral imaging method allows us to examine the interested work under different ranges of electromagnetic wavelengths [Fisher 2006, Bruni 2002, Pelagotti 2008]. An example of multispectral imaging is shown in figure 3.1. Depending upon the specific wavelength and abilities of utilized techniques, each obtained image will reveal particular information about the sample structure, hidden layers, sub-surface damage or artist strategy.

Normally all above mentioned techniques have their own advantages and limitations compared to each others, as described earlier in chapter 1. The suitability of each method can depend on the composition, dimension, condition and nature of the sample under test. Ideally, the method of evaluation should be non-destructive, contactless, non-invasive, spatially precise and applicable in *situ*.

Figure 3.1: Multispectral imaging technique used for the examination of the painting "Madonna and child" by Carlo Crivelli. Different high resolution scan images have been obtained from X-ray to IR regions of the electromagnetic spectrum. (Courtesy of M. Seracini).

For art painting investigation, each technique is limited by the number and thickness of the painting layers that can be studied, since the spatial resolution and penetration depth of the radiation is proportional to its wavelength. A general scheme of accessible painting layers, corresponding to commonly used techniques, is shown in figure 3.2. In the inspection of painting artworks, UV is useful for examining varnish [UV], whereas infrared can reveal the underdrawing. X-ray radiography can reveal older painting hidden below the surface, find dislocations, water damage and other defects [Calza 2007, Nolf 2011].

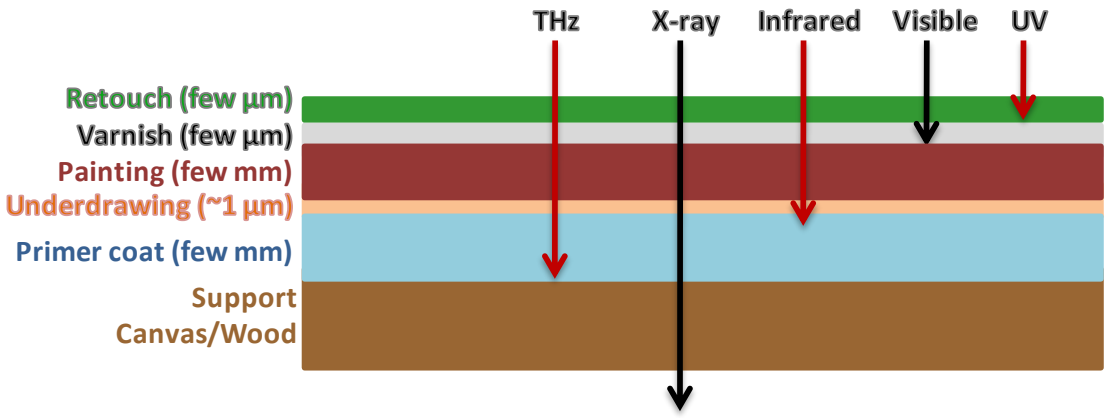

Figure 3.2: Schematic of measurable layers in any artwork by various imaging techniques.

Despite their tremendous applications, each of these techniques has some limitations. As these methods do not use pulses of radiation, they may not have the ability to distinguish the properties of buried interfaces and objects easily that is, they lack depth resolution. For example, an X-ray image looks two dimensional; one cannot tell if a feature is on the surface, just under the surface (paint layer) or buried 5 mm under plaster. UV, Raman, IR spectroscopy may give some good depth resolution, because one can easily measure phase changes in the return signals, but none of them have the penetration depth to probe millimeter thick layers. There are also some crucial pigments used in underdrawing that IR reflectometry (e.g. sanguine, azurite) and X-rays radiography (e.g. lead white) cannot easily distinguish. In addition, X-rays sometimes cannot be applied to delicate samples owing to the fragility/uniqueness of the samples and the problem of sample radiometric dating, especially for ceramic sample, after X-ray irradiation [Aitken 1985].

Considering these short comings of aforementioned techniques, THz radiation has emerged as a possible powerful candidate in the field of art conservation for the non-destructive and non-invasive investigation of various art related materials.

1.2. Application of THz radiation for Art Conservation

THz radiation can provide additional details and complementary spectroscopic data related to each material for a better diagnosis and understanding of artwork. THz radiation can be used to

analyze the materials slightly below the layers of the paint, such as preparation layers. It also has the potential for providing depth information from the paint layers. Particularly evident is the scope of the THz technique for the investigation of mural wall paintings where X-ray radiography cannot be easily applied.

In cultural heritage field, two main aspects of THz technology can be profitably explored: spectroscopy for the analysis of various materials and non-invasive THz imaging. These abilities of THz radiation have been demonstrated in variety of research works reported for the analysis of cultural heritage materials [Manceau 2008]. In anthropology, THz images of an artificially embalmed ancient Egyptian human mummy hand and a macerated human lumbar vertebra were successfully obtained [Öhrström 2010]. The analysis of human cortical bone is performed by THz-TDS system [Stringer 2005]. For dendrochronology applications, THz imaging is applied for tree ring analysis for the purpose of tree ring cross-dating [Jackson 2009]. In the field of artwork, THz imaging has shown a great potential, for the evaluation of mural paintings [Jackson 2008], analysis of fresco and wall paintings [Kouzuma 2003] or even for character recognition in medieval manuscripts [Fukunaga 2008].

THz radiation is widely applied for the investigation of paintings and spectroscopic analysis of pigments [Fukunaga 2007, Kohler 2006]. For spectroscopic analysis, several online free spectral databases are now available. NICT and RIKEN in Japan have developed the first online spectral database (http://www.thzdb.org) in 2008. It contains more than 200 THz spectra of various materials including specific old pigments used in art painting. This spectral database is essential for THz technology to be commonly used in industrial or academic research fields, although it permanently requires wider contribution across the globe for its development.

In pulsed THz time-of-flight imaging system, one can map layer by layer the sub-structure of painting, reveal hidden underdrawings and sometimes spectrally identify pigments, organic/inorganic dyes and varnish. Many research groups such as Adam *et al*. have compared results of THz images with other techniques like X-ray radiography and infrared reflectography [Adam 2009]. They have confirmed that THz radiation is capable of providing information on the thickness of the hidden paint layers and mapping drawing layer from backside of model oil painting on canvas. They also find that X-rays do not easily penetrate layers of high density pigments, such as lead paint, which is ubiquitous in historical painting. Therefore, THz radiation can be alternatively used for conveying 3D build up of paintings.

THz imaging was also applied to analyze the historical mural painting of a Lamaism temple using a transportable commercial THz imaging system (Picometrix) [Fukunaga 2010a]. Utilizing the fact that most pigments and some synthetic polymers have characteristic fingerprint spectra in the THz region, materials used in painting can be identified alone or as a combination of pigments and binders. Fukunaga and Picallo reported an important THz analysis on the master-piece Polittico di Badia by Giotto exposed at the Uffizi Gallery in Florence [Fukunaga 2010b]. Cross-sectional images of

historical medieval panel paintings were obtained revealing the painting and gesso layers from the wooden support. Labaune *et al*. presented the feasibility of THz radiation for the non-contact measurement of papyrus writings. Ancient pigments such as carbon black and red ochre were used for the purpose of writing with Arabic gum as binder based on historical methods. Images of hidden papyri were successfully revealed by THz imaging [Labaune 2010].

After this brief introduction of THz imaging in the field of art conservation, in the next two sections, we will present the results obtained with our THz-TDS imaging system (section 2), especially in the domain of art painting, and the CW imaging system (section 3) with a laboratory study and a final *on-site* study performed at the museum of Aquitaine.

Section 2: Spectroscopy and Imaging of Artwork by THz-TDS System

In this section we will demonstrate the feasibility of our THz-TDS imaging system for the inspection of painting artwork. This section is divided into three main parts. In the first part, we will show the THz imaging inspection of graphite written documents. Spectroscopy of graphite lead mines and THz imaging analysis will be presented. In the second part, we will demonstrate the capability of our THz-TDS system for the inspection of painting artworks. For this study, mainly artificial painting samples have been settled in order to reveal underdrawings and the thickness of the paint layers. In the last part, we will highlight the possible application of THz imaging for the investigation of sigillography work, which refers to the study of seals attached to documents as a source of historical information.

2.1. THz-TDS Imaging of Written Documents

We applied THz-TDS imaging technique for the investigation of spectroscopic properties of various inks and pencil leads on paper in order to evaluate the potential of the technique to directly recognize the characters deposited on a document. This work was carried out as a regional project called "TeraBook" in collaboration with the i2S company (www.i2S.com) which was interested in scanning the pages of written documents without touching them or opening the book.

2.1.1. THz Spectroscopy of Papers

THz radiation is applied for evaluating the spectroscopic properties of paper. Since the THz waveform is directly influenced by the sample transmission, it is possible to determine the optical thickness of the sample (included thickness and refractive index) by analyzing the time-delay of the maximum amplitude of the transmitted waveform. By this way, in the framework of the Terabook project, we investigated the transmission properties of regular papers without any writing inscriptions.

Typically paper composition consists of organic and inorganic material. Organic portion consisting of cellulose, hemi-cellulose, lignin and or various compound of lignin (Na-lignate etc) may be 70 to 100%. Inorganic portion consisting of mainly filling and loading material such as calcium carbonate, clay or titanium oxide, may be 0 - 30% of paper. Depending upon the specific composition of each paper, we may observe a distinct THz fingerprint. Typically, we used regular 80 µm thick white sheet papers (80g/m^2). Figure 3.3(a) indicates the transmission of the THz beam through an increasing number of pages. Considering the limit of the detection, we can evaluate that the THz radiation can propagate through nearly up to 200 pages, corresponding to transmission amplitude of only 0.15%. Moreover, by simply considering the time delay of THz waveforms as a function of page number, we can extract the mean refractive index of the used paper in the 0.1 – 2 THz spectral range. The measurement corresponds to n=1.54±0.05. Finally, the THz-TDS spectrometer can also be used for page counting, with a precision depending on the longitudinal resolution of the system, directly connected to the THz main pulse duration. Figure 3.3(b) shows the THz waveforms corresponding to the THz transmission through a stack of 100 and 101 pages.

By analyzing the waveforms, we can clearly see that the system is able to distinguish the presence of the additional page in the second sample. We can calculate a time-delay of about 158 fs between the two waveforms due to this single page difference. Considering the previous n=1.54 mean refractive index, we can estimate that the page thickness is (90±10) µm from this THz time-of-flight analysis. Here the uncertainty is fixed by the ability to determine the temporal position of the maximum of the transmitted THz waveform. This shows the capability of the system to count and differentiate between various numbers of pages in any document. An additional THz time-of-flight analysis will be presented for art painting investigation, in section 2.2.

(a)

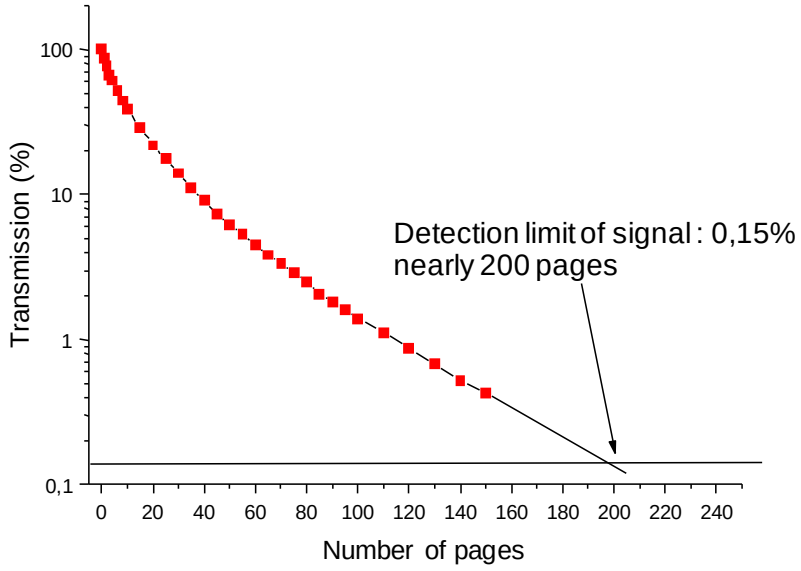

(b)

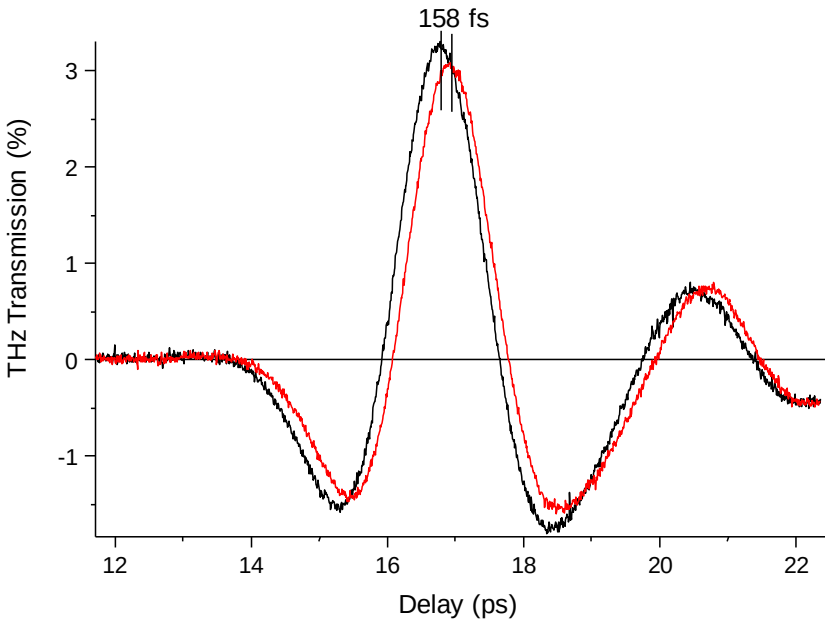

Figure 3.3: (a) Transmission of THz radiation as a function of number of white regular pages, (b) THz waveforms transmitted through stack of 100 and 101 pages.

2.1.2. THz Spectroscopy of Graphite Leads Pencils

In the framework of the Terabook project, THz-TDS imaging of various inscriptions was carried out, by using several inks and graphite pencils. Different commercial inks and various kinds of graphite pencils have been studied. Depending on the writing implement, the THz image contrast will be altered. When the inscription is written with most commercial inks (pen, printer, photocopier), the THz image is not able to reveal the presence of the ink onto the support. The main reason is probably the fact that the dye molecules from main inks are non-polar and thus do not absorb significantly in the THz spectral range. However, significant results have been obtained using graphite leads, which is not surprising owing to the high conductivity of graphite material. Consequently, we focused our work for the investigation of scripts written with various graphite lead pencils. One of the main purposes of this research work was the assessment and identification of the graphite pencil lead grade using THz spectroscopic imaging for the future investigation of underdrawings beneath paintings.

We performed THz imaging of pencil lead on paper in transmission mode using the transmission setup (b) described in figure 2.5. Graphite has a dense, layered molecular structure that makes it a moderate quality semiconductor. It is well-known that graphite can absorb or reflect THz radiation due to its high conductivity [Ji 2006, Brumfiel 2009]. The writing characteristics of graphite based pencils (black colour, hardness, etc.) arise by altering the proportion of graphite to clay. These pencils are usually graded by manufactures using the letter H for hardness (more clay, less graphite) and the letter B for blackness (less clay, more graphite). In this study, we tested several pencil leads

with increasing level of graphite in the lead from the standard writing pencil HB to softer black marking pencils indicated as 2B, 4B, 6B and 8B.

We started by investigating the THz transmission through a square graphite area (1*1 cm^2), drawn with different pencil leads on a regular 80 µm thick white sheet paper (80g/m^2). Although it is difficult to evaluate the graphite quantity deposited onto the paper, owing to the hand drawing process, we can estimate that the sample thickness is less than few micrometers. Moreover, the exact quantity of graphite deposited onto the paper is difficult to evaluate because the pencil lead is made of graphite powder and also various kind of binders. For different pencil grades, figure 3.4(a) shows the temporal transmitted data through the sample. The amplitude of the THz wave can vary depending on the pen pressure and the graphite thickness. To ensure the validity of the method, we repeated several times the measurement taking into account the variations of the pen pressure on the paper during the hand writing process. Finally, the THz signal transmission can be directly related to the graphite absorption/reflection since the scattering of the THz radiation is reduced because its wavelength is larger than the typical spatial dimensions of the surface texture. Obviously, it would have been useful to measure the absorption spectra of graphite pellet to avoid the problem of the unknown quantity of graphite deposited onto the paper. However, the pellets have to be very thin (less than typically 100 µm) due to the low THz transmission through graphite. Since such pellets are difficult to obtain, for future practical applications in art conservation, we also found it interesting to determine at least qualitatively the transmission of graphite directly deposited onto paper.

As a reference, we plotted the data corresponding to the blank paper sheet (Figure 3.4(a)). For the HB pencil (or even harder leads from 2H to 9H) the THz absorption was negligible (data not shown) and the data are similar to the reference. However, from 2B to 8B, we clearly observed a significant attenuation of the transmitted THz beam due to the absorption/reflection of the THz radiation. This difference in transmission is mainly due to the presence of graphite in the pencil lead since the concentration of this mineral increase regularly from HB to 8B. A slight temporal shift is also observed which originates from the variations of the optical path due to increasing sample thickness. This behaviour can be directly used as a pertinent parameter for THz imaging of written documents.

Figure 3.4(b) represents the corresponding transmission spectra of the different graphite leads on paper from 2B to 8B. We can notice that no strong spectral difference is visible in the spectra. This may be explain by the fact that the chemical constitution of the different pencil leads is almost the same for all the samples and only the proportion of graphite changes from 2B to 8B. However, the amplitudes of the spectra are clearly different which offers the possibility to identify different pencils from hard to soft black-marking graphite leads, at least qualitatively. The transmission spectra extend from 0.1 to 2 THz since the paper starts to absorb strongly above this limit. For example at 2 THz, the transmission of 2B pencil is 65% and decreases down to 25% for the 8B pencil. These results

emphasize that even a thin graphite layer deposited by a pencil lead can provide sufficient amplitude and phase contrast in the THz domain.

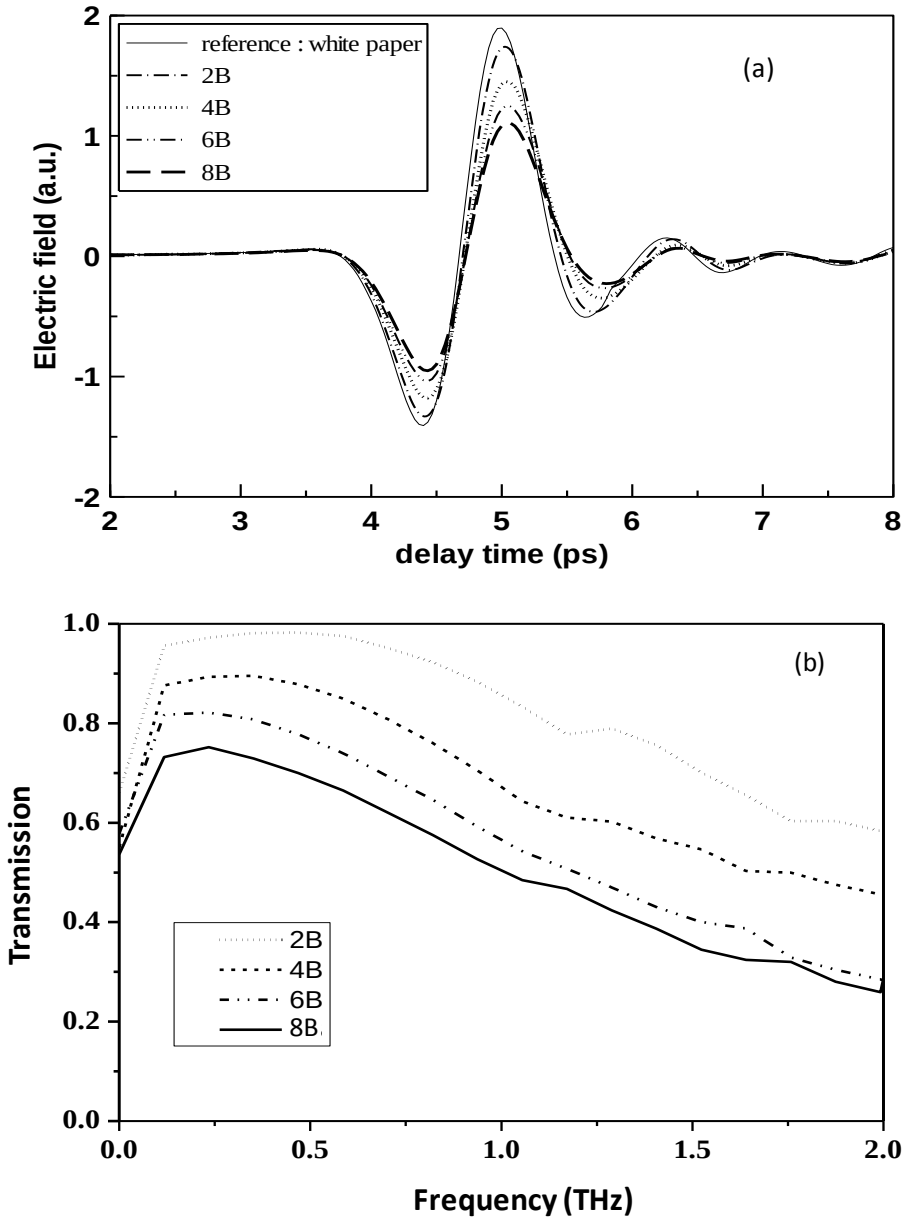

Figure 3.4: THz transmission properties of several graphite pencil grades. (a) THz waveforms obtained after transmission through white paper without writing (reference) and white paper recovered by graphite pencils from 2B to 8B, (b) corresponding transmission spectra in the THz region.

We also performed experiments in reflection mode in order to complete the THz analysis of graphite lead mines. In reflection configuration (Figure 2.5(c)) pellets formed by graphite lead powder from 2B to 8B grades, are used. The pellets are homogenous with a thickness of nearly 1 mm. Figure 3.5 shows the evolution of the THz reflectance as we go from 2B to 8B grades, depending upon the

additional amount of graphite present in each lead. The data have been obtained by simply plotting the maximum amplitude of the reflected THz waveform. The results show an increase of the reflectance from 58% (HB) to 94% (8B), with a 100% reflectance corresponding to an aluminium mirror reflection. From these measurements, we can conclude that the reflectance of the THz radiation is directly related to the concentration of graphite into the pellets. This reflectance analysis can explain the THz transmission properties of graphite previously exposed in Fig. 3.4. The decrease of the THz transmission from 2B to 8B grades is mainly due to the increase of the THz reflectance rather than THz absorption by the sample.

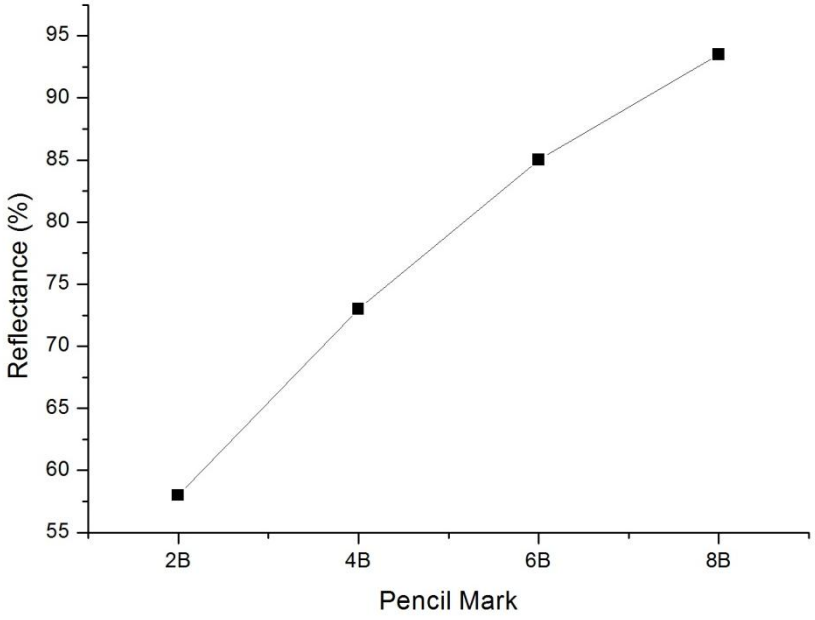

Figure 3.5: THz reflectance of various graphite lead pellets from 2B to 8B grades, measured from the maximum amplitude value of the reflected THz signal.

2.1.3. THz Imaging of Graphite Written Documents

The above mentioned spectroscopic results allow us to assume that THz-TDS imaging system can identify the quantity of graphite, i.e. the label of the pencil lead, deposited onto the paper. For this verification, we imaged in transmission mode the previous CNRS logo where each letter has been written with a different lead grade (2B, 4B, 6B and 8B respectively) and the five oblique lines were made with the harder HB grade. The corresponding visible and THz pictures of the logo are shown in figure 3.6(a) and (b), respectively. In the visible image, it is almost impossible to discriminate which pencils have been used to write the individual letters. It means that the visible image does not allow the identification of chemical nature of different letters. Raster scanning of the sample is performed by the transmission setup (b) shown in figure 2.5. The THz image obtained at 2 THz is shown in figure 3.6(b). Utilizing a false gray colour scale (white colour represents higher transmitted THz signal), we can clearly visualize that the letters of the CNRS logo appear darker and darker due to the increase of

graphite content from the C letter to the S letter. However, around the S letter, the five oblique lines written with the HB pencil are hardly visible in accordance with the low reflection of the HB lead in the THz region as already mentioned. Finally, with the THz image at 2 THz, various letters can be separated from each other due to the selective THz transmission of the graphite.

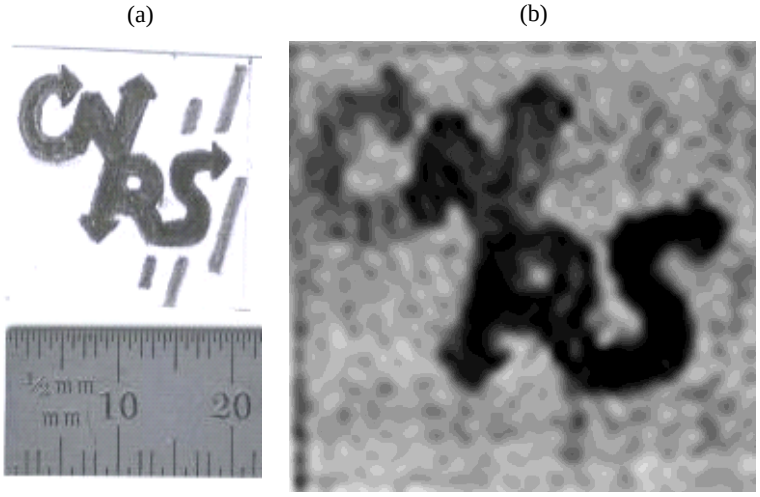

Figure 3.6: (a) Digital photograph of the sample, (b) THz image at 2 THz of the CNRS logo drawn with five different graphite pencil grades (oblique lines around S: HB, C: 2B, N: 4B, R: 6B, S: 8B).

As already mentioned in the previous chapter, it is also possible to compute THz images not only using the spectral amplitude but also directly using the arrival time of the THz pulse (i.e. temporal phase shift). Such image contains information about the optical path of the sample in the THz range. Figure 3.7 represents the THz map of the CNRS logo where the time-delay of THz main pulse has been plotted. This phase-delay image appears different to the previous spectral picture at 2 THz (Figure 3.6(b)). To explain this, we have to take into account that the variations of the colour map do not reflect the variations of the sample chemical properties but either the difference in the sample thickness (in micrometer). The accuracy of the depth measurement is related to the measurement of the arrival time of the THz pulse and the acquisition step of the delay line. With a micrometer scan of the delay line, we can estimate that the accuracy of the depth measurement is about 5 µm. This precision is not as good as a previous work of Hills *et al*. who reported an ultra-high depth resolution of 0.5 µm. However, these authors used a completely different system using a heterodyne detection with a hybrid CW THz source [Hills 2008].

The width of letters seems to be smaller as compared to figure 3.6(b). This may be due to the fact that the phase delay picture (Figure 3.7) is very sensitive to any variation in optical thickness which improves the image resolution. It can also be noticed that the five HB oblique lines around the S letter are well visible in the image since the contrast does not depend anymore on the chemical properties of the pencil leads but only on the paper thickness variations. In short, for the study of

written documents on soft materials such as paper sheet, the phase THz imaging seems to be a powerful tool to determine the variation of the sample thickness. In that sense, the imaging system works as a kind of non-contact THz profilometer. At least, the results described in figure 3.6 and 3.7 shows that it is possible, from a single THz imaging experiment, to combine spectral and temporal THz analysis in order to improve the effective contrast and reinforce the efficiency of the THz imaging.

Figure 3.7: THz map of the CNRS logo obtained using the THz main pulse time-delay representing the paper thickness variations due to the pencil grade writing.

Finally, we present another advantage of the transmission THz-TDS imaging system apparatus, which consists of revealing underdrawings beneath ink layers, to recover buried layer information. For this purpose, the sample is a handmade butterfly drawn on standard paper with a 4B pencil lead (size is 15*15 mm^2). Figure 3.8(a) represents a standard photograph of the object under study. Before performing THz imaging, the butterfly sketch has been fully recovered with a black ink felt-tip pen so that it is impossible to distinguish the drawing with bare eyes (Figure 3.8(b)).

Figure 3.8(c) shows the THz image of the sample formed at 2 THz. In spite of the presence of the black ink, the butterfly is clearly visible with a good contrast and high resolution. However, the fine details at the top of the butterfly wings are hardly visible. In figure 3.8(d) which represents the THz image using the arrival time of the THz pulse (phase), the image quality is improved and the finest details of the sample can be resolved. As mentioned previously, the high quality of the phase image is attributed to the fact that the arrival time of the THz pulse is very sensitive to any thickness variations of the sample.

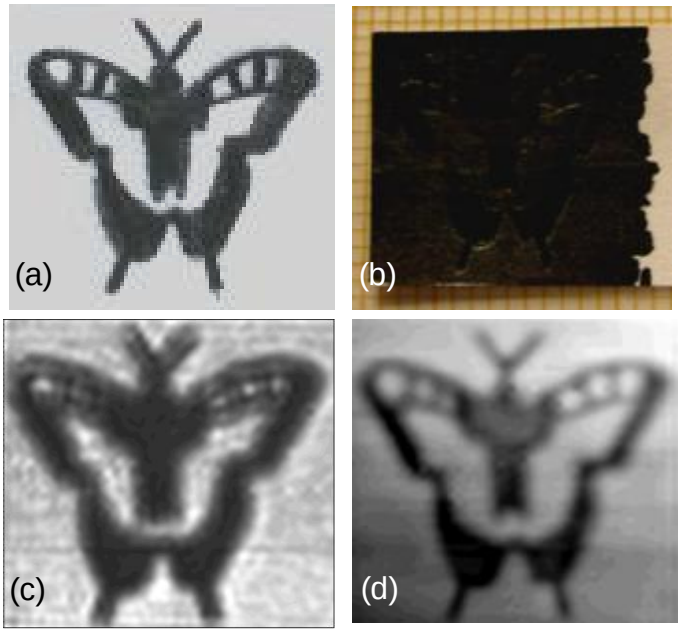

Figure 3.8: Butterfly sketch drawn on paper with a 4B graphite pencil. (a) Digital photograph of the sketch, (b) digital photograph of the sketch painted with a black ink felt-tip pen, (c) THz image at 2 THz, (d) THz image using the THz main pulse time-delay.

In conclusion, we can say that we are able to identify various graphite lead pencils based on their specific transmission properties. The THz-TDS system offers the opportunity to visualize sketches beneath ink layers. We have investigated a drawing under an ink layer and were able to successfully recover the underdrawing. In the next step, we will present THz imaging applied to art painting, demonstrating the ability of THz-TDS imaging system for spectroscopic analysis of pigments and examination of graphite underdrawings.

2.2. THz-TDS Imaging for Painting Artwork

We used THz-TDS imaging technique for the investigation and evaluation of interested artworks, such as paintings which represent one of the most complicated and unique artworks. In paintings, the precise identification of pigments and binders can provide significant insight for the potential authenticity of the artwork. It can help curators and restorers to understand the artist's strategy and can provide information about the sample. Pulsed THz imaging can be safely used for this purpose as it can reveal the sub-structure and can be used for extracting depth information in order to measure the thickness variations of the sample. Here, as a preliminary step of THz imaging for painting artwork, we will present some results of THz transmission and reflection imaging using commercially available paintings.

2.2.1. THz Spectroscopy of Modern Pigments

In the first step, it is necessary to establish a basic understanding of material properties used in paintings. For this purpose, we performed a spectroscopic analysis of various painting pigments in order to determine the transmission spectra of the pigments. For the paintings, we used commercially available gouaches (Van Gogh acrylic colour from Royal Talens). The colours and official pigments codes (giving chemical composition) have been indicated in table 3.1. The binding materials are acrylic resins. Modern paintings have been preferred since the different pigments employed in the gouaches are clearly identified. For spectroscopic measurements, the samples consist of thick pellets of pure gouaches (variable thickness, table 3.1).

Colour and pigment index	Transmission at 0.3 THz (%)	Transmission at 0.7 THz (%)	Thickness (mm)
Oxide black PBk11	8	1	1.55
Titanium white PW6	45	9	1.18
Ultramarine PB29	50	13	1.34
Brilliant blue PB15/PG7/PW6	29	4	1.61
Carmin PR23	44	4	1.23
Naphtol red light PR112/PO34	60	29	1.63
Azo yellow deep PY74/PO43	45	12	1.81
Burnt sienna PR101	50	20	1.63
Azo yellow light PY3/PY74	30	5	1.94

Table 3.1: Transmittance properties of Van Gogh acrylic colours (Royal Talens) at 0.3 THz and 0.7 THz.

The THz transmittance of nine different colours has been investigated using the THz-TDS system. The measurement of the spectra depends on the contents of pigments and binders and also the amount of paints in the pellets. After evaporation of the binders, the measured spectra can give quantitative information concerning the paint transmission (Figure 3.9). Although the frequency response of the system extends up to 3 THz, we cut the THz spectra at 1.5 THz due to the significant absorption of the materials beyond this frequency.

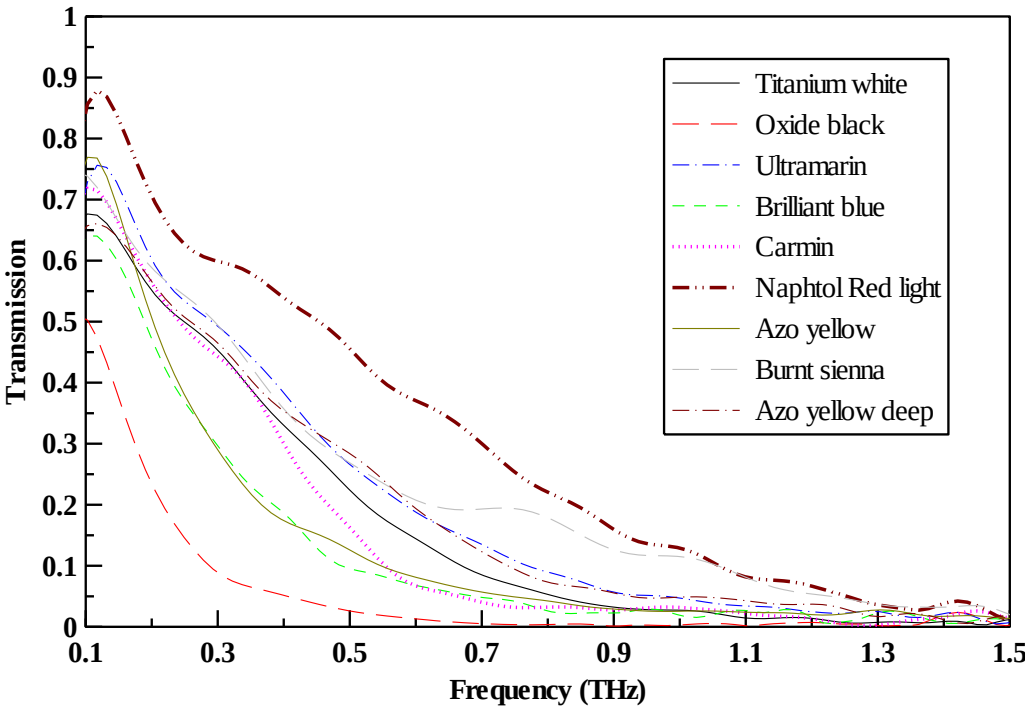

Figure 3.9: THz transmission spectra of the Van Gogh acrylic colours (Royal Talens).

For all colors, we can notice a strong absorption beyond 1.2 THz. It means that between 1.2 THz and 2 THz, only the unpainted canvas will exhibit a significant transmittance. This can be useful to identify painted from unpainted areas in an artwork. Table 3.1 presents the THz transmission at 0.3 THz and 0.7 THz, associated with the thickness of the samples. The best transmittance is for naphtol red light which is about 40% around 0.4 THz. Oxide black has the lowest transmittance (10%) located near 0.2 THz. All other colours have intermediate transmittance located around 0.3 THz.

From the spectroscopic measurements of the different paintings, we can conclude that we cannot distinguish specific fingerprint absorption of the THz radiation by the pigments. We mainly observed a global attenuation of THz amplitude after the transmission through the sample. In the following, we selected four different colours in order to precisely measure their spectroscopic properties (absorption coefficient and frequency resolved refractive index): oxide black (lowest transmittance), naphtol red light (highest transmittance), azo yellow deep and ultramarine (intermediate transmittance). Figure 3.10 presents the corresponding optical index and absorption coefficient of these four different colours. From the results, we can notice the higher absorption and refractive index of oxide black with respect to others, which indicates the possibility of differentiating this colour in any artwork from other used pigments. Absorption coefficients of azo yellow light and naphtol red are smaller and very similar, whereas ultramarine absorption is intermediate. These results will now be used in THz imaging experiments.

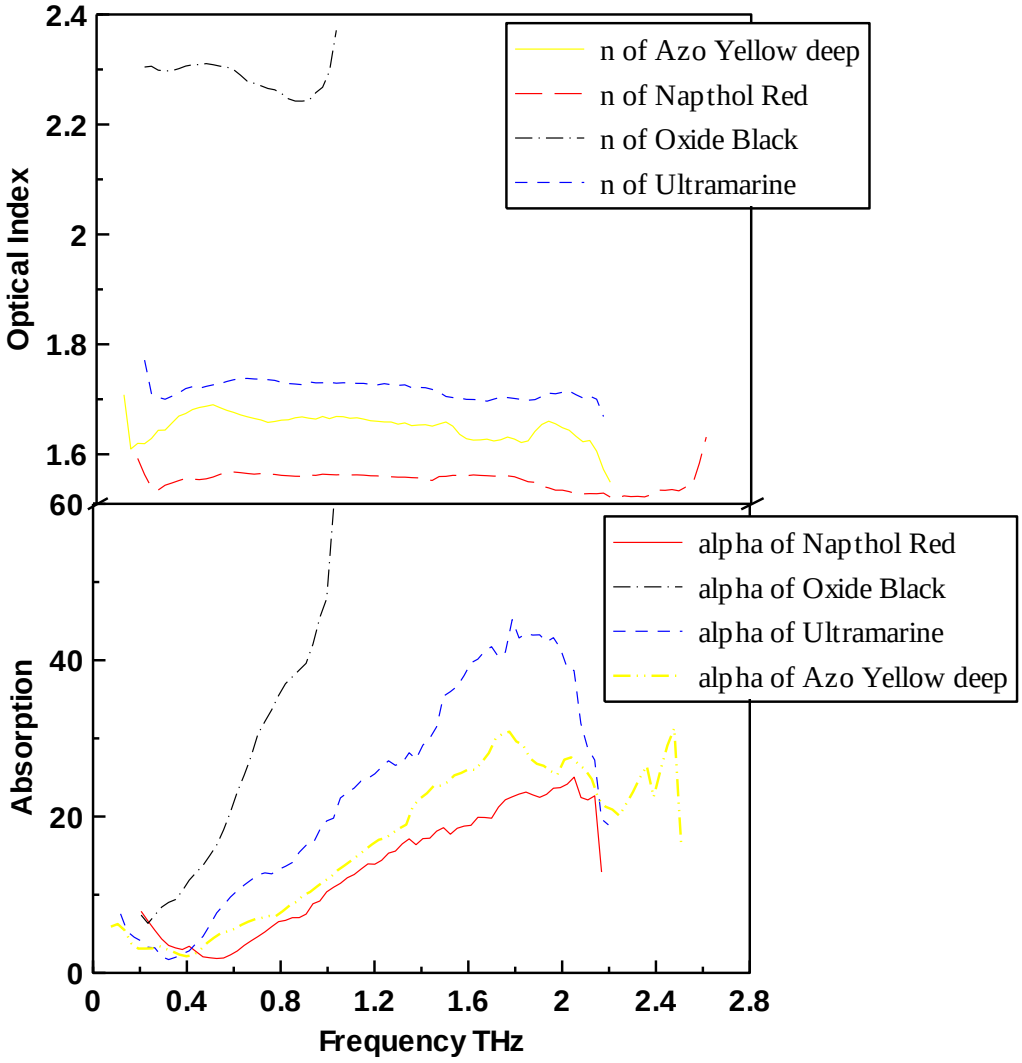

Figure 3.10: Optical index and absorption coefficient of four selected pigment colours.

2.2.2. THz Transmission Imaging of Painting

After spectroscopic analysis, we performed THz imaging of various paintings. The first step is preparation of the samples. For this purpose we used standard painting canvas without applying any specific preparation. First, we used lead pencils to draw a sketch on the canvas. As described earlier the writing characteristics of graphite based pencils (black colour, hardness, etc.) arise from the ratio of graphite to clay. For all samples, we selected a 6B lead pencil to assure a good proportion of graphite associated with a medium hardness of the mine. After drawing sketches, selected colours have been deposited onto the canvas to form the final samples. Thus, the samples consist of hidden handmade graphite sketches covered by various paint layers in such a way that neither the sketch nor the complex tomography of the sample can be distinguished by the naked human eye.

The first sample selected for THz imaging consists of a music note sketch realized with 6B graphite mine on a piece of canvas (Figure 3.11(a)). Then, the sketch has been covered by four paintings as illustrated in figure 3.11(b). These colours are titanium white, ultramarine, azo yellow

light and brilliant blue corresponding to approximately similar THz transmittance. The aim of this first experiment is to visualize the graphite sketch under the paintings and also distinguish the four colours.

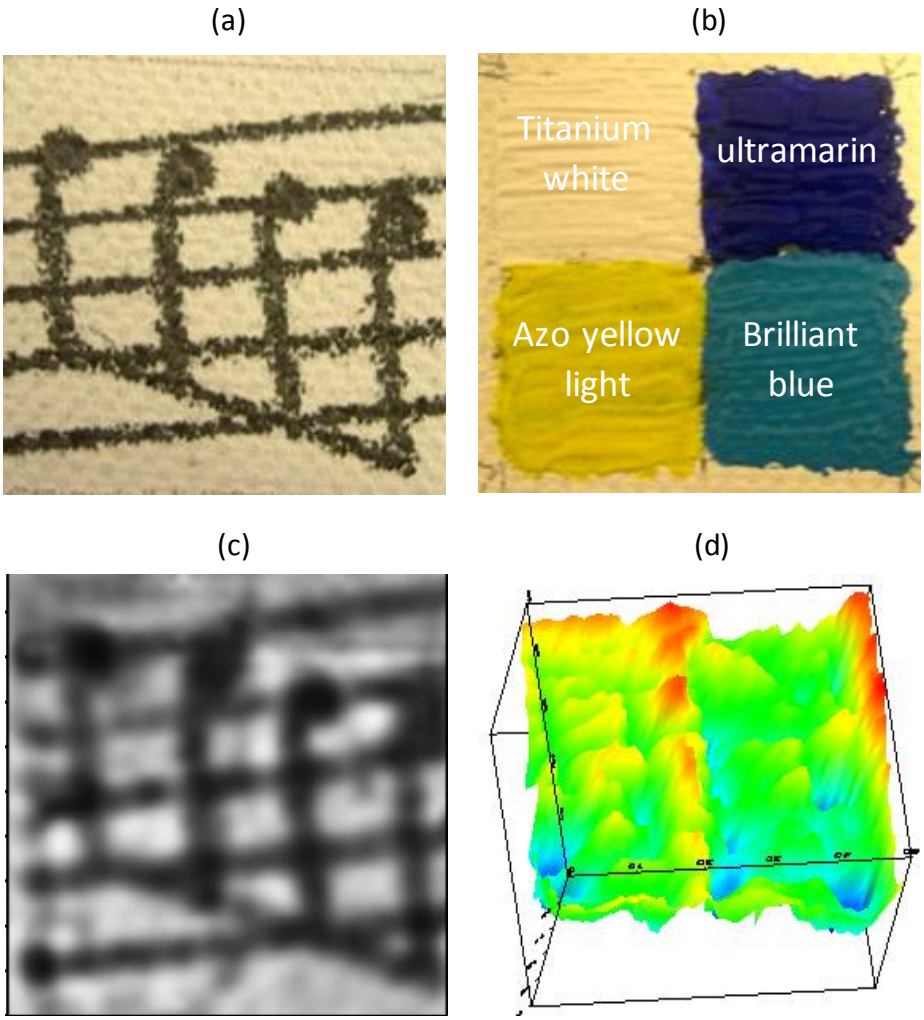

Figure 3.11: (a) Photograph of the graphite sketch, (b) Photograph of the painted surface with four different colours, (c) Transmission THz image (maximum value of the THz waveform), (d) 3D THz map of the sample obtained using the THz main pulse time-delay.

Figure 3.11(c) shows the THz image in transmission mode obtained from the temporal data by plotting for each pixel the maximum value of the THz waveform. The graphite sketch is clearly visible for each part of the sample. It means that, in spite of the pigments absorption, the THz radiation is also significantly reflected by the presence of the graphite. This decrease of transmission is clearly visible in the THz image, which makes it possible to use the THz-TDS technique to visualize sketches of original paintings beneath layers. However in figure 3.11(d), it is impossible to see any significant difference coming from the four different colours. It is understandable if we consider that the four colours have nearly the same transmittance in the 0.1–2 THz region.

The figure 3.11(d) represents a completely different THz image where the colour gradient indicates the optical path variations over the sample. The blue colour indicates an increase of the optical pathway. Indeed, it is also possible to compute THz images not only using the temporal or

spectral amplitude but also directly using the arrival time of the THz pulse (i.e. temporal phase shift). Considering that the refractive indexes of the four colours are quite similar, we can conclude that all four sections have quite the same thickness even if some small irregularities can be observed. As already mentioned, the accuracy of the depth measurement is related to the measurement of the arrival time of the THz pulse and the acquisition step of the delay-line. In transmission imaging, a reference waveform is necessary to measure the thickness variations from this reference. The smallest thickness variation that can be measured is determined by the ability to precisely determine the temporal position of the THz main peak. If we estimate that a change of the temporal position of 70 fs can be measured, we can evaluate that a minimum painting thickness variation of about 30 µm can be calculated by the system (calculation for ultramarine with a refractive index of 1.73). In reflection geometry, the situation is slightly different, as we will explain it later in section 2.2.3.

Our second sample is another 6B graphite sketch (human face, figure 3.12(a)) recovered by three stripes of ultramarine painting with increasing thickness (Figure 3.12(b)). The upper part is a very thin layer (30-40 µm), the thickness of the middle part is 290-350 µm and that of the lower part is 510-550 µm. These thickness measurements have been performed using a digital caliper. The thickness variations within a layer arise from the non-uniformity of the painting deposited onto the support. With this second sample, we want to test the ability of the THz imaging to visualize the graphite sketch under thick painting layers and also the possibility to directly measure the sample thickness. Figure 3.12(c) represents the THz image obtained at 1 THz after Fourier transform of the temporal data. The human face is clearly visible even if the borders of the painting stripes induce a diffraction of the THz beam. This is due to the rapid variation of the sample thickness along these lines. In figure 3.12(d), the phase-delay map shows the three step shape of the sample.

We can estimate the sample thickness by comparison of the arrival times of the THz pulse in each region. Of course, this measurement depends on the pixel position since the painting thickness is non-uniform within a layer, as already mentioned. Here, we present the thickness range for each portion of the sample. In the upper part, we measured a 30-40 µm thickness limited by the precision of the system, in the middle part the thickness range is 270-300 µm and in the lower part, the measured value is 480-530 µm. These values are in agreement with the thickness measured with the digital caliper. The main advantage of the THz imaging is that the technique provides a contactless measurement.

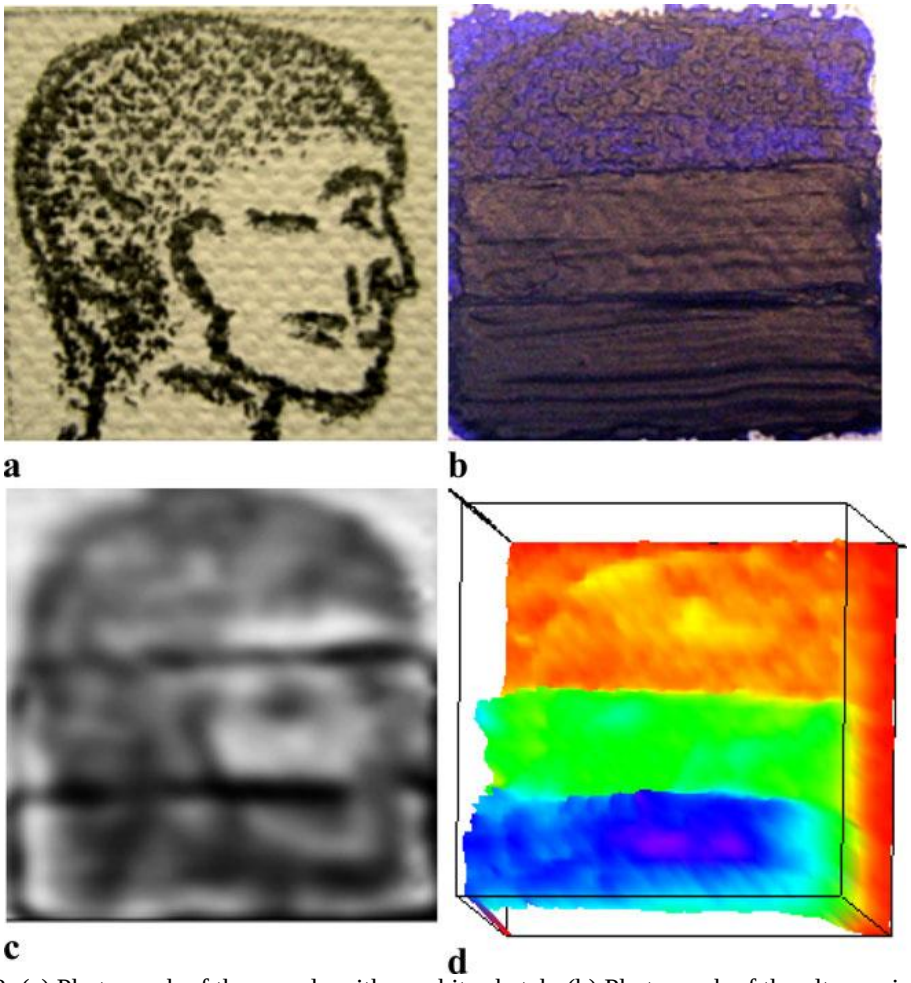

Figure 3.12: (a) Photograph of the sample with graphite sketch, (b) Photograph of the ultramarine painted surface with three different thicknesses, (c) Transmission THz image at 1 THz, (d) 3D THz map of the sample obtained using the THz main pulse time delay.

To demonstrate that our THz-TDS system is able to image a more complicated and realistic sample, we used another sample composed by a graphite sketch (woman face, Figure 3.13(a)) recovered by many layers of paintings of different colours (Figure 3.13(b)). The THz image obtained in a transmission mode at 1 THz shows the ability of the technique to visualize underdrawing in spite of the complexity of the superior painting layers (Figure 3.13(c)). Some artefacts are visible in the image, especially some oblique dark lines coming from the upper thick painting stripes (brown and yellow) that certainly diffract the incident THz beam. This complexity is also revealed by the THz phase image (arrival time of the THz peak signal, figure 3.13(d)) which exhibit the thickness variations of the painting layers. From this image, the graphite sketch is of course not visible but the magnitude of painting layers deposited onto the canvas can be identified. This example proves the ability of the THz-TDS to perform an effective THz imaging of painting artwork.

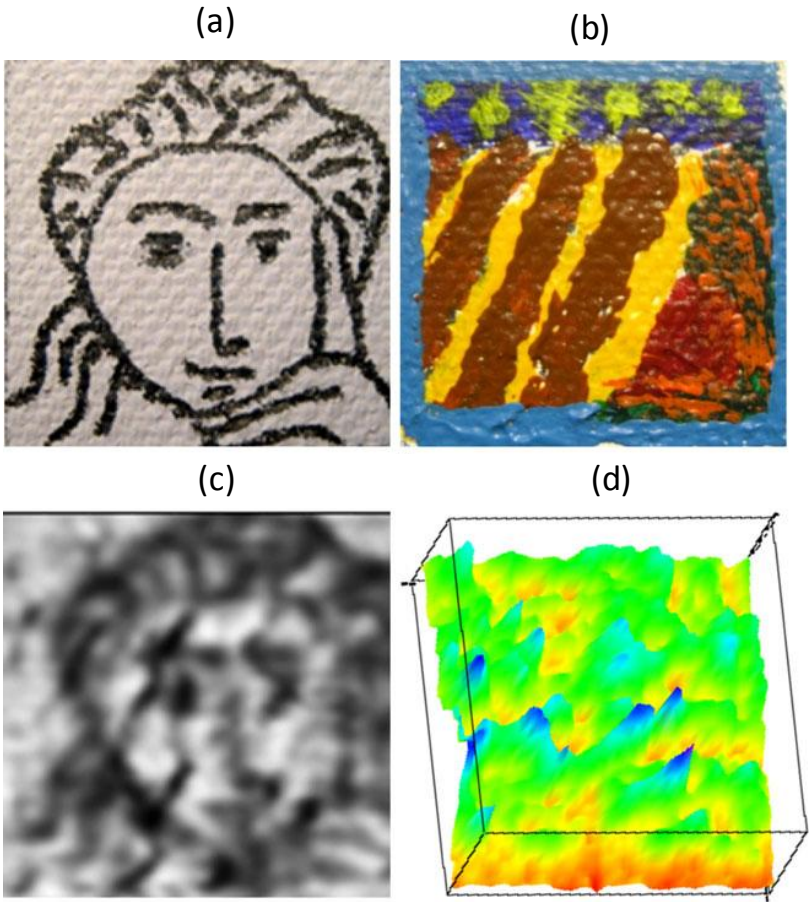

Figure 3.13: (a) Photograph of the graphite sketch, (b) Photograph of the sample recovered by many painting layers and colours, (c) Transmission THz image at 1 THz, (d) 3D THz map of the sample obtained using the THz main pulse time delay.

2.2.3. THz Reflection Imaging of Paintings

THz reflection imaging has been used to study hidden sketch and paint layers under thick, optically opaque materials such as paint and plaster. For this purpose, reflection geometry experimental configuration (c) described in figure 2.5 is utilized. The reflection configuration is often more suitable for future real applications since generally the artworks cannot be dissociated from their supports. In reflection mode, a more complex THz signal is obtained consisting of several peaks which arise due to the reflection of the THz pulse from the various object layers.

At first, we present THz reflection imaging of the previous man sketch covered with blue painting as shown in figure 3.12(a). From the upper part of the sample (paint layer of 20-30 µm), we observe only one THz peak since the paint layer is very thin (Figure 3.14(a), top). It means that here, the system is not able to separate the painting from the canvas. For the middle and lower parts, we obtained two THz peaks, the first one arriving from the paint surface and the second one arriving from the canvas reflection (Figures 3.14(a) middle and bottom). The fact that the second peak is delayed arises from the refractive index of the painting and also the curvature of the sample which is not

completely flat. We can see that the time-delay between the two peaks increases as a function of the painting thickness. By monitoring this time-delay, the thicknesses of both paint layers can be measured: 280-320 µm for the middle one and 550-640 µm for the lower one. These results are compatible with those obtained in transmission geometry. The small differences may arise from the fact that the reflection geometry does not require any previous reference measurement (canvas without painting). This is an advantage of the reflection geometry which provides a direct measurement of the painting thickness taking into account the time-of-flight of the THz pulse. The calculation of the smallest absolute thickness that can be measured in reflection geometry is different than that in transmission geometry due to the reflections of the THz pulse at each sample interface. If we estimate that two THz peaks separated by 500 fs (FWMH of one single peak) can still be identified, it means that theoretically the thinnest paint layer (refractive index of 2) that can still be measured by the system is about 40 µm. We can also estimate the smallest variation in thickness that can be measured. Assuming a precision of 100 fs for the time-delay between the two peaks, the corresponding smallest change in the paint thickness is 7.5 µm (with refractive index of 2) in agreement with similar previous works [Manceau 2008].

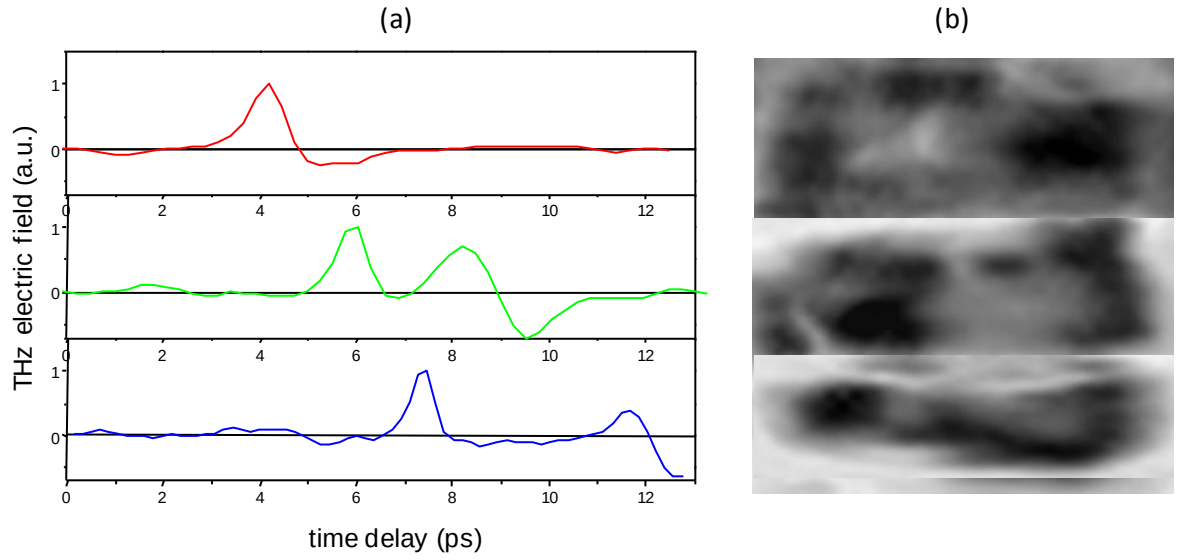

Figure 3.14: Reflection THz imaging with the sample already presented in figure 3.12. (a) Typical THz waveforms from upper, medium and lower parts of the sample, (b) Corresponding THz image obtained using the value of the THz peak corresponding to the THz wave reflected by the canvas (second peak for middle and lower regions).

Finally, we computed the THz image of the sample by monitoring the amplitude of the THz peak, for the upper part of the sample and the amplitude of the second THz peak for the middle and lower part of the sample (Figure 3.14(b)). In all cases, this second peak arises from the canvas reflection and its amplitude is modulated by the presence of graphite on the canvas. Indeed, the corresponding THz image reveals the presence of the human face. The image is not as good as in the transmission geometry due to the complexity of the THz signal after being reflected by the sample.

This is one of the disadvantages of the reflection geometry. In the middle portion of the sample, the image quality is poor. This could be due the intermediate thickness of the paint layer in this region. The THz peak coming from the paint surface is relatively close to the peak coming from the canvas and consequently the effect of graphite absorption can be harder to detect. However, as already mentioned, the reflection geometry provides a very precise and direct measurement of the sample thickness since the arrival time of the reflected THz pulse is very sensitive to any thickness variations of the sample.

Finally, to demonstrate the potential of THz-TDS reflection imaging system, we investigated further samples much close to reality, formed on wooden panels or concrete structures as in mural wall paintings. Additional care has been taken into account concerning the preparation mode of the sample. We tried here to follow a standard artistic preparation process consisting in first applying a preparation layer, called gesso, made of calcium carbonate ($CaC0_3$). This white support is used to get a flat and homogeneous sample surface before applying any sketch or painting layers. Then, usually, the artist uses a graphite or charcoal mine to draw the sketch which represents the main lines and dimensions of the final painting artwork. Finally, various colours and finishing varnish can be applied.

In our study, the sample selected consisted of a support of red clay (1.2 cm thick) fully first covered by the gesso preparation layer (thickness 0.5 mm) before any further treatment (Figure 3.15(a)). Then a butterfly sketch was drawn on the sample utilizing 6B graphite lead pencil as shown in figure 3.15(b). Finally the sketch was covered by applying two painting colours (napthol red and oxide black) on each half of the sample (Figure 3.15(c)). Owing to the low sample transmission, we directly selected the reflection THz imaging performed by using the optical setup (c) in figure 2.6. In practice, as already mentioned, the reflection configuration is much desirable for curators in order to reveal these hidden works, as many samples cannot be detached from their support structure. Figure 3.15(d) shows the THz image formed by utilizing the maximum amplitude of the reflected THz pulse coming from the sample. Here as the paint layer is very thin (40μm) we observe only one peak in time delay THz signal. From this image we can clearly see the hidden underdrawing sketch of the butterfly. Also, we can notice a difference in reflected amplitude of the THz pulse, in two halves of the sample. The reflectance from the oxide black is higher than that of naphtol red, as clearly visible on the horizontal profile indicated by the red line in the figure, this is due to the higher refractive index of oxide black compared to that of napthol red. Also this shows that the measured signal mainly comes from the reflection from the painting layer and graphite mine - and not from the underlying red clay or gesso layer.

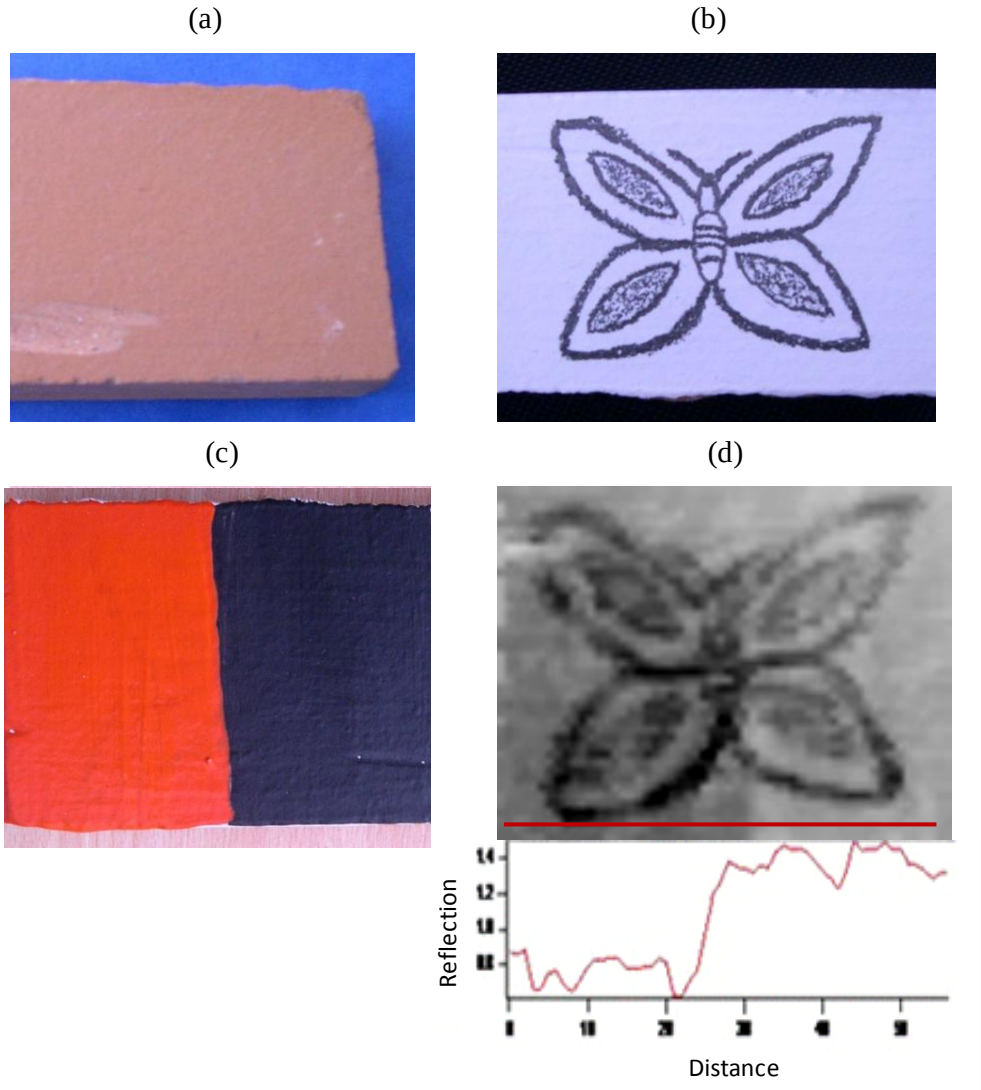

Figure 3.15: (a) Optical picture of the support, (b) image of the sample showing butterfly sketch on gesso layer, (c) recovered sketch by painting, (d) corresponding THz image utilizing amplitude of reflected THz pulse along with the horizontal profile, corresponding to the red line, showing the difference in amplitude of the reflected THz signal in two coloured portions.

In the next step, we were interested in identifying fresco or mural painting hidden behind a plaster layer, as it is a frequently used material in many historical artworks and old churches. For this, we recovered the same sample shown in figure 3.15(c) with an additional layer of plaster (2.2 mm) and a thin layer of varnish for giving a finishing and un-crumbled aspect (Figure 3.16(a)). Figure 3.16(b) shows the typical THz reflected signal having multiple peaks arising from painting interfaces. With this layered sample, we can observe three THz main peaks in the time-domain waveforms. The first two peaks labeled 1 and 2 are very close to each other in time-domain and come from the reflection of varnish and plaster. The more delayed third peak (labeled 3) arises from the reflection of gesso layer having graphite sketch. The THz image corresponding to the maximum amplitude value of reflected first and third pulse is shown in figure 3.16(c) and (d). In figure 3.16(c), the THz image represents the front surface of the sample (varnish and plaster). Figure 3.16(d) represents the THz image obtained

with the third reflected pulse. Although the image quality is poor, we can still identify the hidden butterfly sketch. This shows that THz radiation is strongly attenuated by scattering and material absorption. For this sample, owing to the complex structure of the reflected THz waveforms presenting multiple peaks, it was not possible to determine the thickness of each deposited layer (gesso, painting, plaster, varnish). This is a severe limitation of THz reflection imaging in case of complex multi-layered samples.

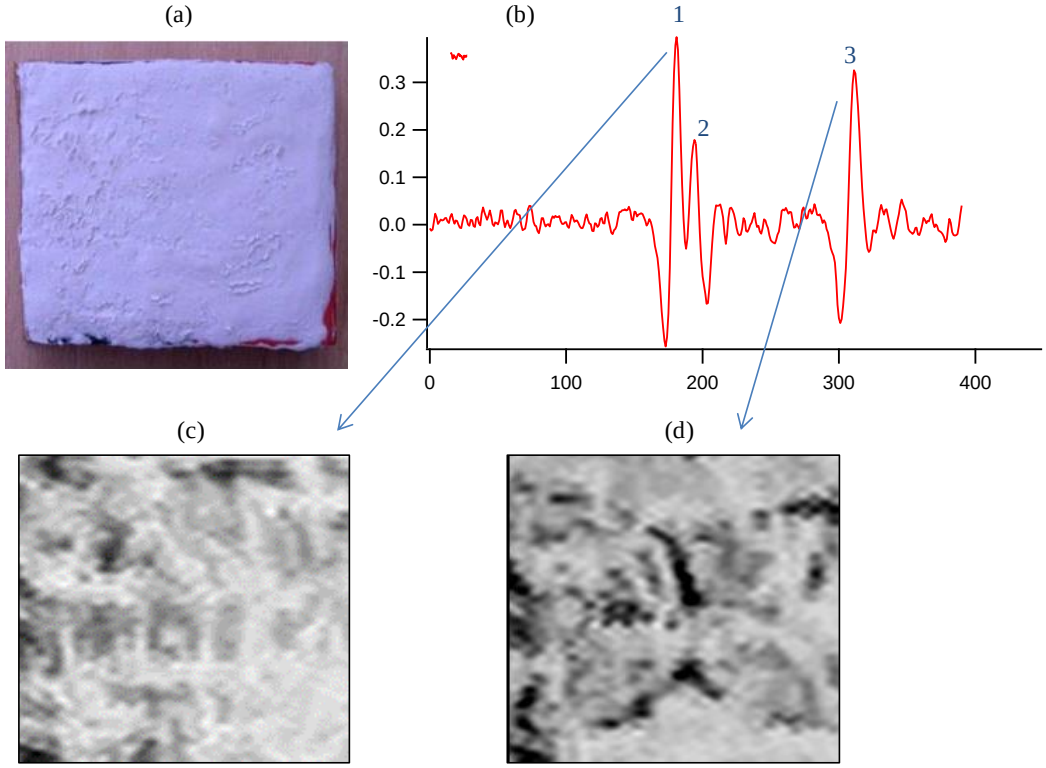

Figure 3.16: (a) Picture of the sample after application of plaster and varnish layers on 3.15(c), (b) Typical reflected THz signal having several peaks in time delay, (c) THz amplitude image corresponding to the first reflected THz pulse, (d) THz image formed by utilizing maximum amplitude of the reflected THz pulse arriving from gesso surface.

In short, we have presented the ability of our THz-TDS system for the non-destructive spectroscopic analysis of painting artwork. We were able to visualize graphite sketches dissimulated under several painting layers. We could also determine the thickness and refractive index for each paint layer. This can be useful for understanding the artist strategy in the formation of any artwork. Future work includes the THz imaging of real master artworks and THz spectroscopy of historic pigments and binders to definitely help art historians and curators in the preservation of our cultural heritage. Such a work could be performed in the future in collaboration with the C2RMF (Centre de Recherche et de Restauration des Musées de France) localized at the Museum of Louvre.

Art science is a vast domain having many aspects and doors to be explored. In the next sub-section we will present some results relating to THz imaging and spectroscopy of sealed waxes - such analysis can be useful in sigillography in order to authenticate some historic document.

2.3. THz-TDS Imaging for Sigillography Applications

Sigillography is the science that studies the manifold aspects of the seals. We used both THz-TDS spectroscopic and imaging techniques for the non-destructive evaluation of natural materials within old seals. THz transmission image are generated in the 0.1-3 THz range. We characterized the dielectric response of several natural wax compounds in the THz spectral range. Refractive index and absorption characteristics in the THz range are extracted and compared in order to discriminate different materials based upon original fingerprints or identical dielectric response over a huge frequency range. Due to low absorption level for certain wax materials, we will show the capabilities offered by THz-TDS system with more realistic samples, demonstrating the availability to image under a thick seal layer.

Wax seals, (mainly of bee wax) formerly used to authenticate documents, are an attractive cultural, historical and art research field. A seal is an imprint obtained by pressing an incised matrix onto a malleable medium (wax). This process transfers the characteristic stamp, signs or herald of a person or an institution. After being cooled down or ageing, these samples are very fragile. They tend to detach from their host documents over time. Although outmoded, seals were however one of the most common ways to proclaim the authenticity of a document in the latter middle ages. Emblematic figures and habitually a name, surrounding it, identify the owner of the seal. Symbolically hair can sometimes be inserted in the seals and finger marks impressed on their back. Their fragility is a crucial drawback to be overcome, to preserve this extraordinary historical source. For imaging these fragile artefacts, THz waves display attractive features and can be used as a complementary tool for material characterization.

Usually, the seal is made of a rather limited variety of materials, mainly poor materials. "Bee Sweat" is a natural (bees) wax extracted from the honeycomb in the beehives of Apis mellifera or Apis cerana (honey bees). Beeswax consists of a mixture of esters of fatty acids and fatty alcohols, hydrocarbons and free fatty acids. Data on the physical chemistry of waxes are complex and difficult to obtain. For example, the different colours of seals have been achieved by the addition of different metallic oxides. We can also found within the seals the addition of ancient fibres. Here, we will present some initial results demonstrating the dielectric properties of basic materials used in most of the seals formed with wax or wax-mixtures. These results are an insight on the average values for extracted physical parameters and clearly the characterization of real old seals will probably gave different results due to the different technological process, materials, chemical reaction and ageing.

Our samples are made with cherry tree gum (sample #1), bee wax from honey harvest in Brittany 1969 (sample #2), honey harvest in Dordogne 2010 (sample #3), the same sample after a slight thermal cycle typically 30°C (sample #4), propolis (sample #6) which is a resinous mixture that honey bees collect from tree buds, sap flows, or other botanical sources. It is used as a sealant for

unwanted open spaces in the hive. Propolis is sticky at and above room temperature. We also measured some samples consisting of mixture of several waxes (sample #7). Sample pellet preparation is made with a compact laboratory press. The maximum pressure of 8 tons per mm^2 is applied for the preparation of solid samples. The thicknesses are ranging between 0.8 and 1.2 mm depending of the quantity of dyes and their viscosity.

Initially in order to get an idea about sample chemical composition, they are analysed by Laser Induced Breakdown Spectroscopy technique and Energy-dispersive X-ray spectroscopy. These measurements reveal a major presence of carbon (82%), oxygen (14%) and in sample #1 a very significant quantity of calcium and a few percent of strontium, as expected.

2.3.1. THz Spectroscopy of Sigillography Samples

We performed THz spectroscopy for all the above mentioned samples in order to determine their optical properties and behavior. The multiple reflections due to finite sample thickness are taken into account. In the case of a homogeneous sample, the complex refractive index related to the complex transmission function was numerically solved as mentioned earlier in chapter 2. For this purpose, we measured the individual absorption spectra for the different samples. The results of the real part of the effective optical index are plotted in figure 3.17, while figure 3.18 represents the absorption variations (plotted here between 0.2 and 3 THz).

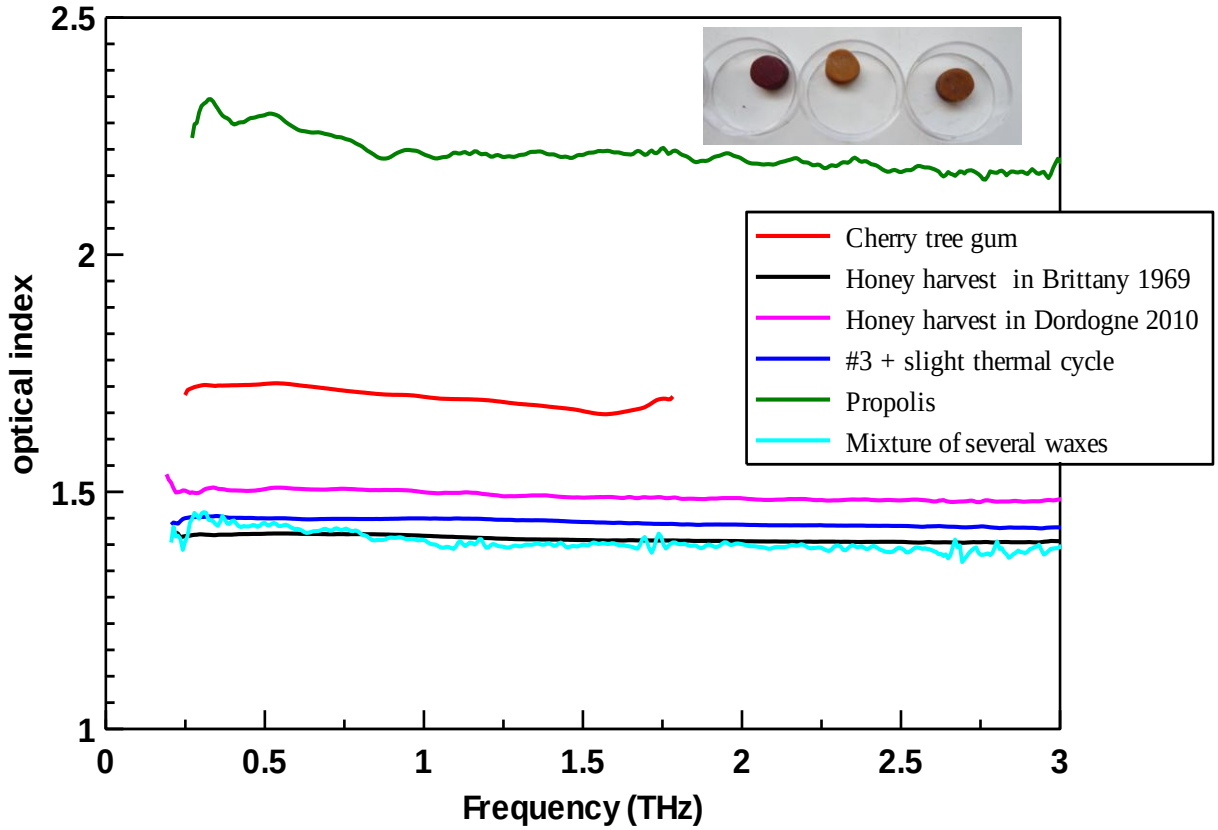

Figure 3.17: Time dependence of the optical index as a function of the frequency. Inset: pellets of different waxes.

For all the materials under investigation, the dispersion of the refractive index values is quite flat all over the THz frequency range with data around 1.4-1.6 which is in good agreement with optical measurements [Waller 1947**]**.

These preliminary results demonstrate that no typical fingerprints are found for the beeswax compounds. In figure 3.18, it is clear that all the sample waxes exhibit a gradual increasing trend with frequency as expected for most amorphous materials. The highest rate of increasing opacity is displayed by the propolis and cherry gum samples, and the lowest rate is displayed by the bee wax materials. Nevertheless, since it was very difficult to discriminate quantitatively or even qualitatively the intrinsic difference of these materials, the clear difference value of the optical index for samples #1 (cherry gum) and #6 (propolis) is a welcome feature to identify these different waxes content by THz-TDS system. To predict the attenuation of the overall transmission through the materials, we can model it, in a first approximation by considering a constant frequency dependent attenuation constant [Bajarnason 2004] or an absorbance spectrum fitting method [Wang 2007]. Due to the complexity (lot of chemical components) of this amorphous material, these simple models fail in the prediction of the absorption dispersion in the THz range. Nevertheless, as a first characterization, it is prime important to prebuilt a library of reference data in order to propose a fitting absorbance for identification method. Another interesting possibility is related to scattering [Zurk 2007] for surface texture of the air-soft materials at room temperature.

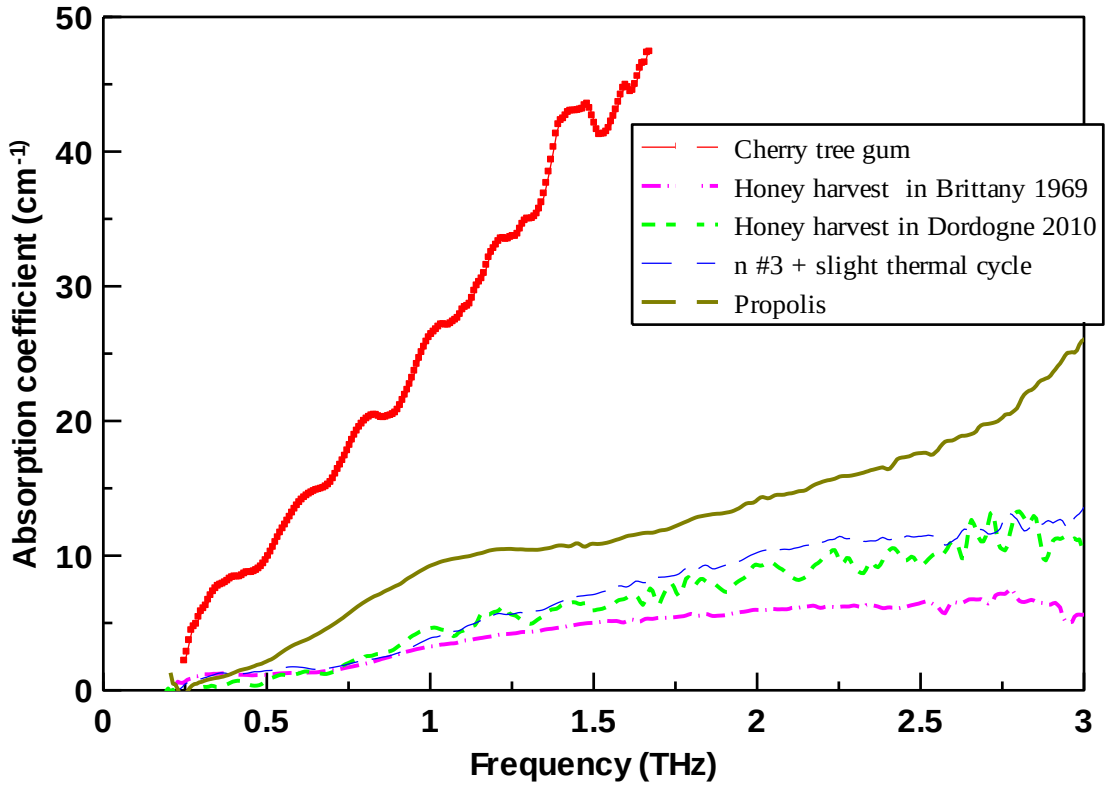

Figure 3.18: Frequency dependence of the absorption coefficient for different type of waxes.

2.3.2. THz Imaging of Sigillography Samples

Above mentioned spectroscopic results confirm that THz radiation can be transmitted through the seal and enables one to non-destructively evaluate the interior structure. Then we applied THz imaging technique which has the capability of showing the presence of a larger number of peculiar materials that would nominally be invisible, if one has to simply visibly inspect the seal surfaces, correlated to the attenuation of the transmitted THz signal. For this purpose the sample is shown in figure 3.19. It represents the optical pictures of the name of our group written onto a sheet of white paper (Figure 3.19(a)) with a 4B lead pencil, the word is further recovered by a thick layer (2.2 mm) of sample #4 (Figure 3.19(b)). The raster scanning of the sample is performed by the transmission optical setup (a) shown in figure 2.5. The image deduced from the time amplitude of THz signal is shown in figure 3.19(c), which is correlated to the average absorption over the frequency bandwidth. Here, the SLAM logo can be revealed in transmission. In figure 3.19(d), we provided different time-delay obtained every 0.5 ps. Since the arrival time is determined by the optical path length (i.e. the product of the real index of refraction and the physical thickness of the sample over each pixel), one would demonstrate in figure 3.19(d) that the contrast in a time-delay or phase image, which is the result of either local variations in the thickness of the sample or variations in the real index of refraction, is not suitable in this case or inhomogeneous materials. Each picture can be considered as a sort of local cutting inside the wax sample, slice by slice. In all images, the dark edge around the sample is caused by diffraction, stronger scattering or absorption due to a thickness difference. Nevertheless, we can observe that the thin layer of graphite lead does not affect the image when we selected the optical thickness as a contrast parameter.

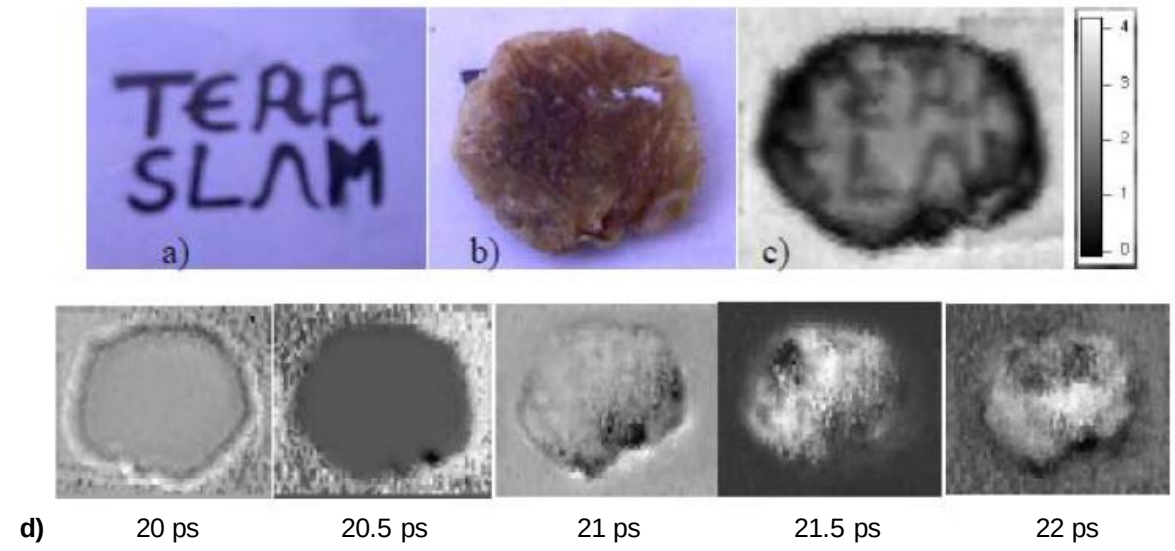

Figure 3.19: (a) Optical view of the logo, (b) The wax onto the paper, diameter is 25 mm, (c) Time amplitude of the transmitted THz pulse, (d) Several time-delay images with an arbitrary scale for the false colour.

This demonstrates that THz-TDS technique could be a powerful tool for the investigation of old under-writing beneath wax layers or foreign objects inserted into the seal. As an example we can mention medieval inks, such as sour galls, aleppo galls, green and blue vitriol. The presence of defects or objects in the seals will be evident in the THz image due to enhanced scattering or absorption of the THz radiation. Pragmatic analysis of the spectral properties of these wax materials shows that the THz absorbance is sufficient low to analyze spectral properties of foreign inclusion and see under a thick layer of old basic materials in relation to official written documents. This study proposes THz radiation as a tool for preserving old archives seals and participating in the vast cultural patrimony.

After demonstrating the ability of the THz-TDS imaging system for the analysis of painting artwork and sigillography, we will now present the potential of the THz CW imaging system in the field of art science.

Section 3: Imaging of Artwork by CW System

We have also utilized the CW imaging system for the 2D visualization of art paintings deposited onto canvas, wood, etc. The advantage of this system is its flexibility, high output power and portable nature so that it can offer essential characteristics for *on-site* THz imaging of unique artworks. Initially, to evaluate the potential of this CW imaging system, we carried some experiments in the laboratory. Further, in collaboration with curators, we performed *on-site* THz imaging at the museum of Aquitaine in Bordeaux, for inspecting real historical objects.

3.1. Potential of CW System for Inspecting Artwork

In order to illustrate the potential of the CW imaging system for investigating artworks, in the continuity of previous THz-TDS investigations, we first performed imaging of some painting samples in the laboratory. For this purpose we used homemade sketches drawn onto canvas and wooden supports. The goal of the study was to compare THz images obtained with CW system from previous THz-TDS images. Especially, taking into account the characteristics of the 110 GHz and 240 GHz CW sources (millimeter wavelength and high output power compared with THz-TDS source), we were interested in comparing transverse resolution and penetration depth into absorbing materials.

3.1.1. Comparison of CW Image with THz-TDS Image

First, we performed imaging with a painting sample and then compared the result with the THz-TDS image obtained at the same frequency. For this work, we investigated a sample consisting of a homemade graphite sketch (woman's face) onto a canvas, covered by a patchwork of painting layers with different colours produced with commercially available gouaches (Van Gogh acrylic colours, same as mentioned earlier) (Figure 3.20(a)). Figure 3.20(b) shows the millimeter CW image

in transmission mode at 240 GHz. The background interference pattern visible in the images is caused by standing waves in the imaged object and the measurement setup, owing to the long coherence length of the Gunn diode. This interference pattern has already been observed and described in chapter 2. It could be removed by Fourier Transform post-treatment or simply by tilting the sample to avoid these interferences.

Figure 3.20(c) shows the final image of the painting after removing the background interference pattern. The fringe pattern also reflects the sample flatness indicating the variations of the local curvature. This feature can be used for an additional surface analysis of the sample. The graphite sketch is clearly visible for each part of the sample, corresponding to a decrease of the transmitted THz signal. First, it means that the different pigments deposited onto the canvas transmit similarly the incident 240 GHz radiation. Then, it also means that the underlying graphite (6B grade) significantly reflects the 240 GHz radiation, as previously exposed with the THz-TDS system.

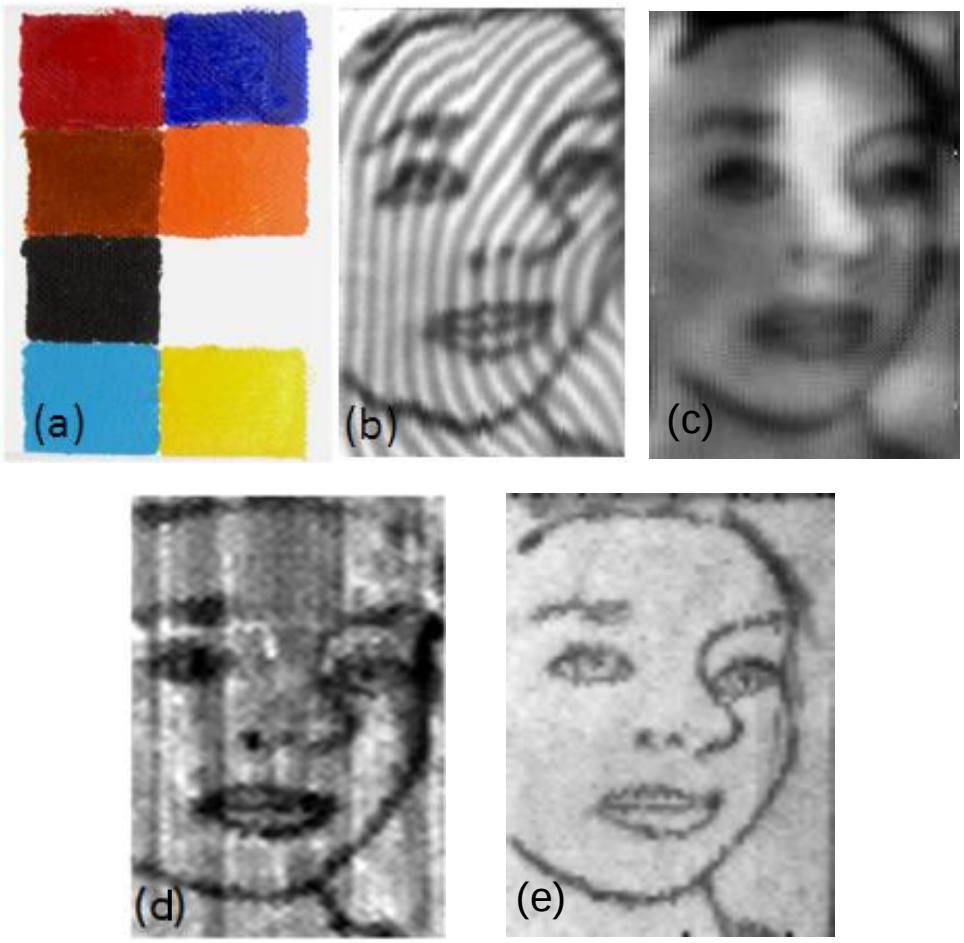

Figure 3.20: (a) Photograph of the sample (paint layers covering a graphite sketch) (90x55 mm^2), (b) Transmission CW image at 240 GHz, (c) Transmission CW image at 240 GHz after treatment to remove back ground interference pattern, (d) Transmission THz-TDS image at 240 GHz, (e) Transmission THz-TDS image at 1.5 THz. From (b) to (d), black level indicates a decrease of THz signal.

For comparison, figure 3.20(d) shows the equivalent THz image at 240 GHz obtained with our THz-TDS system. At this frequency, the CW image exhibits a better SNR (~ 4000) compared with the THz-TDS image which presents a poor image quality owing to the low THz signal amplitude at 240 GHz (SNR ~ 400). However, at higher frequency values the THz-TDS image exhibits a better quality (Figure 3.20(e)).

3.1.2. Reflection CW Imaging of Canvas Painting

In this sub-section, we will present results of CW imaging in reflection mode (oblique incidence setup) at 110 GHz. The sample consists of painting on canvas whose visible appearance resembles a simple two colour painting (naphtol red light and oxide black from Royal Talens) (Figure 3.21(a)). The reflection based CW image clearly reveals the presence of an underlying sketch (copy of the Vitruvian man) formed with a graphite pencil lead, as shown in figure 3.21(b). As for the previous transmission experiment, the reflection imaging makes it possible to investigate drawings beneath paintings in order to discover the history of an artwork and discover how it has been technically elaborated. However, in this second experiment, the reflection from the graphite induces an increase of the 110 GHz radiation, whereas in transmission it caused a decrease of the 240 GHz radiation. This explains the inverted gray-scale representation of the underlying sketch between the figures 3.20 and 3.21.

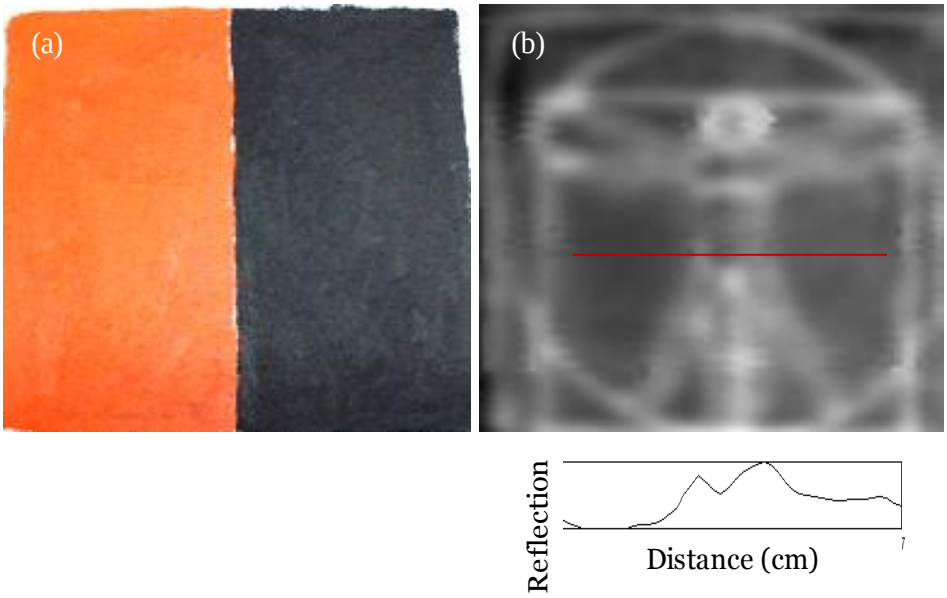

Figure 3.21: (a) Photograph of the sample (paint layers covering a graphite sketch) (150x150 mm^2), (b) Reflection CW image at 110 GHz revealing the copy of the Vitruvius man. White colour indicates a higher reflection. The profile shows the variation in reflected signal corresponding to the horizontal line inside the CW image.

A finer analysis of figure 3.21(b) also reveals the higher reflected signal from the black painting (approximately +10%) compared to the one reflected by the red painting. This indicates that the reflection coefficients of these two commercial paintings are different at 110 GHz. In order to

explain the observed variations of the reflection coefficients in relation with the measurement of the painting refractive indexes at 110 GHz, we also measured the reflectance of the four different Van Gogh acrylic colours previously selected in the THz-TDS analysis (oxide black, naphtol red, azo yellow deep, ultramarine). For this purpose, the colours were used in the form of pellets, filled inside a glass support having some holes inside (Figure 3.22(a)). A difference in the value of reflected coefficient R is recorded at 110 GHz for various colours. Figure 3.22(b) presents the reflection imaging of the four pellets sample. The white colour indicates an increase of the amplitude of the THz reflected signal. We can visually observe that oxide black has the highest reflectance, then ultramarine as intermediate reflectance and finally azo yellow deep and naphtol red as lowest reflectance. This result is also quantitatively presented in figure 3.21(c), which shows the evolution of the measured reflected signal in millivolts. These results were found in accordance with the previous values find out in transmission mode with our THz-TDS system.

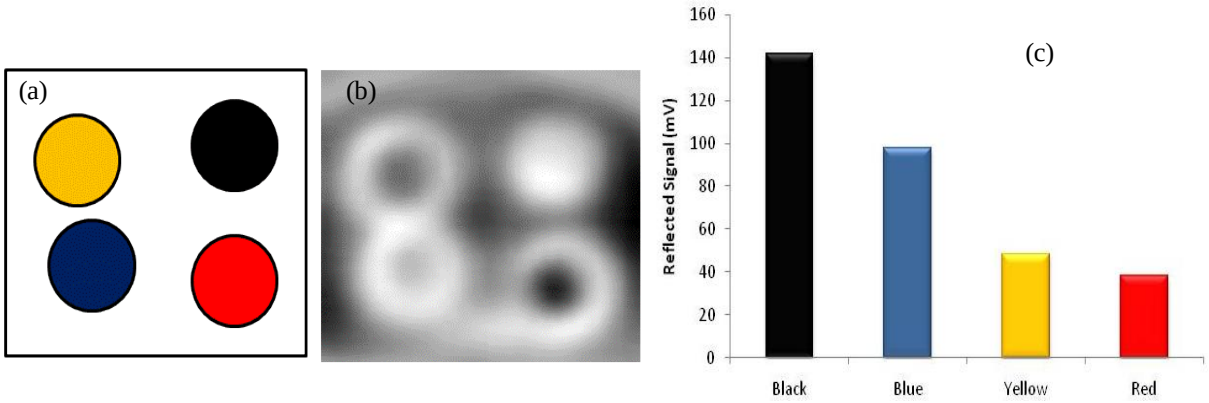

Figure 3.22: (a) Sample design (50*50 mm), (b) reflection image at 110 GHz, white colour indicating higher reflection, (c) corresponding curve revealing the difference in reflection by various colour pigments.

We also measured with the CW system the reflection coefficients of several graphite pencil leads, from the standard writing pencil HB to softer black marking pencils indicated as 2B, 4B, 6B and 8B (Figure 3.23). For the measurements, the graphite has been simply deposited onto a standard paper sheet and the reflection coefficients of the different mines have been compared to a flat mirror. In that sense, this sample is different from previous one presented in figure 3.5 where 1 mm thick pellets and maximum of the reflected THz waveforms had been used. As already measured by THz-TDS system, the results indicate that the amplitude of the reflected THz signal increases as a function of the graphite concentration, indicating a probable increase of the refractive index of the lead mine from HB to 8B at 110 GHz. Consequently, the graphite reflectance could be used to identify the quantity of graphite, i.e. the label of the pencil lead, deposited onto a sample.

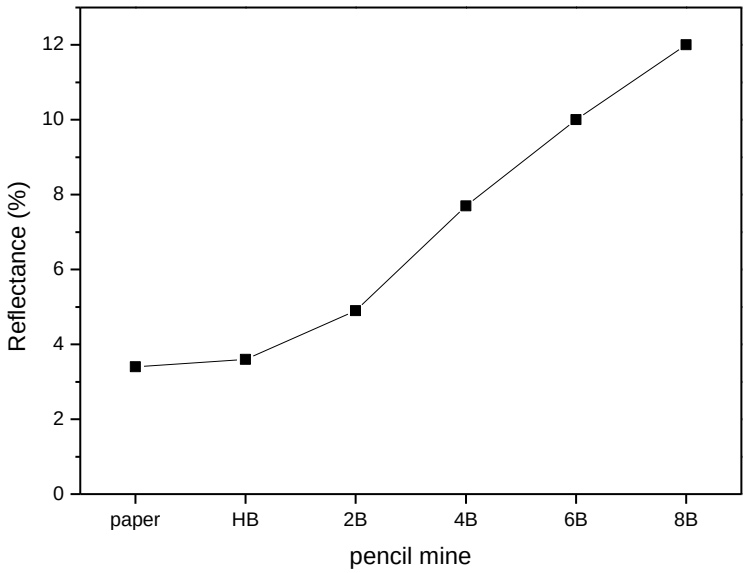

Figure 3.23: Reflectance (in %) of different graphite pencil grades deposited onto a blank paper sheet (measurement at 110 GHz).

3.1.3. CW Imaging of Wooden Panel Painting

The last result which we present here consists of wooden panel painting. The sample is a *Madonna* panel painting shown in figure 3.24(a). The sample has been obtained with the courtesy of Computer Vision and Systems Laboratory (Laval University, Quebec). It consists of a 15 cm x 21 cm x 2 cm panel made of poplar wood that was coated with the usual priming layers of canvas, gesso and glue traditionally employed in forming paintings. The specimen was originally conceived for the inspection of subsurface artificially detached regions inside the layered structure simulated by inserting thin Mylar sheets at different depths. In addition, the specimen contains some underpaintings that have been detected by near Infrared reflectography (NIR) [Ebeid 2010]. This technique is widely used by museums for the detection of guiding sketches and signatures drawn by the artist prior to the application of painting layers; the detection of hidden paintings (painters often use a previously painted canvas or change their mind during the painting progression), the monitoring of the restoration processes required on aging cultural heritage artworks and the detection of intentional and unintentional alterations. Ebeid *et al*. used InGaAs camera in the reflection mode to reveal the underdrawings (black circled) by NIR method (Figure 3.24(b)). Figure 3.24(c) and (d) are the NIR image acquired with the CCD camera in the reflection mode using a 940 nm and 850 nm sources, respectively. These previously reported results reveal some hidden underdrawings such as a maple leaf and a sort of bird (upper left corner), the inverted inscription "CE" (upper right corner), as well as the artist's signature in the bottom right.

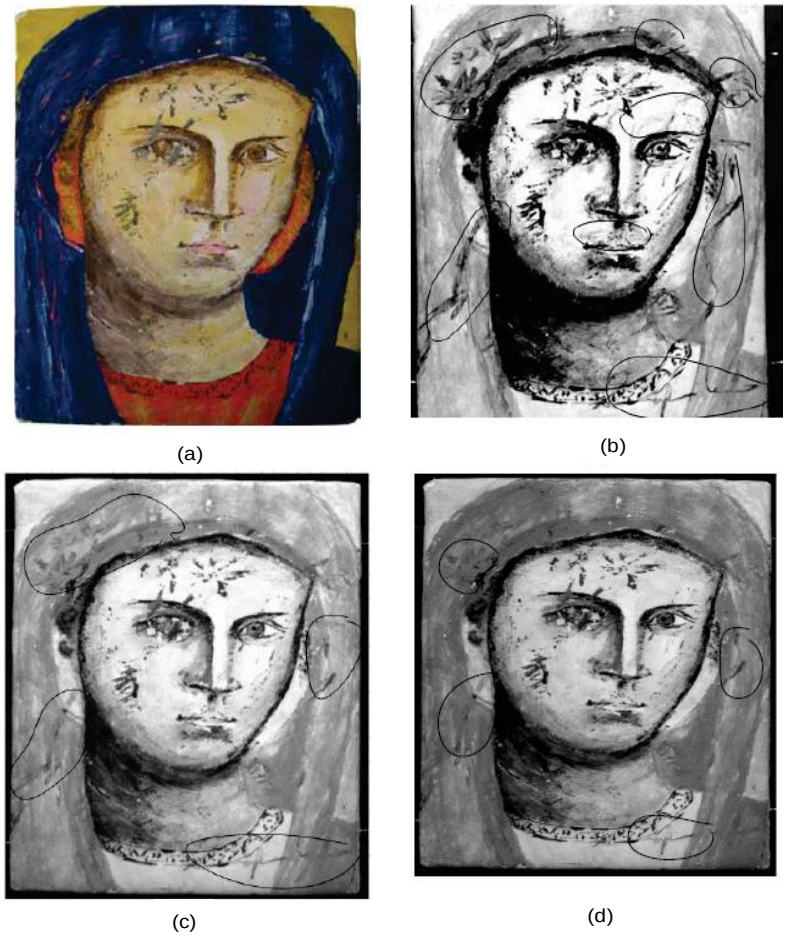

Figure 3.24: (a) Photograph of the Madonna specimen (courtesy of Laval University, Quebec), (b) NIR image of Madonna obtained with a InGaAs camera, (c) NIR image obtained with a CCD camera with 940 nm illuminator, (d) NIR image from a CCD camera and the 850nm illuminator [Ebied 2010].

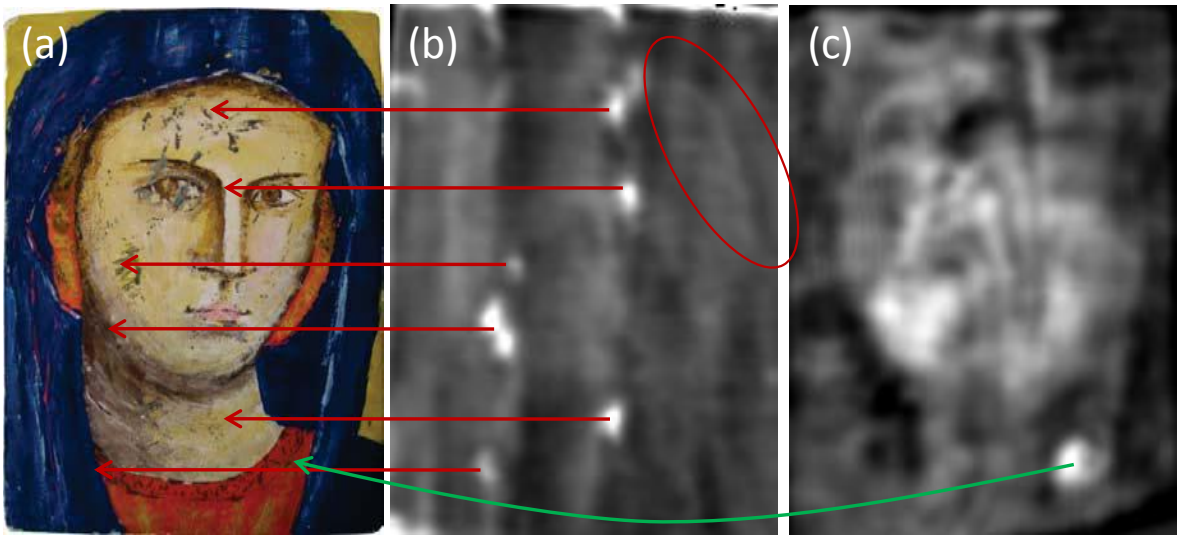

Figure 3.25: (a) Photograph of the sample, (b) Transmission CW image obtained at 110 GHz, (c) Reflection CW image at 110 GHz (oblique incidence setup).

With our CW imaging system, it was difficult to reveal these hidden sketches. Figure 3.25(b) shows the transmission THz image of the painting obtained at 110 GHz. It can be seen that the

differences in transmission are not sufficient to provide enough contrast in order to reveal the hidden or visual sketches, previously revealed by NIR. However, visible as lower transmitted signal (white colour), we can notice multiple additional defect areas or flaws in the painting (Figure 3.25(b)), which were not initially visible with the NIR technique. The corresponding locations of these defects in the photograph are indicated by the red lines. However, from the transmission CW imaging, we can not determine the depth position of these defects. On the right upper corner of the THz image, indicated by the red circle, we can distinguish the headscarf of the madonna, althought the contrast is very poor. Figure 3.25(c) shows the reflection based CW image of the sample obtained at 110 GHz. In this image, all the previous defects are not visible anymore, indicating that they might be located in depth within the sample. Indeed, in that case the amplitude of the reflected THz beam becomes too low after the round trip travel into the sample. Here, we can distinguish the woman face and the headscarf and another feature which was not noticed in transmission THz imaging and NIR: a large higher reflected signal (white colour) is visible in the right lower corner. However, it is difficult to explain the reason why this feature, which could be attributed to another defect, was not previously revealed in THz transmission imaging (Figure 3.25(b)).

We demonstrated the ability of the THz CW imaging system to analyze artifical artworks in the laboratory. The system is capable of giving a quick and prompt view of the selected artworks and hidden sketches have been revealed successfully. It can also distinguish the difference in THz signal coming from various elements which can be used to determine the corresponding absorption or reflection coefficients of the sample. Finally, to prove the potential and capability of this portable THz CW scanner, we investigated real historical and unique objects.

3.2. CW *on-site* Imaging for Inspecting Artwork

In order to emphasize on the real advantage of this system, we have performed some *on-site* imaging in collaboration with conservators working at museum of Aquitaine, Bordeaux. At the museum of Aquitaine, many historic art samples have been scanned from ancient Egyptian and Roman objects to more contemporary ones such as an apothecary jar (~1920 A.D). Here, we will only present some results regarding two sealed Egyptian pieces of pottery from the XVIIIth Dynasty (New Kingdom period). The original use of these two jars remains a mystery for curators. Without any specific decoration, they look like simple red-clay vessels hermetically sealed with a clay cork. Their shape (a jar with a neck) indicates that they were most likely used for liquids, not ointment, perfumed cream or unguent because the jars shape would not allow easy access to these less liquid contents for skin application. However, the existence of Menkheperre Tuthmosis III's cartouche (1479-1425 B.C.) on the pottery's clay corks allow us to infer that these objects were probably very important, may be used during funerary rituals. Indeed, a sticker under one of the objects indicates that they were purchased in 1861 in Gournah, on the famous necropolis of Thebes (on the west bank of Luxor)

[Saragoza 2008]. Thus, according to experts, these nearly 3500 years old pottery bottles probably did not contain viscera - usually preserved in canopic jars - but most likely food offerings.

The first opaque jar (museum inventory number 8606) is shown in figure 3.26(a). It is worth mentioning that, by gently shaking the object, it was not possible to conclude if the jar was filled or not. Neither internal sound nor moving materials could be noticed. For the THz experiment, the sample was horizontally positioned inside the THz scanner in order to determine the presence of internal content. Indeed, due to gravitation effects, a mobile content should have spread along the internal volume of the jar. Figure 3.26(b) represents the THz transmission image plotted in logarithmic scale with the white colour indicating a decrease of the transmitted signal. The image can be decomposed into three parts: (1) the sealed clay cork where the THz transmission is very low probably due to the large thickness of the object in this area, (2) the neck which seems empty owing to the higher THz transmission, (3) the bottom of the jar which is certainly filled with a solid material owing to the low THz transmission. Moreover, this material seems to be attached to the bottom of the jar since a liquid or mobile content would have spread owing to the horizontal orientation of the object. This solid content fills in all the bottom cavity of the jar but not the upper neck.

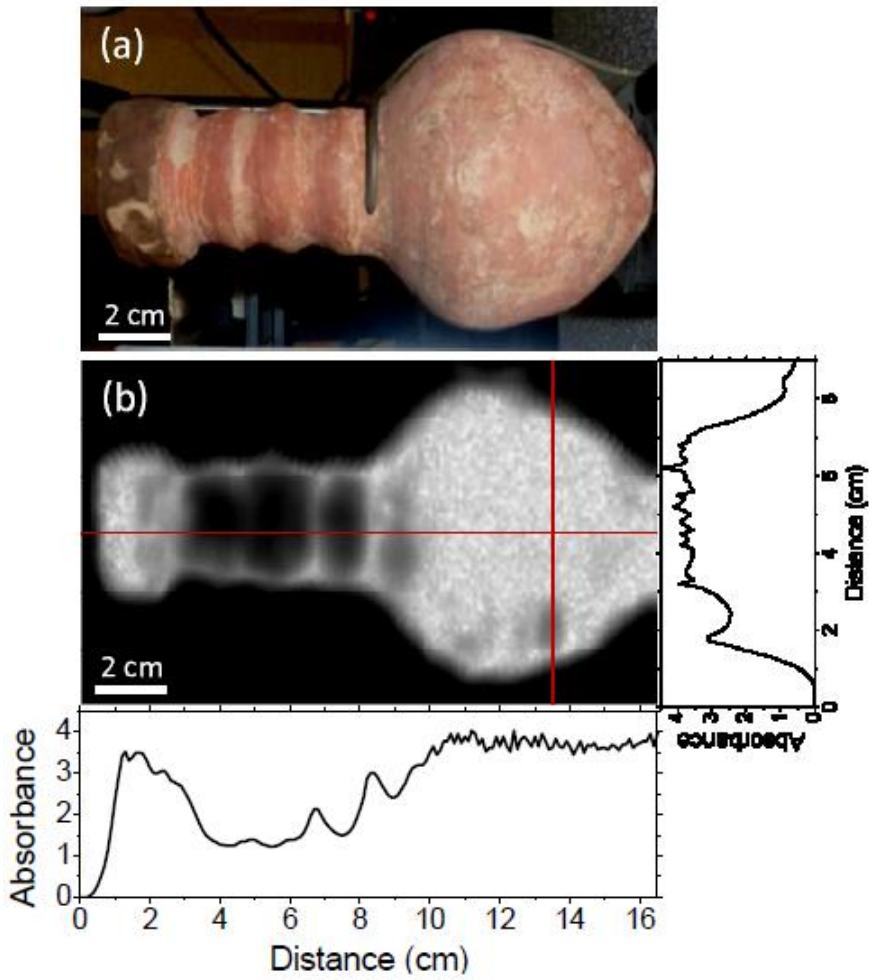

Figure 3.26: (a) Photograph of the Egyptian jar (reference number 8606), (b) 2D THz transmission image and intensity profiles (absorbance) along the horizontal and vertical red lines.

A more precise analysis of the THz transmitted signal can be obtained from the horizontal and vertical intensity profiles measured along the red lines drawn in figure 3.26(b). Corresponding absorbance plots are associated with figure 3.26(b), with the classical calculation *Absorbance* =Log(I_0=I), where I_0 is the transmitted THz signal measured out of the sample and I is the transmitted THz signal measured along the horizontal or vertical profile. Inside the jar, the absorbance varies from 1.2 (empty neck) to 3.9 (full bottom). Surprisingly, a lower signal intensity region (absorbance around 2.5) can be observed in the bottom part of the jar (2D image and vertical slice around abscissa 2.5). This nearly 1 cm^2 area may be attributed to the presence of a lower density material although its origin and composition remain unknown.

The second jar (museum inventory number 8608) is presented in figure 3.27(a). According to curators, shaking of the object indicates that it contains an internal material which is not attached to the pottery. X-ray imaging cannot be performed on the sample in order to reveal this internal content, due to irreversible irradiation and consecutive dating alteration, as explained earlier. Figures 3.27(b) and (c) present the THz transmission images of the horizontal jar and turned upside down jar, respectively. These positions have been selected in order to determine the presence of the internal content. As previously explained, due to gravitation effects, a mobile content should move depending on the orientation of the sample. Both images clearly reveal that the jar contains two independent masses, one attached to the bottom and another one free-to-move inside the internal cavity.

Absorbance of both materials can be measured from the horizontal and vertical profiles along the red lines (Figure 3.27(c)). The fixed bottom material exhibits a global absorbance around 3.4 with a lower absorbance zone (absorbance around 2.3) close to the base of the pot. The origin of the lower density area remains unknown. In the central part of the pottery bottle, the mean absorbance is around 0.8 corresponding to an empty part of the jar. This absorption is simply attributed to the thickness of the pottery walls. The area concerning the mobile content is characterized by an absorbance around 3.

Here, we would like to emphasize that the THz analysis of the object reveals an important feature concerning the physical aspect of this unidentified mobile content. From Figures 3.27(b) and (c), we can surely affirm that this content is deformable since its shape can fit the inner contour of the pottery bottle. From these absorbance measurements, assuming a constant and homogeneous pottery wall thickness, we can also estimate that the absorbance corresponding to the fixed and mobile contents themselves, without the contribution of the pottery walls should be around 2.6 and 2.2 respectively. The 110 GHz absorption coefficients of the materials characterizing these contents will be estimated in the following chapter from the 3D THz imaging and thickness measurements.

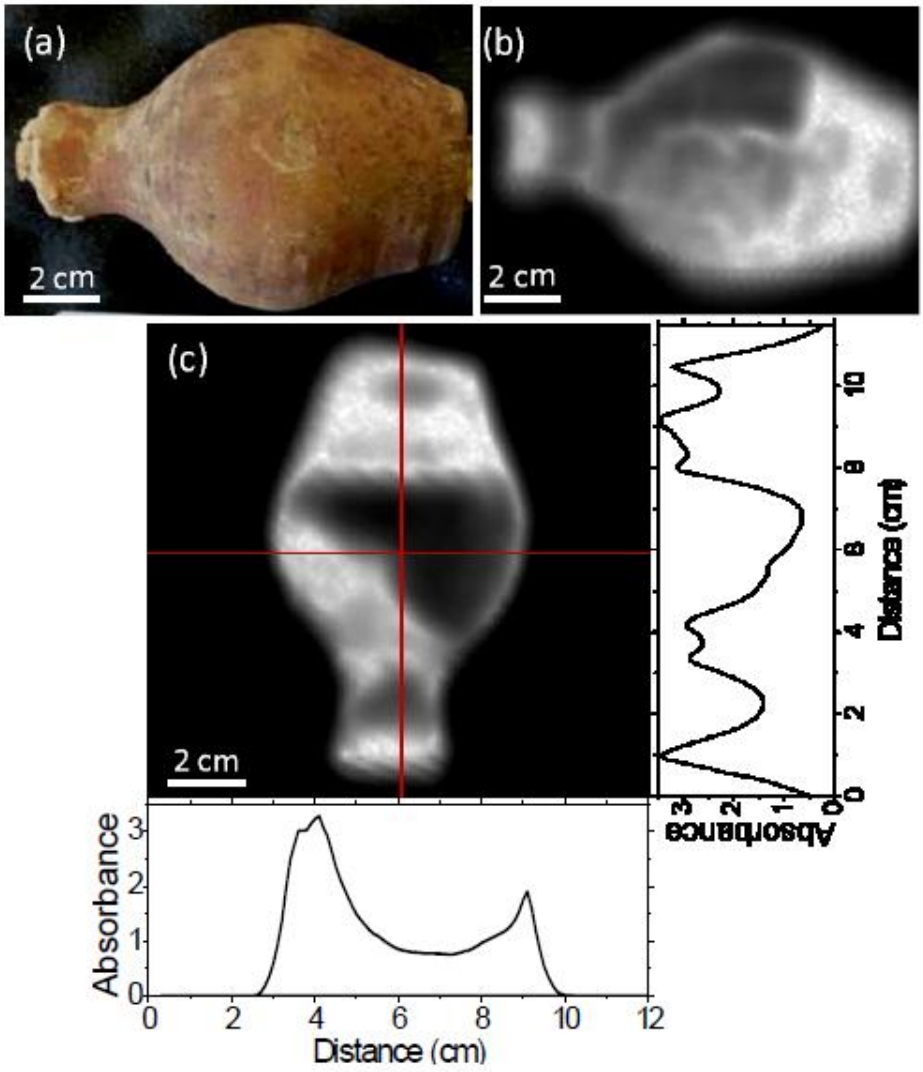

Figure 3.27: (a) Photograph of the Egyptian jar (reference number 8608), (b) 2D THz transmission image of the horizontal jar, (c) 2D THz transmission image from the turned upside down jar and intensity profiles (absorbance) along the horizontal and vertical red lines.

In conclusion, in this last section, we have presented the capability of this portable CW imaging system. The measurements performed at the museum of Aquitaine revealed internal contents in two XVIIIth Dynasty Egyptian sealed jars demonstrating that THz imaging system can be used for the detection of hidden materials in historic objects. Especially, for the investigation of Egyptian antiquities, the technique may be used in the future for the non-invasive and non-destructive analysis of canopic jars used as containers by the Egyptians to store and preserve the viscera during the rituals of mummification.

Conclusion

In this chapter we have demonstrated the ability of THz radiation for the non-destructive analysis of various artworks. The THz-TDS imaging system is capable of providing wide

spectroscopic information about the sample under test. We can distinguish between various pencil leads depending upon their composition and used proportion of graphite mine. Hidden underdrawings and sketches can be revealed from buried layers of paintings and plaster. We can access the thickness and nature of each painting layer. This system can also provide complementary data in order to understand various seals and wax materials commonly used in sigillography science. The alternative compact CW imaging system has the potential to give a non-contact and non-invasive internal overview of opaque art samples. This system is useful in performing *on-site* imaging at interesting sites such as museums.

All the results presented in this chapter concern 2D THz imaging. However, in order to explore the complete volumetric structure of the samples, a 3D imaging procedure has to be performed. In the next chapter, we will present 3D THz tomographic imaging along with different signal analysis techniques and reconstruction algorithms.

CHAPTER 4

THz Computed Tomographic Imaging

In this chapter we will present the ability of THz radiation for visualizing complete 3D volumetric opaque objects. THz computed tomography (CT) imaging is performed by utilizing both THz-TDS and CW imaging systems. This work has been performed in close collaboration with the group of Pascal Desbarats in LABRI, specialized in 3D image reconstruction from tomographic data. This chapter is divided into three main parts. First section will cover the general introduction of tomography techniques along with some frequently used methods reported in literature. In the second part we will present and discuss some tomographic results obtained with the pulsed THz-TDS imaging system. General imaging procedure, reconstruction technique and signal analysis methods will be mentioned along with the obtained results. In the last section, we will present the results obtained with the CW imaging apparatus. After describing the system potential for 3D tomography, a comparison study among three different reconstruction algorithms will be shown. The final reconstructed image quality will be discussed as a function of specific parameters.

Section 1: Introduction

Tomography refers to sectioning. The name is derived from the Greek word "*tomo"* which means part or section, representing the idea of "slice" or "cutting". This imaging technique allows the 3D visualization of the internal structures of an object, by the use of any kind of penetrating wave. Many tomography techniques already exist like single photon emission CT [Amen 1997, Amen 2008], optical coherence tomography [Arecchi 2005, Targowski 2006], nuclear magnetic resonance tomography, ocean acoustic tomography, positron emission tomography [Ter-pogssian 1975, Toft 1994], transmission electron microscopy and of course X-ray CT [Hounsfield 1973, Hiriyannaiah 1997]. Some of these techniques, generally referred as CT, involve gathering projection data from multiple directions and feeding the data into a tomographic reconstruction software processed by a computer.

All tomographic modalities measure a different physical quantity e.g. the number of transmitted X-ray photons in case of X-ray CT, along an individual projection line. In all cases, the task is to estimate from these measurements, the distribution of a particular physical quantity into the sample, which is further used to reconstruct 3D volume of the test object. While above mentioned tomography techniques are frequently used, there is always a hot discussion on their safety issues and possible hazards. In such situation, THz tomographic techniques have emerged as a possible solution for visualizing the 3D internal structure of objects in a complete non-destructive manner.

1.1. THz Techniques for 3D Visualization

Benefiting from the unique characteristics of THz radiation, there exist several methods for visualizing a complete 3D structure of sample. 3D THz tomography coupled with spectroscopic

analysis has many potential applications. Commonly used techniques in THz range to view 3D inner structure of objects are mentioned below.

1.1.1. THz Time-of-flight Tomography

THz pulsed imaging has the unique feature of providing 3D image "map" of the object by using the time-of-flight of the reflected THz pulses. Briefly, a THz pulse is directed on the target and the amplitude and timing (time-of-flight) of reflected pulse are measured. The temporal position of reflected pulses directly correlates with the location of the interfaces along the propagation direction of the beam. In this way, depth information of the 3D profiles of the target can be obtained by using the difference of time-of-flight, which is converted into the difference of the depth.

Mittleman *et al.* were the first to report on such 3D THz imaging. The 3D image of a floppy disk was successfully reconstructed by using the reflected THz pulses via a digital signal processing algorithm [Mittleman 1997]. However, this early THz tomography was based on three assumptions:

(1) Targets have no dispersion and diffraction,

(2) Reflection is weak so that multi-reflection can be neglected,

(3) Refractive index is uniform within each layer.

After this first demonstration, this technique was widely adapted by various research groups. 3D imaging of many opaque materials, like metallic coins, razor blade, SD card and pharmaceutical tablet was successfully carried out by using pulsed THz radiation [Zhang 2004, Wallace 2008]. The technique was also used to identify the distribution of defects in foam materials. Pre-build defects in foam insulation of space shuttle fuel tanks were detected using THz tomography [Zhong 2005]. Tomography system based on reflective THz-TDS and 2D electro-optic sampling using a high speed complementary metal-oxide semiconductor (CMOS) camera was demonstrated. The inner structures of layered samples (stacked Si and Vinyl chloride plates) were identified with 3D volume visualization within 3 minutes [Kitahara 2010].

In this technique, as the arrival time of the THz waveforms can be determined with an accuracy of a few femtoseconds, i.e. much less than the pulse duration, the position of reflecting surfaces within the test object, can be determined with an accuracy of a few micrometers, when successive reflections are well separated in time. A very high depth resolution in the order of 1 μm has been demonstrated [Takayanagi 2009]. However, this type of tomography is well adapted for layered targets with well-defined boundaries. If the object has a more complicated structure (internal or external shape), the multiple reflections and refractions of the THz radiations make indistinguishable the detection of the back-reflected signal. In such a case, the best solution is to perform a THz CT analysis with a set of projection images.

1.1.2. THz Diffraction Tomography

Diffraction tomography employs a probe beam to interact with a target and then reconstructs the 3D image of the target using the waves scattered by the target [Testorf 1999, Gbur 2001, Wederberg 1995]. This is the main difference with CT which generally utilizes the amplitude signal directly transmitted by the sample. THz diffraction tomography uses the same principle as CT and in same manner the target structural information is measured and processed by diffracted THz distribution. This technique is more adapted for complex targets with fine structure in which diffraction effects dominate the measurements. The first implementation of this method was reported by Ferguson *et al*. who imaged a simple polyethylene cylinder and proposed a reconstruction method based on the born linearization of the wave equation [Ferguson 2002].

Wang *et al*. performed THz diffraction tomography by using a mode-locked femtosecond laser, generating THz radiation by optical rectification in ZnTe crystal and detecting the signal with a CCD camera [Wang 2004]. They proposed a reconstruction method based on the electromagnetic wave scattering theory. Three rectangular polyethene cylinders (n=1.5) were imaged by using the diffraction THz pattern at various projection angles. The application of THz diffraction tomography was able to provide the refractive index distribution of the target. A comparison of image quality as a function of the THz frequency was also carried out. THz diffraction tomography often provides poor reconstruction images owing to the problem of suitable reconstruction algorithms and signal interpretation. However, the image acquisition speed of THz diffraction tomography is relatively faster than THz CT.

1.1.3. THz Binary Lens Tomography

THz binary lens tomography uses the frequency dependent focal length property of binary lenses to obtain tomographic images of an object. A binary lens is a Fresnel zone plate with phase or amplitude modulated patterns formed by a series of concentric ring structures [Jahns 1990]. Unlike an ordinary refractive lens, the focal length of a binary lens exhibits linear wavelength dependence. By using such a lens in conjunction with a multiple-frequency source of illumination and a CCD camera, it is possible to obtain tomographic image slices of a 3D object. Minimin has demonstrated 3D Fresnel lens imaging in the microwave frequency range [Minimin 2000]. Wang *et al*. presented the high resolution tomographic imaging at THz frequencies using binary lens [Wang 2003]. More details about typical experimental procedure and reconstruction algorithm can be found in [Wang 2004].

This type of tomographic measurement is suitable if the rotation of the sample is not possible: for example, if the sample is too large or its location prohibits rotation. The binary tomography method is potentially easy to implement and requires less computer processing power than other tomographic imaging techniques. Therefore, this technique can provide a fast tomographic imaging

system. However, the drawback is that it does not yield any spatially resolved spectroscopic information about the sample.

1.1.4. THz 3D Holography

3D THz holography combines radar and conventional holography technology [Javidi 2000, Wolf 1969]. It is based on the assumption that the separations between scattering centers are much larger than the incident wave pulse width. By separating the multiple scattered THz waves of different scattering orders, a digital holography method can be used to reconstruct the distributed scattering centers [Wang 2004]. Digital holography records holograms using a CCD and then a computer is used to perform the reconstruction of these digitized holograms according to Fourier optics theory. Ruffin *et al.* have demonstrated time-reversal imaging that can be considered as 2D holographic imaging in the time-domain [Ruffin 2001].

This technology relies on measuring the multiple scattering, with a usually poor SNR owing to the high order scattering measurement. To obtain a good 3D holograph, one may need to accumulate the signal to obtain a sufficient SNR. As the image quality of the THz holography strongly depends on the incident wavelength, THz 3D holography is not a good method to extract spectroscopic information about the target.

1.1.5. THz Computed Tomography

THz CT inspired by conventional X-ray CT is based on geometrical optics. This technique offers the potential to extract the frequency dependent 3D properties of the target. In THz CT, cross-sectional images of an object are obtained by analyzing the transmitted THz radiation (amplitude and phase) through the sample at different incidence angles. Then a specific algorithm, using a Radon inverse transform (explained in section 2.5), is usually used to reconstruct the cross-sectional images. In this way, both absorption and refractive index based images could be obtained.

The idea of THz CT technique was first demonstrated by Ferguson *et al.* who imaged a cross-sectional structure of a turkey bone [Ferguson 2002]. THz CT along with spectral analysis offers the opportunity of wide spectral information in time and frequency domains, so one may reconstruct images at each frequency value [Ewers 2009]. Brahm *et al*. also performed a volumetric spectral analysis of materials using THz CT [Brahm 2010]. Based on their characteristic absorption spectrum, lactose and glucose filled inside two holes of polystyrene block have been identified.

An alternative study is the development of depth resolving THz imaging with tomosynthesis, which is similar to CT except that the number of projections is much smaller [Sunaguchi 2009]. Here, the authors use only five projections instead of general value of 15 to 20 in THz CT. However, the efficiency of their system is mainly limited to thin and wide samples (50 sheets of post-it notes). In THz CT, it is important to employ a powerful THz source in order to properly detect the THz radiation

transmitted by the sample, especially in the practical case of thick or absorbing samples. Zhang *et al*. generally use an amplified laser source and optical rectification [Wang 2003]. Such a system is complicated and expensive for real applications. The development of alternative THz sources, such as frequency multiplied Gunn diodes or cascade quantum lasers, allows the development of cheaper and more compact systems for THz CT [Nguyen 2006, Sunaguchi 2009].

Although THz CT seems powerful, structures with sizes of the order of the wavelength of the THz radiation cause severe diffraction of the THz pulse. This imposes problems in reconstruction process, as diffraction is not accounted in the reconstruction algorithm and results in artifacts in the final image. THz CT is suitable to obtain the spectroscopic images, but the main drawback is the low acquisition speed.

All above mentioned tomographic techniques (THz diffraction tomography, 3D holography, binary lens tomography) are used for volumetric material inspection. The choice of tomography methods depends upon the researcher individual desire, interest and requirement. In this thesis, we restrict ourselves to the THz CT as we have collaborated with programming experts in LaBRI, specialist of X-ray CT reconstruction, who offer their capabilities for final image reconstruction in case of THz CT.

1.2. X-ray Vs THz Computed Tomography

As described later, THz CT is analogous to X-ray CT and uses the same principles and reconstruction algorithms developed for X-ray CT. One reason why THz CT enables attractive new applications instead of X-ray tomography is the collection of much more information about the sample. X-rays CT provides intensity measurement data to resolve the absorption characteristics of materials [Hounsfield 1980]. In addition, THz pulses provide a time-resolved analysis. Thus not only the absorption information of the THz pulses can be evaluated with standard tomographic algorithms, but information like time-delay, spectrum and phase of the THz pulses can be utilized as well. Using the variations of time-delay, it is possible to determine the inner structure, the refractive index or the thickness of samples [Duvillaret 1996]. The biggest potential enables the application of spectral information. Thereby not only the inner structures of the sample can be localized, but also the materials themselves can be identified from their characteristic absorption spectra.

Moreover, X-ray CT can visualize dense materials such as wood [Morigi 2010], bones and biological tissues but cannot be easily applied to soft materials such as plastics, papers or paintings owing to the low absorption of the X-ray radiation. In such case, THz CT can be used as an alternative technique to visualize 3D objects with THz radiation. In some cases like in anthropology and paleontology, X-ray CT is not recommended owing to the fragility/uniqueness of the samples and the problem of sample radiometric dating after X-ray irradiation as explained earlier. Comparatively, THz

CT is a non-destructive and non-invasive technique which can be safely applied to visualize 3D structure of the sample.

THz CT utilizes the similar reconstruction procedure as already adopted by X-ray CT. However, there are some important points which should be noted. The THz beam propagation cannot be accurately described by a straight ray-line that is valid for X-rays. The wavelength of the THz beam is larger than that of X-rays by several orders of magnitude, so the diffraction or scattering effect may blur or deform the reconstructed image. Keeping this in mind, we have to formulate the reconstruction algorithm for THz CT. As already reported by Wang *et al*. it is possible to reconstruct the final image based upon Radon transform propagation model if two conditions are fulfilled [Wang 2004]:

(1) The target's lateral extent in the direction of the THz wave vector is less than the Rayleigh range of the THz beam,

(2) Within the Rayleigh range, the THz beam propagates as a planar Gaussian wave.

As it will be pointed out later in the description of the experimental results, both imaging systems (THz-TDS, CW) well satisfy the above mentioned assumptions. Now after this brief introduction of various tomographic techniques, we will present tomographic results obtained with our THz-TDS imaging and CW imaging systems for the non-destructive evaluation of opaque phantoms and more realistic 3D objects.

Section 2: THz-TDS Computed Tomography

In this section we will present the results of THz CT obtained by THz-TDS imaging system. We will explain the problem of THz beam propagation through high refractive index targets and present a specific procedure to overcome the difficulty in signal analysis. After, we will show the general procedure adapted for tomographic measurements along with the description of reconstruction method. Finally, results obtained by THz CT for mapping the 3D structure of opaque samples will be shown.

2.1. THz Transmission through High Refractive Index Materials

In the previous reported results of THz CT, most samples that have been correctly imaged are low refractive index materials (refractive index typically less than 1.2). It was found, that as soon as the refractive index starts increasing, THz beam experience severe refraction. Consequently the transmitted THz signal is difficult to detect. Keeping this point in mind, before starting THz CT, we want to evaluate THz beam transmission through higher refractive index materials. For this purpose, we selected a Teflon (n=1.45) plain cube. To illustrate the problem of the THz beam propagation, let's consider that the sample (Teflon plain cube) is placed in THz beam path, with a face perpendicular to the incident THz beam (incident angle referenced as 0°). In this case the transmission is high (between 90 and 95%) in agreement with the Fresnel losses at each interfaces (about 4% at the entrance and

another 4% at the output of the cube). However, if the cube is rotated by an angle of 45° for instance, we observe a strong decrease of the transmitted THz signal. This decrease is not really due to the Fresnel losses which are in the same order as for angle 0°. The main reason is rather the refraction of the THz beam which is strongly deviated from its original direction. Consequently, the THz beam cannot be properly detected by the photoconductive antenna, which works as a punctual detector.

This first observation indicates that in THz CT, the problem with high refractive index objects arises, from the strong deviation of the THz beam due to refraction. Depending on the shape of the 3D sample, the angle of incidence (from 0° to 170°) and the numerical aperture of the lens collimating the THz beam after the sample (NA=0.29), the deviation can be severe and dramatically disturb the detection of the transmitted THz wave.

2.2. Deviation of THz Beam in High Refractive Index Samples

To illustrate experimentally the above mentioned phenomenon of THz deviation, we utilized a Teflon cylinder (10 mm diameter). The sample is illuminated by the THz beam and then raster scanned in the *x*-direction with a 0.5 mm step (Figure 4.2(a)). Figure 4.1(b) shows the detected THz waveforms for different lateral positions of the sample. If the THz beam is not intercepted by the cylinder (beam 1, figure 4.1(a)), the THz waveform simply corresponds to a simple propagation in the air (beam 1, figure 4.1(b)). The maximum amplitude is about 2 nA. Then, theoretically, as the THz beam penetrates into the sample, the THz waveform should be slightly attenuated (8% total Fresnel losses) and gradually delayed due to the progressive increase of the optical pathway. This assumption has been provided by Zhang *et al*. who indicated that the shape of the THz pulse should not change after transmission through the sample except being delayed and attenuated [Wang 2003].

The obtained results are quite different. If the THz beam is slightly intercepted by the cylinder (x = -3 mm with x = 0 mm being the centre of the cylinder, beam 2 in figure 4.1(a) and figure 4.1(b), with a magnification factor of 4), the THz peak corresponding to the transmission in the air is still present (amplitude 440 pA) and another delayed peak appears around 7.2 ps with a very small amplitude (140 pA). For x = -2 mm (beam 3, figure 4.1(a) and figure 4.1(b) with a magnification factor of 4), the waveform is very disturbed and a small signal is observed at 7.2 ps with an amplitude of 110 pA, which corresponds to the maximum of the transmitted THz signal at the receiver position. Finally for x = 0 mm, the THz beam is in the middle of the cylinder (beam 4, figure 4.1(a)) and the THz waveform recovers its original shape. The maximum amplitude of the main THz peak is 1.7 nA and the time delay is 13.1 ps, in agreement with the values of the mean refractive index of Teflon (1.45 at 1 THz) and the sample thickness (beam 4, figure 4.1(b)).

From these observations, we can conclude that the THz beam is not deviated if its pathway is close to the centre of the cylinder, whereas a strong refraction is observed for all other situations. Consequently, this situation is problematic to apply the Back Filtered Projection (BFP) algorithm (will be described later in sub-section 2.5) since it is very difficult to quantitatively determine the amplitude

and time position of the THz pulse in case of strong refraction. This problem was already pointed out by Wang *et al*. [Ferguson 2002, Wang 2003]. The authors emphasized that the BFP algorithm assumes that the sample should have a low refractive index (as close to unity) with features that are large relative to the wavelength of the THz radiation (0.3 mm at 1 THz). In that case, diffraction effects and Fresnel losses can be neglected. We can add that the refraction is also a very limiting factor. Afterwards, we applied a specific procedure to properly determine the amplitude and the time-delay of the THz pulse even if the THz waveform is strongly disturbed by the propagation through a sample inducing important refraction losses.

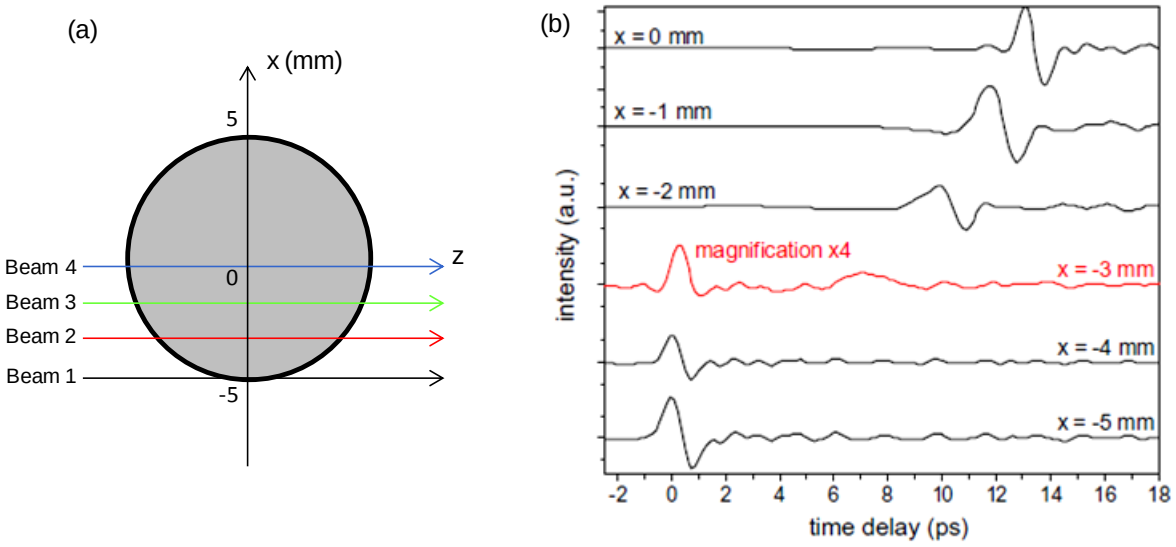

Figure 4.1: (a) Teflon cylinder having a diameter of 10 mm along with direction of the incident THz beam, (b) THz waveforms for different lateral positions of the sample from x = -5 mm to x = 0 mm. For clarity, the amplitude of the THz waveform corresponding x = -3 mm (red colour) has been multiplied by 4.

The next sample is the same Teflon cylinder (10 mm diameter) drilled with a non-concentric (1.83 mm off-axis) cylindrical hole with a 3.4 mm diameter (Figure 4.2(a)). In a first experiment, the sample is not rotated and the center of the cylindrical hole is located at x = 0 mm, as shown in figure 4.2(a). The sample is then scanned in the *x*-direction from -7 mm to 7 mm with a 0.5 mm step. For each *x*-position, we record the THz waveform and need to choose the pertinent parameters to perform the THz CT. As pointed out previously, the main parameters in pulsed THz CT are the amplitude and the time-delay of the transmitted THz pulse.

In figure 4.2(b), the black circles represent the THz main pulse time-delay after passing through the sample and the green curve is the corresponding theoretical values taking into account the main cylinder and the cylindrical hole. We notice that the experimental values are in agreement with theory if the deviation of the THz beam due to the refraction is small, i.e. out of the edges of both the main cylinder and the smaller cylindrical hole. However, if the refraction strongly modifies the

direction of the THz wave, the experimental values are different from the theory, as clearly visible for x = -4.9, -4.4, -3.9, -3.4, -1.4, 1.1, 4.1 and 4.6 mm. As explained previously in figure 4.1, for these positions, the problem arises from the presence of several peaks in the THz waveform. In this case, it is not clear which peaks have to be selected to determine the time delay to be plotted in figure 4.2(b). This situation is quite problematic and in order to correct these values, we propose a multi-peak averaging procedure which is explained below, along with the corresponding corrected results.

2.3. Multi-peak Averaging Method

In "multi-peak averaging" procedure, we first fix a minimal amplitude threshold to identify the presence of multiple peaks in a single THz waveform. In situations where refraction is important, two or even three peaks can be visible over the threshold. In such case, we calculate a mean time-delay taking into account the amplitude and the time-delay of the different peaks above the threshold value. The efficiency of the proposed multi-peak averaging method mainly comes from the selection of correct amplitude thresholds for both positive and negative peaks and the following consideration of all the THz peaks detected above these thresholds.

The origin of these multiple peaks arises from the larger size of the THz beam as it interacts with the sample owing to the Gaussian shape of the THz beam. We can estimate that the THz beam diameter is about 1.4 mm at the limit of the Rayleigh range. Consequently, this larger THz beam will simultaneously provides information from different parts of the sample, visible as the different THz peaks. The averaging of all these peaks will give a better estimation of the mean time-delay experienced by the THz beam. In that manner, the attenuation of the refraction losses is minimized and the complex shape of the object can be analyzed. In order to explain clearly this procedure, we will show the difference in corresponding results after the application of this specific "multi-peak" procedure in the above experiment (Teflon cylinder with a hole).

For this purpose, the figure 4.2(c) shows the THz waveform corresponding to x = -1.4 mm. The THz main pulse time delay is 10.6 ps. This value is clearly out of the theoretical curve. To correct this error, we selected two horizontal red lines as thresholds (for both positive and negative peaks). Three negative peaks are over the negative threshold and two positive are over the positive one. The corresponding average of the time-delay is calculated to x = 11.3 ps, given by the vertical purple line. This corrected value is now in agreement with the theoretical curve. By applying such a procedure for each waveform, we finally obtain the red squares in figure 4.2(b) which are in better agreement with the theoretical curve especially near the edges of the sample, even if the recalculated value is still not correct for x = -3.9 mm.

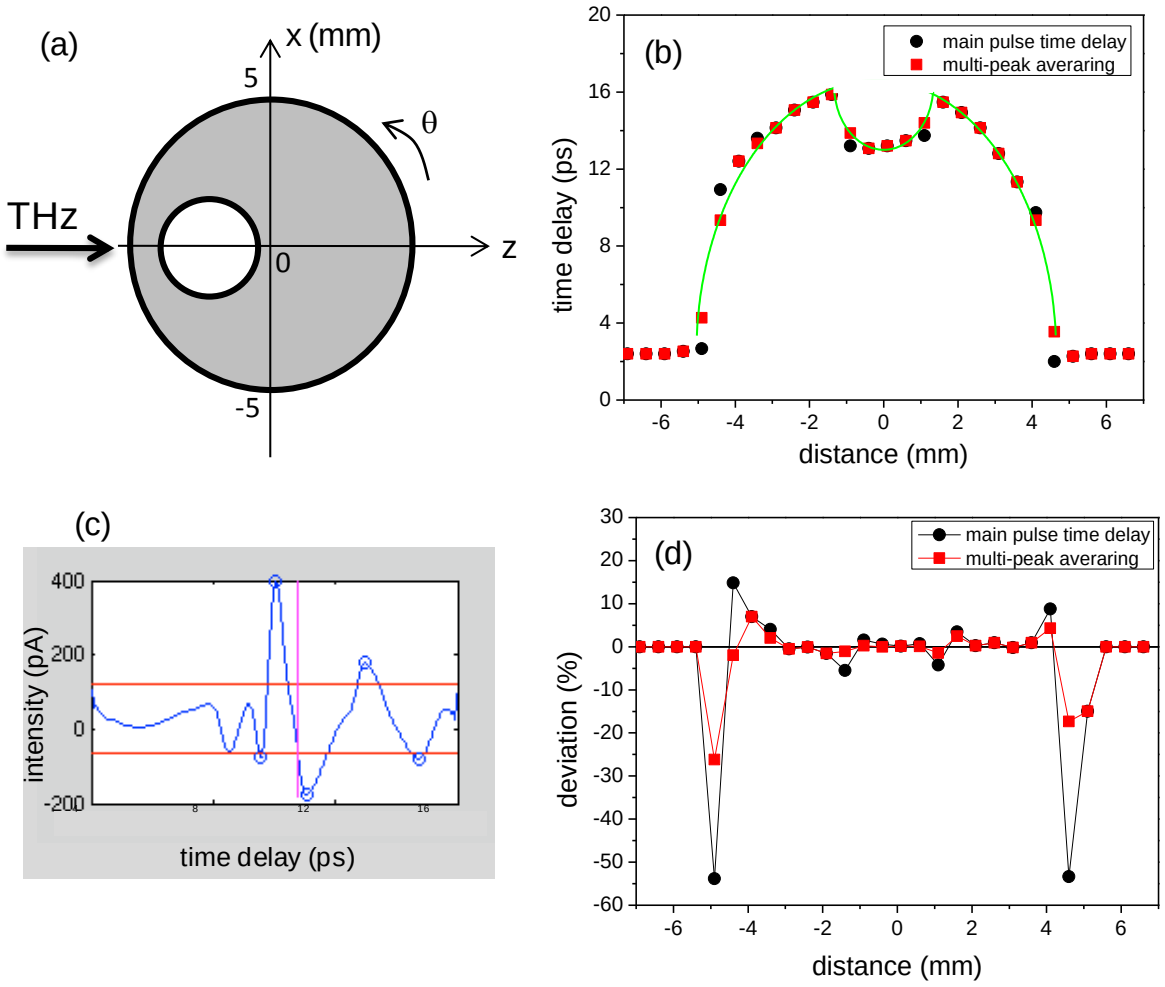

Figure 4.2: (a) Ten millimeter diameter Teflon cylinder with off-axis 3.4 mm cylindrical hole, (b) THz time-delay for different positions of the THz beam along the x-direction (black circles: main pulse time-delay, red squares: corrected values using the multi-peak averaging procedure, green curve: theoretical values), (c) THz waveform for x = -1.4 mm with thresholds (horizontal red lines) and calculated mean time-delay (vertical purple line), (d) deviation of the experimental data to the theoretical values from graph (b).

From these measurements it is also possible to plot the deviation of the experimental data to the theoretical data. The figure 4.2(d) shows this deviation calculated classically as (experiment-theory)/theory*100. This new representation makes it possible to clearly visualize the deviation of the experimental data especially near the edges of the main plain Teflon cylinder. For x = -4.9 mm, the deviation for the multi-peak averaging is reduced to -26% compared to -54% for the main pulse time-delay. For x = 4.6 mm, the situation is even better with a deviation for the multi-peak averaging at -17% compared to -53% for the main pulse time delay. Concerning the non-concentric cylindrical hole, the analysis of the deviation is remarkable. For x = 1.4 mm (respectively x = 1.1 mm), the deviation for the multi-peak averaging is -1% (respectively -1.4%) compared to -5.2% (respectively -4.2%) for the main pulse time-delay. This analysis emphasizes the efficiency of the multi-peak averaging

procedure for THz CT. Moreover, considering an unknown complex shape object, this representation allows to instantaneously identify the presence of high refractive structures along the pathway of the THz radiation. Practically, this can be useful to reveal internal defects within a sample.

2.4. Procedure for Performing THz Tomography

For performing THz CT with our TDS system, we used the optical setup (a) mentioned in figure 2.5 of chapter 2. This imaging configuration (Figure 2.5(a)) is in agreement with the assumptions of Wang *et al.* [Wang 2004]. As already mentioned in chapter 2, the beam waist of the THz wave is about 0.8-1 mm at 2 THz with a corresponding Rayleigh range of 5 mm. Consequently, the samples should have a maximum extend of 10 mm in the direction of the THz beam propagation, corresponding to twice the Rayleigh range.

For tomography the sample is first raster scanned along the *x*-direction with a 0.5 mm step. Then the sample is rotated with a 10° step and the raster scan along the *x*-direction is performed again. This process is repeated from 0 to 170° (due to symmetric reasons angles from 180° to 360° are avoided to keep time) with a 10° step, which represents a set of 18 projections for the application of the final BFP algorithm. The acquisition time depends upon the sample dimensions, the step size and the number of points taken in the temporal domain. For the tomographic measurements, we obtain a single slice in the *x*-direction in 2-3 min, but the procedure should be repeated for 18 projections. Finally, it takes nearly 35-45 min to obtain a final sinogram which will provide a single cross-sectional image of the sample after the application of BFP algorithm.

2.5. Reconstruction of Final Image

Once the cross-sectional tomographic THz data is acquired for each point, a 2D cross-sectional image can be obtained, with the help of a specific reconstruction algorithm. Then the final 3D image is obtained by stacking together all the cross-sectional images. The most widely used algorithm to reconstruct these measured data is based on the inverse Radon transform, usually applied with special filters [Ramanchandran 1971] in the frequency range for image quality enhancement. This stabilized transform is called BFP, which is invented by Bracewell and Riddle [Bracewell 1967] and was first used in X-ray CT by Hounsfield and Cormerk [Hounsfield 1973]. The BFP algorithm uses Fourier theory to arrive at a closed form solution to the problem of finding the linear attenuation coefficient at various points in the cross-section of an object. The fundamental result linking Fourier transforms to cross-sectional images of an object is the Fourier slice theorem [Shepp 1974]. A brief description of reconstruction process is given below.

Let us consider $f(x, y)$, a 2D function representing the shape of a given cross-section of the 3D object, and a projection line along the angle θ with a position given by a module t (Figure 4.3). As proved by Radon [Radon 1917], it is possible to determine the function $f(x, y)$ with the knowledge of the line integrals of a 2D function $P_\theta(t)$ along a straight line (i.e. at every angle through every point).

Forming all these line integrals is called radon transform, defined by Johann Radon in 1919. It transforms a 2D function *f(x,y)* into a 1D projection along an angle θ. It is given by the following formula:

$$P_\theta(t) = \iint f(x,y)[\delta(xcos\theta + ysin\theta - t)]dxdy \quad (4.1)$$

where θ and *t* are the angular and radial coordinates of the projection line (*θ,t*) and δ is the Dirac impulse. The function $P_\theta(t)$ represents the absorption sum of all points traversed by the line and corresponds to the theoretical attenuation of THz radiation into the matter along this line. This function is often referred as the Radon transform of the 2D object. As the parameters t and θ vary, the function $P_\theta(t)$ provide a 2D image referred as the "sinogram" of the corresponding cross-section of the sample. Figure 4.4(b) shows a typical sinogram obtained by imaging a horizontal slice of cubic sample (Figure 4.4(a)) at various angles. The sinogram represents the transmitted THz signal corresponding to each horizontal slice for a given projection angle θ.

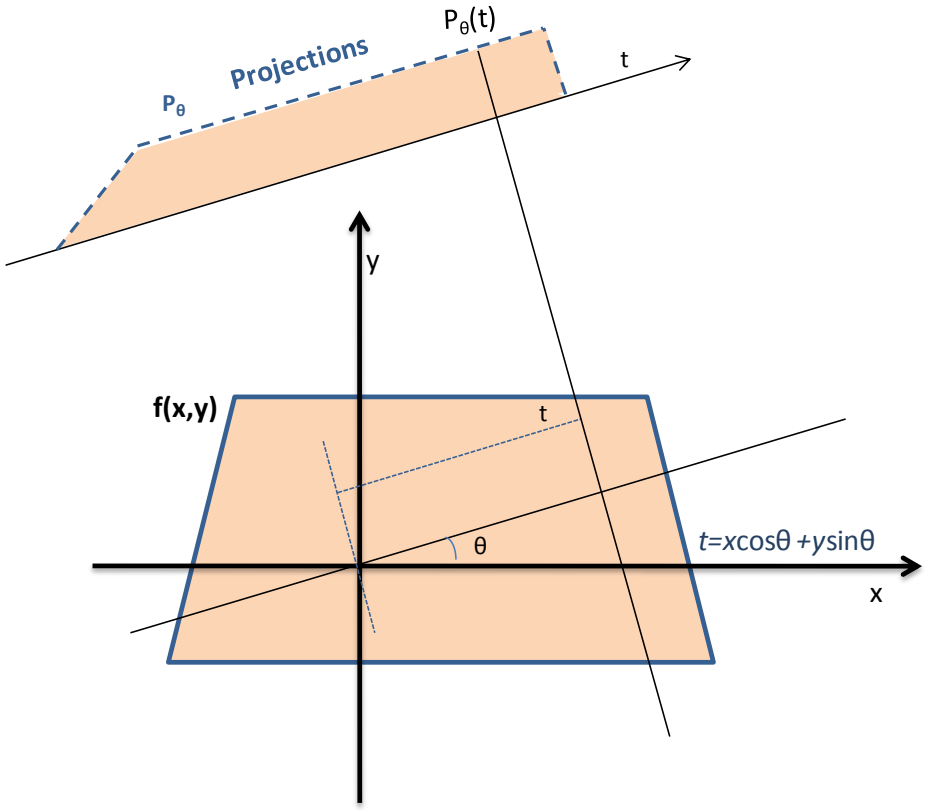

Figure 4.3: Illustration of projection formation. A projection line is defined by angle θ and position t, its value depend on traversed f(x,y) values and corresponds to the attenuation undergone by the rays.

The task of tomographic reconstruction is to find *f(x,y)* given the knowledge of $P_\theta(t)$. The sinogram has many nice mathematical properties, an important of which is

$$P_\theta(t) = P_{\theta+\pi}(-t) \quad (4.2)$$

which explains the reason for neglecting angles from 180° to 360° due to symmetric reasons.

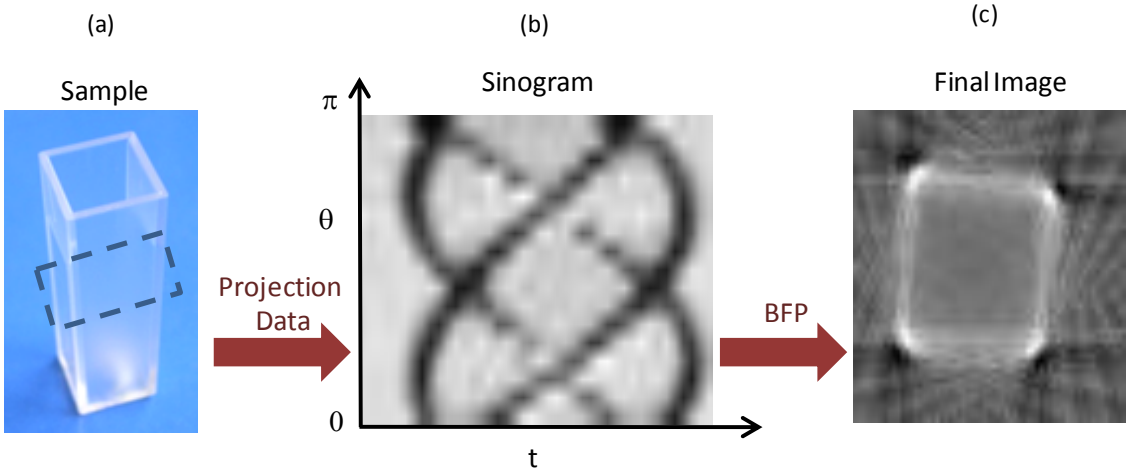

Figure 4.4: (a) Photograph of the sample, projection data is collected for a single horizontal slice of the sample, (b) corresponding sinogram, giving the transmitted THz signal at each horizontal line for each angle θ, (c) final reconstructed cross-sectional image by BFP algorithm.

The inverse reconstruction recovers the function *f(x,y)* from the projections. First, this inversion applies a ramp filter on the frequency domain of each projection to increase details. Second, the point *(x,y)* is computed from the sum of the filtered projections. This method is denoted by Back-Filtered Projection (BFP). Supposing a sinogram with an infinity of projection values $P_\theta(t)$ such as $\theta \in [0, \pi[$, the 2D function f(x,y) is recovered according to:

$$f(x,y) = \int_0^{\pi} \int_{-\infty}^{+\infty} F^{-1}[(|\omega|) * [P_\theta(t)]\delta(x\cos\theta + y\sin\theta - t)]d\theta dt \qquad (4.3)$$

where *F* is the Fourier transform and the new term $|\omega|$ represents a filter, which improves inner structures and removes artefact. The overall reconstruction process is shown schematically in figure 4.5.

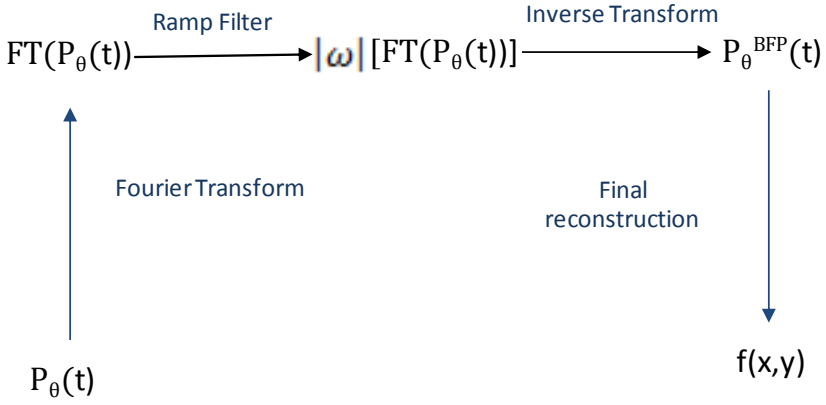

Figure 4.5: General scheme for reconstructing CT images by BFP algorithm.

In practice, this reconstruction process in continuous domain has to be changed to discrete domain. Indeed, contrary to ideal acquisition, a real acquisition is composed of finite number of projections N_θ uniformly distributed between 0 to π. The module number (number of points in one horizontal line of sinogram) denoted by N_t is finite too and remains constant during all acquisition. Figure 4.6 shows a pattern of imaged sample consisting of various pixels. Depending upon the projection sampling the traversed THz ray (t) crosses each pixel in irregular manner. As an example the crossed distance in various pixels is shown in different colours in case of ray t_3. The central pixel denoted "A" is crossed by two lines t_3 and t_4, but another pixel "B" is crossed by only one single line (t_4). To reduce the effect of this irregular sampling problem in final image, the contribution from each pixel defined by specific pixel kernel has to be taken into account.

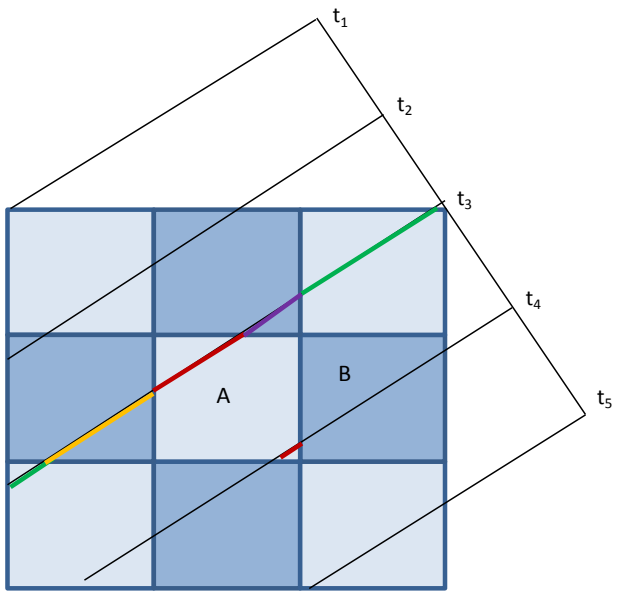

Figure 4.6: Projection sampling leads to irregular pixel crossing, some pixels are crossed by only one line and several others are crossed by multiple lines; contribution from each pixel should be considered based on pixel kernel.

In discrete domain, the angular step between two consecutive projections is denoted by $\Delta_\theta=\pi/N_\theta$. Similarly we denote Δ_t the sampling step on the projection, i.e. the distance between two successive projection lines. During the discrete image reconstruction *I* sized W*H pixels, the sampling step is:

$$\Delta_t = \frac{\max(W, H)}{N_t} \tag{4.4}$$

For one horizontal cross section the acquisition along several angles gives a 2D image (the sinogram) having a size of N_t*N_θ. The discrete radon transform reconstructs an image *I* from an acquisition using the formula:

$$I(i,j) = \sum_{i_\theta=0}^{N_\theta-1} \sum_{i_t=0}^{N_t-1} P_\theta^{BFP}(t) pk(\theta, t, i, j) \quad (4.5)$$

where *pk* is a pixel kernel used to determine the manner that the projection line crosses the pixel and $P_\theta^{BFP}(t)$ is the BFP value given by:

$$P_\theta^{BFP}(t) = \sum_{t_s} |\omega| \left(\sum_{\omega} P_\theta(t_s) e^{-2\pi i \omega t_s} \right) e^{2\pi i \omega t} \quad (4.6)$$

In this manner, starting from the projection data and the resulting sinogram, one can obtain the final BFP reconstructed image with the help of the inverse radon transform [Recur 2010]. With our THz-TDS tomographic system, we adopted this reconstruction process. Corresponding results are presented in the next sub-section.

2.6. THz 3D Computed Tomography

After consideration of possible refraction losses and developing specific procedure for analyzing the results, we finally performed THz CT of some phantoms and real objects. Our first sample was Teflon cylinder with a hole which is rotated from 0 to 170° (in figure 4.2(a), the angle θ was set to 90°) and scanned in the *x*-direction (from x = -7 mm to 7 mm) for each angle. This resulted in 522 THz waveforms, each consisting of 150 data points over a time window of 21.2 ps. In the first step, data was displayed in the form of a sinogram, as already mentioned, which represents a 2D image as a function of the projection angle θ and the projection offset corresponding to the *x*-position.

Without any correction, we can obtain the raw amplitude (Figure 4.7(a)) and raw time (Figure 4.7(b)) sinograms from the amplitude and time-delay of the THz main pulse. The amplitude sinogram (Figure 4.7(a)) reflects the absorption of the sample (black colour for high absorption, white colour for lower absorption) and the time sinogram exhibits the variation of the refractive index (black colour for low refractive index, white colour for higher refractive index). With the multi-peak averaging, we also get the corrected time sinogram (Figure 4.7(c)). In figure 4.7(d), we plotted the theoretical time sinogram of the target obtained by measuring the variations of the sample thickness depending on the projection offset. Sinograms in figures 4.7(b) and 4.7(c) should be compared to that in figure 4.7(d). We notice that the experimental sinograms are slightly clockwise rotated with respect to the theoretical sinogram. This is explained by the fact that the centre of the target does not exactly correspond to the rotation axis.

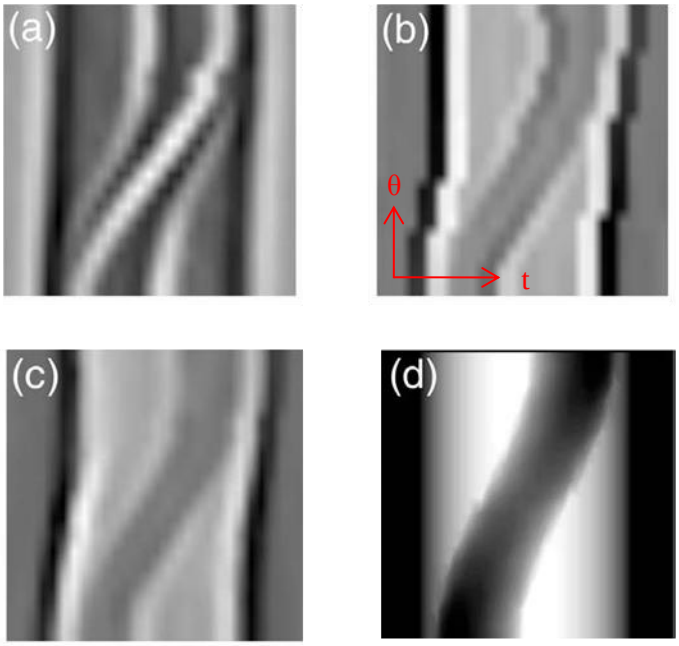

Figure 4.7: Ten millimeters diameter Teflon cylinder with off-axis 3.4 mm cylindrical hole: (a) amplitude sinogram from the THz main pulse amplitude, (b) time sinogram from the THz main pulse time-delay, (c) time sinogram from the multi-peak averaging, and (d) time sinogram from theoretical values (thickness variations of the target).

Simultaneously, the target image is reconstructed from the filtered projections using usual BFP algorithm. From the acquisition parameters (raster scan in *x*-direction and rotation angle), we deduce the target image dimensions and accumulate the THz waveforms for each pixels. We finally repeat this process for the whole projections to obtain the final reconstructed target image. From the amplitude and time sinograms, two cross-sectional images can be obtained. The amplitude image corresponds to the bulk absorption of the sample whereas the time image corresponds to the bulk refractive index of the sample. The reconstructed cross-sections (amplitude and time) of the sample are shown in figure 4.8. The first analysis is that the amplitude clearly reveals the edge of the main cylinder whereas the inner hole is not properly located (Figure 4.8(a)). Concerning the raw time sinogram (Figure 4.7(b)) and cross-section (Figure 4.8(b)) obtained with the main THz peak delay, both the main cylinder and the inner hole are resolved but the shape is not perfectly cylindrical due to refraction artifacts, as pointed out previously. Here, the black colour indicates a refractive index close to unity (air) and the white colour corresponds to the refractive index of Teflon close to 1.45.

From these raw data, we can notice that severe refraction losses degrade the images especially in the regions where the THz radiation is strongly deviated from its original direction. This observation emphasizes that the direct BFP algorithm is not well appropriated for high refractive index samples as pointed out previously. A specific additional procedure is necessary to improve the final reconstruction. The corrected time sinogram (Figure 4.7(c)) and cross-section (Figure 4.8(c)), obtained with the multi-peak averaging procedure, exhibit a better definition and a more precise location of the inner hole. Only for this representation, the shapes of the main cylinder and the inner hole are really

cylindrical. As for the sinogram, we also plotted the theoretical cross-section (Figure 4.8(d)) obtained from the theoretical time sinogram (Figure 4.7(d)).

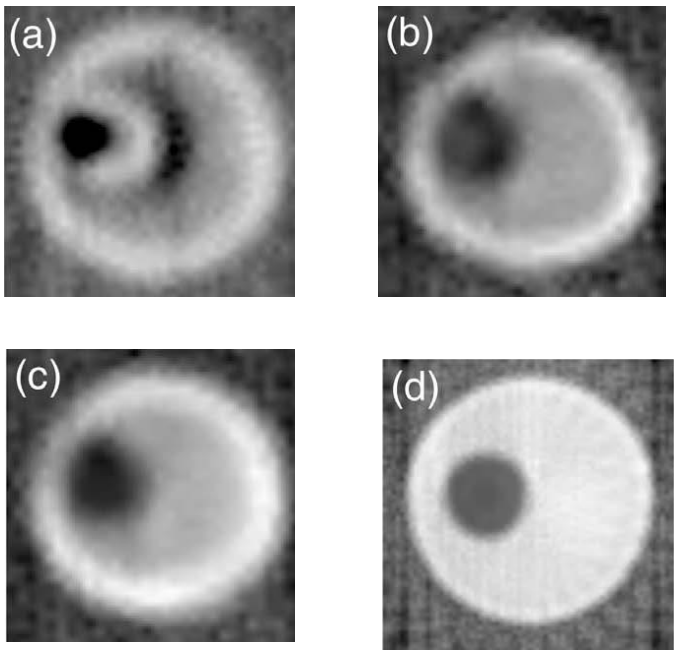

Figue 4.8: Ten millimeters diameter Teflon cylinder with off-axis 3.4 mm cylindrical hole: (a) amplitude cross-section from the THz main pulse amplitude, (b) time cross-section from the THz main pulse time-delay, (c) time cross-section from the multi-peak averaging, and (d) time cross-section from theoretical values (thickness variations of the target).

We can notice that the cross-section obtained with the multi-peak averaging procedure is similar to the theoretical cross-section even if the periphery of the main cylinder seems to have a higher refractive index compared with the interior of the cylinder. This problem can be explained by reconstruction artifacts inherent in the BFP operation, refraction losses or the difficulty to properly determine the absorption or the refractive index at the interface between air and Teflon. These artifacts could be reduced by acquiring more projection angles. From the theoretical representations (sinogram and cross-section), we can also conclude that the BFP algorithm is able to properly reconstruct the shape of the target with a good precision. From the reconstructions, the calculated diameter of the main cylinder is 9.8 mm (2% error) and the diameter of the inner hole is 3.2 mm (6% error). This conclusion was important to state that the final reconstruction artifacts observed in the experimental cross-sections were mainly due to experimental losses (refraction, diffraction).

Finally, we tested a more realistic sample composed of a dried chicken femur (Figure 4.9(a)). By THz-TDS, the refractive index of a dried cortical human bone has been previously measured between 2.2 and 2.4 [Stringer 2005]. This sample represents a highly refractive target for the incident THz radiation. Here, the THz CT is used to visualize and analyze the internal structures of the sample in a non-invasive and non-destructive manner. Such an application should particularly interesting in anthropology and archeology. Figure 4.9(b) shows the THz amplitude cross-section of the bone (about

1 cm^2), in the region indicated by the horizontal black line in figure 4.9(a). We conclude that the THz radiation is mainly attenuated by the external structure of the bone (white colour), which strongly absorbs the THz radiation.

In the heart of the bone, a softer material is revealed (black colour) with a lower absorption coefficient. This is also clearly visible from the time cross-section (Figure 4.9(c) with multi-peak averaging), which identifies with a better accuracy the structure of the target and also reveals the variations of the refractive index. Especially, the internal structure of the bone presents a lower refractive index than the external structure. However, for both amplitude and time cross-sections, the internal structure of the bone is poorly reconstructed owing to the long wavelength of the THz radiation which causes a severe diffraction. However, this diffraction is not taken into account in the reconstruction algorithm which causes some artifacts in the final image if the sample presents some structures whose dimensions are in the same order of the THz wavelength.

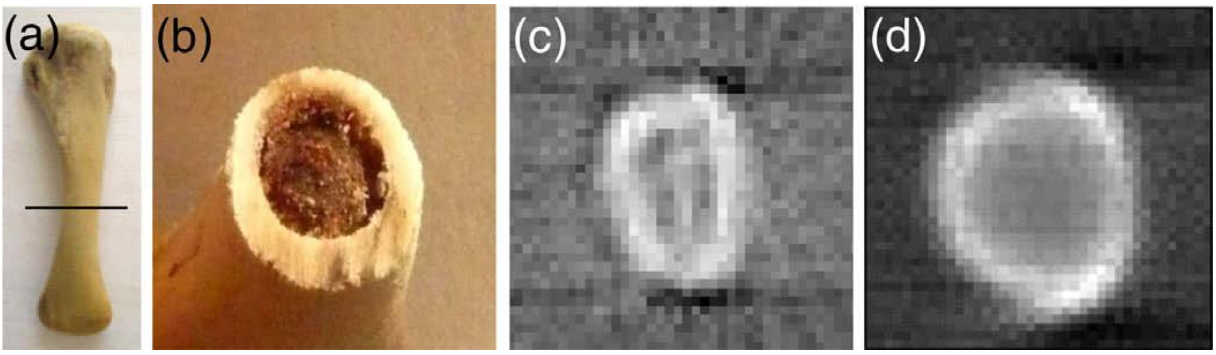

Figure 4.9: (a) Digital photograph of the dried chicken femur (the horizontal black line indicates the region of the cross-sectional image), (b) Digital photograph of the sectioned chicken femur, section size is (7*9) mm^2, (c) Amplitude cross-section, (d) Time cross-section obtained from multi-peak averaging.

Time amplitude and delay (phase) values are the usual parameters for reconstructing final tomographic images. However, THz waveform contains a lot of information about the sample. As described earlier in previous chapters, lot of other parameters, like the amplitude for a specific time delay, the maximum or minimum amplitudes or the contrast (difference between maximum and minimum values) in time-domain can be used. In the frequency domain, we can simply select the amplitude for a specific frequency in order to reconstruct final THz tomographic image. In such a way, wide information about the investigating sample can be extracted. However, the data is more difficult to be analyzed in frequency domain, owing to the presence of multiple peaks, resulting in a complex spectrum harder to process and reconstruct final images.

In summary, we presented a THz-TDS CT analysis of complex shape targets. After passing through the sample, the severe refraction of the THz beam makes it difficult to properly identify the amplitude and the time delay of the THz pulse. By proposing a specific procedure based on a multi-peak averaging analysis, a BFP algorithm was employed to reconstruct the amplitude and time cross-sections of the samples.

In the next section we will show the potential of CW imaging system for performing tomography. This imaging system has the advantage of fast acquisition and single value data. This simplicity helps analyzing and manipulating signal in an easy way, which further facilitates study of various reconstruction algorithms.

Section 3: CW Computed Tomographic Imaging

In this section we present THz CT performed with the CW imaging system. At first, large size 3D visualizations of manufactured opaque phantoms with different refractive index contrasts have been compared. This was possible due to the fast and simple acquisition performed by the mono-element pyroelectric detector. Challenges for precise and efficient tomographic reconstruction of complex refraction index materials will be underlined. Various reconstruction algorithmic procedures will be compared in order to visualize the cross-sectional images. Finally, THz CT for 3D volume inspection of materials will be highlighted, including examples of historical objects from Museum of Aquitaine.

3.1. Procedure for Performing CW THz Tomography

For performing THz CT with our CW setup, we adapted the same procedure as explained in THz-TDS CT. We utilized the configuration in transmission mode explained earlier in figure 2.15 fully satisfying the standard assumptions for performing THz CT. The sample is scanned along x-direction to obtain a single horizontal slice, and then it is rotated to obtain data at some other projection angle. The acquisition time is much faster as compared with THz-TDS system so it takes nearly 10-15 min to obtain a final sinogram of a cross-section of the sample. Before investigating complex samples, it is important to test the potential of 3D CW tomographic scanner with calibrated phantom objects, with determined absorbance and THz refractive index. In this sense, the first sample simply consists of two metallic bars (12 mm diameter) separated by a distance of 50 mm (Figure 4.10(a)). With this simple object, we want to investigate the potential of the scanner to precisely localize the two bars and reconstruct their cylindrical shape.

The experiment has been performed with the 110 GHz source, a number of projections N=72 and only one horizontal *x*-scanning of the object. The acquisition time is about 15 minutes to get a cross-sectional image of the sample. Figure 4.10(b) shows the corresponding sinogram where the horizontal direction is the scanning *x* direction, whereas the vertical one is the rotation angle θ, from 0° to 180°. Clearly the sinogram exhibits the position of the two bars as a function of the projection angle θ. The symmetry of the sinogram comes from the simplicity of the two-component object. With the application of the BFP algorithm (explained earlier), we are able to visualize the cross-section of the sample which clearly reveals the position and the size of the two metallic bars (Figure 4.10(c)).

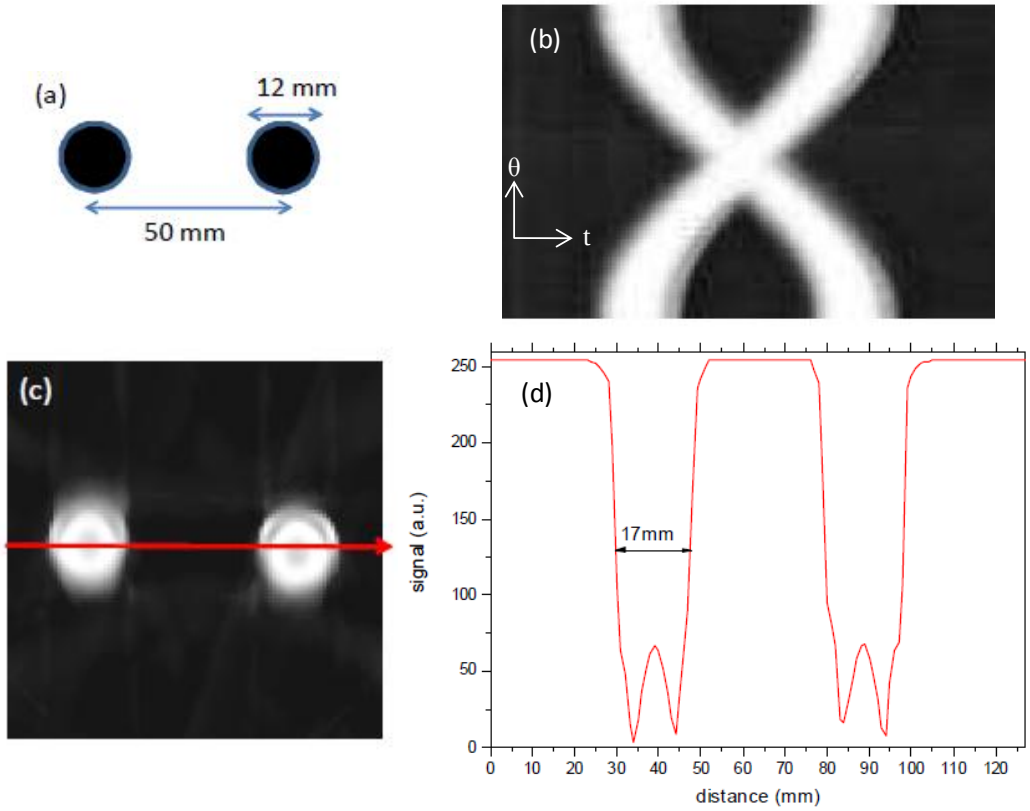

Figure 4.10: (a) Object: Two metallic bars in air, (b) Corresponding Sinogram, (c) Reconstructed horizontal cross-section, (d) 1D profile along the red curve indicated in (c).

The high contrast of the reconstructed image in the region of the metallic bars comes from the absence of THz transmitted signal in these regions. Also, figure 4.10(d) illustrates the variations of the transmitted THz radiation along the red line indicated in figure 4.10(c). This shows the sub-centimeter spatial resolution of the system, as already pointed in chapter 2. At middle height of the transmitted signal, we can estimate that the diameter of the metallic bars is about 17 mm which is larger than the real value owing to the convolution with the THz beam size at the beam waist.

3.2. Fresnel losses in THz Tomography

A sample consisting of a simple Teflon cylinder (15 mm diameter) is used to illustrate the Fresnel losses experienced by the THz wave (Figure 4.11(a)). Indeed, owing to refractive index of the material (n=1.45), the THz beam will not only be attenuated after the transmission through the sample but also deviated according to the Snell laws and diffraction, as already pointed out in sub-section 2.2. This effect is very annoying for CT reconstruction since the algorithm only takes into account the absorption of the radiation. Figure 4.11(b) shows the deviation D of the THz beam as a function of the incidence angle *i*, as defined in figure 4.11(a). The angle *i=0°* means that the center of the THz beam penetrates the sample through its diameter. In that case, the deviation D is zero. Then, the deviation increases according to the Snell law, D=2(i-arcsin(sini/n)) where n is the refractive index of Teflon

(red line in figure 4.11(b)). This obvious observation denotes that THz CT cannot be simply compared to X-ray CT since the deviation of the THz beam is severe depending on the refractive index of the materials.

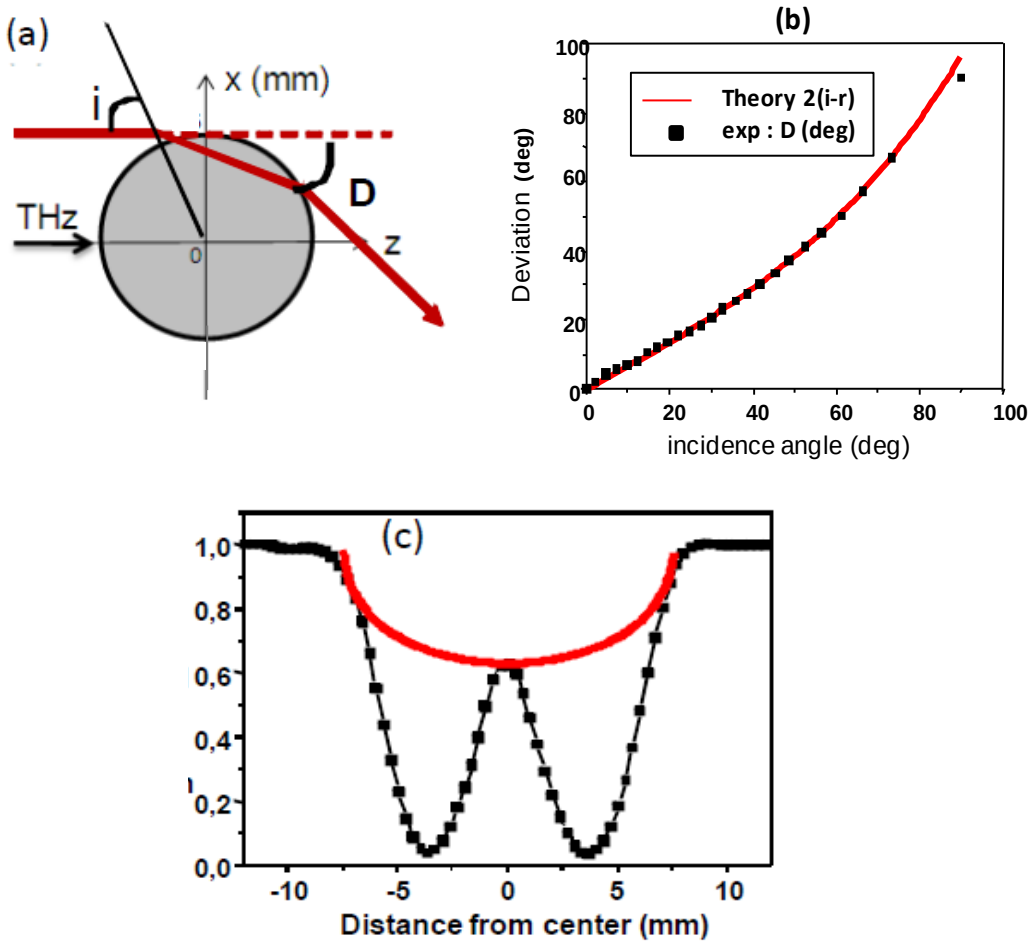

Figure 4.11: (a) Object: Teflon cylinder (diameter 15 mm), (b) Deviation D of the THz radiation as a function of the incidence angle *i* (black squares: experiment, red line: theory according to Snell law), (c) Transmitted THz signal for different position of the Teflon cylinder (black squares: experiment, red line: simulation neglecting refraction and reflection losses).

To illustrate this behaviour, we can also plot the transmitted THz signal as the sample is scanned transversally across the THz beam (black squares, figure 4.11(c)). The "W" shape of the signal reflects that the THz signal is maximum in the air (the Teflon cylinder does not intercept the THz beam) or in the center of the cylinder. However, near the edges of the cylinder, the intensity of the THz signal strongly decreases due to the deviation of the beam which does not enter anymore into the fixed pyroelectric sensor. For comparison, the red curve in figure 4.11(c) illustrates the theoretical transmission of the THz beam if we could neglect the effect of refraction and reflection losses. In that case, the attenuation of the THz signal is simply determined by the absorbance of the material, as for X-ray CT. Finally, these simple observations emphasizes that the experimental data obtained in THz CT are not consistent with those obtained in X-ray CT. In spite of this restriction, in the next sub-

section, we will show that standard CT algorithms can successfully be applied with CW imaging system.

3.3. Reconstruction Methods for THz CT

The choice of proper reconstruction method plays a vital role in the quality of final reconstructed image. Usually, the standard BFP algorithm, as described in sub-section 2.5, is employed for this purpose. However, it is known that BFP suffers from several drawbacks such as noise sensitivity and beam hardening. Especially the beam hardening phenomenon induces artifacts such as cupping, streaks and blurring because rays from some projection angles are hardened to a differing extent than rays from other angles, confusing the reconstruction algorithm. Moreover BFP is very sensitive to the projection number N_θ. If this number is too low, beam hardening artifacts will be enhanced. This number N_θ is also very critical because it acts on the global acquisition time, which is particularly important in THz CT imaging. In this context we investigated other existing iterative methods of tomographic reconstruction. As mentioned earlier, this was possible by the collaboration and aid of researchers from the LABRI. Taking the advantage of simplicity of CW THz data (only one single value for each pixel) and easy manipulation of signal, we employed two alternative iterative methods (SART: Simultaneous Algebraic Reconstruction Technique, OSEM: Ordered Subsets Expectation maximization) for image reconstruction and compared their quality with the standard BFP algorithm.

3.3.1. SART Algebraic Method

Algebraic methods are iterative methods introduced in the 1970's by Gordon *et al*. based on Karzmarz theorem [Gordon 1970, Gordon 1974]. Algebraic Reconstruction Technique (ART) iterative algorithm approaches the linear equation system solution through an update of each pixel value. The pixel correction is done according to the error measured between an initial sinogram and the sinogram recomputed from the image at the previous iteration [Recur 2010].

Considering the discrete geometry, the projection line value $P_\theta(t)$ is a linear combination of pixel (i,j) values weighted by a pixel kernel *pk*. It is defined by:

$$P_\theta(t) = \sum_{i=0}^{W-1} \sum_{j=0}^{H-1} pk(\theta, t, i, j)\, I(i,j) \tag{4.7}$$

Let the weight matrix A with $N_\theta * N_t$ lines (size of the sinogram) and W*H columns (size of the reconstructed cross-section) such as $A_{lt}=pk(\theta,t,i,j)$ with $l(\theta,t)$ and $t(i,j)$. The following linear equation system gives the overall pixel contribution P in the projection lines:

$$P = AI \tag{4.8}$$

Inversion of the system allows recovering the original domain from the projection:

$$I = A^T P \tag{4.9}$$

The Karzmarz method approaches the solution by successive estimation of the vector I^k at iteration k. Each pixel $I^k(i,j)$ is updated by comparing the measured values $P_\theta(t)$ with the sinogram value $P_\theta{}^k(t)$ computed from image I^{k-1}. Iteratively the result converges to the solution minimizing the error between P and P^k and approaching the ideal solution I. The pixel update is:

$$I^k(i,j) = I^{k-1}(i,j) + \lambda pk(\theta,t,i,j)\frac{P_\theta(t) - P_\theta^{k-1}(t)}{D_\theta(t)} \tag{4.10}$$

where

$$D_\theta(t) = \sum_{i=0}^{W-1}\sum_{j=0}^{H-1} pk(\theta,t,i,j) \tag{4.11}$$

is the norm of the segment (θ,t) crossing the image and λ is a relaxation parameter affecting the convergence speed. This method needs an initial image I^0 which can be the result of a direct method (BFP) [Herman 1993, Kaufman 1987]. Several variations of the ART methods have been developed. In our work we selected the so-called Simultaneous Algebraic Reconstruction Technique (SART) algorithm.

The SART algebraic method is also based on the Karczmarz algorithm used to approach the solution of the linear equation system [Gordon 1970, Recur 2010]. It uses all the projection lines at once to update the image. The pixel error is then averaged by the use of several values (at once) in the sinogram and the update is optimized by a projection access scheme. SART is an iterative process following $k \in [0 \cdots N_{iter}[$. Each sub-iteration *s*, $0 \leq s < N_\theta$, updates each pixel of the image $I^{k,s}$ by comparing the original projection $P_{\theta s}$ with $P^k_{\theta s}$ (computed from $I^{k,s-1}$ by using direct Radon transform). A super-iteration *k* is over when all the projections have been used. Consequently, pixel update using SART is computed as follows:

$$I^{k,s}(i,j) = I^{k,s-1}(i,j) + \lambda \frac{\sum_{t=0}^{N_t-1} A_{(\theta_s,t),(i,j)}\left[\frac{P_{\theta_s}(t) - P^k_{\theta_s}(t)}{D_{\theta_s}(t)}\right]}{\sum_{t=0}^{N_t-1} A_{\theta_{(s,t),(i,j)}}} \tag{4.12}$$

where $D_{\theta_s}(t) = \sum_{i=0}^{W-1}\sum_{j=0}^{H-1} A_{(\theta_s,t),(i,j)}$ is the norm of the segment (θ_s, t) crossing the image and (W*H) is the image size. Iterations are performed until the convergence of the solution.

3.3.2. OSEM Iterative Method

Ordered Subsets Expectation maximization (OSEM) algorithm is another iterative process based on statistic interpretation [Shepp 1982], which slightly differs from the SART. The update is done from a subset of several projections at once and the error correction is multiplicative:

$$I^{k+1}(i,j) = I(i,j)^k \frac{\sum_{i_\theta=0}^{N_\theta-1} \sum_{t=0}^{N_t-1} A_{(\theta,t),(i,j)} \frac{P_\theta(t)}{P_\theta^k(t)}}{\sum_{t=0}^{N_t-1} A_{(\theta,t),(i,j)}} \quad (4.13)$$

With the OSEM method, the convergence of the solution is longer than with the SART method because OSEM directly uses all the projections at once. Moreover, after convergence to the solution, OSEM is very sensitive to any solution divergence so that it needs non-trivial regularizations to reduce induced artifacts. If we assume that the complete computation time is 1 second for BFP, we can estimate that this time increases to 4 seconds for SART and 6 seconds for OSEM. In all cases, even if the OSEM computation time is longer than other methods, it is still negligible compared to the long acquisition time required for THz CT. This method OSEM employing ordered subsets of projection can be used to enhance image quality.

3.4. Image Quality and Reconstruction Accuracy

Final image quality and accuracy depends upon the selected algorithmic method used to reconstruct images. In this sub-section, we will compare the above mentioned three reconstruction methods (BFP, SART, OSEM) applied to CW THz tomography. Especially, a particular interest will concern the optimization of the number of projections associated with the preservation of the image quality. Then, the reconstruction methods will be exposed and evaluated taking into account the number of projections and the quality (intensity, contrast, and geometric preservation) of the final reconstructed cross-sections.

3.4.1. Quality According to Reconstruction Method

Here, we will describe the image accuracy and quality according to the choice of the reconstruction method (BFP, SART and OSEM). First, to evaluate the accuracy of the reconstruction, let us consider the same sample composed of two metallic bars (12 mm diameter) as described earlier in figure 4.10(a). The data was acquired along N_θ =72 projections, which represents the maximum projection number selected in our study. In this case, with a rather important projection number, we want to investigate our potential to precisely localize the two bars and reconstruct their cylindrical shape, depending on the choice of the reconstructed method. The reconstructions of the corresponding cross-sections are presented in figure 4.12. Here, we can point out that the depth resolution of the

cross-sectional images is also directly related to THz spot size at the sample position since the projection corresponding to the angle θ +π/2 will provide the depth information of the projection corresponding to the angle θ. Consequently, the lateral resolution is equal to the depth resolution of the cross-sectional images.

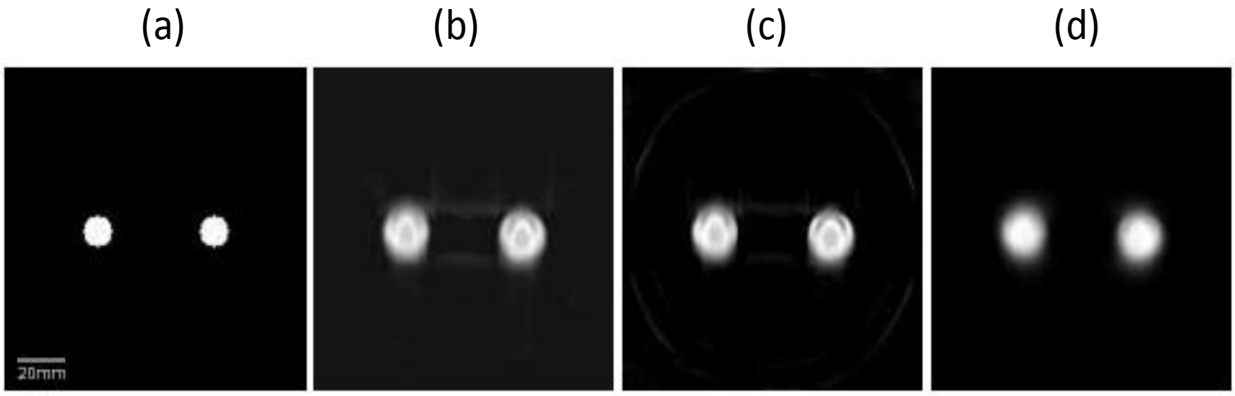

Figure 4.12: Cross sections of two metallic bars (12 mm diameter) separated by 50 mm. (a) Ideal synthetic cross section of the sample, (b) BFP reconstruction, (c) SART reconstruction, (d) OSEM reconstruction. Same scale in all images.

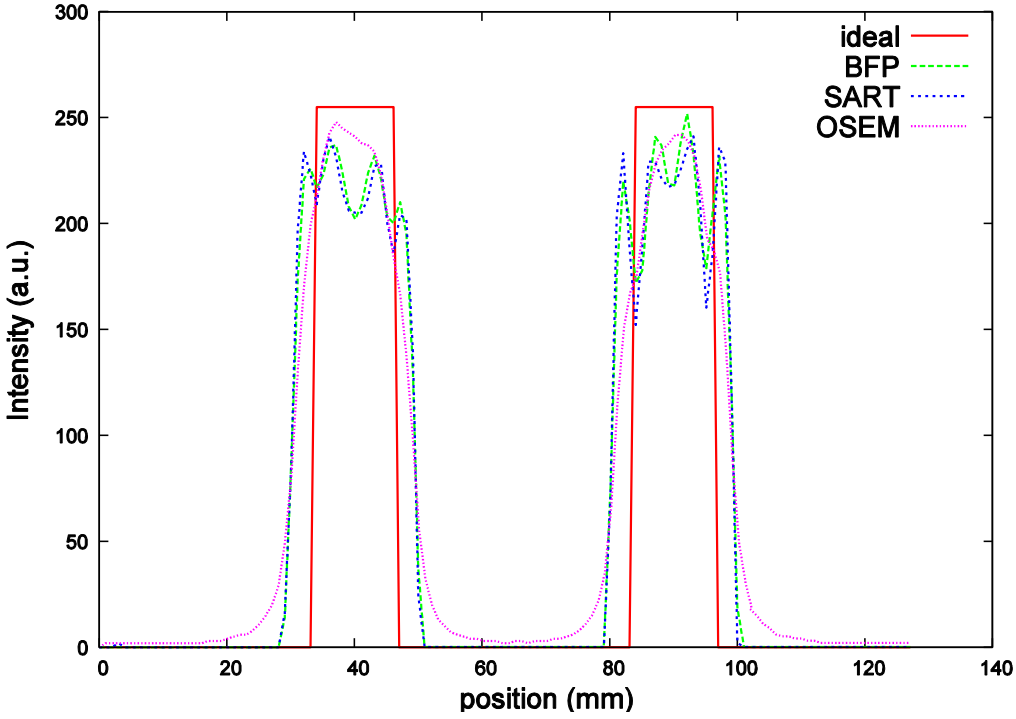

Figure 4.13: Intensity profiles along the horizontal line intercepting the center of both metallic bars (from figure 4.12).

The ideal theoretical cross-section presented in figure 4.12(a) has been calculated from a synthetic representation of the sample. Arbitrarily, using 8-bit encoding imaging, a 256 grey level pixel represents the position of the metallic bars, whereas a 0 grey level pixel stands for the air. It appears that all the reconstruction methods are able to properly localize both metallic bars. However, it

seems that both BFP (Figure 4.12(b)) and SART (Figure 4.12(c)) slightly suffer from noise artifacts around the bars, whereas the OSEM cross-section (Figure 4.12(d)) presents a more uniform background. To investigate into more details the accuracy of the reconstruction, figure 4.13 represents for the ideal case, and the three reconstruction methods, the intensity profiles along the horizontal line intercepting the center of both metallic bars. The profiles show that the three methods are limited by insufficient experimental imaging resolution. Whatever the reconstruction method is, we can observe a spreading of the profile compared to the ideal result. The spreading is slightly intensified in the case of OSEM, which indicates that this method will provide stronger image degradation compared with BFP and SART.

3.4.2. Image Quality According to Projection Number

We analyzed the quality of the reconstruction methods depending upon the number of projections. For this purpose we used a sample consisting of black foam parallelepiped (absorbance $\alpha = 0.02$ cm^{-1}, refractive index 1.1) with a (41×49) mm^2 cross section. The parallelepiped is drilled by two holes (15 mm diameter): one hole with air and another hole filled by a Teflon cylinder (absorbance $\alpha < 1$ cm^{-1}, refractive index 1.45) having a small cylindrical air hole inside (6 mm diameter) (Figure 4.14(a)). For one horizontal cross-section, the acquisition along several angles gives sinogram composed with N_θ lines, corresponding to the number of projections, and N_t columns corresponding to the number of pixels in the horizontal direction. For instance, figure 4.14(b) represents the sinogram acquired with the 110 GHz source with $N_\theta = 72$ projections ($\Delta_\theta = 2.5^\circ$) and $N_t = 128$ horizontal pixels ($\Delta_t = 0.5$ mm). The black colour corresponds to a maximum transmitted signal whereas the white colour indicates a decrease of the transmitted signal. Low signal intensity can be due to either absorption, or deviation of the THz beam due to refraction. Here, owing to the low absorbance of Teflon, mainly refraction losses have to be considered. Before the application of any reconstruction method, this sinogram already reflects the global geometric structure of the sample cross-section with especially the presence of the refracting Teflon material.

Reconstructions are performed using the three methods from sinograms obtained with 12 to 72 projections. Results are shown in figure 4.15. For all reconstruction methods, we can notice that the image quality does not present any significant improvement from 36 to 72 projections. Consequently, the projection number has been limited to 72 in our study. Whatever the reconstruction method is, the black foam parallelepiped, the air hole and the Teflon cylinder are revealed. However, the air hole inside the Teflon cylinder, which appears as sideways T in the reconstructed cross sections, is hardly distinguished owing to the strong refraction experienced by the THz beam at the Teflon cylinder interfaces.

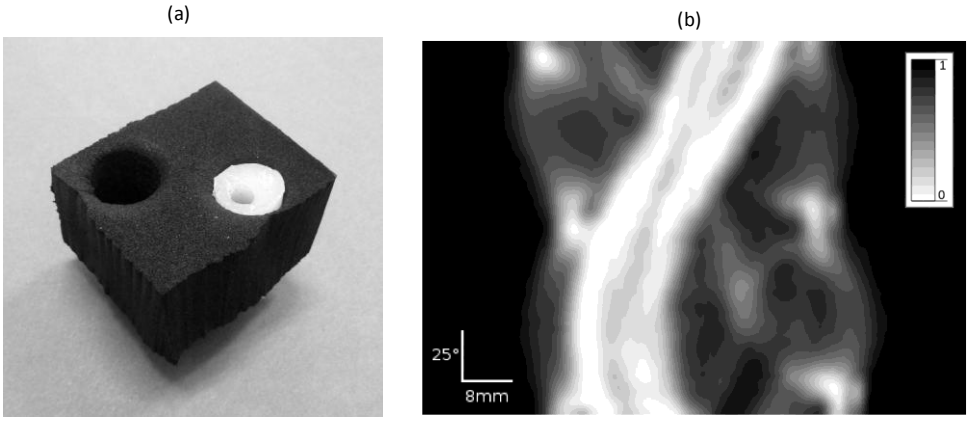

Figure 4.14: (a) Photograph of original object: parallelepiped black foam (41×49) mm^2 with 2 holes, diameter 15 mm (1 hole with air and 1 hole containing a Teflon cylinder with a 6 mm cylindrical air hole inside), (b) Sinogram with $N\theta = 72$ projections (lines) and $N_t = 128$ samples per projection (columns). System acquisition with 110 GHz source.

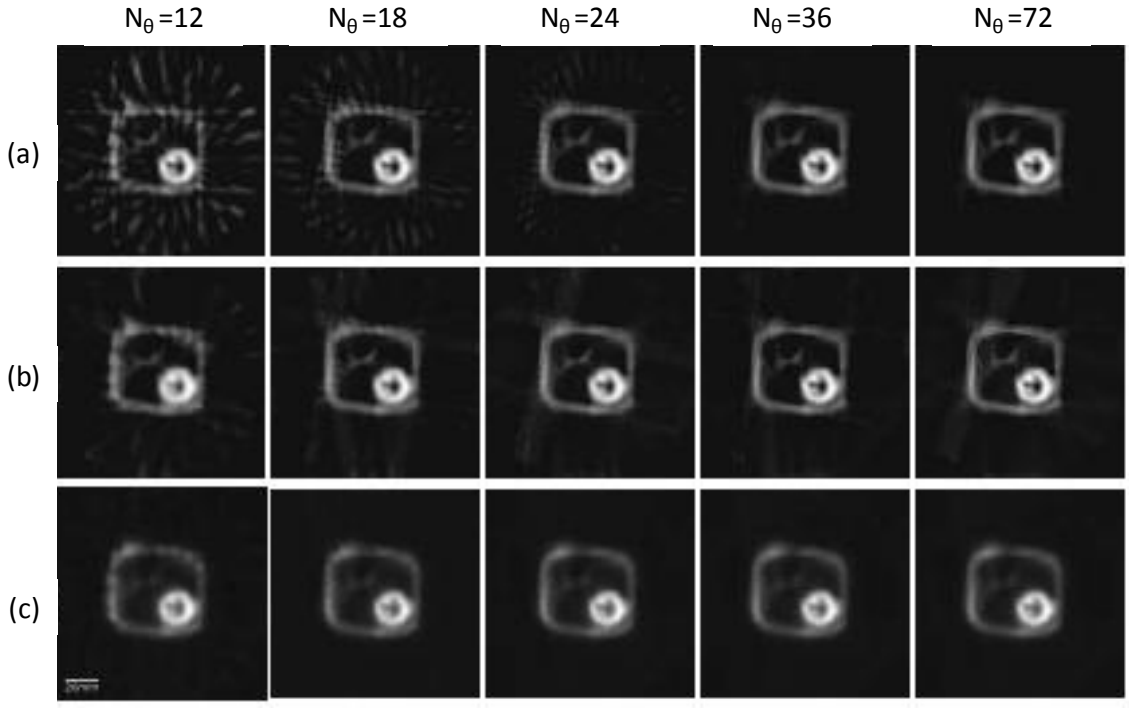

Figure 4.15: Reconstructions using sinograms with 12, 18, 24, 36, 72 projections and the BFP (a), SART (b) and OSEM (c), methods. Same scale has been used for all cross sections.

For BFP, we notice a significant improvement of the reconstruction if the number of projections increases from 12 to 72. Especially, serious background artifacts identified as beam hardening are visible for $N_\theta = 12$. This behaviour is well known in tomography since BFP is very sensitive to the number of projections. For SART, this problem is strongly reduced even if some background artifacts are still noticeable for $N_\theta = 12$. For OSEM, it seems that the reconstruction quality is constant whatever the number of projection taken in the range of 12 to 72. However, as pointed out previously with the two metallic bars, we can observe a small degradation of the reconstruction accuracy for OSEM compared with BFP and SART with blurred contours of the foam

parallelepiped. This degradation is directly connected to the OSEM algorithm which uses a subset of several projections at once with a multiplicative error correction.

3.4.3. Image Accuracy from Qualitative View

The final image quality is also analyzed on a quantitative point of view. Numerically, a complete comparison of BFP, SART and OSEM has already been performed from synthetic digital images [Recur 2010]. It clearly indicates that, if the number of projections is sufficient (to be defined depending on the experimental technique), OSEM image quality is worse (especially contour accuracy) than BFP and SART images. However, in case of THz CT, we are mostly interested in the evolution of the image quality as a function of the projection number. Especially, the key-point concerns the preservation of the image quality for a limited number of projections (typically less than 20 projections). Quantitatively, the image quality can be determined using the structural similarity (SSIM) parameter measured between a reference image *I* and a transformed image *J*. Three comparisons are taken into account for this purpose.

- **Luminosity Comparison**

In CT, the reconstruction has to preserve the intensity which defines the nature of transverse matter. Image luminosity (denoted by $\bar{I}$), is the average pixel intensity value among the whole image. The luminosity correlation l(I,J) between two images I and J is given by:

$$l(I,J) = \frac{2\bar{I}.\hat{J} + C_1}{\bar{I}^2 + \hat{J}^2 + C_1} \tag{4.14}$$

where C_1 is a constant parameter. Tomographic reconstruction quality is characterized by a luminosity correlation close to 1.

- **Contrast Comparison**

Contrast preservation is essential in reconstructed image to distinguish the different transverse areas. The intensity standard deviation σ(I), calculated among all the pixels of the image I, can be used to estimate the image contrast, whose correlation is given by:

$$c(I,J) = \frac{2\sigma(I)\sigma(J) + C_2}{\sigma(I)^2 + \sigma(J)^2 + C_2} \tag{4.15}$$

where C_2=1 generally. A reconstruction is reliable when contrast is equal to 1.

- **Geometric Correlation**

The image geometry is dependent on luminosity and contrast and is given by:

$$s(I) = \sum_{p=1}^{N} \frac{I(p) - \bar{I}}{\sigma(I)} \tag{4.16}$$

The geometric comparison between two images is given by the correlation coefficient r(I,J) as follows:

$$r(I,J) = s(I).s(J) \tag{4.17}$$

The more r(I,J) is close to 1, the more equivalent are the images I and J.

Depending on these quantities the SSIM parameter is given by:

$$SSIM(I,J) = l(I,J).c(I,J).r(I,J) \tag{4.18}$$

where *l(I,J), c(I,J) and r(I,J)* are the intensity, contrast and geometric equivalence rates between two images. This SSIM parameter is generally used to evaluate quantitatively the image quality.

In our study, the image *I* is the reference corresponding to the 72 projection sinogram, whereas the images *J* are reconstructed from N_θ = 12 to N_θ = 36. Table 4.1 details the three equivalence rates obtained by BFP (Table 4.1(a)), SART (Table 4.1(b)) and OSEM (Table 4.1(c)) methods according to the projection number, corresponding to the data obtained by sample shown in figure 4.14 and 4.15. Here, it is important to notice that these tables are independent and cannot be compared to each other since, for each table, the reconstructed image obtained with N_θ = 72 is considered as the reference with all metric values set to unity. However, for each reconstruction method and depending on the projection number, the tables indicate the image degradation with respect to the intensity, contrast and geometric preservation. We can notice that all metric values slightly decrease whatever the method, but *r*(*I*, *J*) especially decreases significantly with BFP (indicated in red colour in Table 4.1(a)). Then, the SSIM parameter of BFP is mainly deteriorated because the geometrical aspect of the image is not well preserved. For SART, the global image quality is already optimized with N_θ = 18.

For OSEM, it appears that the method is almost insensitive to the projection number. However, as pointed out previously, we have to keep in mind that this method also provides a general vagueness in the final reconstructed image. For each reconstruction method, the evolution of the SSIM parameter is also represented as a function of the projection number N_θ in figure 4.16. Independently from each others, the curves illustrate the reconstruction quality losses depending on the number of projections.

(a)

N_θ	l	c	r
12	0.965	1.000	0.902
18	0.989	1.000	0.977
24	0.998	1.000	0.995
36	1.000	1.000	1.000
72	1.000	1.000	1.000

(b)

N_θ	l	c	r
12	1.000	0.999	0.973
18	1.000	1.000	0.986
24	0.999	1.000	0.992
36	0.991	1.000	0.994
72	1.000	1.000	1.000

(c)

N_θ	l	c	r
12	0.999	0.999	0.996
18	0.999	1.000	0.999
24	1.000	1.000	0.999
36	1.000	0.999	1.000
72	1.000	1.000	1.000

Table 4.1: Details of the SSIM parameter for BFP (a), SART (b) and OSEM (c). $l(I, J)$: intensity, $c(I, J)$: contrast, $r(I, J)$: geometric equivalence rates. (Red colour indicates significant results).

As previously noticed in Table 4.1, we can remark that the SART and OSEM algorithms compute almost without quality loss whatever the projection number. Inversely, the BFP quality decreases if the projection number is less than 25. This observation is essential in case of THz CT since the projection number is limited owing to the long acquisition time. Here, one can clearly point out that, for a limited number of projection data (typically less than 20), SART and OSEM methods are more appropriated for efficient THz CT.

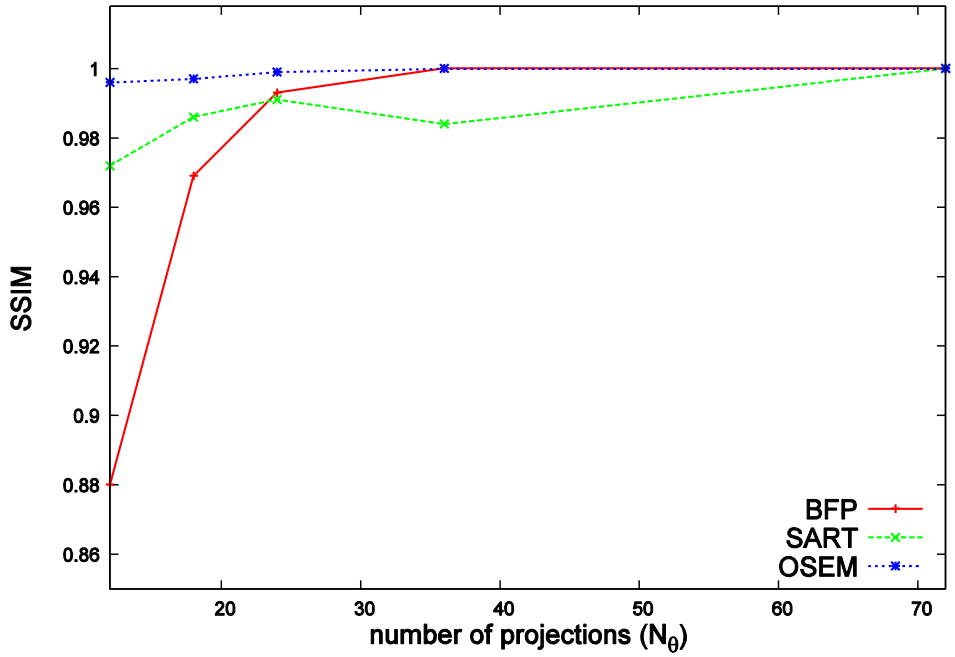

Figure 4.16: Manufactured sample presented in figure 4.14(a), SSIM parameter as a function of the projection number and the reconstruction method.

After a complete description of various reconstruction algorithms and final image quality analysis with calibrated phantoms, finally we will present 3D THz tomography of real samples.

3.5. Complete Volumetric Reconstruction of Objects

Some realistic samples have been investigated in order to test the ability of the CW THz tomographic scanner and the choice of the reconstruction method to properly reconstruct the complete 3D structure of complex objects. Possible applications are non-destructive inspection of manufactured objects, visualization and analysis of internal structures with a non-invasive imaging technique. The first 3D sample, presented in figure 4.17(a), is a white foam parallelepiped (30 mm cube size, $\alpha = 0.1$ cm^{-1}, refractive index 1.15) drilled by two oblique metallic bars (6 mm diameter). The experimental data obtained with the 240 GHz source, correspond to 2D transmission images, with a $\Delta_t = 1$ mm both in the horizontal and vertical directions. The tomography is achieved with a set of 18 projections (rotation angle step $\Delta_\theta = 10^\circ$) representing an acquisition time of nearly 9 hours. Figure 4.17 represents the THz 3D volume reconstruction of the sample obtained by BFP (Figure 4.17(b)), SART (Figure 4.17(c)) and OSEM (Figure 4.17(d)), respectively. Complete 3D videos are available, which correspond to a full 360◦ rotation of the sample.

As revealed in the previous section, since the BFP reconstruction suffers by the lack of projection data, the background surrounding the sample is not uniform with multiple artifacts even if the contours of the parallelepiped and the presence of the two oblique bars are precise. With the SART

method, the background is more uniform even if some high intensity spots are still visible as artifacts. Contour quality is similar to BFP. Finally, as explained in the previous section, OSEM reconstruction is excellent even if the number of projection is limited but the method provides a final image which is more blurred.

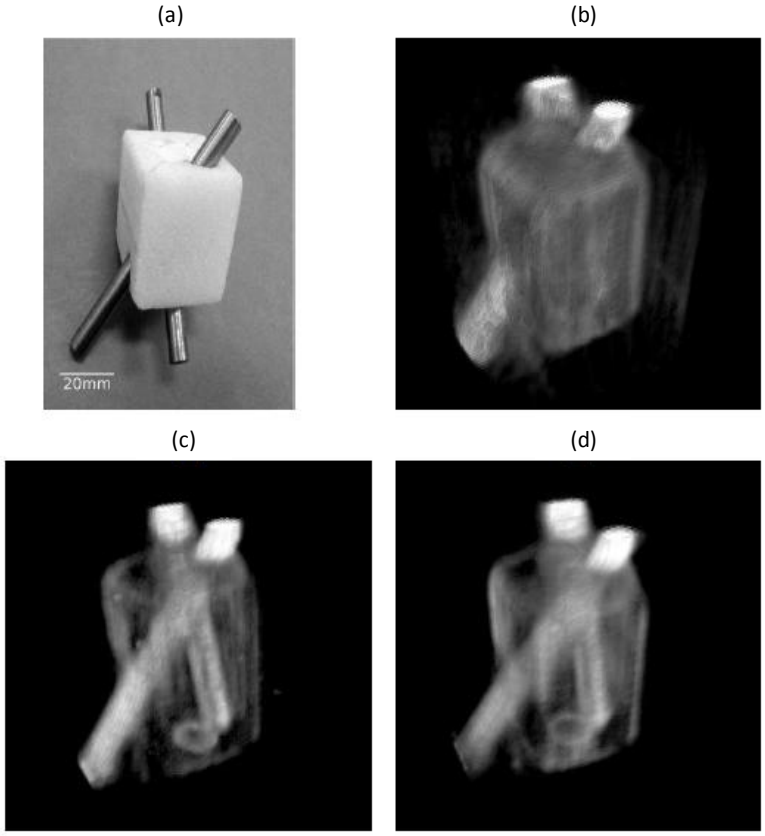

Figure 4.17: White foam parallelepiped (30 mm cube size) drilled by two oblique metallic bars (6 mm diameter). (a) Photograph of the 3D sample, (b) BFP reconstruction, (c) SART reconstruction, (d) OSEM reconstruction. Acquisition performed with a 240 GHz source.

The next sample is a wooden Russian doll *Matriochka* (total height 160 mm, figure 4.18(a). Before starting tomographic measurements, a second smaller doll is positioned inside the main doll. Figure 4.18 represents the 3D object reconstructed with the 110 GHz source (from a set of 18 projections). The THz 3D video recordings of the sample volume reconstruction (Figure 4.18(b) for BFP), Figure 4.18(c) for SART, Figure 4.18(d) for OSEM) clearly reveal the shape of the outer doll and the presence of the smaller doll inside the main doll (measured size 95 mm). This example of 3D reconstruction of complex object emphasize on the potential of the SART method which provides high quality contour and reasonable artifacts despite the insufficient number of projections.

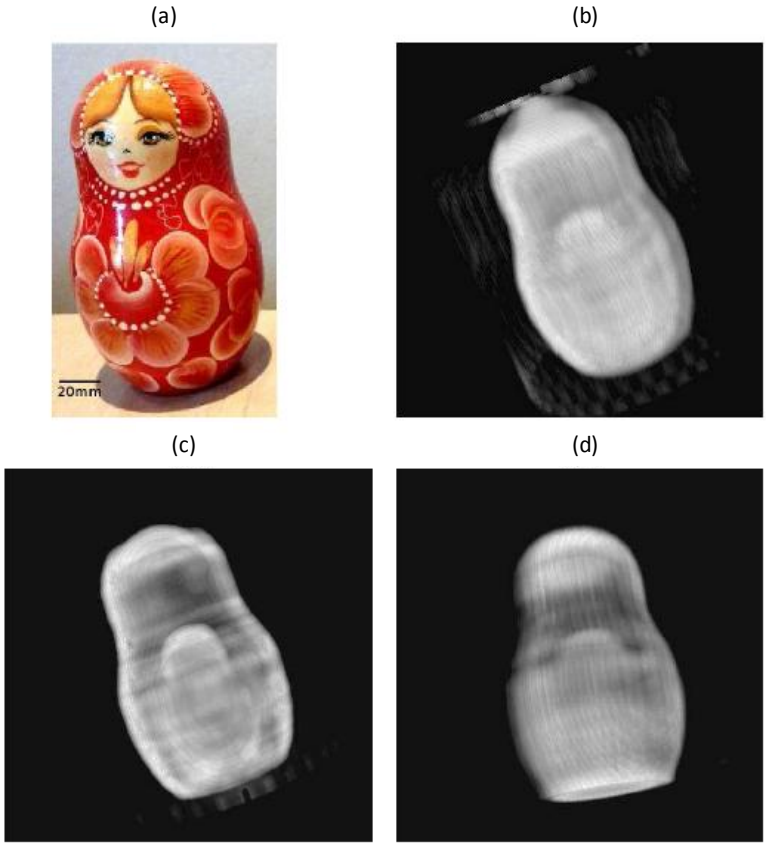

Figure 4.18: Wooden Russian doll *Matriochka* (total height 160 mm). (a) Photograph of the 3D sample. (b) BFP reconstruction, (c) SART reconstruction, (d) OSEM reconstruction (Acquisition with the 110 GHz source).

3.6. Tomography of Historical Art Objects

Finally, after presenting the potential of this compact tomographic system with possible reconstruction methods, we applied it for evaluating the volumetric structure of historical objects from Museum of Aquitaine. Here, we present the results concerning two Egyptian potteries already described in chapter 3. The tomography has been completed by rotating the object (Figure 3.27(a)) in a turned upside down position around the vertical axis, in order to reveal the 3D geometrical aspects of both solid and mobile contents, previously identified using 2D THz imaging.

Figure 4.19 presents the tilted series obtained from 18 projections (Δ_θ = 10°). From these projection data, we were able to reconstruct and visualize the volume of the jar. Here the SART method has been selected for 3D reconstruction.

Figure 4.19(a) represents the 3D THz recording of the complete jar obtained with a volume rendering software. From the reconstruction, the internal volume of the jar has been estimated to 650 cm^3. With the volume rendering software, it is also possible to visualize independently the different parts of the object. Figure 4.19(b) presents the 3D THz video recording of the bottom solid contents of the jar with an estimated volume of 125 cm^3. Moreover, the 3D reconstruction makes it possible to reveal a trough in the central part of the contents, which was not visible from the 2D THz

images presented in chapter 3. Finally, figure 4.19(c) presents the 3D THz video recording of the deformable mobile contents with an estimated volume of 25 cm^3. As explained previously, from the tilted series and the 3D reconstructions, we can measure the dimensions of the fixed and mobile contents of the jar and the global thickness of the pottery wall.

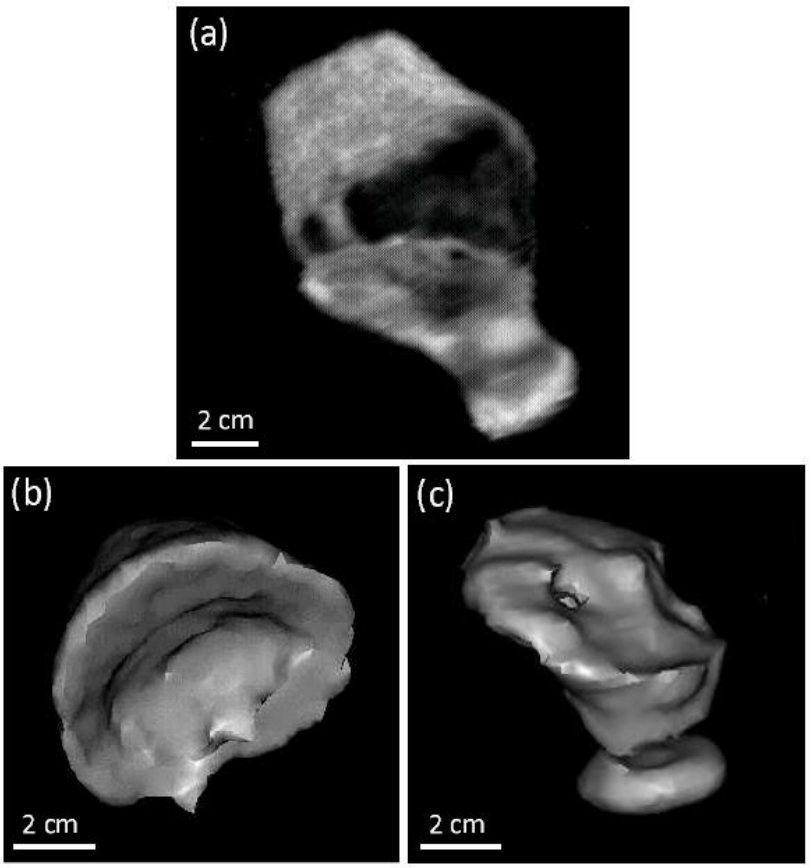

Figure 4.19: 3D THz CT of the Egyptian jar (inventory number 8608) turned upside down. (a) Complete 3D reconstruction of the jar, (b) 3D reconstruction of bottom jar content, (c) 3D reconstruction of mobile content.

Assuming that the thickness of the pottery wall varies from 5 to 8 mm, we first can estimate at 110 GHz absorption coefficients α of the wall jar according to the expression Absorbance = α*l*, where *l* is the distance THz wave travels through the materials. For the pottery wall, taking into account measurement uncertainties, we found $\alpha = 1.3 \pm 0.3$ cm^{-1}, the large uncertainty coming from the difficult evaluation of the wall thickness owing to the limited transverse spatial resolution. Taking into account this wall absorbance, we can finally deduce the 110 GHz absorption coefficients of the internal contents.

For the fixed and the mobile contents, taking into account measurement uncertainties, we found the same absorption coefficient: $\alpha = 0.7 \pm 0.15$ cm^{-1}. This result indicates that the fixed and

mobile contents could be constituted of the same material, even if its nature remains unknown. As previously explained, according to Egyptologists, these contents could consist of residual dried materials, probably organic, resulting from possible funerary offerings. At present, to further investigate the pottery's origin, the irreversible opening of the jars would be necessary in order to perform complementary chemical analysis of the internal contents. After our analysis, we can point out that THz imaging let us know that the jars have to be opened in order to penetrate their secrets deeper.

In short, we presented the potential of CW tomographic scanner for performing 3D volumic analysis of opaque samples. In spite of the existence of severe refraction losses experienced by the millimeter radiation after its transmission through the samples, we were able to reconstruct the cross-sectional views of sample. After, comparing with the commonly used BFP reconstruction algorithm, we pointed out the ability of the SART and OSEM algorithms to properly reconstruct cross-sectional images. In the end, we demonstrated the potential of the system for possible applications in non-destructive inspection and art material analysis.

Conclusion

In this chapter we have demonstrated the ability of THz radiation for a complete 3D visualization scan of volumetric objects. Severe diffraction and refraction experienced by THz radiation, while interacting through high density materials, can be problematic in the final reconstruction of images. We are able to successfully obtain the cross-sectional images. In case of THz-TDS CT we propose a specific multi-peak averaging procedure for the analysis of THz signal. After presenting THz CT of some calibrated phantoms, we utilized this technique in order to view cross-section of a chicken femur. With the CW system, taking advantage of simpler data acquisition, we have compared various parameters which can play a vital role in the final quality of 3D THz images. With the collaboration of LaBRI, we proposed the utilization of two iterative methods (SART and OSEM) for THz tomographic reconstruction and compared their performance with the standard BFP algorithm. Image accuracy and quality is analyzed as a function of projection numbers and reconstruction methods. Finally, we can state that THz CT tomography can be utilized beside existing technologies like X-ray CT, in order to provide complementary information about the 3D scan of sample in a complete non-destructive manner. We also proved that THz CT can be useful in art science and archeology.

Summary

Here, we will summarize the main results presented in preceding chapters obtained with the developed THz-TDS and CW imaging systems. Then we will propose ideas for systematic progress and future improvements.

Section 1: Conclusion

THz imaging was determined to be a robust tool for the non-destructive evaluation of multilayered materials and volumetric opaque objects. THz imaging has advantage over several other evaluation techniques because of its penetration depth, transparency and lower absorption in addition to wide spectral bandwidth. Two principal imaging architectures (pulsed THz-TDS system and millimeter CW system) were developed for performing THz imaging.

THz-TDS imaging technique has the ability to gather material dependent spectroscopic information about the sample. In addition, the time-of-flight of THz electric field allows one to obtain image data that provide information about the thickness, composition and structure of the surface and hidden layers. Far infrared transmission spectra of several graphite pencil leads on paper have been measured up to 2 THz using THz-TDS system. The observation of the gradual absorption depending on the graphite proportion has been assessed for different pencils from hard to soft black-marking graphite leads. The resulting graphite transmittance is used to perform two-dimensional transmission THz imaging of written documents.

Multilayered painting samples and various artists' medium were also investigated with the THz-TDS system. The spectral properties of several modern paint pigments were obtained and spectroscopic regions of interest were determined in order to aid in their identification in multi-spectral images of artworks. THz time-of-flight technique was utilized in order to resolve sketches and paintings embedded beneath both paint and plaster, and to determine the thickness of painting layers. The quality of the imaged artworks was dependent on the contrast of the spectral responses of the media with respect to each other as well as absorption of the covering layers. THz-TDS imaging is also applied for non-destructive evaluation of original seals. Pragmatic analysis of the spectral properties of these materials shows that the THz absorbance is sufficient low to analyze spectral properties of foreign inclusion and see under a thick layer of old basic materials in relation to official written documents. This study can be particularly useful in the preservation and restoration of the interested seals and propose a tool to preserve old archives for participating in this immense vast cultural patrimony.

A monochromatic CW imaging system has also been used to investigate historical artworks. The system is easy-to-align, low-cost and portable which represents a major advantage compared to

standard time-domain spectroscopic imaging. We demonstrated the potential of this portable CW imaging system for the investigation of historic samples preserved at the museum of Aquitaine (France). In particular, 2D and 3D analysis have been performed in order to reveal the internal structure of nearly 3500 years old sealed Egyptian jars. THz experiments reveal the presence of solid content attached to the bottom of jar and confirm another mobile content inside the internal cavity, with their respective absorbance.

Afterwards, we presented CT analysis of complex shape targets causing important refraction losses by pulsed THz-TDS system. We found that severe refraction of the THz beam makes it difficult to properly interpret the THz signal. By proposing a specific procedure based on a multi-peak averaging analysis, we were able to reconstruct the cross-sections of various samples. Taking into account the simplicity of CW imaging system, we investigated the reconstruction methods applied to THz CT. We pointed out the ability of the SART and OSEM algorithms for reconstructing cross-sectional images and compared final image quality with existing BFP method. The SART method applied to THz CT obtains equivalent accuracy and quality than BFP. However, for a limited number of projections (less than 25), we noticed a quantitative degradation of the BFP reconstruction whereas SART and OSEM methods can already offer an optimized reconstruction quality. These quantitative results, well known in standard tomography such as X-Ray CT, are here pointed out for THz CT imaging, which provides a new insight for the improvement of 3D THz imaging.

Section 2: Perspectives

For the THz-TDS system, the door is wide open for further exploration and application of non-destructive THz imaging skills in various fields. Taking advantage of this research work, our group was able to launch a European project DOTNAC for the development and optimization of THz non-destructive techniques for aeronautics composites having multilayered structures.

In the field of art science, since the ultimate goal of non-destructive measurements is to extract information that will aid in the contextualization, preservation, and restoration of artifacts, many further applications are wide open for exploration. A complete database of the THz properties of pigments, dyes, binding media, varnishes, substrates and other commonly used art materials is necessary for the full THz spectral range. This will promote the identification of composition using principle component analysis. In collaboration with curators and art scientists, for example from C2RMF: Centre de Recherche et de Restauration des Musées de France, future work may include THz imaging of real master artworks. One application of THz reflection imaging could be for instance the analysis of the preparation layer (e.g. gesso) to determine its composition, thickness and homogeneity.

More generally, further analysis includes THz spectroscopy of old pigments and binders to definitely help art historians and curators in the preservation of our cultural heritage.

The results of tomographic measurements by THz-TDS imaging system, presented in this thesis were very preliminary. Many options for further exploration are opened. A thorough study comparing various data processing techniques in order to minimize refraction losses and enhance image reconstruction quality should be done. Various other parameters in time and frequency domain should be explored for THz image reconstruction in order to get maximum information about the sample. THz CT in the reflection geometry should also be explored which can be significantly more complex than in transmission mode.

THz CW imaging scanner offers a wide range of potential applications favored by its simple and portable nature. After this initial development phase conducted by the close collaboration between LOMA (Laboratoire Ondes et Matière d'Aquitaine) and ALPhANOV (Centre Technologique Optique et Lasers) for the application of CW scanner to inspect artwork, several other collaborative projects are now under progress. The research work includes industrial projects to facilitate various component analysis and the development of a THz camera for real-time THz imaging. Also an interdisciplinary project "Tera-scan" funded by CNRS will be devoted for the analysis of antiques and archaeological objects. This work in collaboration with archaeologists, aims to demonstrate non-invasive and non-destructive 2D and 3D CW imaging to inspect safely historical objects. 3D THz scanner is ready to further analyze scientifically objects from our cultural heritage, preserved in the Museums. For instance in the continuity of the Egyptian pottery analysis presented in this thesis, it can be used for the non-invasive analysis of canopic jars used as containers by the Egyptians to store and preserve the viscera during the rituals of mummification. Other objects that can be investigated include wall paintings and other environmentally-damaged archaeological sites, oxidized metalwork, fragile objects (manuscripts, tapestries, etc.) and enclosed objects (coffins, pottery, etc.).

Appendices

Terahertz dielectric characterisation of photopolymer resin used for fabrication of 3D THz imaging phantoms

A. Younus, P. Desbarats, S. Bosio, E. Abraham, J.C. Delagnes and P. Mounaix

Terahertz time-domain spectroscopy (THz-TDS) measurements have been performed to characterise a photopolymer resin (FullCure Materials®) in the 0.1–3.5 THz range. A loss tangent less than 7% has been revealed up to 1.5 THz along with a weak frequency dependence of the real part of the optical index and the dielectric permittivity. This study underlines the promising applications of such a material for the fabrication of 3D THz imaging phantoms in the 0–1.5 THz range.

Introduction: For imaging purpose and owing to the abundance of relevant technological devices, short wavelength radiations such as infrared, visible light and X-rays are frequently used to meet the Rayleigh criterion. Nevertheless, between microwave and infrared frequencies lies now the well-known terahertz (THz) radiation. Recently, terahertz time-domain spectroscopic (THz-TDS) imaging has become an interesting new tool for low-energy, nondestructive testing and other applications. Since the first demonstration of THz transmission imaging [1], several promising THz imaging techniques have emerged such as reflection tomography [2], computed tomography [3], near-field imaging [4], CW imaging [5], real-time imaging [6] and spectroscopic imaging. THz waves offer attractive features such as good penetration depth, low scattering, low photon energy and broad spectral bandwidth. Furthermore, the availability of coherent optical imaging has made THz imaging an attractive non-contact, non-ionising method for a variety of applications. For example, with a time domain spectrometer (THz-TDS), to obtain such data, a terahertz beam is raster scanned across an object along two spatial dimensions (x, y) and a time-domain transmitted terahertz field E(t) is recorded at each spatial co-ordinate in reflexion or transmission configuration. If the refractive index of the material under investigation is well known, then the time domain data can be converted to a third spatial dimension (z). There are many similarities between terahertz pulsed imaging in reflexion mode and optical coherence tomography (OCT). They both provide 3-D information over a similar size scale by converting time information into depth information.

In the field of nondestructive testing, security analysis and biomedical applications, it is mandatory to visualise with a high fidelity and accuracy the samples not only in two but also in three dimensions. The calibration and the resolution of the imaging setup might be optimised using a so-called 'phantom object'. Moreover, it is sometimes difficult to directly analyse the objects, especially for biomedical or anthropology domain where samples are difficult to obtain or manipulate. In such a situation, an alternative solution consists in modelling a 3-D reproduction of the object of interest.

In this case, the complementary work for 3-D imaging development is the precise calibration using the well-defined (calibrated) phantom. The calibration aims at minimising the re-projection error, i.e. the error between the detected phantom marker locations in the acquired projection image and the projected marker locations. In particular, this approach involves preliminary determination of the THz dielectric function of the phantom material. Recently, 3-D printing systems provide an elegant way to elaborate high-quality 3-D prototyping with fine details. Moreover, since they are UV polymerised, models produced are durable. In the work reported in this Letter, with a THz-TDS system, we imaged a sample and characterised the dielectric properties of a photopolymer resin used with a 3-D printing system for the fabrication of imaging phantoms. Refractive index, absorption properties, permittivity and dielectric loss tangent have been measured from 0.1 to 3.5 THz [7].

Sample: Phantom samples were modelled using a commercial printing system designed for professional rapid prototyping applications. Printing with a high accuracy of ultra-thin 16 µm layers, this system produces phantom models with exceptionally fine details without any surface treatment such as polishing or waxing. For this printer, the maximum building size is 260 × 260 × 200 mm and the printer resolution is 42 µm (x-axis), 84 µm (y-axis), 16 µm (z-axis).

The family of FullCure Materials® [8] is acrylic-based photopolymer materials. The wide variety of resins within the FullCure family, including transparent, coloured, opaque, flexible and rigid properties, enables models that meet a wide range of fits, forms and functions with an unlimited array of complex geometries including overhangs and undercuts. The mechanical values of the FullCure resin are well established [8]. After 3-D printing, no post-processing is required since the phantom model is fully cured.

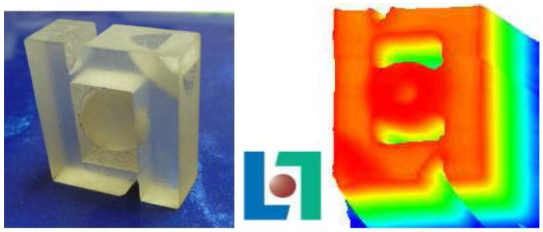

Fig. 1 *Example of complex forms obtained with 3-D printer*
3-D logo of LaBRI realised with transparent FullCure 720 and 2-D THz image of sample

All these properties make this material very appealing for 3-D THz imaging and motivate our study on the dielectric properties of the FullCure resin in the THz bandwidth. We tested two different samples within the FullCure product: the transparent FullCure® 720 (the 2-D THz LaBRI Lab image in Fig. 1) and the VeroWhite. For spectroscopy experiments, each sample consists of a photopolymerised resin slab of 20 × 20 × e mm with e equal to 1 and 2 mm.

Technique: The femtosecond THz pulse spectrometer consists of a Kerr-lens modelocked Ti-sapphire laser yielding 80 fs pulses at 76 MHz repetition rate. For THz emission, an InAs surface field emitter was employed and a 3.5 THz bandwidth was obtained. After collimation with a set of off-axis parabolic mirrors, the THz beam was focused within the sample and the transmitted beam was measured by photoconductive sampling. The whole THz beam diameter waist was estimated to be about 2 mm at the sample position. Finally, this setup makes it possible to measure a THz frequency response in the 0.1–3.5 THz range.

The determination of the frequency-dependent complex dielectric constant of the sample is achieved by computing the complex ratio between the transmitted amplitude spectrum and the spectrum of the reference pulse. In that manner, the refractive index $n(\omega)$ and the absorption coefficient $\alpha(\omega)$ can be simultaneously extracted with:

$$\alpha(\omega) = \frac{4\pi f}{c} k(\omega) \tag{1}$$

where f, c and $k(\omega)$ are the frequency, the light velocity in air and the extinction coefficient, respectively. More details on the procedure can be found in [9]. Finally, the complex permittivity ε is deduced from:

$$\varepsilon = \varepsilon' - i\varepsilon'', \quad \varepsilon' = n^2 - k^2, \quad \varepsilon'' = 2nk \tag{2}$$

where the complex index of refraction is $n^* = n - ik$. The extracted data precision is estimated to be 3% for the refractive index mainly due to thickness uncertainty and 5% for the absorption coefficient $\alpha(\omega)$ [10].

Results: Fig. 2 shows the measured amplitude of the Fourier transform waveforms obtained with and without the sample. Multiple echoes have been taken into consideration within the transfer function if necessary (see [9] and references therein). Our results clearly demonstrate a strong absorption above 1.5 THz. Straightforward calculations give an almost constant and extremely flat value for the refractive index of 1.65 +/− 0.05 between 0.1 to 2.5 THz. We believe that the refractive index variation is due to the small variation of the computed refractive index or may arise from sample inhomogeneities or irregular interfaces. The extinction coefficients (imaginary part of n^*) of all samples remain less than the value of 0.07 for frequencies up to 2 THz (not shown in Fig. 2).

Fig. 3 shows the absorption coefficient for each photoresin. We observed a significant increase of absorption against frequency and we can empirically fit this variation as $\alpha = 0.2 + 3.48\ X + 7.69\ X^2$ with α in cm^{-1} and X varying between 0 and 2 THz. For each photoresin, we also plotted the dielectric tangent losses $\tan\delta = \varepsilon''/\varepsilon'$. Since we did not know precisely the chemical content of the resin, we adopted this pragmatic approach to provide users with an idea of the resin

dielectric behaviour at terahertz wavelength. The dielectric constant will be affected by these relatively high dielectric tangent losses (about 7%) and would probably limit the thickness of the samples in a transmission imaging configuration. Nevertheless, these materials could be used to elaborate a complex shape system such as an integrated matrix of lenses in the millimetre and sub-millimetre wavelength with a lateral dimension between 50 to 300 μm for example.

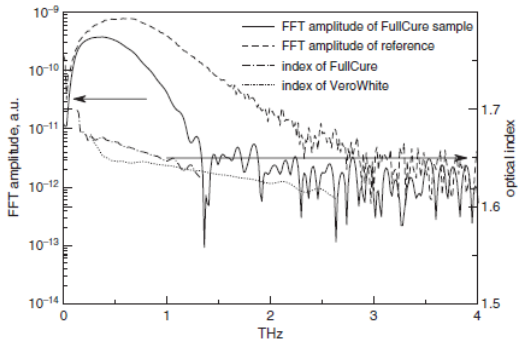

Fig. 2 *FFT amplitude of reference signal and transmitted signal through photoresin under investigation (optical index against frequency for both materials also shown)*

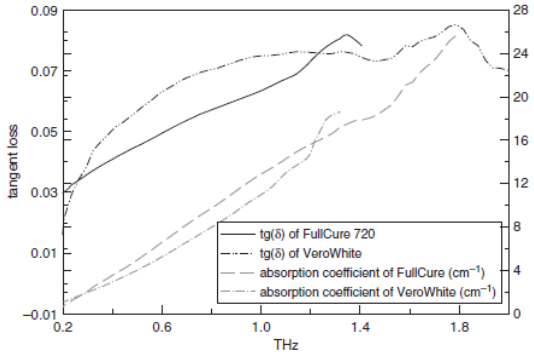

Fig. 3 *Measured tanδ and absorption coefficient against frequency for two different photoresin materials*

Conclusion: We have presented THz-TDS measurements on photopolymer resin for 3-D THz imaging. We demonstrated that these materials present a flat dependence of the optical index in the THz range (from 0.1 to 2.5 THz). The tangent dielectric losses tanδ is less than 7% in the sub-millimetre wavelength. These dielectric properties augur that FullCure photoresin would be an interesting material for the fabrication of phantoms for millimetre and terahertz imaging. It could be very convenient since 3-D system printers produce models with exceptionally fine details since it supplies an elegant solution for the accurate building of any geometry for terahertz engineering.

13 March 2009
doi: 10.1049/el.2009.0688

A. Younus, S. Bosio, E. Abraham, J.C. Delagnes and P. Mounaix (*Centre de Physique Moléculaire Optique et Hertzienne (CPMOH), Université Bordeaux, I UMR CNRS 5798, 351 Cours de la Libération, Talence cedex 33405, France*)

E-mail: p.mounaix@cpmoh.u-bordeaux1.fr

P. Desbarats (*LaBRI – Laboratoire Bordelais de Recherche en Informatique, Université de Bordeaux, 1 UMR 5800, 351 Cours de la Libération, Talence cedex 33405, France*)

References

1 Hu, B.B., and Nuss, M.C.: 'Imaging with terahertz waves', *Opt. Lett.*, 1995, **20**, p. 1716
2 Mittleman, D.M., Hunsche, S., Boivin, L., and Nuss, M.C.: 'T-ray tomography', *Opt. Lett.*, 1997, **22**, p. 904
3 Ferguson, B., Wang, S., Gray, D., Abbot, D., and Zhang, X.-C.: 'T-ray computed tomography', *Opt. Lett.*, 2002, **27**, p. 1312
4 Hunsche, S., Koch, M., Brener, I., and Nuss, M.C.: 'THz near-field imaging', *Opt. Commun.*, 1998, **150**, pp. 22–26
5 Siebert, K.J., *et al.*: 'Continuous-wave all-optoelectronic terahertz imaging', *Appl. Phys. Lett.*, 2002, **80**, p. 3003
6 Yasui, T., Sawanaka, K.I., Ihara, A., Abraham, E., Hashimoto, M., and Araki, T.: 'Real-time terahertz color scanner for moving objects', *Opt. Express*, 2008, **16**, p. 1208
7 Nguema, E., Vigneras, V., Miane, J.L., and Mounaix;, P: 'Dielectric properties of conducting polyaniline films by THz time-domain spectroscopy', *Eur. Polym. J.*, 2008, **44/1**, pp. 124–129
8 http://www.objet.com
9 Mounaix, P., *et al.*: 'High frequency response in ferroelectric $BaSrTiO_3$ thin films studied by terahertz time domain spectroscopy', *Jpn. J. Appl. Phys.*, 2005, **44**, p. 5058
10 Roman, C., Ichim, O., Sarger, L., Mounaix, L.P., and Vigneras, V.: 'Terahertz dielectric characterisation of polymethacrylimide rigid foam: the perfect sheer plate?', *Electron. Lett.*, 2004, **40**, p. 1167

LABVIEW Program:

Labview (Laboratory Virtual Instrumentation Engineering Workbench) is a platform and development environment for a visual programming language. The purpose of such programming is automating the usage of processing and measuring equipment in any optical setup. Labview is commonly used for data acquisition and instrument control. With the help of an engineer and labview expert William Benharbone, we have developed a specific program code for automatically controlling XYθ motors synchronized with rapid delay line. The program also controls the LIA parameters, communicates with digital oscilloscope, visualizes and stores the THz data. Here we present some screen-shot images of the developed labview program.

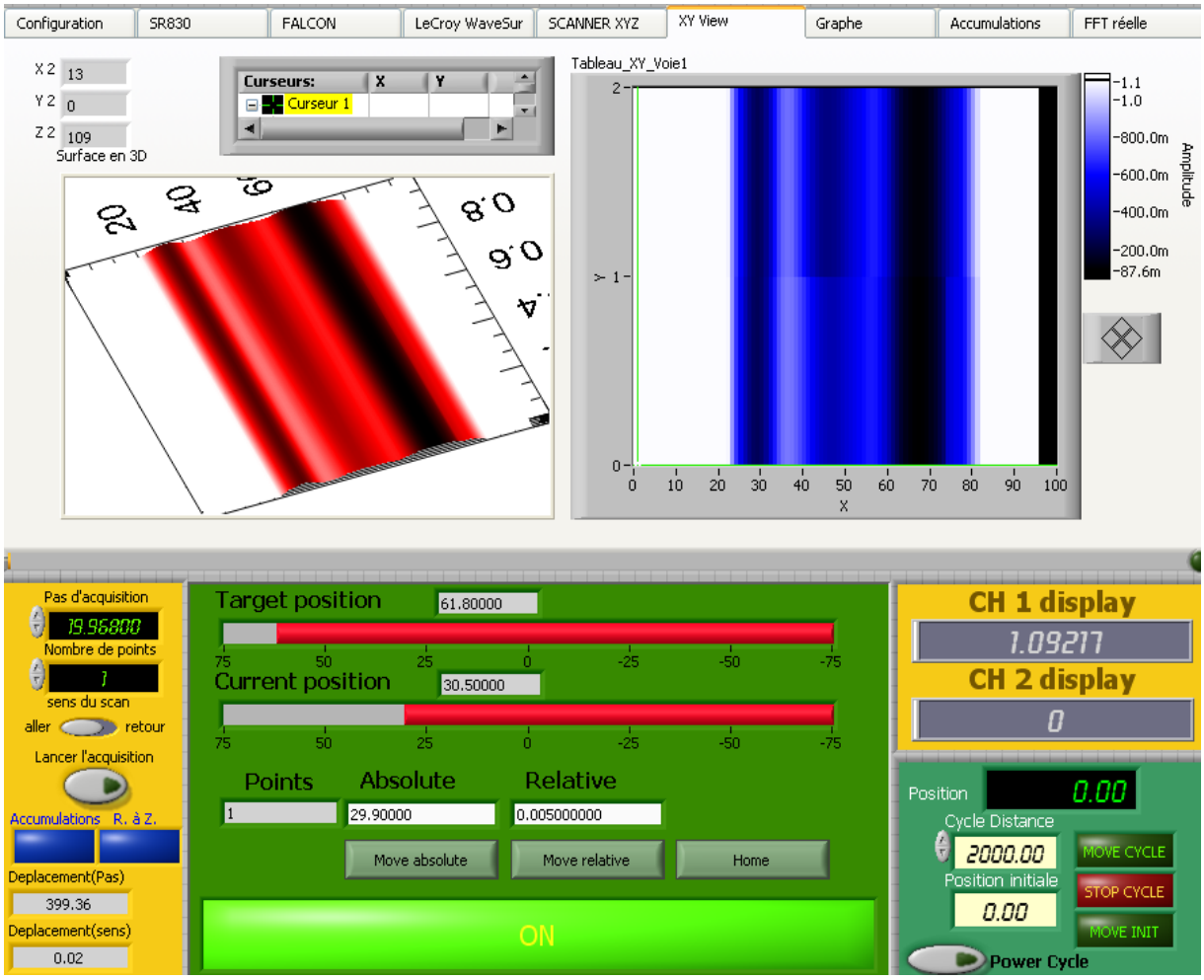

Figure B.1: XY View panel of the Labview program showing the quick 2D THz image during the experiment.

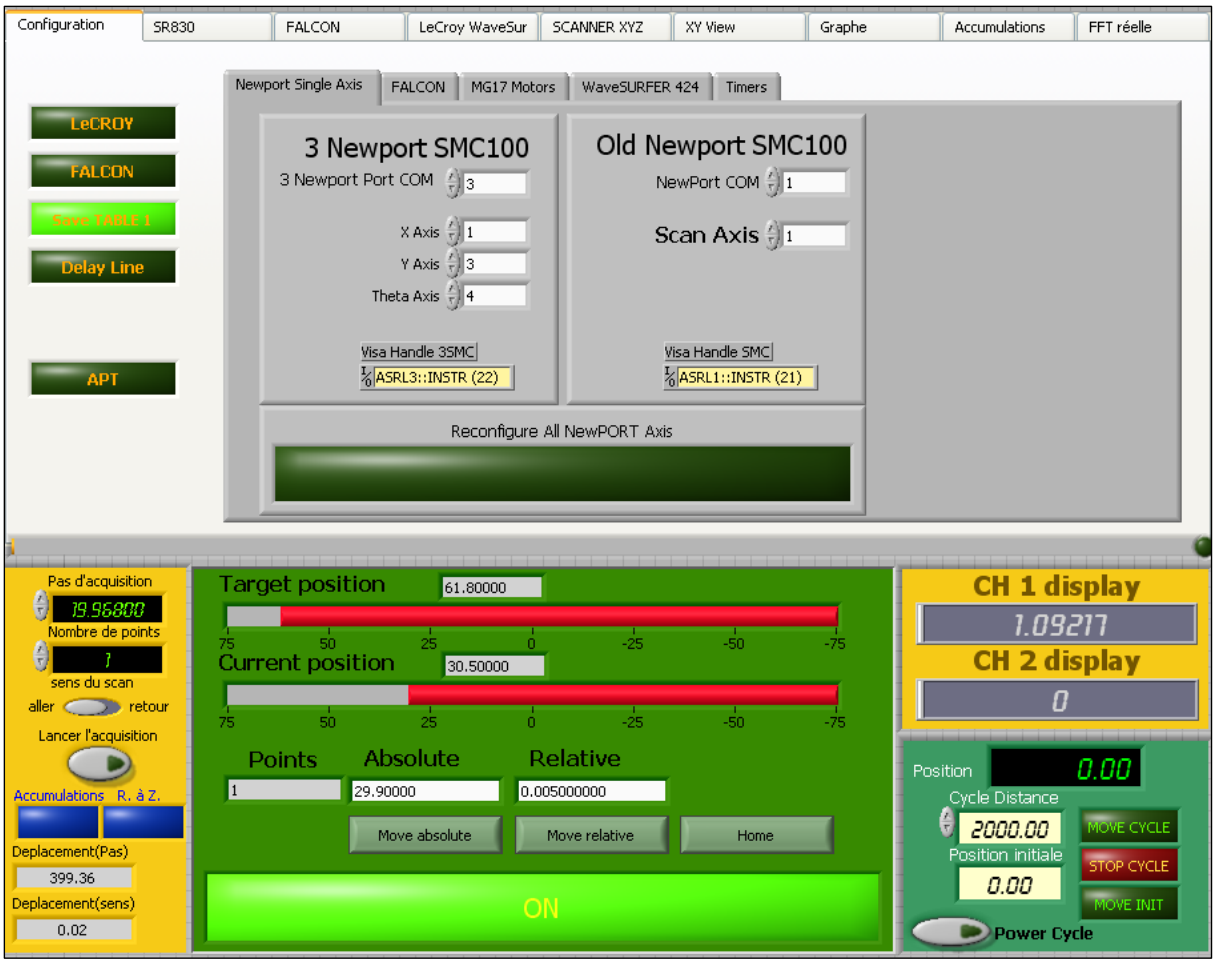

Figure B.2: Configuration panel of the labview program, from where user can command the three translational motors stages (X, Y, θ).

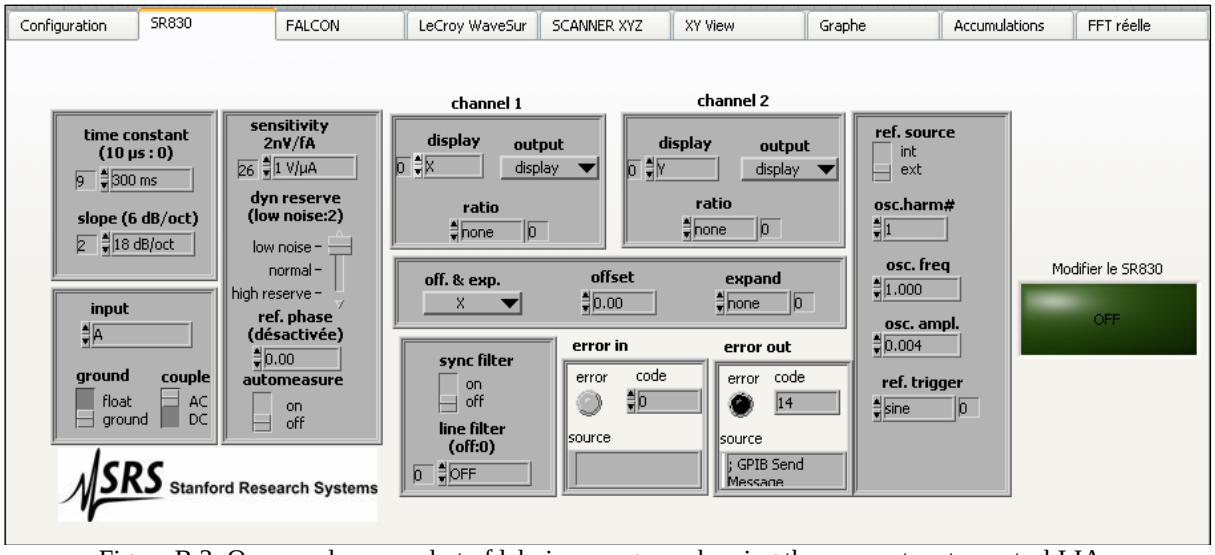

Figure B.3: One panel screen-shot of labview program showing the parameters to control LIA.

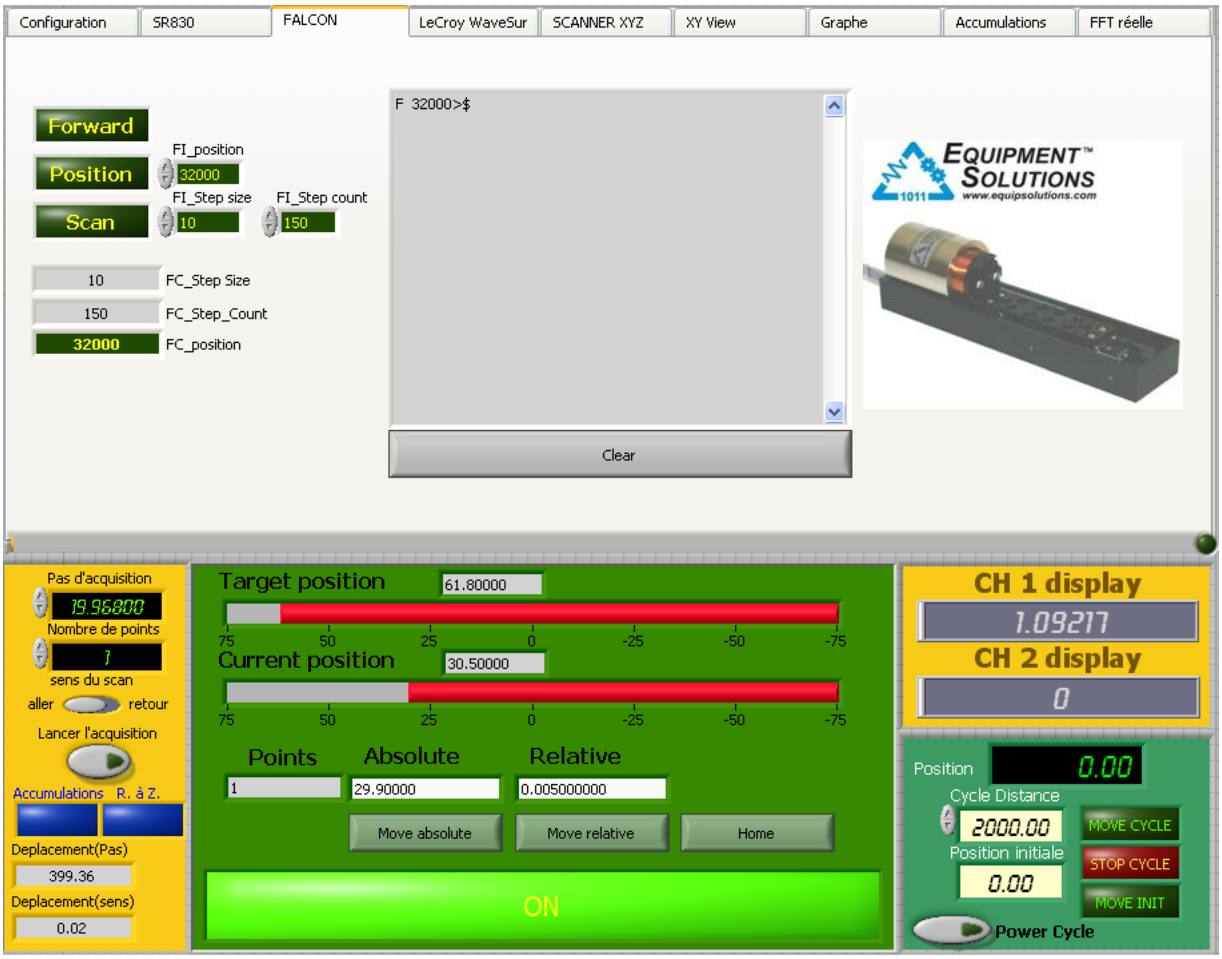

Figure B.4: Screen-shot of another window of labview showing commands to control the fast delay-line motor.

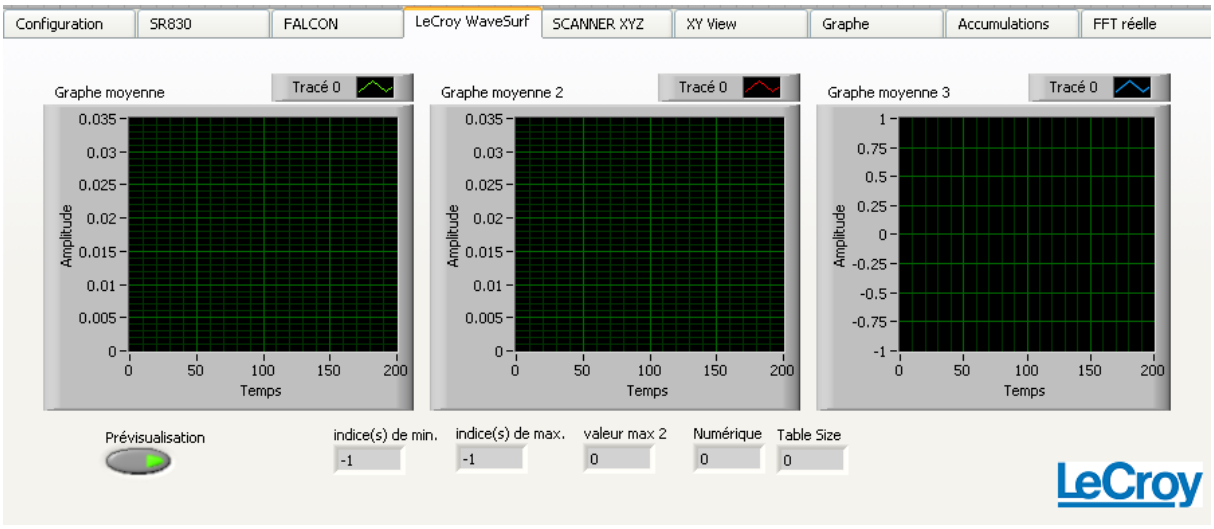

Figure B.5: One panel of labview program, where THz waveforms are displayed after communicating with digital oscilloscope.

Software for THz Data Analysis:

Analyzing THz data and image processing was an important job in this research work. We have utilized various softwares for data processing and signal analysis depending upon their potential and ability. For 2D THz-TDS imaging and spectroscopic analysis we have used Igor and Pk-Graph software respectively, which offer powerful and extensible scientific graphing, data analysis, image processing and programming tool for scientists. For 2D and 3D visualization of THz CW data, we used Image J program which can display, edit, analyze and process multiple image stacks with the ability to form sinograms and volumetric photos. As mentioned earlier, for complete 3D CT reconstruction and formation of cross-sectional images we collaborated with specialists of programming in LaBRI. They specially developed Q-Terahertz program with appropriate filters, smoothing, convolution, contrast manipulation and processing tools to enhance final image quality.

Given below are some screen-shot images of programs utilized for 2D THz image formation and spectroscopic analysis.

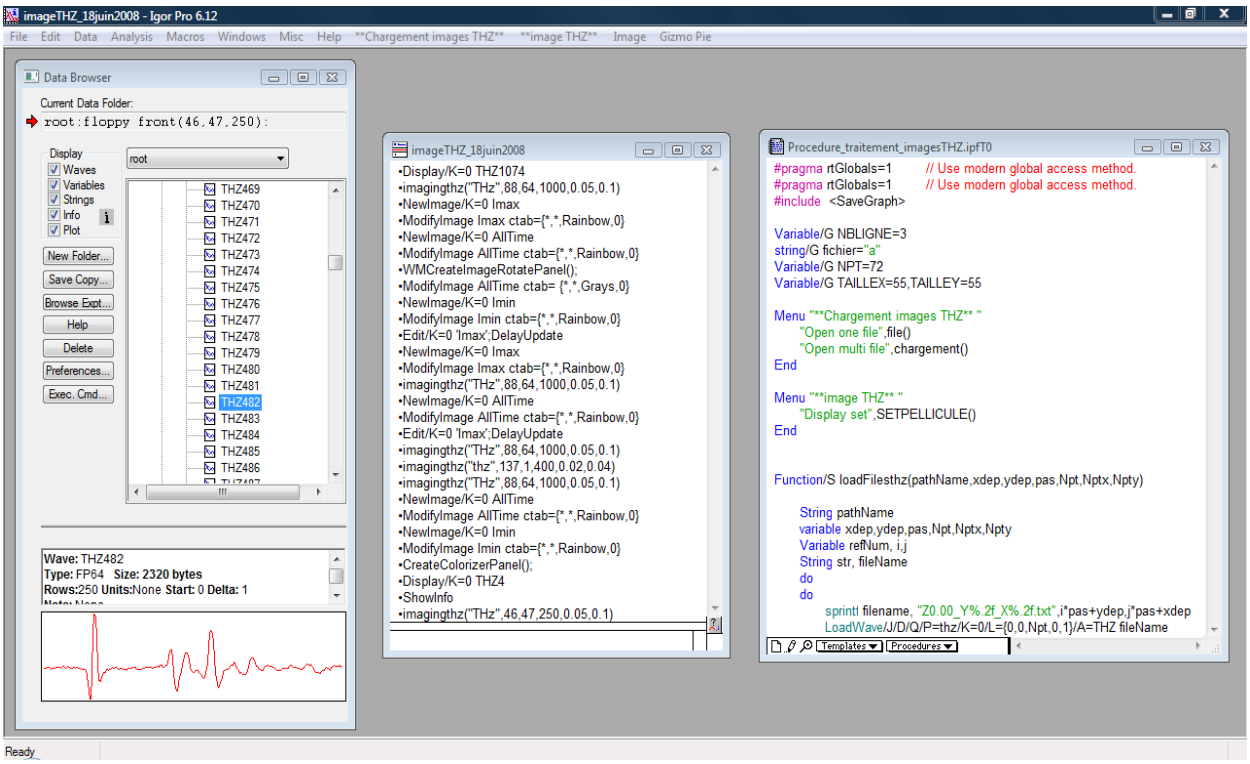

Figure B.6: Screen-shot image of Igor software illustrating the loaded THz data and specific data treatment procedure.

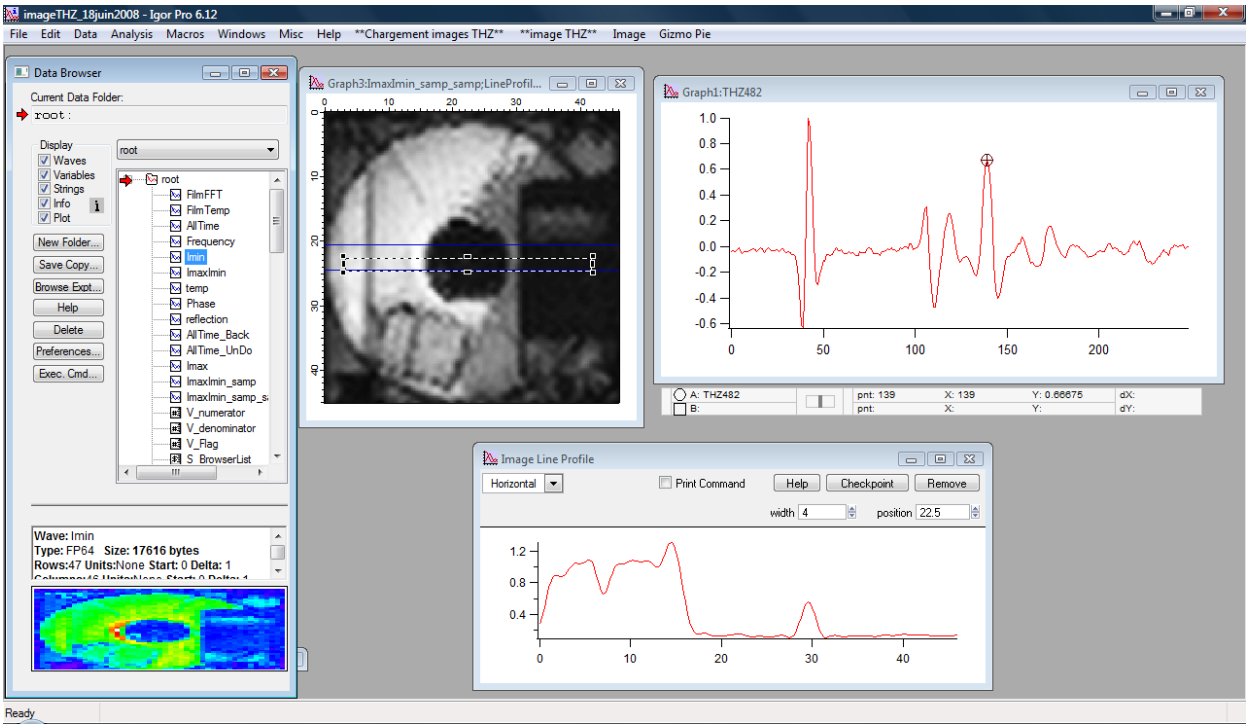

Figure B.7: Another view of the Igor software, showing 2D THz image of a floppy disc with a reflected THz signal.

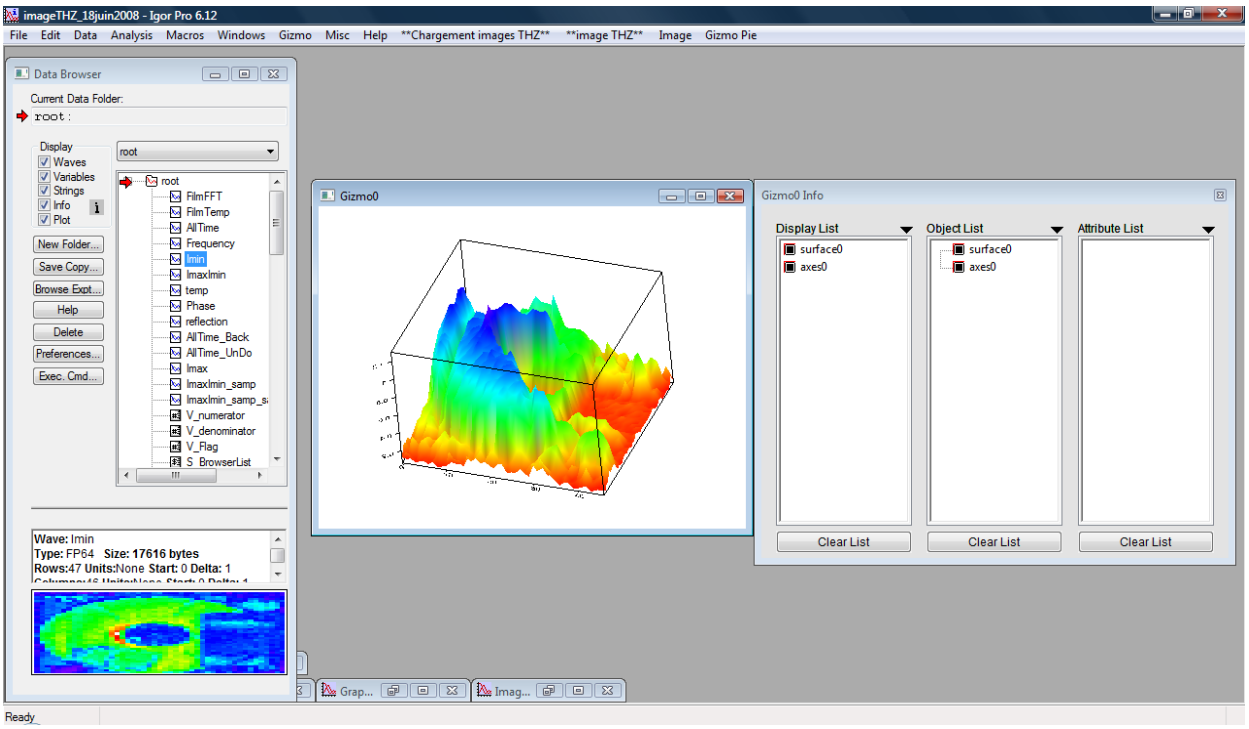

Figure B.8: Igor program is also capable of mapping 3D view of the volumetric sample.

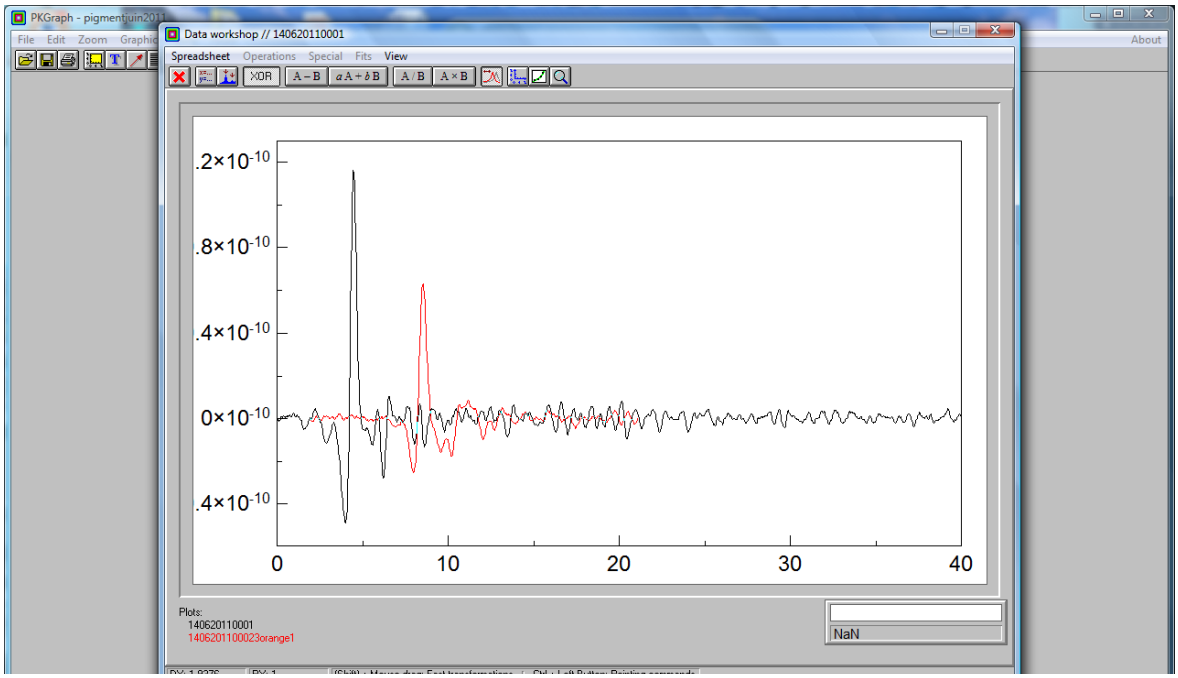

Figure B.9: Screen-shot image of Pk-Graph: Comparison of two THz waveforms to extract spectroscopic information about the sample.

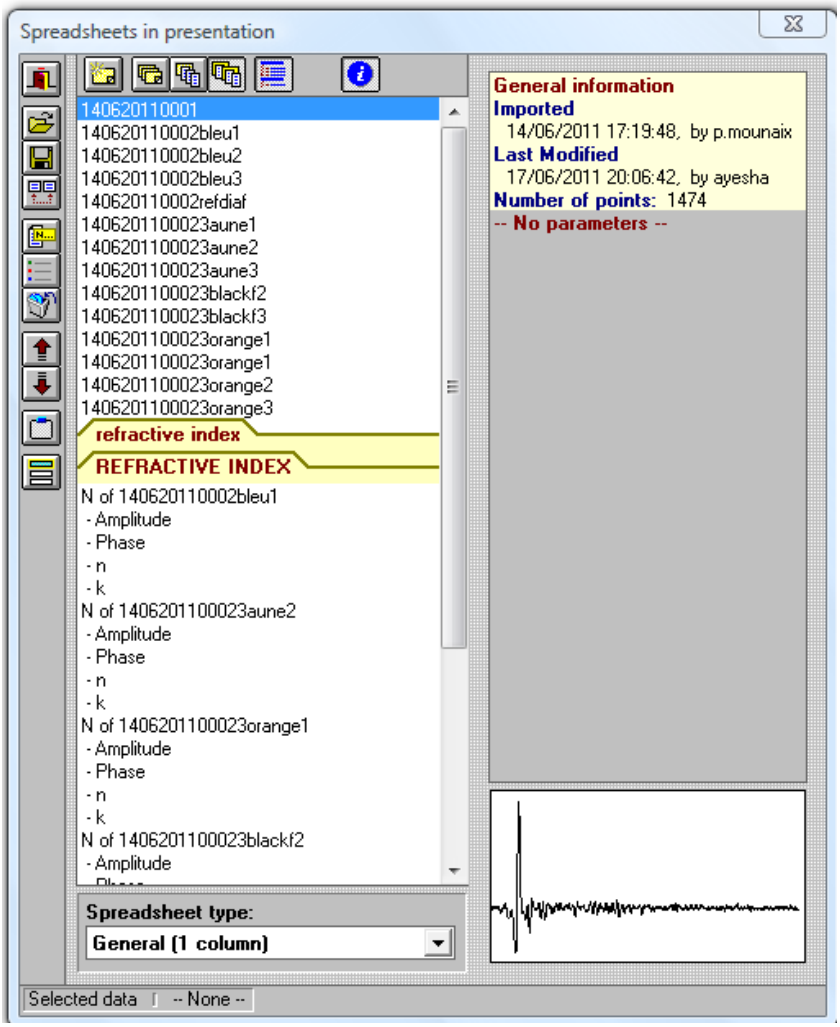

Figure B.10: One window in Pk-Graph software showing the spreadsheet panel having THz data.

Biblography

[Adam 2009] A. J. L. Adam, P. C. M. Planken, S. Meloni, and J. Dik, "Terahertz imaging of hidden paint layers on canvas," Opt. Express 17, 3407-3416 (2009).

[Adomavičius 2005] R. Adomavičius, G. Molis, A. Krotkus, and V. Sirutkaitis, "Spectral dependies of terahertz emission from InAs and InSb," Appl. Phys. Lett. 87, 261101 (2005).

[Aitken 1985] M. J. Aitken, "Thermoluminescence Dating," Academic Press London, (1985).

[Alekseev 2004] K. N. Alekseev, "New approaches to THz Bloch oscillator," Conference Digest of Joint 29th International Conference on Infrared and Millimeter Waves and 12th International Conference on Terahertz Electronics, 163-164 (2004).

[Andersen 1984] A. H. Andersen and A. C. Kak, "Simultaneous algebraic reconstruction technique (SART): a superior implementation of the ART algorithm," Ultrason Imaging 6, 81-94 (1984).

[Arecchi 2005] T. Arecchi, M. Bellini, C. Corsi, R. Fontana, M. Materazzi, L. Pezzati, and A. Tortora, "Optical coherence tomography for painting diagnostics," Optical Methods for Art and Archaeology, SPIE-Int. Soc. Opt. Eng. Munich Germany, 278-282 (2005).

[Auston 1975] D. H. Auston, "Picosencond optoelectronic switching and gating in silicon," Appl. Phys. Let. 26, 101-103 (1975).

[Auston 1983] D. H. Auston and P. R. Smith, "Generation and detection of millimeter waves by picosecond photoconductivity," Appl. Phys. Lett. 43, 631-633 (1983).

[Banerjee 2008] D. Banerjee, W. Von Spiegel, M. D. Thomson, S. Schabel, and H. G. Roskos, "Diagnosing water content in paper by terahertz radiation," Opt. Express 16, 9060-9066 (2008).

[Barilaro 2005] D. Barilaro, V. Crupi, D. Majolio, G. Barone, R. Ponterio, "A detailed spectroscopic study of an Italian fresco," Journal of Applied Physics 97, 044907 (2005).

[Barrett 1981] H. H Barrett and W. Swindell, "Radialogical Imaging: The theory of image formation, detection and processing," New York: Academic press (1981).

[Belkin 2008] M. A. Belkin, F. Capasso, F. Xie, A. Belyanin, M. Fischer, A. Wittmann, and J. Faist, "Room temperature terahertz quantum cascade laser source based on

intracavity difference-frequency generation," Appl. Phys. Lett. 92, 201101 (2008).

[Berry 2003] E. Berry, G. C. Walker, A. J. Fitzgerald, N. N. Zinovev, M. Chamberlain, S. W. Smye, R. E. Miles, M. A. Smith, "Do in vivo terahertz imaging systems comply with safety guidelines," J. Laser. Appl. 15, 192-198 (2003).

[Bičiūnas 2009] A. Bičiūnas, V. Pačebutas and A. Krotkus, "Terahertz pulse emission from semiconductor surfaces illuminated by femtosecond Yb: KGW laser pulses," Physics B 404, 3386-3390 (2009).

[Bigourd 2006] D. Bigourd, A. Cuisset, F. Hindle, S. Matton, E. Fertein, R. Bocquet and G. Mouret, "Detection and quantification of multiple molecular species in mainstream cigarette smoke by continous-wave terahertz spectroscopy," Opt. letters. 31 (2006).

[Bjarnason 2004] J. E. Bjarnason, T. L. J. Chan, A.W. M. Lee, M. A. Celis, and E. R. Brown, "Millimeter-wave, terahertz, and mid infrared transmission through common clothing," Appl. Phys. Lett. 85, 519-521 (2004).

[Bosch 1975] B. G Bosch, R. W. H. Engelmann, "Gunn-effect Electronics," Pitman Publishing London (1975).

[Bourne 2008] N. Bourne, R. H. Clothier, M. D'Arienzo and P. Harrison, "The effects of terahertz radiation on human keratinocyte primary cultures and neural cell cultures," Altern. Lab. Anim. 36, 667-684 (2008).

[Brahm 2010] A. Brahm, M. Kunz, S. Riehemann, G. Notni, and A. Tunnermann, "Volumetric spectral analysis of materials using terahertz-tomography techniques," Appl. Phys. B 100, 151-158 (2010).

[Brasier 2006] M. Brasier, N. McLoughlin, O. Green and D. Wacey, "A fresh look at the fossil evidence for early archaean cellular life," Philosophical Transactions of the Royal Society: Biology 361: 1470, 887-902 (2006).

[Brodschelm 2000] A. Brodschelm, F. Tauser, R. Huber, J. Y. Sohn, and A. Leitenstorfer, "Amplitude and phase resolved detection of tunable femtosecond pulses with frequency components beyond 100 THz," Springer Ser. Chem. Phys. 66, 215-217 (2000).

[Brumfiel 2009] G. Brumfiel, "Graphene gets ready for the big time," Nature 458: 7237, 390-391 (2009).

[Brun 2010] M. A. Brun, F. Formanek, A. Yasuda, M. Sekine, N. Ando and Y. Eishii, "Terahertz imaging applied to cancer diagnosis," Phys. Med. Biol. 55, 4615-4623 (2010).

[Bruni 2002] S. Bruni, F. Cariati, L. Consolandi, A. Galli, V. Guglielmi, N. Ludwig and M. Milazzo, "Field and laboratory spectroscopic methods for the identification of

pigments in a northern Italian eleventh century fresco cycle," Applied Spectroscopy 56, 827-833 (2002).

[Burrafato 2004] G. Burrafato, M. Calabrese, A. M. Guieli, S. O. Troja and A. Ziccarello, "ColoRaman Project: Raman and fluorescence spectroscopy of oil, tempera and fresco paint pigments," Journal of Raman Spectroscopy 56, 879-886 (2004).

[Bracewell 1967] R. H. Bracewell and A. C. Riddle, "Inversion of fan beam scan in radio astronomy," Astrophysics Journal 150, 427-434 (1967).

[Calza 2007] C. Calza, M. J. Anjos, S. M. F. MendoncadeSouza, A. Brancaglion, R. T. Lopes, "X-ray microuorescence analysis of pigments in decorative paintings from the sarcophagus cartonnage of an Egyptian mummy," Nucl. Instr. and Meth. B (2007).

[Carr 2002] G. L. Carr, Michael C. Martin, Wayne R. McKinney, K. Jordan, George R. Neil and G. P. Williams, "High power terahertz radiation from relativistic electrons," Nature 420, 153-156 (2002).

[Carroll 1970] J. E Carroll, "Hot Electron Microwave Generators," Edward Arnold Publishers London (1970).

[Carter 1996] H. A. Carter, "The chemistry of paper preservation," Journal of chemical education 73, No.11 (November 1996).

[Casini 1999] A. Casini, F. Lotti, M. Picollo, L. Stefani, and E. Buzzegoli, "Image spectroscopy mapping technique for non-invasive analysis of paintings," Studies in Conservation 44, 39-48 (1999).

[Chan 2007] W. L. Chan, J. Deibel and D. M. Mittleman, "Imaging with T-rays," rep.Prog.phys.70, 1325-1379 (2007).

[Chen 2001] Q. Chen and X-C. Zhang, "Semiconductor dynamic aperture for near-field terahertz wave imaging," IEEE J. Sel. Top. Quantum Electron. 7, 608-614 (2001).

[Chen 2003] H. T. Chen, R. Kersting and G. C. Cho, "Terahertz imaging with nanometer resolution," Appl. Phys. Lett. 83, 3009-3011 (2003).

[Ciesla 2000] C. M. Ciesla, D. D. Arnone, A. Corchia, D. Crawley, C. Longbottom, E. H. Linfield and M. Pepper, "Biomedical applications of terahertz pulse imaging," Proc. SPIE, 3934, 73-81 (2000).

[Clark 2007] R. J. H. Clark, "The scientific investigation of artwork and archaeological artefacts: Raman microscopy as a structural, analytical and forensic tool," Appl. Physics A: Mat. Sci. Processing, 89, No. 4, 833-840 (December 2007).

[Coutaz 2008] J. L. Coutaz, R. Boquet, N. Breuil, L. Chusseau, P. Crozat, J. Denaison, L. Duillarent, G. Gallot, F. Garet, J. F. Lampin, D. Lippens, J. Maneney, P. Mouanix, G. Mouret, and J. F. Roux, "Optoélectronique Térahertz," (2008).

[Delaney 2010] J. K. Delaney, J. G. Zeibel, M. Thoury, R. Littleton, M. Palmer, K. M. Morales, E. R. de la Rie and A. Hoenigswald, "Visible and infrared imaging spectroscopy of Picasso's Harlequin Musician: mapping and identification of artist materials in Situ," Applied spectroscopy 64, No. 6, 584-594 (2010).

[Dekorsy 1993] T. Dekorsy, W. Pfeifer, T. Kutt, and H. Kurz, "Subpicosecond carrier transport in GaAs surface-space-charge-field," Phys. Rev. B 47, 3842 (1993).

[Derrick 1999] M. R. Derrick, D. Stulik and J. M. Landry, "Infrared Spectroscopy in Conservation Science," The Getty Conservation Institute Los Angeles, (1999).

[Dietlein 2006] C. R. Dietlein, A. Luukanen, F. Meyer, Z. Popovic, and E. N. Grossman, "Phenomenology of passive broadband terahertz images," 4th ESA Workshop on Millimetre-wave Technology and Applications, 405-410 (2006).

[Dobroiu 2004] A. Dobroiu, M. Yamashita, Y. N. Ohshima, Y. Morita, C. Otani, and K. Kawase, "Terahertz imaging system based on a backward-wave oscillator," Appl. Opt. 43, 5637-5646 (2004).

[Dougherty 2007] J. P. Dougherty, G. D. Jubic, and W. L. Kiser, "Terahertz imaging of burned tissue," Proc. SPIE 6472 (2007).

[Duvillaret 1996] L. Duvillaret, F. Garet and J-L. Coutaz, "A reliable method for extraction of material parameters in terahertz time domain spectroscopy," IEEE Journal of selected topics in quantum electronics 2, No. 3 (1996).

[Duvillaret 1996] L. Duvillaret, F. Garet and J-L. Coutaz, "A reliable method for extraction of materials parameters in THz time-domian spectroscopy," IEEE J. Sel. Top. Quantum Electron. 2, 739-746 (1996).

[Ebeid 2010] A. Ebeid, S. Rott, E. Talmy, C. Ibarra-Castanedo, A. Bendada and X. Maldague, "Near infrared imaging for multi-polar civilian applications," 10th international conference on quantitative infrared thermography, July 27-30 Québec Canada (2010).

[Eisele 2005] H. Eisele, M. Naftaly and R. Kamouna, "Generation of sub millimeter wave radiation with GaAs TUNNETT diodes and InP Gunn devices in a second or higher harmonic mode," Int. J. Infrared Millim. Waves 26, 1-14 (2005).

[El Fatimy 2009] A. El Fatimy, J.C. Delagnes, A. Younus, E. Nguema, F. Teppe, W. Knap, E. Abraham, P. Mounaix, "Plasma wave field effect transistor as a resonant detector for 1 terahertz imaging applications," Optics Communications 282, Issue 15, 3055-3058 (2009).

[Ewers 2009] B. Ewers, A. Kupsch, A. Lange, B. R. Muller, A. Hoehl, R. Muller and G. Vlm, "Terahertz spectral computed tomography," IEEE 978, 1-2 (2009).

[Faist 1994] J. Faist, F. Capasso, D. L. Sivco, C. Sirtori, A. L. Hutchinson, and A. Y. Cho, "Quantum cascade laser," Science 264: 5158, 553-556 (1994).

[Ferguson 2002] B. Ferguson, S. Wang, D. Gray, D. Abbot, and X.-C. Zhang, "T-ray computed tomography," Opt. Lett. 27, 1312 (2002).

[Ferrer 2005] N. Ferrer and M. C.Sistach, "Characterisation by FTIR Spectroscopy of Ink Components in Ancient Manuscripts," Restaurator 26, 105-117 (2005).

[Filipovic 1993] D. F. Filipovic, S. S. Gearhart, and G. M. Rebeiz, "Double-slot antennas on extended hemispherical and elliptical silicon dielectric lenses," IEEE Trans. Microwave Theory Tech. 41, 1738-1749 (1993).

[Fischer 2006] C. Fischer and I. Kakoulli, "Multispectral and hyperspectral imaging technologies in conservation: current research and potential applications," Reviews in conservation 7, 3-16 (2006).

[Fitzgerald 2006] A. J. Fitzgerald, V. P. Wallace, M. Jimenez-Linan, L. Bobrow, R. J. Pye, A. D. Purushotham and D. D. Arnone, "Terahertz pulsed imaging of human breast tumors," Radiology 239, 533-540 (2006).

[Fleming 1974] J. W. Fleming, "High resolution submilimeter-wave Fourier-transform spectrometry of gases," IEEE Trans. Microwave Theory Tech. 22, 1023 (1974).

[Fujiwara 2003] M. Fujiwara, T. Hirao, M. Kawada, H. Shibai, S. Matsuura, H. Kaneda and M. P. Nakagawa, "Development of a gallium-doped germanium far-infrared photoconductor direct hybrid two-dimensional array," Appl. Opt. 42 21, 66-73 (2003).

[Fukunaga 2007] K. Fukunaga, Y. Ogawa, S. Hayashi, and I. Hosako, "Terahertz spectroscopy for art conservation," IEICE Electron. Express 4, 258-263 (2007).

[Fukunaga 2008] K. Fukunaga, Y. Ogawa, S. Hayashi, and I. Hosako, "Application of terahertz spectroscopy for character recognition in a medieval manuscript," IEICE Electron. Expr. 5, 223-228 (2008).

[Fukunaga 2010a] K. Fukunaga, I. Hosako, Y. Kohdzuma, T. Koezuka, M.-J. Kim, T. Ikari, X. Du, "Terahertz analysis of an east asian historical mural painting," Jour. of EOS: Rapid publications 5, 10024 (2010).

[Fukunaga 2010b] K. Fukunaga, and M. Picollo, "Terahertz spectroscopy applied to the analysis of artists materials," Appl. Phys. A. 100, No. 3, 591-597 (2010).

[Gaidis 2000] M. C. Gaidis, H. M. Pickett, C. D. Smith, S. C. Martin, R. P. Smith and P. H. Siegel, "A 2.5 THz receiver front-end for spaceborn applications," IEEE Trans. Microwave Theory Technol. 48, 733-739 (2000).

[Gallerano 2008] G. P. Gallerano, A. Doria, E. Giovenale, G. Messina, A. Petralia, I. Spassovsky, K. Fukunaga and I. Hosako, "THz-ARTE: non-invasive terahertz diagnostics for art conservation," Proc. IRMMW-THz, No. T2G2 (2008).

[Gbur 2001] G. Gbur and E. Wolf, "Relation between computed tomography and diffraction tomography," J. Opt. Soc. Am. A 18, 2132 (2001).

[Gebbie 1964] H. A. Gebbie, N. W. B. Stone and F. D. A. Findlay, "A stimulated emission source at 0.34 millimeter wavelength," Nature 202, 685 (1964).

[Giakoumaki 2006] A. Giakoumaki, I. Osticioli and D. Anglos, "Spectroscopic analysis using a hybrid LIB-Raman system," Applied Physics A 83, 537-542 (2006).

[Gold 1997] S. H. Gold, G. S. Nusinovich, "Review of high power microwave source research," Rev. Sci Instrum. 68, 3945 (1997).

[Gora 2006] M. Gora, M. Pircher, E. Goetzinger, T. Bajraszewski, M. Strlic, J. Kolar, C. K. Hitzenberger, and P.Targowski, "Optical coherence tomography for examination of parchment degradation," Laser Chem., Article ID 68679 (2006).

[Gordon 1970] R. Gordon, R. Bender, and G. T. Herman, "Algebraic Reconstruction Techniques (ART) for Three-dimensional Electron Microscopy and X-ray Photography," J. Theor. Biol. 29, 471-481 (1970).

[Grachev 2010] Y. V. Grachev, I. A. Kuklin, I. V. Gerasimov, O. A. Smolyanskay, S. A. Kozlov, and V. G. Bespalov, "Study of how radiation of the frequency range 0.05–2 THz affects biological tissues of various thickness in medical diagnosis," J. Opt. Technol. 77, No. 11 (November 2010).

[Greenwald 1988] Z. Greenwald, D. W. Woodard, A. R. Calawa and L. F. Eastman, "The Effect of a High Energy Injection on the Performance of mm Wave Gunn Oscillators," Solid-State Electronics 31, No. 7, 1211-1214 (1988).

[Gribnikov 2001] Z. S. Gribnikov, R. R. Bashirov, and V. V Mitin, "Negative effective mass mechanism of negative differential drift velocity and terahertz generation," IEEE Journal of Selected Topics in Quantum Electronics 7, No. 4, 630-640 (2001).

[Grossman 2010] E. Grossman, C. Dietlein, J. Ala-Laurinaho, M. Leivo, L. Gronberg, M. Gronholm, P. Lappalainen, A. Rautiainen, A. Tamminen, and A. Luukanen, "Passive terahertz camera for standoff security screening," Applied optics 49, No. 19 (2010).

[Gu 2002] P. Gu, M. Tani, S. Kono, K. Sakai et X.-C. Zhang, "Study of terahertz radiation from InAs and InSb," J. Appl. Phys. 91, 5533 (2002).

[Hahn 2005] O. Hahn, "X-ray fluorescence analysis of iron gall inks, pencils and coloured crayons," Studies in conservation 50, 23-32 (2005).

[Hargreaves 2007] S. Hargreaves and R.A. Lewis, "Terahertz imaging. Materials and methods," J. Mater. Sci. Mater. El. 18, 299-303 (2007).

[Herman 1980] G. T. Herman, "Image Reconstruction From Projections: The Fundamentals of Computerized Tomography," Academic Press Inc. (1980).

[Herman 1995] G. T. Herman, "Image reconstruction from projections," Real-time imaging 1, 3 -18 (1995).

[Hermann 2000] M. Herrmann, M. Tani and K. Sakai, "Display modes in time-resolved terahertz imaging," Japan. J. Appl.Phys. Part 1 39, 6254-6258 (2000).

[Hills 2008] B. Hills, M. D. Thomson, T. Löffler, W. Von Spiegel, C. Am Weg, H. G. Roskos, P. De Maagt, D. Doyle and R. D. Geckeler, "Terahertz profilometry at 600 GHz with 0.5 μm depth resolution," Opt. Express 16, 11289-11293 (2008).

[Hiriyannaiah 1997] H. P. Hiriyannaiah, "X-ray computed tomography for medical imaging," IEEE signal processing magazine, 42-58 (1997).

[Homes 2007] C. C. Homes, G. L. Carr, R. P. S. M. Lobo, J. D. L. Veigne and D. B. Tanner, "Silicon beam splitter for far-infrared and terahertz spectroscopy," Applied optics 46, No. 32 (2007).

[Hounsfield 1973] G. N. Hounsfield, "Computerized transverse axial scanning (tomography): part 1.description of system," British journal of Radiology 46, 1016-1022, (July 1973).

[Hounsfield 1980] G. N. Hounsfield, "Computed medical imaging: Nobel lecture," J. Comput. Assist. Tomogr. 4, 665-674 (1980).

[Hu 1995] B. B Hu and M. C. Nuss, "Imaging with Terahertz waves," Opt. Lett. 20, 1716-1719 (1995).

[Huber 2000] R. Huber, A. Brodshelm, F. Tauser, and A. Leitenstorfer, "Generation and field-resolved detection of femtosecond electromagnetic pulses tunable up to 41 THz," Appl. Phys. Lett. 76, No. 22, 3191-3193 (2000).

[Hubers 2008] H. W. Hubers, "Terahertz heterodyne receivers," IEEE J. Sel.Top. Quant. Electron 14, 378-391 (2008).

[Hudson 1994] H. M. Hudson and R. S. Larkin, "Accelerated image reconstruction using ordered subsets of projection data," IEEE Trans. Med. Imaging 13, 601-609 (1994).

[Hudson 1994] H. M. Hudson and R. S. Larkin, "Accelerated image reconstruction using ordered subsets of projection data," IEEE Trans. Med. Imaging 13, 601-609 (1994).

[Hunche 1998] S. Hunche, D. M. Mittleman, M. Koch and M. C. Nuss, "New dimensions in T-ray imaging," IEICE Trans. Electron. 81, 269 (1998).

[Ishibashi 1997] T. Ishibashi, N. Shimizu, S. Kodama, H. Ito, T. Nagatsuma, and T. Furuta, "Uni-traveling-carrier photodiodes," Incline Village, NV USA (1997).

[Ishihara 2006] K. Ishihara, K. Ohashi, T. Ikari, H. Minamide, H. Yokoyama, J. Shikata, and H. Ito, "Terahertz wave nearfield imaging with subwavelength resolution using surface-wave-assisted bow-tie aperture," Appl. Phys. Lett.89, 201120 (2006).

[Jackson 2008] J. B. Jackson, M. Mourou, J. F. Whitaker, I. N. Duling III, S. L. Williamson, M. Menu, and G. A. Mourou, "Terahertz imaging for non-destructive evaluation of mural paintings," Opt. Commun. 281, 527-532 (2008).

[Jackson 2009] J. B. Jackson, M. Mourou, J. Labaune, J. F. Whitaker, I.N. Duling III, S. L. Williamson, C. Clavier, M. Menu, G. A. Mourou, "Terahertz pulse imaging for tree-ring analysis: a preliminary study for dendrochronology applications," Meas. Sci. Technol. 20, 075502 (2009).

[Jahns 1990] J. Jahns and S. J. Walker, "Two-dimensional array of diffractive microlenses fabricated by thin film deposition," Appl. Opt. 29, 931-936 (1990).

[Jansen 2010] C. Jansen, S. Wietzke, O. Peters, M. Scheller, N. Vieweg, M. Salhi, N. Krumbholz, C. Jördens, T. Hochrein, and M. Koch, "Terahertz imaging: applications and perspectives," Applied optics 49, No. 19 (July 2010).

[Javidi 2000] B. Javidi and T. Nomura, "Securing information by use of digital holography," Opt. Lett. 25, No. 28 (2000).

[Jepsen 1995] P. Jepsen and S. R. Keiding, "Radiation patterns from lens coupled terahertz antennas," Opt. Lett. 20, 807-809 (1995).

[Jepsen 1996] P. U. Jepsen, R. H. Jacobsen, and S. R Keiding, "Generation and detection of terahertz pulses from biased semiconductor antennas," J. Opt. Soc. Am. B 13, 2424 (1996).

[Jepsen 2011] P. Jepsen, D. G. Coke and M. koch, "Terahertz spectroscopy and imaging-modern techniques and application," laser photonic rev.5, No.1, 124-166 (2011).

[Ji 2006] T. Ji, M. Ge, W. Wang, Z. Zhang, X. Yu, H. Xu, "Characteristics of some members of carbon family in terahertz region," He Jishu/ Nuclear Techniques 29, 561-564 (2006).

[Jiang 1998] Z. Jiang and X-C. Zhang, "Single-shot spatio temporal terahertz field imaging," Opt. Lett. 23, 1114-16, (1998).

[Jiang 1999] Z. Jiang and X-C. Zhang, "2D measurement and spatio-temporal coupling of few-cycle THz pulses," Opt. Express 5, 243-248 (1999).

[Johnson 2001] J. L. Johnson, T. D. Dorney and D. M. Mittleman, "Enhanced depth resolution in terahertz imaging using phase-shift interferometry", Appl. Phys. Lett. 78, 835-837 (2001).

[Johnston 2002] M. B. Johnston, D. M. Whittaker, A. Corchia, A. G. Davies, and E. H. Linfield, "Simulation of terahertz generation at semiconductor surfaces," Phys. Rev. B 65, 165301 (2002).

[Karpowicz 2005] N. Karpowicz, H. Zhong, C. Zhang, K. Lin, Jenn-Shyong Hwang, J. Xu, and X.-C. Zhang, "Compact continuous-wave sub-terahertz system for inspection applications," Applied physics letters 86, 054105 (2005).

[Kaufman 1987] L. Kaufman, "Implementing and accelerating EM algorithm for positron emission tomography," IEEE transactions on medical imaging 6, 37-51 (1987).

[Kawase 2003] K. Kawase, Y. Ogawa and Y. Watanabe, "Non-destructive terahertz imaging of illicit drugs using spectral fingerprints," Opt. Express 11, 2549-2554 (2003).

[Kawase 2004] K. Kawase "Terahertz imaging for drug detection and large-scale integrated circuit inspection," Opt. Photonics News 15, 34-39 (2004).

[Kawase 2005] K. Kawase, Y. Ogawa, H. Minamide and H. Ito, "Terahertz parametric sources and imaging applications," Semiconductor Science and Technology 20, 258-265 (2005).

[Kitahara 2010] H. Kitahara, M. Tani, and M. Hangyo, "Three-Dimensional Tomographic Imaging in Terahertz Region," Japanese Journal of Applied Physics 49 (2010).

[Klatt 2010] G. Klatt, F. Hilser, W. Qiao, M. Beck, R. Gebs, A. Bartels, K. Huska, U. Lemmer, G. Bastian, M. B. Johnston, M. Fischer, J. Faist, and T. Dekorsy, "Terahertz emission from lateral photo-Dember currents," Opt. Express 18, 4939-4947 (2010).

[Knap 2002] W. Knap, Y. Deng, S. Rumyantsev, J.-Q. Lu, M. S. Shur, C. A. Saylor and L. C. Brunel, "Resonant detection of sub-terahertz radiation by plasma waves in the submicron field effect transistor," Appl. Phys. Lett. 80, 3433-3435 (2002).

[Knap 2009] W. Knap, M. Dyakonov, D. Coquillat, F. Teppe, N. Dyakonova, J. Lusakowski, K. Karpierz, M. Sakowicz, G. Valusis, D. Seliuta, I. Kasalynas, A. El Fatimy, Y. M. Meziani, and T. Otsuji, "Field effect transistors for

terahertz detection: physics and first imaging applications," J. Infrared Milli. Terahz. Waves 30, 1319-1337 (2009).

[Ko 2008] Y. Ko, S. Sengupta, S. Tomasulo, P. Dutta, and I. Wilke, "Emission of terahertz-frequency electromagnetic radiation from bulk Ga*x*In1−*x*As crystals," Physical review B 78, 035201 (2008).

[Köhler 2006] W. Köhler, M. Panzer, U. Klotzach, S. Winner, M. Helm, F. Rutz, C. Jördens, M. Koch, and H. Leitner, "Non-destructive investigation of paintings with THz-radiation," P. Europ. Conf. N-Destr. Test. P181 (2006).

[Komiyama 1982] S. Komiyama, "Far-infrared emission from population-inverted hot-carrier system in p-Ge," Phys. Rev. Lett. 48, 271 (1982).

[Kono 2000] S. Kono, P. Gu, M. Tani, and K. Sakai, "Temperature dependence of terahertz radiation from n-type InSb and n-type InAs surfaces," Appl. Phys. B 71, 901 (2000).

[Kono 2001] S. Kono, M. Tani, P. Gu and K. Sakai, "Detection of up to 20 THz with a low temperature grown GaAs photoconductive antenna gated with 15 fs light pulses," Appl. Phys. Lett. 77, 4104-4106 (2001).

[Kouzuma 2003] Y. Kouzuma, T. Koezuka, M. Sawada, X. Du, and X. Du, "Non destructive analysis of wall paining fragment of Dazhao Monastrey," P. Ann. Meet. J. Soc. Cons. Cult. Prop. (2003).

[Kreisler 2000] A. J. Kreisler and A. Gaugue, "Recent progress in high-temperature superconductor bolometric detectors: from the mid-infrared to the far-infrared THz range," Superconductor Science and Technology 13, 1235-1245 (2000).

[Labaune 2010] J. Labaune, J. B. Jackson, S. Pags-Camagna, I. N. Duling, M. Menu, and G. A. Mourou, "Papyrus imaging with terahertz time domain spectroscopy," Appl. Phys. A. Materials Science and Processing 100, No. 3, 607-612 (2010).

[Lee 2006] A. W. M. Lee, B. S. Williams, S. Kumar, Q. Hu and J. L. Reno, "Real-time imaging using a 4.3-THz quantum cascade laser and a 320 × 240 microbolometer focal-plane array," IEEE Photon. Technol. Lett. 18, 1415-1417 (2006).

[Lewis 2006] R. A. Lewis, M. L. Smith, R. Mendis and R. E. M. Vikers, "THz generation in InAs," Physics B, 376-377, 618-621(2006).

[Liu 2006] K. Liu, J. Xu, T. Yuan, and X. C. Zhang, "Terahertz radiation from InAs induced by carrier diffusion and drift," Phys. Rev. B 73, 155330 (2006).

[Löffler 2007] T. Löffler, T. May, C. Weg, A. Alcin, B. Hils and H. G. Roskos, "Continuous-wave terahertz imaging with a hybrid system," Appl. Phys. Lett. 90 (2007).

[Luukanen 2008] A. Luukanen, L. Grönberg, T. Haarnoja, P. Helistö, K. Kataja, M. Leivo, A. Rautiainen, J. Penttilä, J. E. Bjarnason , E. N. Grossman, C. R. Dietlein and M. D. Ramirez, "Passive THz imaging system for stand-off identification of concealed objects: results from a turn-key 16 pixel imager," Proc. SPIE 6948 (2008).

[Maev 2006] R. G. Maev, R. E. Green, and A. M. Siddiolo, "Review of Advanced Acoustical Imaging Techniques for Nondestructive Evaluation of Art Objects," Research in Nondestructive Evaluation 17, 191-204, (2006).

[Manceau 2008] J-M. Manceau, A. Nevin, C. Fotakis and S. Tzortzakis, "Terahertz time domain spectroscopy for the analysis of cultural heritage related materials," Applied Physics B 90, 365-368 (2008).

[Mann 2006] C. Mann, "A compact real time passive terahertz imager," Proc. SPIE 6211, 6211-6214 (2006).

[Minin 2000] I. V. Minin and O. V. Minin, "System of microwave radiovision of three-dimensional objects in real time," Proc. SPIE. Int. Soc. Opt. Eng. 4129, 616 (2000).

[Mitrofanov 2001] O. Mitrofanov, M. Lee, J. W. P. Hsu, I. Brener, R. Harel, J. Federici, J. D. Wynn, L. N. Pfeiffer and K. W. West, "Collection-mode near-field imaging with 0.5-THz pulses," IEEE J. Sel. Top. Quantum Electron.7, 600-607 (2001).

[Mittleman 1997] D. M. Mittleman, S. Hunsche, L. Boivin and M. C. Nuss, "T-ray tomography", Optics Letters 22, No. 12, 904-906 (1997).

[Mittleman 1998] D. M. Mittleman, R. H. Jacobsen, R. Neelamani, R. G. Baraniuk and M. C. Nuss, "Gas sensing using terahertz time-domain spectroscopy," Applied Physics B 67, 379-390 (1998).

[Morigi 2010] M. P. Morigi, F. Casali, M. Bettuzzi, R. Brancaccio and V. D. Errico, "Application of X-ray computed tomography to cultural heritage diagnostics," Appl. Phys. A 100, 653-661 (2010).

[Morris 1977] R. Morris and Y. R. Shen, "Theory of far infrared generation by optical mixing," Phys Rev. A 15, 1143-1156 (1977).

[Mueller 2000] E. R. Mueller, J. Fontanella, R. Henschke, "Integrated Far-Infrared Laser System for NASA/Goddard Space Flight Center," 11th International Symposium on Space Terahertz Technology, Ann Arbor, MI (2000). Available at http://www.coherentinc.com/downloads/NASA-Goddard.pdf.

[Nagai 2004] N. Nagai and R. Fukaswa, "Abnormal dispersion of polymer films in the THz frequency," Chem.phys. let. 338, 479-482 (2004).

[Nagai 2009] M. Nagai, M. Jewariya, Y.Ichikawa, H. Ohtake, T. Sugiura, Y. Uehara, and K. Tanaka, "Broadband and high power terahertz pulse generation beyond

excitation bandwidth limitation via $\chi^{(2)}$ cascaded processes in $LiNbO_{3,}$" Opt. Express 17, 11543-11549 (2009).

[Nagatsuma 2003] T. Nagatsuma, A. Hirata, T. Minotani, A. Sasaki, Y. Hirota, and T. Ishibashi, "High-power photonic millimetre wave generation at 100 GHz using matching-circuit-integrated uni-travelling-carrier photodiodes," Opto electronics, IEE Proceedings 150, 138-142 (2003).

[Nahata 1999] A. Nahata, J. T. Yardley and T. F. Heinz, "Free-space electro-optic detection of continuous-wave terahertz radiation," Appl. Phys. Lett. 75, 2524-2526 (1999).

[Nakajima 2007] S. Nakajima, H. Hoshina, M. Yamashita, C. Otani and N. Miyoshi "Terahertz imaging diagnostics of cancer tissues with a chemometrics technique," Appl. Phys. Lett. 90, 041102 (2007).

[Nguyen 2006] K. L. Nguyen, M. L. Johns, L. F. Gladden, C. H. Worral, P. Alexander, H. E. Beere, M. Pepper, D. A. Ritchie, J. Alton, S. Barbieri, and E. H. Linfield, "Three-dimensional imaging with a terahertz quantum cascade laser," Opt. Express 14, 2123-2129 (2006).

[Nolf 2011] W. D. Nolf, J. Dik, G. V. D. Snickt, A. Wallert and K. Janssens, "High energy X-ray powder diffraction for the imaging of (hidden) paintings," J. Anal. At. Spectrom 26, 910 (2011).

[Ohrstrom 2010] L. Ohrstrom, A. Bitzer, M.Walther, and F. J. Ruhli, "Technical Note: Terahertz Imaging of Ancient Mummies and Bone," American Journal of Physical Anthropology 142, No. 3, 497-500 (2010).

[Ortolani 2011] M. Ortolani, A. Di Gaspare and R. Casini, "Progress in producing terahertz detector arrays," SPIE Newsroom. DOI: 10.1117/2.1201101.003449 (2011).

[Pelagotti 2006] A. Pelagotti, L. Pezzati, A. Piva, and A. Del Mastio, "Multispectral UV fluorescence analysis of painted surfaces," Proc.14th European Signal Processing Conf. EUSIPCO, Firenze Italy, Sept. 4-8 (2006).

[Pelagotti 2008] A. Pelagotti, A. Del Mastio, A. De Rosa, A. Piva, "Multispectral imaging of paintings," IEEE Signal Processing Magazine, July 27-36 (2008).

[Peterson 2008] L. M. Peterson, D. A. Mankoff, T. Lawton, K. Yagle, E. K. Schubert, S. Stekhova, A. Gown, J. M. Link, T. Tewson and K. A. Krohn, "Quantitative imaging of estrogen receptor expression in breast cancer with PET and 18F-fluoroestradiol," J. Nucl. Med. 49, 367-374 (2008).

[Piao 2000] Z. Piao, M. Tani, and K. Sakai, "Carrier dynamics and terahertz radiation in photoconductive antennas," Jpn. J. Appl. Phys. 39, 96 (2000).

[Pickwell 2006] Pickwell and V. P. Wallace, "Biomedical applications of THz technology," J. Phys. D: Appl. Phys. 39, No. 17 (2006).

[Pieraccini 2005] M. Pieraccini, D. Mecatti, G. Luzi, M. Seracini, G. Pinelli and C. Atzeni, "Non-contact intrawall penetrating radar for heritage survey: the search of the `Battle of Anghiari' by Leonardo da Vinci," NDT and E International 38, Issue 2, 151-157 (March 2005).

[Pinna 2009] D. Pinna, M. Galeotti, and R. Mazzeo, "Scientific Examination for the Investigation of Paintings, A Handbook for Conservator-Restorers," Centro Di Firenze (2009).

[Pye 2001] E. Pye, "Caring for the Past: Issues in Conservation for Archaeology and Museums," London: James and James (2001).

[Radon 1917] J. Radon, "U¨ ber die Bestimmung von Funktionen durch ihre Integralwerte langs gewisser Mannigfaltigkeiten," Ber. Ver. Sachs. Akad.Wiss. Leipzig, Math-Phys. Kl 69, 262-277 (1917).
In German: An english translation can be found in S. R. Deans: The Radon Transform and Some of Its Applications.

[Recur 2010] B. Recur, "Qualité et Précision en Reconstruction Tomographique: Algorithmes et Applications," Ph.D. thesis, LaBRI, University Bordeaux 1 (2010).

[Reid 2005] M. Reid, I. V. Cravetchi, and R. Fedosejevs, "Terahertz radiation and second-harmonic generation from InAs: Bulk versus surface electric-field induced contributions," Phys. Rev. B 72, 035201 (2005).

[Reklaitis 2010] A. Reklaitis, "Terahertz emission from InAs induced by photo-Dember effect: Hydrodynamic analysis and Monte Carlo simulations," Journal of Applied Physics 108, 053102 (2010).

[Renaud 2006] C. C. Renaud, M. Robertson, D. Rogers, R. Firth, P. J. Cannard, R. Moore, and A. J. Seeds, "A high responsivity, broadband waveguide uni-travelling carrier photodiode," Strasbourg France (2006).

[Rice 1994] A. Rice, Y. Jin, X. F. Ma, X.-C. Zhang, D. Bliss, J. Larkin and M. Alexander, "Terahertz optical rectification from <110> zinc-blende crystals," Appl. Phys. Lett. 64, 1324-1326 (1994).

[Rubens 1897] H. Rubens and E. F. Nichols, "Heat rays of great wave length," Physical review 4, No. 4, 314-323(1897).

[Ruffin 2001] A. B. Ruffin, J. Decker, L. Sanchez-Palencia, L. Lehors, J. F. Whitaker, T. B. Norris and J. V. Rudd, "Time reversal and object reconstruction using single-cycle terahertz pulses," Opt. Lett. 26, 681 (2001).

[Rungsawang 2004] R. Rungsawang, A. Mochiduki, S. Okuma, and T. Hattori, "Single-shot terahertz imaging," 14th International Conference on Ultrafast Phenomena, Technical Digest (CD), Optical Society of America, WB5 (2004).

[Saragoza 2008] F. Saragoza, "La collection thébaine du Dr Godard au musée d'Aquitaine," Revue archéologique de Bordeaux, tome IC, 131-151 (2008). In French.

[Schade 2004] U. Schade, K. Holldack, P. Kuske, G. Wüstefeld and H.-W. Hübers, "THz near-field imaging employing synchrotron radiation," Applied Physics Letters 84, 1422-1424 (2004).

[Schimer 2010] M. Schirmer, M. Fujio, M. Minami, J. Miura, T. Araki, and T. Yasui, "Biomedical applications of a real-time terahertz color scanner," Biomed Opt Express 1, No. 2, 354-366 (2010).

[Schuster 2011] F. Schuster, D. Coquillat, H. Videlier, M. Sakowicz, F. Teppe, L. Dussopt, B. Giffard, T. Skotnicki, and W. Knap, "Broadband terahertz imaging with highly sensitive silicon CMOS detectors," Optics Express 19, No. 8, 7828 (2011).

[Shao-wei 2003] W. Shao-Wei, W. Lu, X-S. Chen, Z-F. Li, X-C. Shen and W. Wen, "Two-dimensional photonic crystal at THz frequencies constructed by metal-coated cylinders," Journal of Applied Physics 93, 9401-9403 (2003).

[Shen 2005] Y. C. Shen, T. Lo, P. F. Taday, B. E. Cole, W. R. Tribe, and M. C. Kemp, "Detection and identification of explosives using terahertz pulsed spectroscopic imaging," Appl. Phys. Lett. 86, 241116 (2005).

[Shepp 1982] L. A. Shepp and Y. Vardi, "Maximum likelihood reconstruction for emission tomography," IEEE Trans. Med. Imaging 1, 113-122 (1982).

[Shiktorov 2006] P. Shiktorov, E. Starikov, V. Gružinskis, S. Perez, T. Gonzalez, L. Reggiani, L. Varani, and J.C. Vaissičre, "Theoretical investigation of Schottky barrier diode noise performance in external resonant circuits," Semicond. Sci. Tech.21, 550-557 (2006).

[Siegel 2002] P. H. Siegel, "Terahertz technology," IEEE T. Microw. Theory 50, 910-928 (2002).

[Staguhn 2003] J. G. Staguhn, D. J. Benford, F. Pajot, T. J. Ames, J. A. Chervenak, E. N. Grossman, K. D. Irwin, B. Maffei, S. H. Moseley, T. G. Phillips, C. D. Reintsema, C. Rioux, R. A. Shafer, and G. M. Voellmer, "Astronomical demonstration of superconducting bolometer arrays," Proc. SPIE 4855, 100-107 (2003).

[Stoik 2008] C. D. Stoik, M. J. Bohn, J. L. Blackshire, "Nondestructive evaluation of aircraft composites using transmissive terahertz time domain spectroscopy," Opt. Express 16, No. 21, 17039-17051 (2008).

[Stoner 2005] J. H. Stoner, "Changing Approaches in Art Conservation: 1925 to the present," Sackler NAS Colloquium Scientific Examination of Art: Modern Techniques in Conservation and Analysis, Proceedings of the National Academy of Sciences, 41 (2005).

[Sunaguchi 2009] N. Sunaguchi, Y. Sasaki, N. Maikusa, M. Kawai, T. Yuasa, and C. Otani, "Depth-resolving terahertz imaging with tomosynthesis," Opt. Express 17, 9558-9570 (2009).

[Suzuki 2005] M. Suzuki and M. Tonouchi, "Fe-implanted InGaAs terahertz emitters for 1.56 μm wavelength excitation," Appl. Phys. Lett. 86, 051104 (2005).

[Takahashi 2004] H. Takahashi, M. Sakai, A. Quema, S. Ono, N. Sarukura, G. Nishijima, and K. Watanabe, "Physical origin of magnetically induced periodic structure observed in terahertz radiation spectrum emitted from InAs," J. Appl. Phys. 95, 4545 (2004).

[Takayanagi 2009] J. Takayanagi, H. Jinno, S. Ichino, K. Suizu, M. Yamashita, T. Ouchi, S. Kasai, H. Ohtake, H. Uchida, N. Nishizawa, and K. Kawase, "High-resolution time-of-flight terahertz tomography using a femtosecond fiber laser," Opt. Express 17, 7549-7555 (2009).

[Tani 1997] M. Tani, S. Matsuura, K. Sakai, and S. Nakashima, "Emission characteristics of photoconductive antennas based on low-temperature-grown GaAs and semi-insulating GaAs," Appl. Opt. 36, No. 30, 7853-7859 (1997).

[Tani 2002] M. Tani, M. Nakajima, S. Kono, K. Sakai, "Generation of ultra broadband terahertz radiation with a photoconductive emitter," Lasers and Electro-Optics Society, The 15th Annual Meeting of the IEEE 2, No. 2, 532-533 (10-14 Nov. 2002).

[Targowski 2004] P. Targowski, B. Rouba, M. Wojtkowski, and A. Kowalczyk, "The application of optical coherence tomography to non-destructive examination of museum objects," Stud. Conserv. 49, 107-114 (2004).

[Targowski 2006] P. Targowski, M. Gora, T. Bajraszewski, M. Szkulmowski, B. Rouba, T. Lekawa-Wyslouch, and L.Tyminska-Widmer, "Optical coherence tomography for tracking canvas deformation," Laser Chem. article ID 93658, (2006).

[Teppe 2006] F. Teppe, M. Orlov, A.El Fatimy, A. Tiberj, W. Knap, J. Torres, V. Gavrilenko, A. Shchepetov, Y. Roelens, and S. Bollaert, "Room temperature tunable detection of subterahertz radiation by plasma waves in nanometer InGaAs transistors," Appl. Phys. Lett. 89, 222109 (2006).

[Ter-Pogossian] M. Ter-Pogossian, M. Phelps, E. Hoffman, and N. Mullani, "A positron-emission transaxial tomograph for nuclear imaging (pett)," Radiography 114, 89-98 (1975).

[Testorf 1999] M. Testorf and M. Fiddy, "Diffraction tomography based on McCutchen's theorem," J. Opt. Soc. Am. A 16, 1806 (1999).

[Thomas 2005] G.H. Thomas, "Overview of nondestructive evaluation technologies," Proceedings in SPIE 2455, 6-9 (2005).

[Thomson 2010] M. D. Thomson, H.G. Roskos, "Extreme-bandwidth THz pulses from laser-generated air plasmas," Infrared Millimeter and Terahertz Waves (IRMMW-THz), 35th International Conference, 1-2 (5-10 Sep 2010).

[Toft 1994] P. Toft, "Iterative methods for reconstructing pet images," (1994).

[Toft 1996] P. Toft, "The Radon Transform: Theory and Implementation," Ph.D. thesis: Department of Mathematical Modelling, Section for Digital Signal Processing, Technical University of Denmark (1996).

[Valk 2002] N. C. J van der Valk and P. C. M Planken, "Electro-optic detection of sub-wavelength terahertz spot sizes in the near field of a metal tip," Appl. Phys. Lett. 81, 1558-60 (2002).

[Voelcker 1989] J. Voelcker, "The Gunn effect," IEEE Spectrum, 24 (July 1989).

[Wade 2008] A. Wade, G. Fedorov, D. Smirnov, S. Kumar, B. S. Williams, Q. Hu, and J. L. Reno, "Magnetic-field-assisted terahertz quantum cascade laser operating up to 225 K," Nat. Photonics 3, 41-45 (2008).

[Wallace 2008] V. P. Wallace, E. MacPherson, J. A. Zeitler and C. Reid, "Three dimensional imaging of optically opaque materials using nonionizing terahertz radiation," JOSA A 25, 3120-3133 (2008).

[Waller 1947] M. C. Waller, M. A. Seibert, "Studies of refractive indices of binary wax mixtures," The american oil chemists society 32, 709-712 (1947).

[Walther 2010] M. Walther, B. M. Fischer, A. Ortner, A. Bitzer, A. Thoman, H. Helm, "Chemical sensing and imaging with pulsed terahertz radiation," Bio. Anal. Chem. 397, 1009-1017 (2010).

[Wang 2003] S. Wang, B. Ferguson, D. Abbott, and X. C. Zhang, "T-ray imaging and tomography," J. Biol. Phys. 29, 247-256 (2003).

[Wang 2004] S. Wang and X-C. Zhang, "Pulsed terahertz tomography," J. Phys. D: Appl. Phys. 37, 1-36 (2004).

[Wang 2004a] Z. Wang, A. C. Bovik, H. R. Sheikh, and E. P. Simoncelli, "Image quality assessment: from error visibility to structural similarity," IEEE Trans. Image Process. 13 600-612 (2004).

[Wang 2007] Y. Wang, Z. Zhao, Z. Chen, K. Kang, B. Feng, and Y. Zhang, "Terahertz absorbance spectrum fitting method for quantitative detection of concealed contraband," J. Appl. Phys. 102, 113108 (2007).

[Wederberg 1995] T. C. Wederberg and J. J. Stamnes, "Experimental examination of quantitative imaging properties of optical diffraction tomography," J. Opt. Soc. Am. A 12, 493 (1995).

[Williams 2002] G. P. Williams, "Far-IR/THz radiation from the Jefferson Laboratory, energy recovered linac, free electron laser," Rev. Sci. Instrum. 73, 1461-1463 (2002).

[Wolf 1969] E. Wolf, "Three-dimensional structure determination of semitransparent objects from holographic data," Opt. Commun. 1, 153 (1969).

[Wu 1995] Q. Wu and X-C. Zhang, "Free-space electro-optic sampling of terahertz beam," Appl. Phys. Lett. 67, 3523 (1995).

[Xie 2006] X. Xie, J. Dai, and X.-C. Zhang, "Coherent control of THz wave generation in ambient air," Phys. Rev. Lett. 96, No. 7, 075005 (2006).

[Yahiaoui 2009] R.Yahiaoui, H. Němec, P. Kužel, F. Kadlec, C. Kadlec, and P. Mounaix, "Broadband dielectric terahertz metamaterials with negative permeability," Optics Letts. 34, No. 22 (2009).

[Yamamoto 2004] K. Yamamoto, M. Yamaguchi, F. Miyamaru, M. Tani, M. Hangyo, T. Ikeda, A. Matsushita, K. Koide, M. Tatsuno, and Y. Minami, "Non invasive inspection of C-4 explosive in mails by terahertz time-domain spectroscopy," Jpn. J. Appl. Phys. 43, 414-417 (2004).

[Yang 1971] K. H. Yang, P. L Richards and Y. R. Shen, "Generation of far-infrared radiation by picosecond light pulses in $LiNbO_3$," Appl. Phys. Lett. 19, 320-332 (1971).

[Yang 2008] J. Yang, R. Shang-chen, Z. Min and Z. Wei, "Real time continous wave imaging with a 1.63 THz OPTL and pyroelectric camera," Journal of optoelectrics Letters 4, No. 4, 295-298 (2008).

[Yasuda 2006] T. Yasuda, T. Yasui, T. Araki, and E. Abraham, "Real-time two-dimensional terahertz tomography of moving objects," Opt. Commun. 267, 128-136 (2006).

[Yasui 2008] T. Yasui, K. Sawanaka, A. Ihara, E. Abraham, M. Hashimoto and T. Araki, "Real-time terahertz color scanner for moving objects", Opt Express. 21, 1208-1221(2008).

[Yin 2009] X. Yin, B. W. H. Ng, B. Ferguson, and D. Abbott, "Wavelet based local tomographic image using terahertz techniques," Digit. Signal Process. 19, 750-763 (2009).

[Zeitler 2007] J. A. Zeitler, Y. Shen, C. Baker, P.F. Taday, M. Pepper, T. Rades "Analysis of coating structures and interfaces in solid oral dosage forms by three dimensional terahertz pulsed imaging," J Pharm Sci 96, 330-340 (2007).

[Zhang 1990] X. C. Zhang, B. B. Hu, J. T. Darrow and D. H. Auston, "Generation of femtosecond electromagnetic pulses from semiconductor surfaces," Appl. Phys. Lett. 56, No. 11 (1990).

[Zhang 1992] X-C. Zhang, X. F. Ma and Y. Jin, "Terahertz optical rectification from a nonlinear organic crystal," Appl. Phys. Lett. 61, 3080-3082 (1992).

[Zhao 2002] G. Zhao, R. N. Schouten, N. Van-der-Valk, W. T. Wenckebach, and P. C. M. Planken, "Design and performance of a THz emission and detection setup based on a semi-insulating GaAs emitter," Rev. Sci. Instrum. 73, No. 4, 1715-1719 (2002).

[Zhong 2005] H. Zhong, J. Xu, X. Xie, T. Yuan, R. Reightler, E. Madaras, and X-C. Zhang, "Non-destructive Defect Identification with Terahertz Time-of-Flight Tomography," IEEE sensors Journal 5, No. 2, 203 (April 2005).

[Zinoyev 2002] N. N. Zinovev, A. F. Fitzgerald, S. M. Strafford, D. J. Wood, F. A. Carmichael, R. E. Miles, M. A. Smith and J. M. Chamberlain, "Identification of tooth decay using terahertz imaging and spectroscopy," Twenty Seventh International Conference on Infrared and Millimeter Waves, (2002).

[Zurk 2007] L. Zurk, B. Orlowski, D. Winebrenner, E. Thoros, M. Leahy-Hoppa, and L. Hayden, "Terahertz scattering from granular material," J. Opt. Soc. Am. B 24, 2238-2243 (2007).

[Gunn Diode] http://gunn.winterwolf.co.uk/reports/interim (Gunn Diode oscillations)

[hw.Perry] http://www.hwperry.com/?p=873

[Nrao] http://www.nrao.edu/meetings/isstt/about.shtml

[Picarin] http://www.mtinstruments.com/thzlenses/index.htm

[Picometrix] http://www.picometrix.com/pico_products/terahertz_products.asp

[Radiography] http://en.wikipedia.org/wiki/Radiographic_testing

[Spectrum detector] http://www.spectrumdetector.com/pdf/whitepapers/LFWTHz05-10.pdf

[Thruvision] http://www.thruvision.com/

[Times] http://www.nytimes.com/2002/04/21/magazine/the-leonardo-cover-up.html

[Tydex] http://www.tydexoptics.com/products/thz_optics/golay_cell/

[UV] http://www.intach.org/divi-m-heritage-wc-eoaw.asp?links=dhecs2c

http://staff.ee.sun.ac.za/wjperold/Research/Semiconductors/MC%20PDF/mtt98.PDF (Gunn diode fundamentals and fabrication)

Contributions of Author

Articles in International Journals

[J1] E. Abraham, **A. Younus**, A. El Fatimy, J.C. Delagnes, E. Nguéma and P. Mounaix: "Broadband terahertz imaging of documents written with lead pencils", Opt. Commun. 282 (2009) 3104-3107.

[J2] A. El Fatimy, J. C. Delagnes, **A. Younus**, E. Nguema, F. Teppe, W. Knap, E. Abraham and P. Mounaix: "Wave field effect transistor as a resonant detector for 1 Terahertz imaging applications", Opt. Commun. 282 (2009) 3055-3058.

[J3] **A. Younus**, P. Desbarats, S. Bosio, E. Abraham, J.C. Delagnes, P. Mounaix: "Terahertz dielectric characterization of photopolymer resin used for the fabrication of 3D THz imaging phantoms", Electron. Lett. 45(13), (2009) 702-703.

[J4] E. Abraham, **A. Younus**, J.C. Delagnes and P. Mounaix: "Non-invasive investigation of art paintings by terahertz imaging", Appl. Phys. A. Materials Science and Processing, 100(3) (2010) 585-590.

[J5] E. Abraham, **A. Younus**, C. Aguerre, P. Desbarats and P. Mounaix: "Refraction losses in terahertz computed tomography", Opt. Commun. 283 (2010) 2050-2055

[J6] B. Recur, **A. Younus**, S. Salort, P. Mounaix, B. Chassagne, P. Desbarats, J-P. Caumes and E. Abraham : "Investigation on reconstruction methods applied to 3D terahertz computed tomography", Opt. Express, 19(6) 5105–5117 (2011).

[J7] **A. Younus**, J. C. Delagnes, E. Abraham, L. Canioni, M. Fabre and P. Mounaix, "Spectroscopy and terahertz imaging for sigillography applications", J. Europ. Opt. Soc. Rap. Public. 11002 Vol 6 (2011).

[J8] J-P. Caumes, **A. Younus**, S. Salort, B. Chassagne, B. Recur, A. Ziéglé, A. Dautant, and E. Abraham, "Terahertz tomographic imaging of XVIIIth Dynasty Egyptian sealed pottery", APPLIED OPTICS, Vol. 50, No. 20 (10 July 2011).

[J9] **A. Younus**, J-P. Caumes, S. Salort, B. Chassagne, A. Dautant, A. Ziéglé and E. Abraham, Advances in optical technologies, 2011 (Accepted).

Proceedings of International/National Conferences

[P1] **A. Younus**, C. Aguerre, E. Abraham, P. Desbarats and P. Mounaix : « Imagerie terahertz : Super-résolution 2D et reconstruction 3D d'objets en volume », J. Phys. IV (2009).

[P2] **A. Younus**, S. Salort, J-P. Caumes, P. Mounaix and E. Abraham : "Millimeter continuous wave imaging for non-destructive investigation of artistic materials", Proceedings of IEEE Conference in 33rd International Conference on Infrared, Millimeter and Terahertz Waves, IRMMW-THz 2010, Rome.

[P3] **A. Younus**, S. Salort, J-P. Caumes, P. Desbarats, P. Mounaix and E. Abraham : "Non-destructive inspection of opaque objects with a 3D millimeter-wave tomographic scanner", Proceedings of IEEE Conference in 33rd International Conference on Infrared, Millimeter and Terahertz Waves, IRMMW-THz 2010, Rome.

[P4] E. Abraham, **A. Younus**, J.C. Delagnes, and P. Mounaix : "Terahertz-pulse imaging for non-destructive analysis of layered art paintings", Proceedings of IEEE Conference in 33rd International Conference on Infrared, Millimeter and Terahertz Waves, IRMMW-THz 2010, Rome.

[P5] E. Abraham, **A. Younus**, C. Aguerre, P. Desbarats, and P. Mounaix : "Consideration of refraction losses for time-domain terahertz computed tomography", Proceedings of IEEE Conference in 33rd International Conference on Infrared, Millimeter and Terahertz Waves, IRMMW-THz 2010, Rome.

[P6] **A. Younus**, S. Salort, B. Recur, P. Desbarats, P. Mounaix, J-P. Caumes and E. Abraham : "3D millimeter wave tomographic scanner for large size opaque object inspection with different refractive index contrasts", in Millimetre Wave and Terahertz Sensors and Technology III, K.A. Krapels and N.A. Salmon, eds. Proc. SPIE **7837**, 783709-1 – 783709-7 (2010), doi:10.1117/12.867943.

[P7] **A. Younus**, P. Mounaix, S. Salort, J.P. Caumes, B. Recur, J.P. Domenger, P. Desbarats and E. Abraham, "Fresnel losses in terahertz computed tomography", EOSAM 2010 TOM—THz Sci.Technol., Paris, France, (2010) 26–27.

Oral Presentations in International/National Conferences

[O1] **A. Younus**, J.C. Delagnes, E. Abraham and P. Mounaix : « Imagerie terahertz pour l'analyse des œuvres d'art », oral communication at Journées des Phénomènes Ultrarapides, Talence, 27-30 avril 2009.

[O2] **A. Younus**, J.C. Delagnes, E. Abraham and P. Mounaix : « Imagerie terahertz hyperspectrale : applications au contrôle non destructif de matériaux et à l'analyse des œuvres d'art », oral communication at 5^{e} journées Terahertz, Villeneuve d'Asc, 10-12 juin 2009.

[O3] **A. Younus**, P. Mounaix, S. Salort, J.P. Caumes, B. Recur, J.P. Domenger, P. Desbarats and E. Abraham : "Fresnel losses in terahertz computed tomography", oral communication in EOS Annual Meeting 2010, Paris, 26-29 octobre 2010.

[O4] **A. Younus**, J.C. Delagnes, E. Abraham and P. Mounaix : **«** Broadband terahertz imaging for non-invasive evaluation of written documents », oral communication at E-MRS (European Materials Research Society) Spring Meeting , Symposium : Precise processing of materials for art diagnostics, characterization, identification & restoration, Strasbourg, 8-12 juin 2009.

[O5] **A. Younus**, E. Abraham, P. Mounaix, S. Salort, J-P. Caumes, B. Recur, J.-P. Domenger and P. Desbarats : "Three-dimensional terahertz computed tomography for the inspection of opaque objects", oral communication at 2nd Conference on 3D-Imaging of Materials and Systems 2010 (3D IMS 2010), Hourtin, 6-10 sept. 2010.

[O6] E. Abraham **A. Younus**, J.C. Delagnes, and P. Mounaix : "Terahertz-pulse imaging for non-destructive analysis of layered art paintings », oral communication in IRMMW-THz 2010, Rome, 5-10 sept. 2010.

[O7] **A. Younus**, S. Salort, J-P. Caumes, P. Desbarats, P. Mounaix and E. Abraham : "3D millimeter wave tomographic scanner for large size opaque object inspection with different refractive index contrasts", oral communication in SPIE Europe Security and Defense 2010, Toulouse, 20-23 sept. 2010.

Posters Presented in International/National Conferences

[P1] **A. Younus**, C. Aguerre, E. Abraham, P. Desbarats and P. Mounaix : « Super-résolution 2D appliquées à l'imagerie terahertz et reconstruction 3D d'objets en volume », poster at 5e journées Terahertz, Villeneuve d'Asc, 10-12 juin 2009.

[P2] **A. Younus**, C. Aguerre, E. Abraham, P. Desbarats and P. Mounaix : « Imagerie terahertz : Super-résolution 2D et reconstruction 3D d'objets en volume », poster at Coloq11, Nice, 7-9 sept. 2009, J. Phys. IV (2009).

[P3] E. Abraham, **A. Younus**, J.C. Delagnes and P. Mounaix, « Terahetz imaging for 2D and 3D inspection of opaque materials », poster at 4th Annual Symposium of Japanese-French Frontiers of Science, Futuroscope (Poitiers), 21-24 janvier 2010.

[P4] **A. Younus**, S. Salort, J-P. Caumes, P. Mounaix and E. Abraham : "Millimeter continuous wave imaging for non-destructive investigation of artistic materials", poster at IRMMW-THz 2010, Rome, 5-10 sept. 2010.

[P5] **A. Younus**, S. Salort, J-P. Caumes, P. Desbarats, P. Mounaix and E. Abraham : "Non-destructive inspection of opaque objects with a 3D millimeter-wave tomographic scanner", poster at IRMMW-THz 2010, Rome, 5-10 sept. 2010.

[P6] E. Abraham **A. Younus**, C. Aguerre, P. Desbarats and P. Mounaix : "Consideration of refraction losses for time-domain terahertz computed tomography", poster at IRMMW-THz 2010, Rome, 5-10 sept. 2010.

2D and 3D Terahertz Imaging: Application to Art Science

The scope of this thesis is to demonstrate the potential of terahertz (THz) imaging for non-destructive evaluation of various artworks associated with a complete 3D volumetric inspection. For this purpose we used a pulsed THz time-domain spectrometer and a portable millimeter continuous wave scanner. Time-of-flight of THz electric field and material dependent spectroscopic information allows the analysis of various artistic samples. THz imaging was able to reveal buried layer information, covered by several layers of painting and plaster. It was also possible to evaluate the variations of the painting thickness along with their spectroscopic features in the THz range. The portable imaging system was used for the inspection of real historical art samples preserved at museum of Aquitaine (France). THz computed tomography has been performed for visualizing volumetric objects. Different reconstruction methods have been compared in order to enhance final image quality with the optimization of the number of projections. Finally the tomographic technique was used for a complete 3D inspection of historical art objects.

Keywords: Terahertz, optical systems, spectroscopy, imaging, tomography.

Imagerie Térahertz 2D et 3D: Application pour l'étude des Matériaux du Patrimoine Culturel

La portée de cette thèse est de montrer le potentiel de l'imagerie térahertz (THz) pour l'évaluation non-destructive et non-invasive d'objets liés à notre héritage culturel. A cette fin, nous avons développé un spectro-imageur THz permettant une analyse spectroscopique des objets sur la gamme de fréquence 0-3 THz. Le système permet aussi de mesurer des variations d'épaisseur inférieures à 30 µm suite à une analyse du « temps de vol » lié à la propagation des impulsions THz entre l'émetteur et le détecteur. Ainsi, nous avons pu révéler des esquisses dissimulées sous diverses couches de peinture ou de plâtre. Nous avons également mis au point un scanner THz portable monochromatique pour une analyse tomographique des objets. Après une étude en laboratoire, une campagne de mesures a été réalisée au Musée d'Aquitaine (France) afin de démontrer l'intérêt de ce système de caractérisation optique 3D pour diverses pièces du musée et notamment certaines antiquités égyptiennes vieilles de 3500 ans qui ont pu ainsi livrer une partie de leurs mystères.

Mots-clés: Térahertz, optique, analyse spectroscopie, imagerie, tomographie.

Laboratoire Ondes et Matière d'Aquitaine, UMR 5798

Université de bordeaux 1, 351 Cours de la libération, 33405 Talence